Physics of the Solid State, Vol. 44, No. 12, 2002, pp. 2211–2215. Translated from Fizika Tverdogo Tela, Vol. 44, No. 12, 2002, pp. 2113–2116.
Original Russian Text Copyright © 2002 by Tkachuk.

SEMICONDUCTORS AND DIELECTRICS

X Centers in ZnSe⟨Ga⟩ and ZnSe⟨As⟩ Single Crystals

P. N. Tkachuk
Chernovtsy National University, Chernovtsy, 58012 Ukraine
e-mail: ptkachuk@chnu.cv.ua

Received December 13, 2001

Abstract—The results of experimental studies of the energy spectrum of *X* centers in ZnSe⟨Ga⟩ and ZnSe⟨As⟩ single crystals are presented; the results are in accord with the available calculations. The Stokes shift, the stabilization of the Fermi level near the extrema of allowed bands of ZnSe, anomalies in thermoluminescence and interband photoluminescence, and some other effects are explained on the basis of configuration-coordinate diagrams for associated defects V_{Zn}–Ga_i and V_{Se}–As_i, taking into account tetrahedral and hexagonal positions of interstitial atoms. The absence of residual photoconductivity is attributed to the presence of *r*- and *s*-recombination centers in the crystals.© *2002 MAIK “Nauka/Interperiodica”.*

1. INTRODUCTION

The *X* centers in semiconducting crystals are characterized by a strong electron–phonon interaction leading to the emergence of barriers between different charge states of the system in the configuration space. Specific effects, such as the Stokes shift and residual photoconductivity, can be observed in this case. In addition, strong polarization of the lattice in the vicinity of an impurity atom brings about, in some cases, the formation of a state with a negative correlation energy (U^- centers), which leads to a peculiar statistics of charge carriers manifested in the stabilization of the Fermi level irrespective of the concentration of other impurities.

The mechanism of formation of U^- centers in the course of separate doping of ZnSe by shallow hydrogen-like impurities Ga_{Zn} and As_{Se} has been mainly studied theoretically [1–3]. The authors of those publications used a model of crystal lattice distortion according to which a displacement of a center-forming atom along the [111] direction to the nearest interstitial site leads to rupture of the bond with an atom of the neighboring sublattice, which is accompanied by the trapping of an additional charge carrier at the neutral states of a donor (d^0) or an acceptor (a^0). In this case, a Ga : *DX* center (state D^-) forms a metastable resonance level above the minimum of the conduction band, while an As : *AX* center (state A^+) forms a stable level in the forbidden gap below the state a^0. The results of new calculations performed in [2] on the basis of this model indicate the possible formation of a neutral state A^0.

The experimental analysis of deep lying centers in ZnSe with a heterovalent substitution of components is complicated by a complexity of phenomena typical of wide-band $A^{II}B^{VI}$ compounds, such as monopolar conductivity, low efficiency of doping with group V elements, complex formation, compensation of the effect of the introduced impurity, and the presence of rapid (*r*) and slow (*s*) recombination centers. In this connection, new concepts concerning the configuration of *X* centers in ZnSe may appear as a result of accumulating experimental data. Some aspects of the problem are considered in this communication.

2. SAMPLES AND EXPERIMENTAL TECHNIQUE

Zinc selenide single crystals were grown by the method of chemical transport reactions (CTR). The maximal doping level was 0.1–0.4 at. % for the As impurity and 1.0 at. % for the Ga impurity. It was shown in [4] that, due to the limited solubility of these crystals, an increase (>0.1 at. %) in the As doping level can be attained by introducing Ga and As simultaneously into the crystal lattice of ZnSe; however, the electrical parameters of ZnSe⟨Ga,As⟩ samples are identical to those of ZnSe⟨Ga⟩ crystals.

We investigated high-resistivity ZnSe⟨Ga⟩ samples ($\sigma = 2.0 \times 10^{-11}$–$4.2 \times 10^{-12}$ Ω^{-1} cm^{-1}, $n = 3.3 \times 10^4$–4.0×10^6 cm^{-3}) and ZnSe⟨As⟩ samples ($\sigma < 10^{-10}$ Ω^{-1} cm^{-1}, $p < 10^7$ cm^{-3}). Some of the measurements were made on ZnSe⟨Ga,As⟩ samples. Calculations show that the strong-doping condition ($a^3N \gg 1$, where a is the Bohr radius and N is the maximum impurity concentration) does not hold for either type of impurity. Taking into account the small values of concentration of free charge carriers, we can treat such crystals as strongly compensated semiconductors. It should be noted that the effect of introduced impurities can be compensated both through the generation of intrinsic defects in the crystal lattice of ZnSe and as a result of transitions between shallow and deep levels during the formation of *X* centers [5].

The methods of studying thermoluminescence (TL) of samples and of determining the thermal activation

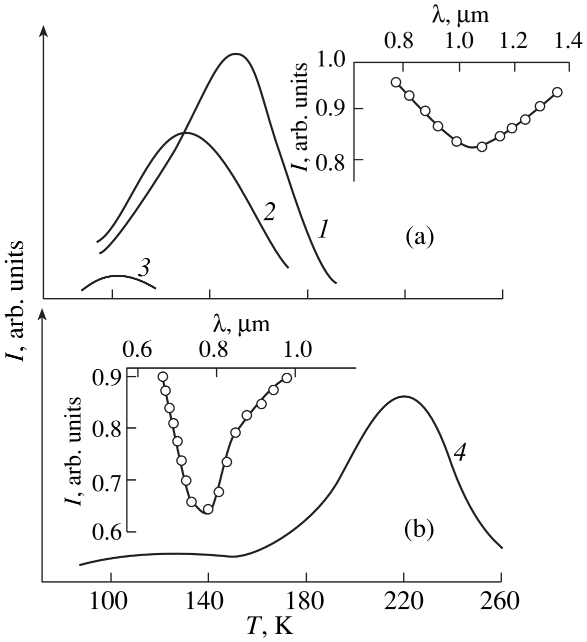

Fig. 1. Thermoluminescence curves for single crystals of (*1*) ZnSe⟨0.1 at. % Ga⟩, (*2*) ZnSe⟨0.5 at. % Ga⟩, (*3*) ZnSe⟨0.1 at. % Ga⟩ annealed in strongly saturated Zn vapor, and (*4*) ZnSe⟨0.1 at. % As⟩. The insets show the spectral dependences of IR photocurrent quenching ($T = 300$ K) for samples (a) ZnSe⟨0.1 at. % Ga⟩ and (b) ZnSe⟨0.9 at. % Ga, 0.4 at. % As⟩.

energy E_t of deep centers from the thermoluminescence curves are described in [6]. The spectrum of TL was studied using a set of standard light filters. The optical activation energy E_o was estimated from the long-wavelength boundary of the spectral dependences of infrared quenching of photoconduction (IRQP): $I = I_1/I_0 \sim \lambda$ (I_1 is the photocurrent value in the presence of quenching monochromatic radiation, and I_0 is the photocurrent intensity excited by background radiation from an incandescent lamp).

Thermal (E_t) and optical (E_o) activation energies of local states in ZnSe crystals taking into account the available data from the literature

Center	State	E_t, eV	E_o, eV
Ga : *DX*	d^0	0.0036 [7]	–
	D^0	0.26	0.75
	D^-	~0.4	1.55
			1.53* [1]
As : *AX*	a^0	~0.1	–
	A^0	0.6	1.28
		0.6** [8]	1.2* [2]
	A^+	–	~2.15** [2]

*Calculated value, **experimental value.

The photoluminescence (PL) spectra were excited at 300 and 77 K by molecular-nitrogen laser radiation ($E = 3.51$ eV, $\tau_i = 8$ ns). Standard schemes of photoelectric recording and synchronous detection were used. A diffraction monochromator with a linear dispersion of 12 Å/mm was used as the dispersive device. The optical excitation level was 10^{23} cm^{-2} s^{-1}.

3. EXPERIMENTAL RESULTS AND DISCUSSION

Analysis of the TL of ZnSe⟨Ga⟩ single crystals (curves *1*–*3* in Fig. 1) at 100, 130, and 150 K gives values of E_t equal to 0.20, 0.26, and ~0.4 eV, respectively. A low-intensity TL peak at 100 K takes place only for samples prepared in an excess-zinc atmosphere (such a thermoluminescence is also observed for ZnSe crystals grown from melt [6]). In a higher temperature range, a TL peak is observed for the ZnSe sample (0.1 at. % As) (curve *4* in Fig. 1); analysis of this peak gives the value $E_t = 0.6$ eV. The values of E_0 for deep centers, whose classification is given in the table, are determined from the IRQP spectral dependences for the corresponding samples (see insets to Fig. 1).

The PL spectra at 300 K (both for the initial ZnSe and doped crystals) have the form of a wide band (ΔE = 60 meV) with a peak at 2.72 eV. The luminescence features for ZnSe at room temperature are due to many-particle effects [9], which are not considered here. Only the following remark should be made. Upon an increase in the gallium doping level, the value of ΔE increases, the PL intensity decreases, and no radiation is observed for an impurity concentration of 1.0 at. %. On the contrary, the introduction of an arsenic impurity increases the radiation intensity, while the value of ΔE decreases insignificantly.

Curves *1*–*3* in Fig. 2a show the exciton PL spectra of crystals at 77 K. For a purposefully undoped ZnSe sample, a free exciton emission line localized at 2.793 eV is observed. The introduction of As impurity in an amount up to 0.01% leads to the emergence of a line localized at 2.780 eV whose intensity is much higher than that corresponding to the emission of a free exciton; i.e., the features typical of exciton–impurity complexes (EIC) are manifested. The activation energy of the a^0 state (~0.1 eV) can be determined from the binding energy of an exciton at a neutral acceptor. An increase in the As impurity concentration (up to 0.05%) leads to broadening of the EIC line, the position of its peak becoming less determinate. At a concentration equal to 0.1%, the nature of luminescence changes since a strongly extended wing in the low-energy region appears (curve *3* in Fig. 2b).

Calculations of the Debye radius R_e (taking into account the Debye–Hückel correlations [10]) and of the exciton radius R_{ex} show that $R_e < R_{\text{ex}}$ for both types of

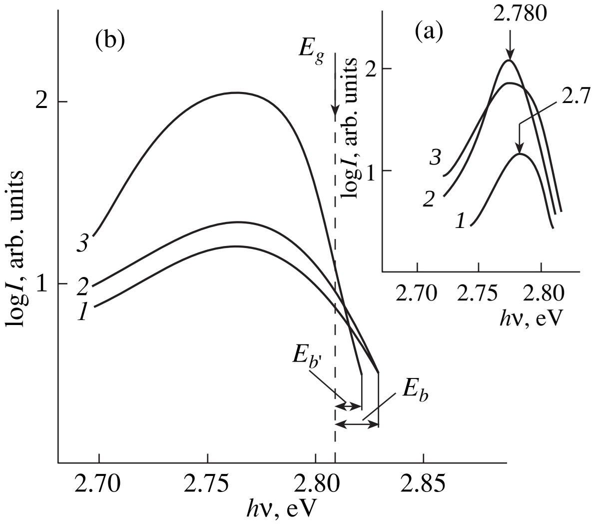

Fig. 2. (a) Exciton and (b) interband photoluminescence spectra at $T = 77$ K for (a) (*1*) ZnSe, (*2*) ZnSe⟨0.01 at. % As⟩, and (*3*) ZnSe⟨0.05 at. % As⟩; and (b) (*1*) ZnSe⟨0.1 at. % Ga⟩, (*2*) ZnSe⟨0.5 at. % Ga⟩, and (*3*) ZnSe⟨0.1 at. % As⟩.

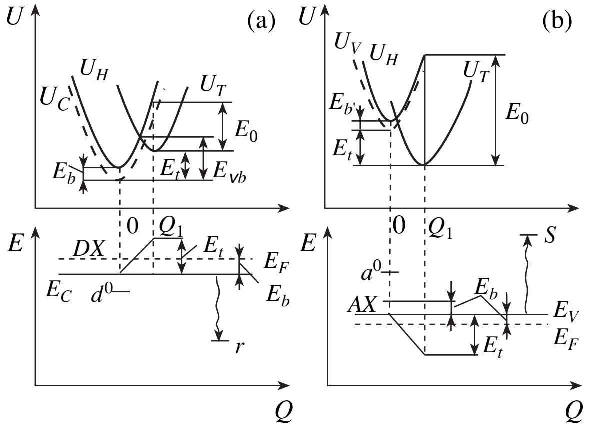

Fig. 3. Configuration-coordinate diagrams for (a) Ga : *DX* and (b) As : *AX* centers in ZnSe single crystals. $U_{T(H)}$ is the crystal–*X*-center energy in the case of a tetrahedral (hexagonal) position of a center-forming atom in the interstitial position, $U_{C(V)}$ is the crystal–free-electron (hole) energy, E is the energy of a free charge carrier, $E_{b(b')}$ is the binding energy of an electron (hole), and E_{vb} is the vibronic barrier between the ionized and nonionized states of an *X* center.

impurity if the concentration exceeds 0.1 at. %. Thus, excitons cannot be formed and the most probable mechanism of edge luminescence is interband recombination of charge carriers; the long-wavelength radiation wing can be attributed to the formation of impurity bands and density-of-states tails.

The location of the high-energy wing in the edge PL for doped crystals in the energy range above E_g (Fig. 2b) is considered to be a feature of degenerate semiconductors. A similar spectral distribution of the PL intensity was observed in [11] for degenerate low-resistivity CdS⟨Cl⟩ crystals; however, we did not observe any short-wavelength shift of the emission line upon an increase in the concentration of Ga impurity (curves *1*, *2* in Fig. 2b).

3.1. Local States

The data presented in the table lead to the following conclusions.

1. The existence of the a^0 state indicates a high structural perfection of the crystals (see, e.g., [12]), since a more stable, strongly relaxed state A^0 usually dominates in experimental investigations [8].

2. Two values of E_t (0.26 and ~0.4 eV) correspond to two charge states (D^0 and D^-) of a Ga : *DX* center; the value of E_t equal to 0.6 eV corresponds to the neutral charge state (A^0) of an As : *AX* center.

3. Two experimental values of E_0 (1.55 and 1.28 eV) virtually coincide with the calculated energies of the D^- and A^0 states, respectively. The value of $E(D^-)$ equal to 1.53 eV is obtained from an analysis of the results obtained in [1], while the value of $E(A^0)$ equal to 1.2 eV was obtained in [2].

4. The ratio of the values of E_0 for the D^- and D^0 states agrees with the theoretical value of 2 determined in [1].

3.2. Configuration-Coordinate Diagram

If deep centers in ZnSe⟨Ga⟩ and ZnSe⟨As⟩ crystals are formed as a result of Jahn–Teller type lattice distortions, a vacancy (or a “part” of a vacancy) remains at a lattice site; i.e., associated defects V_{Zn}–Ga_i and V_{Se}–As_i are created. It should be noted that, according to [13], V_{Zn} is a deep (0.2–0.4 eV) acceptor, while V_{Se} is a shallow (0.01 eV) donor. This type of defect formation is confirmed (i) by the disappearance of thermoluminescence peaks of deep centers in ZnSe⟨Ga⟩ crystals grown with an excess of zinc and (ii) by a high intensity of the interband PL of ZnSe⟨0.1 at. % As⟩ single crystals, which can apparently be due to an increase in the charge carrier concentration in the allowed bands upon ionization of a defect pair and its element V_{Se}. In addition, we must take into account the position of Ga_i and As_i atoms which can occupy tetrahedral (*T*) or hexagonal (*H*) interstitial positions. It is these two positions that determine the two (*T* and *H*) configurations of associated defects with strongly differing binding energies of the charge carriers (curves U_T and U_H in Fig. 3). The U_H curves are closely spaced relative to the $U_{C(V)}$ curves; i.e., the state of the center is quite shallow relative to the allowed band of the host matrix. In the case of $A^{II}B^{VI}$ compounds, this type of model was used for the first time in [14] for CdTe⟨Cl⟩ crystals, wherein the role of the *X* center is played by the associated complex Cl_{Te}–Cl_i. Thus, the binding energy $E_{b(b')}$ of a charge carrier for the *H* configuration of an associated defect has an insignificant (negative or positive) value, which leads to ionization of the center at the thermoluminescence temperature of the crystals. Therefore (see Fig. 3), the value of the activation energy E_t measured using the TL method characterizes the energy barrier separating the *T* and *H* configurations of the center (with allowance for $E_{b(b')}$). On the other hand, the value of activation energy E_0 determines the depth of traps relative to the allowed bands and the application of the Franck–Condon principle concerning the invariability of the configuration coordinate in an optical transition explains the Stokes shift, viz., the difference in the values of E_0 and E_t (see table).

It should be noted that classical *X* centers are characterized not only by the Stokes shift but also by a large lifetime of charge carriers photoexcited at low temperatures (residual photoconductivity), which is due to the presence of a vibronic barrier (E_{vb}) between the ionized and nonionized states of a deep center. However, we did not observe any residual photoconductivity in the temperature interval 77–300 K, which can apparently be explained using the following arguments. First, a charge carrier may be localized at a center in the *H* configuration at low temperatures ($kT < E_{b(b')}$). Second, as the temperature increases ($kT > E_{b(b')}$), released electrons (holes) may recombine in the allowed band with holes (electrons) trapped at the *r*(*s*) centers of the host ZnSe matrix (Fig. 3). The latter mechanism is supported by the correspondence of the spectral composition of the low- and high-temperature TL (radiative transitions in Fig. 3) to the energy position of the *s* and *r* recombination centers (see [6]).

3.3. Stabilization of the Fermi Level

We assume that an associated defect in the *T* configuration at liquid-nitrogen temperature is excited by high-power laser radiation. Optical excitation (ionization) of a deep center leads to a nonequilibrium state of the crystal lattice, and the center passes jumpwise to a more stable shallow state (*H* configuration).

The probability that photoexcited charge carriers possess the required minimal energy for localization in this stable state of the system is given by [15]

$$f(E_b) = [1 + \exp(E_b - E_F)/kT]^{-1}. \qquad (1)$$

For strongly compensated ZnSe samples, the Fermi level is located near the middle of the forbidden gap (E_g = 2.7 eV at 300 K) and, in the entire temperature range, we have $(E_b - E_F)/kT \gg 1$. In this case, the stable existence of a Ga : *DX* center in the *H* configuration ensures the stabilization of the Fermi level near the minimum of the conduction band ($E_b = E_F$). This effect is confirmed by the absence of a shift in the high-energy wing of the edge PL (curves *1*, *2* in Fig. 2b) upon an increase in the impurity concentration. The same considerations concerning the location of the Fermi level near the top of the valence band are apparently also valid for the samples ZnSe⟨0.1 at. % As⟩. Unfortunately, the limited solubility of arsenic in the zinc selenide matrix does not permit one to analyze the dependence of the position of the interband PL line for impurity concentrations >0.1 at. %.

It would be interesting to analyze the stability of associated defects. In the framework of the model described in [16], the recombination barrier separating an interstitial position from a vacancy decreases sharply as a result of ionization of one of the elements of a defect pair under the action of laser radiation. In this simplest case, the probability of recombination of the pair in the absence of degeneracy is determined by a dependence similar to Eq. (1). The inclusion of degeneracy gives a value of recombination probability lower than 0.3.

4. CONCLUSIONS

The experimental study of single crystals of ZnSe⟨Ga⟩ and ZnSe⟨As⟩ leads to the following conclusions.

(1) The energy spectrum of *X* centers is in accord with the available calculated data.

(2) Anomalies in the thermoluminescence and edge photoluminescence and the effect of stabilization of the Fermi level near extrema of the allowed bands of zinc selenide can be explained with the use of a configuration-coordinate diagram taking into account the difference in the positions of the interstitial atom in associated pairs V_{Zn}–Ca_i and V_{Se}–As_i.

ACKNOWLEDGMENTS

The author is deeply indebted to O.G. Sarbeĭ and N.D. Raranskiĭ for discussion of the results and for valuable comments.

REFERENCES

1. D. J. Chadi, Phys. Rev. Lett. **72**, 534 (1994).
2. D. J. Chadi, Appl. Phys. Lett. **59** (27), 3589 (1991).
3. D. J. Chadi and K. J. Chang, Appl. Phys. Lett. **55**, 575 (1989).
4. A. V. Voĭtsekhovskiĭ, N. P. Baran, and P. N. Tkachuk, Izv. Akad. Nauk SSSR, Neorg. Mater. **14**, 2177 (1978).
5. Y. Marfaing, J. Cryst. Growth **161**, 205 (1996).
6. V. S. Blashkiv, V. S. Manzhara, P. N. Tkachuk, and V. M. Tsmots', Fiz. Tekh. Poluprovodn. (Leningrad) **14**, 1621 (1980) [Sov. Phys. Semicond. **14**, 961 (1980)].

7. G. N. Ivanova and D. D. Nedeoglo, Fiz. Tekh. Poluprovodn. (Leningrad) **13**, 37 (1979) [Sov. Phys. Semicond. **13**, 21 (1979)].
8. R. H. Bube and E. L. Lind, Phys. Rev. **110**, 1040 (1958).
9. R. Baltramiejunas, J. Vaitkus, and É. Kuokstis, Litov. Fiz. Sb. **19**, 809 (1979).
10. A. P. Levanyuk and V. V. Osipov, Fiz. Tekh. Poluprovodn. (Leningrad) **7**, 1069 (1973) [Sov. Phys. Semicond. **7**, 727 (1973)].
11. V. Chvostov, M. Moin, and E. Salkov, Phys. Status Solidi A **26**, 261 (1974).
12. T. Yao and Y. Okada, Jpn. J. Appl. Phys. **25**, 821 (1986).
13. J. Jacobs and H. Arnold, Krist. Tech. **10**, K71 (1975).
14. R. Legros, Y. Marfaing, and R. Triboulet, J. Phys. Chem. Solids **39**, 179 (1978).
15. D. J. Chadi and K. J. Chang, Phys. Rev. B **39**, 10063 (1989).
16. J. Bourgoin and M. Lannoo, *Point Defects in Semiconductors* (Springer, New York, 1983; Mir, Moscow, 1985).

Translated by N. Wadhwa

Physics of the Solid State, Vol. 44, No. 12, 2002, pp. 2216–2218. Translated from Fizika Tverdogo Tela, Vol. 44, No. 12, 2002, pp. 2117–2119.
Original Russian Text Copyright © 2002 by Agekyan, Il'chuk, Rud', Stepanov.

Photoluminescence of ZnTe and CdTe Single Crystals Grown with Halogen-Containing Transport Gases

V. F. Agekyan*, G. A. Il'chuk, Yu. V. Rud'***, and A. Yu. Stepanov***
** Institute of Physics, St. Petersburg State University, ul. Pervogo Maya 100, Petrodvorets, 198504 Russia*
*** Lviv Politekhnika National University of Ukraine, Lviv, 79013 Ukraine*
**** Ioffe Physicotechnical Institute, Russian Academy of Sciences,*
Politekhnicheskaya ul. 26, St. Petersburg, 194021 Russia

Received February 12, 2002

Abstract—Bulk ZnTe and CdTe single crystals were grown using Cl-, Br-, and I-containing transporting gas agents. Photoluminescence spectra consisting of a free-exciton band and a low-energy band of extrinsic origin were studied at various temperatures, excitation levels, and time delays. It is shown that the low-energy band can be assigned to the emission of donor–acceptor pairs. No noticeable differences were observed between the emission spectra of crystals grown with Cl, Br, and I. © *2002 MAIK "Nauka/Interperiodica".*

1. INTRODUCTION

The effect that the technology of growth and subsequent processing exerts on the optical and electrical properties of bulk II–VI single crystals is presently enjoying considerable attention despite the fact that these studies have had a long history. The interest focused on this area is initiated by new applications of binary crystals and solid solutions of the II–VI group, which stimulate progress in growth technologies. These crystals are employed to advantage as fast optical switches, detectors of ionizing radiation in nuclear physics and tomography, in Schottky barrier structures, etc. (see, e.g., [1–4]). In this connection, the response time of crystals to external factors, the ranges of linearity of their optical and electrical characteristics as a function of excitation intensity, and the noise level become important. These parameters depend on the elemental crystal composition and the type, concentration, and charge state of defects, as well as on the uniformity of their distribution [5]. The properties of crystals of CdTe and ZnTe and of their solid solutions are determined both by impurities and by intrinsic defects, in particular, by the vacancies, whose charge can be compensated by doping the crystal with Group VII elements. By doping a crystal during growth, one can control the concentration, structure, and passivation of structural defects. It is possible to create deep complex centers combining an intrinsic defect and an impurity, particularly in zinc compounds, which have cubic and hexagonal modifications. Such centers act as electron traps and usually confer semi-insulating properties to II–VI crystals, which improves the performance of these crystals as detectors of ionizing radiation. Group VII elements can be introduced by a variety of methods; it is well known that ZnTe and CdTe with a relatively low concentration of intrinsic defects can be prepared by chlorine doping in the course of crystallization. In specific cases, growth of II–VI crystals with the desired type of conduction encounters difficulties, which can be overcome through the simultaneous creation of donor and acceptor states [6].

We report here on the preparation of ZnTe and CdTe bulk single crystals doped uniformly by halogens and on an investigation of their photoluminescence (PL) spectra under pulsed pumping. The growth was carried out following the chemical transport method, with a halogen contained in the transport gas NH_4X, where X = Cl, Br, and I, doped into the lattice [7]. Simulation of the mass transport process where the starting material is a purposefully undoped ZnTe or CdTe crystal and comparison of the calculations with the amount of transported substance make it possible to conclude that the growth of cadmium and zinc tellurides has a diffusive character [8]. Single crystals of the best quality are grown at temperatures 750–850°C, which are substantially below the melting points of CdTe (1090°C) and ZnTe (1290°C). The single crystals grown from the vapor phase have natural specular faces and reach a size of $2 \times 3 \times 4$ mm after 100 h of deposition. When NH_4Cl and NH_4Br are used, the crystals obtained are always *n* type, whereas in the presence of NH_4I, both *n*- and *p*-type crystals can be prepared. In the latter case, the relative concentrations of the donor and acceptor defects are controlled by the growth conditions and can vary across the crystal thickness. The PL was excited by 5-ns-long nitrogen laser pulses generated at a repetition frequency of 100 Hz. Time-resolved PL spectra were measured at 4 and 80 K, with a delay t_0 with respect to the pump pulse varied from 0 to 100 ns and a measurement time of about 2 ns. Unless otherwise specified, the excitation level at the laser pulse maximum is considered to be about 10 kW/cm^2 in what follows.

2. ZINC TELLURIDE

ZnTe crystals grown with the use of different halogens exhibit identical PL spectra. The only difference is in the positions of the maxima of the low-energy band associated with defects (Fig. 1a). This band is characterized by slow kinetics as compared with the exciton emission in the 2.36-eV region; indeed, the rise time of its intensity to maximum is 3 ns and the decay time is about 50 ns (Fig. 1b). The separation between the exciton and the defect bands is about 0.13 eV and depends on the actual halogen used in crystal growth only weakly. The maximum of the defect band shifts weakly toward higher energies with increasing optical excitation level, and the band saturates under strong pumping. These properties and the energy position give one grounds to assign the 2.23-eV band to the emission of donor–acceptor pairs, with the donor level being due most likely to the halogen. The band maximum measured with delays t_0 = 0 and 40 ns is shifted toward lower energies compared to its position at t_0 = 3 ns (Fig. 1b). This also correlates with the donor–acceptor origin of the band, because at the beginning of the population process, as in its late enough stages, deeper levels corresponding to large-radius pairs are predominantly filled.

Inhomogeneous broadening associated with lattice defects provides a considerable contribution to the exciton band width; indeed, the narrowest exciton bands are observed in samples with a relatively low intensity of the donor–acceptor band. The comparatively small contribution of exciton–phonon coupling to the width of the exciton band is indicated by its narrowing only slightly with the temperature decreasing from 80 to 4 K. No significant modification of the exciton radiation corresponding to the free-to-bound exciton transition was observed to occur in our samples cooled to 4 K under the experimental conditions used.

3. CADMIUM TELLURIDE

The PL spectrum of CdTe consists of a free-exciton band at 1.58 eV and of a band peaking at about 1.44 eV (Fig. 2). The position of the maximum of this band varies depending on the actual halogen used in the growth more strongly than is the case with ZnTe. The luminescence rise and decay times at the maximum of the 1.44 eV band are close to those of the band observed for ZnTe; as the delay time increases, this band begins to dominate in the spectrum and its maximum shifts toward lower energies (Fig. 2). The 1.44-eV band saturates with increasing pumping level, and its maximum shifts toward higher energies (Fig. 2b). The difference between the CdTe band gap (1.63 eV) and the energy of the 1.44-eV band considerably exceeds the typical binding energies of donors in CdTe. Thus, the energy position and the kinetic characteristics of the band, as well as the effect of the pumping level on its profile, permit one to assign the band, as in the case of ZnTe, to donor–acceptor emission. The donor is apparently a halogen atom; as for the acceptor level, CdTe crystals grown without purposeful doping are usually *p* type. Structural defects are most likely involved in the formation of acceptor states. The spectra of CdTe crystals exhibit a strong spread in the relative intensities of the exciton and the defect bands.

At 4 K, an increase in the delay t_0 results in a shift of the maximum of the donor–acceptor band maximum toward lower energies (Fig. 3), which is one of the most characteristic properties of this band. The temperature dependence of the PL of the CdTe and ZnTe samples studied also supports the assignment of the low-energy

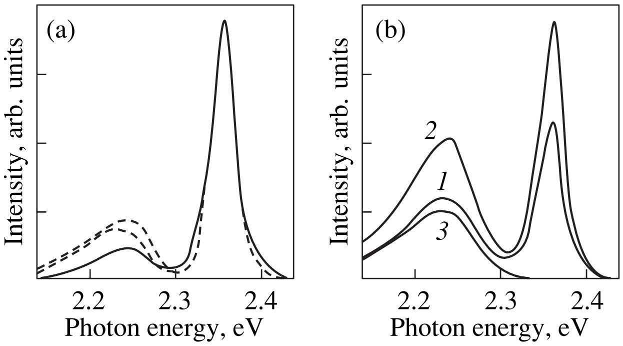

Fig. 1. Photoluminescence spectra of ZnTe single crystals grown with halogens obtained at 80 K: (a) spectra of three samples normalized against the exciton band intensity with delay time t_0 = 0 and (b) spectra of a ZnTe:Br crystal measured with delays t_0 equal to (*1*) 0, (*2*) 3, and (*3*) 40 ns.

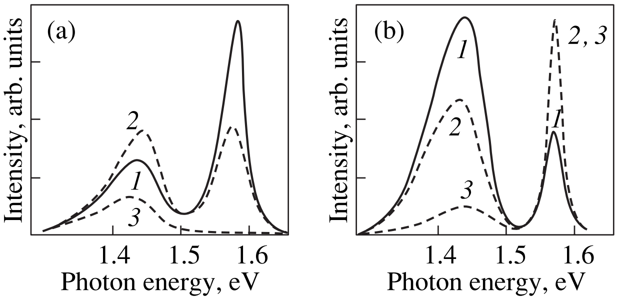

Fig. 2. Photoluminescence spectra of CdTe single crystals obtained at 80 K: (a) spectra of CdTe:Br measured with delays t_0 equal to (*1*) 0, (*2*) 3, and (*3*) 70 ns and (b) CdTe:I spectra normalized against maximum intensity and measured at excitation levels (*1*) 10, (*2*) 40, and (*3*) 250 kW/cm^2.

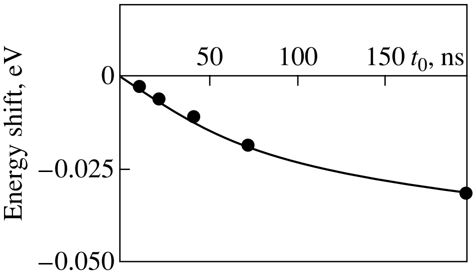

Fig. 3. Shift of the donor–acceptor band maximum in the CdTe : Br emission spectrum plotted vs. delay time t_0 for $T = 4$ K.

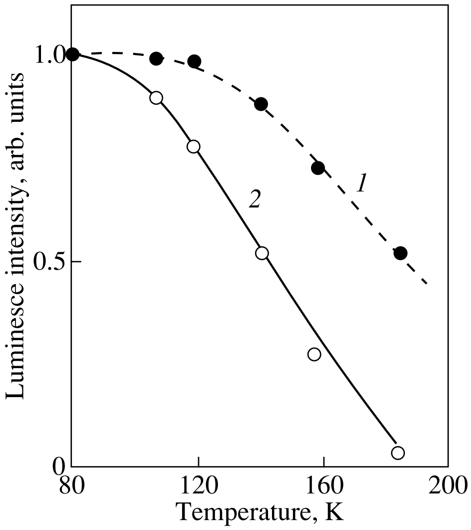

Fig. 4. Temperature dependence of the intensities of (*1*) exciton and (*2*) donor–acceptor emission bands of CdTe : I (the intensities of both bands are normalized to those at 80 K).

bands to interimpurity radiative recombination; indeed, as the temperature increases, these bands become progressively weaker in comparison with the exciton emission band (Fig. 4). This corroborates the involvement in the radiative process of a state with a binding energy considerably smaller than the energy separation between the interband transition edge and the maximum of the low-energy band.

Thus, 80-K PL spectra of ZnTe and CdTe crystals grown by the gas transport method with NH_4X as the transporting agent, where X stands for a halogen, exhibit free-exciton and donor–acceptor emission bands. Decreasing the temperature to 4 K does not modify the photoluminescence spectrum noticeably. The energy distance of the donor–acceptor bands from the exciton band, i.e., from the fundamental absorption edge, differs little in both crystals. This does not come as a surprise, because the electron and hole effective masses and the dielectric permittivity of CdTe are similar to their respective values for ZnTe; in other words, the depths of analogous impurity levels in these semiconductors do not differ much. Halogen atoms can play a substantial role in the passivation of lattice defects in ZnTe and CdTe, which, combined with the low growth temperature of the crystals tending to decrease the concentration of structural defects, brings about a large contribution from excitons to radiative recombination.

REFERENCES

1. H. Okada, J. Appl. Phys. **80**, 6740 (1996).
2. S. Pietralunga, P. Boffy, and M. Martinelli, J. Nonlinear Opt. Phys. Mater. **5**, 247 (1996).
3. G. Tessaro and P. Mascher, J. Cryst. Growth **197**, 581 (1999).
4. O. A. Matveev and A. I. Terent’ev, Fiz. Tekh. Poluprovodn. (St. Petersburg) **34**, 1316 (2000) [Semiconductors **34**, 1264 (2000)].
5. G. M. Khattak, J. M. Majid, C. G. Scott, and D. Shaw, Solid State Commun. **84**, 1073 (1992).
6. H. Katayma-Yoshida, T. Sasaki, and T. Oguchi, J. Cryst. Growth **117**, 625 (1992).
7. G. A. Il’chuk, V. I. Ivanov-Omskiĭ, V. Yu. Rud’, *et al.*, Fiz. Tekh. Poluprovodn. (St. Petersburg) **34**, 1327 (2000) [Semiconductors **34**, 1275 (2000)].
8. G. A. Il’chuk, Neorg. Mater. **35**, 812 (1999).

Translated by G. Skrebtsov

Physics of the Solid State, Vol. 44, No. 12, 2002, pp. 2219–2223. Translated from Fizika Tverdogo Tela, Vol. 44, No. 12, 2002, pp. 2120–2124.
Original Russian Text Copyright © 2002 by Gudaev, Malinovskiĭ.

SEMICONDUCTORS AND DIELECTRICS

Temperature Dependence of Thermopower in Polar Noncrystalline Materials

O. A. Gudaev and V. K. Malinovskiĭ

Institute of Automation and Electrometry, Siberian Division, Russian Academy of Sciences,
pr. Akad. Koptyuga 1, Novosibirsk, 630090 Russia
e-mail: malinovsky@iae.nsk.su

Received December 25, 2001; in final form, March 11, 2002

Abstract—The reasons for anomalous growth in the thermopower of metal borides at high temperatures is analyzed. It is shown that this behavior of thermopower cannot be explained within the present models of charge transfer in disordered semiconductors. The anomalous growth of thermopower in polar materials can be interpreted by taking into account the temperature dependence of the elastic coupling constant or of the polarizability. *© 2002 MAIK "Nauka/Interperiodica".*

1. INTRODUCTION

The magnitude, sign, and temperature dependence of thermopower, as well as the conductivity, yield important information on the mechanism of charge transfer in semiconductors. Charge transfer in disordered materials is governed by three possible conduction mechanisms [1]. These are conduction in extended states, in localized states of the conduction- and valence-band tails, and in localized states near the Fermi level. In all three cases, the conductivity is described by an activation law $\sigma \sim \exp(-E_\sigma/kT)$, where the activation energy E_σ is determined by the actual charge transfer mechanism. An exception is the low-temperature domain, where variable-range carrier hopping within localized states near the Fermi level becomes possible; this mechanism is described by Mott's law $\sigma \sim \exp(-T_0/T^{1/4})$, where T_0 is a parameter. The behavior of thermopower in these charge transfer conditions has been treated in a number of publications [1–3].

For all the mechanisms considered, it was shown that the thermopower decreases with increasing temperature as $S \sim \frac{E_s}{kT} + A$ (where A is a parameter) and that the activation energy of thermopower E_s is closely related to that of conductivity E_σ. When carriers are transferred in extended states, we have $E_\sigma = E_s$. The activation energies in hopping charge transfer, according to the model proposed in [1], should differ by the hopping activation energy W, i.e., $E_\sigma - E_s = W$. This relation has been used by a number of authors to determine the hopping activation energy. For most materials, however, the hopping energies are small, $W \sim 0.01$ eV. The experimental technique employed did not make it possible to reliably determine the activation energies E_σ and E_s with such an accuracy. In some cases, for instance, for chalcogenide glasses [1] and lithium niobate [1], a considerably larger difference $E_\sigma - E_s$ (~0.1 eV) was reported to have been measured. Such a large value of W is difficult to associate with conventional hopping transport.

An attempt was made to describe charge transfer in these materials in terms of small-radius polaron hopping [4–6]. However, the laws describing the $\sigma(T)$ and $S(T)$ behavior within the small polaron model turned out to be very close to those governing conventional electron transport [7]; namely, $\sigma \sim T^{-n}\exp(-E_W/kT)$, where E_W is the polaron hopping activation energy, and $n \approx 1$; $S = E_{WS}/kT + A$ (E_{WS} is the activation energy of thermopower in the case of polaron-mediated transport, and A is a parameter). This similarity hampers the interpretation of experimental results.

It was shown in [8] that the conduction laws describing charge transfer by electrons and small polarons are different to such an extent that the mechanism of transfer and the polaron contribution to the conductivity can be found from the character of the $\sigma(T)$ relation.

This paper considers the specific features in the behavior of thermopower $S(T)$ in polar materials. One of the most remarkable features is the strong growth of thermopower in the high-temperature domain, which is observed to occur in some polar materials and does not fit any of the models mentioned above.

2. EXPERIMENTAL RESULTS

A strong increase in the thermopower with increasing temperature, up to very high temperatures, is characteristic of a number of metal borides. Figure 1 dis-

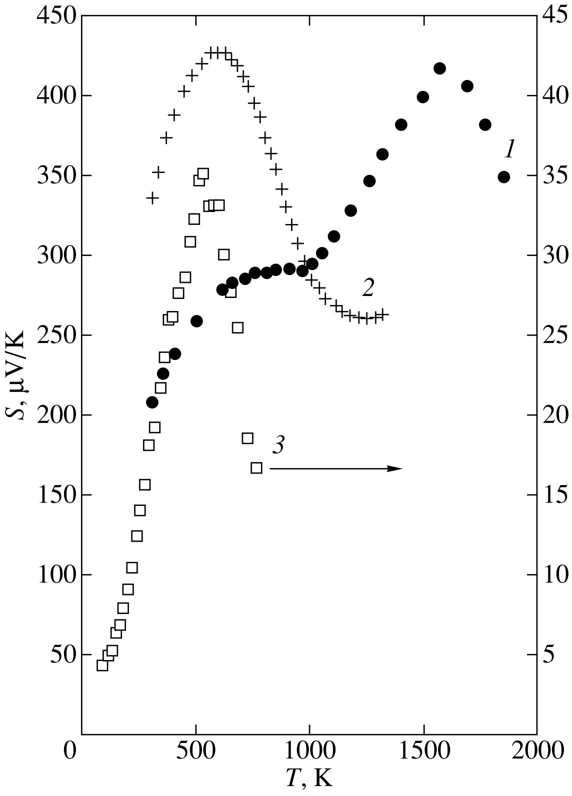

Fig. 1. Temperature dependence of thermopower in (*1*) α-AlB_{12}, (*2*) $B_{14}Si$, and (*3*) $FeB_{29.5}$.

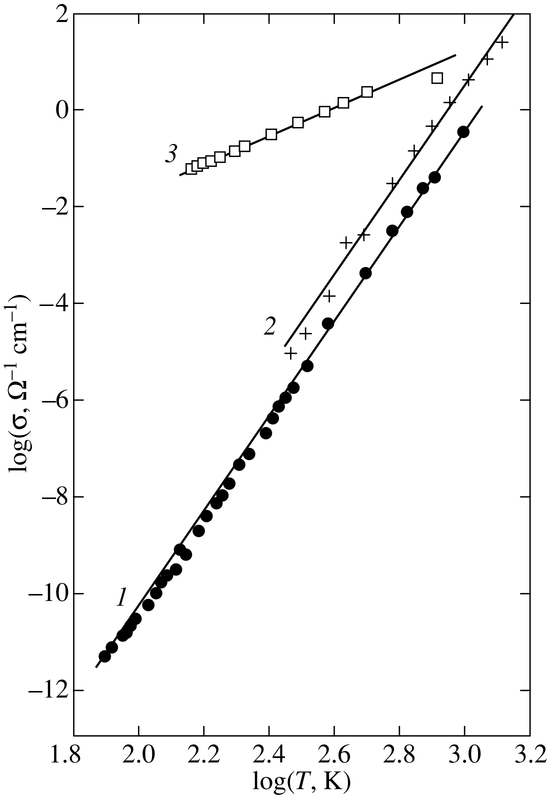

Fig. 2. Temperature dependence of conductivity of (*1*) α-AlB_{12}, (*2*) $B_{14}Si$, and (*3*) $FeB_{29.5}$.

plays a typical behavior of the thermopower for $FeB_{29.5}$, α-AlB_{12}, and $B_{14}Si$. Thermopower behaves in a similar way in DyB_{66}, GdB_{66}, and $MgAlB_{14}$ [9, 10]. Boron carbide exhibits a growth of thermopower up to ~1200 K [4, 5]. One of the explanations proposed for this behavior of the thermopower suggests a crossover from the hopping mechanism to charge transfer in extended states at high temperatures. Figure 2 presents temperature dependences of the conductivity for these metal borides. These dependences obey a power-law relation, $\sigma \sim T^n$, over a broad temperature range and do not have features which could signal a change in the charge transfer mechanism from carrier motion in the band of extended states to hopping transport.

3. DISCUSSION

The magnitude of thermopower is found from the condition of equality of counterpropagating diffusion and drift flows in a sample in the presence of a temperature gradient. Fritzsche [2] derived a general expression for thermopower through the conductivity of the material σ:

$$S = \frac{k}{e}\int\frac{E-E_F}{kT}\frac{\sigma(E)}{\sigma}dE, \tag{1}$$

where E_F is the Fermi level energy and the conductivity of the material is given by

$$\begin{aligned}\sigma &= \int\sigma(E)dE \\ &= e\int N(E)\mu(E)f(E)[1-f(E)]dE.\end{aligned} \tag{2}$$

Here, $N(E)$ is the density of electronic states, $\mu(E)$ is the carrier mobility, and $f(E)$ is the Fermi–Dirac function

$$f(E) = \frac{1}{1+\exp[(E-E_F)/kT]}. \tag{3}$$

If the $N(E)$ and $\mu(E)$ functions are known, one can calculate $S(T)$ using Eqs. (1)–(3).

It was shown in [3] that if the conductivity of a material follows an activation law

$$\sigma = \sigma_0\exp(-E_\sigma/kT) \tag{4}$$

with a constant activation energy E_σ, the temperature dependence of the thermopower assumes a well-known form:

$$S = -\frac{1}{e}\frac{E_\sigma}{kT} + A, \tag{5}$$

where A is a temperature-independent kinetic term.

In the region where Mott's law holds for the variable-range hopping conductivity, the dependence of the thermopower on temperature is different; it scales either as $S \sim T^{1/2}$ or as $T^{-1/4}$ [3].

Suggestions have been put forward that in polar materials, including metal borides, the charge transport is mediated by small polarons. Isolation of the polaron contribution to the conductivity and determination of the parameters of polarons turned out, however, to be a difficult problem. The reason for this lies in that, according to the present models, the temperature dependence of polaron-mediated conductivity differs little from that of conductivity mediated by electrons. The same applies to the temperature dependence of thermopower. The experimentally measured temperature dependences of conductivity drawn in the activation coordinates are curves with an activation energy varying smoothly with temperature. These dependences can be approximated, as a rule, by a sum of several activation laws, which correspond presumably to different charge transfer mechanisms. It has been shown, however, that in a large number of disordered polar materials [11–13], including metal borides [8], the conductivity can be described, within a broad temperature range (of about a thousand degrees), not by a sum of several activation laws but rather by one power-law relation (Fig. 2):

$$\sigma = \sigma_0 T^n. \tag{6}$$

According to our model [8, 11–13], temperature dependence of the type of Eq. (6) is characteristic of polaron conductivity wherein polaron transitions from one state to another actually represent a multiphonon process. The polaron is a slowly moving conduction electron (or hole) in a polar crystal. The energy of the potential well created by the polaron in a crystal [1] can be written as [1]

$$W_p(r_0) = e^2/\varepsilon_p r_0, \tag{7}$$

where r_0 is the distance and ε_p is determined by the difference between the high-frequency (ε_∞) and static (ε) dielectric permittivities:

$$\varepsilon_p^{-1} = \varepsilon_\infty^{-1} - \varepsilon^{-1}. \tag{8}$$

It follows that polaron effects play a substantial part in the conductivity of materials with ionic or partially ionic bonding. The probability of multiphonon polaron hopping from one well to another at not too high temperatures was shown to be [1]

$$Z \sim [kT/(\hbar\omega)]^n. \tag{9}$$

Here, ω is the phonon frequency and n is the number of phonons. As shown in the charge transfer model proposed in [12], the power-law relation for the polaron transition probability from one state to another results finally in a power-law temperature dependence (6) for the polaron-mediated conductivity. It should be pointed out that in the conditions where charge transfer is effected by electrons hopping from one state to another in a single-phonon process, in contrast to the case of polaron conductivity, the conductivity is described within a broad temperature range not by a power law but rather by the inverse Arrhenius relation [11, 13]

$$\sigma = \sigma_0 \exp(T/T^*), \tag{10}$$

where T^* is a parameter. The obvious difference in behavior between the polaron and nonpolaron conductivities permits one to reliably isolate the cases of charge transfer by small polarons. An analysis of charge transfer mechanisms in boron and a number of borides can be found in [8]. The results presented in Fig. 2 for metal borides are typical of polaron-mediated conductivity throughout the temperature range covered.

Let us consider the behavior of thermopower in the cases of power-law and inverse-Arrhenius temperature dependences of conductivity. We shall use again Eqs. (1)–(3) for calculations. In accordance with the assumptions underlying the model developed in [11–13], we shall, however, consider charge transfer in states corresponding to the percolation (or Fermi) level located within the region of exponential energy dependence of the density of states:

$$N(E) = N_V \exp[-(E_V - E)/kT_0]. \tag{11}$$

Here, N_V is the density of states at the band edge, E_V is the band edge energy, and T_0 is a parameter characterizing the density-of-states decay. Consider, for instance, charge transfer in the states corresponding to the density-of-states tail near the valence band. The integration will be performed over the interval from $E_c + \Delta E$ to $E_c - \Delta E$ near the percolation level E_c. We assume that $\Delta E = \alpha kT$, with α being a number of order unity. As a first approximation, we also assume that the Fermi–Dirac function is constant within the narrow interval ΔE: $f(E_c) = \text{const} = C$. If the Boltzmann factor provides a major contribution, the temperature dependence of the thermopower will have the form of Eq. (5). On integrating Eqs. (1)–(3), we readily see that in the case of single-phonon transitions, the temperature dependence of the thermopower can be cast in the form

$$S = -\frac{k}{e}\left\{\frac{(E_c - kT_0) - E_F}{kT} + \alpha\right\}. \tag{12}$$

In the case of multiphonon transitions, we have

$$S = -\frac{k}{e}\frac{E_c - E_F}{kT}. \tag{13}$$

In the final count, the thermopower is again described by relations of the type of Eq. (5).

Thus, taking into account dynamic equilibrium between the diffusion and drift flows in the way done in deriving Eq. (1) does not provide an explanation for the strong growth of thermopower with increasing temperature in polar materials. The reason for this lies apparently (as in the calculation of thermopower using a kinetic equation) in the assumption that the internal field in a sample is temperature-independent. While this assumption is valid for most semiconductors, it is not applicable to polar materials where $\varepsilon \gg 1$. Let us show that in order to account for the strong increase in $S(T)$ in the high-temperature domain, one has to include into consideration the temperature dependence of polarizability in polar materials possessing strong electron–phonon coupling.

Thus, if a temperature gradient is maintained in a semiconductor, a diffusion current of majority carriers J_{dif} will flow in it from the heated to the cold end and, hence, a nonzero mean internal electric field F_{in} will occur. The internal field will induce a drift current J_{drift} directed opposite to the diffusion current. In a nonpolar material, in equilibrium, the following equality will hold:

$$J_{\text{dif}} = J_{\text{drift}} = F_{\text{in}}\sigma = \frac{V_{\text{emf}}}{R}, \tag{14}$$

where R is the sample resistance and V_{emf} is the electromotive force. If there is no polarization P in the material ($P \approx 0$), the internal field F_{in} will be determined by the applied voltage only, $F_{\text{in}} = F_0$.

In a polar material ($P \neq 0$), an electric field F_0 in the sample creates polarization P, which reduces the internal field:

$$F_{\text{in}} = F_0 - 4\pi P. \tag{15}$$

In this case, the equality of the diffusion and drift currents assumes the form

$$J_{\text{dif}} = J_{\text{drift}} = F_{\text{in}}\sigma = (F_0 - 4\pi P)\sigma = \frac{V_{\text{emf}} - V_p}{R}. \tag{16}$$

Here, V_p is the electromotive force of polarization, which was introduced as far back as by Ioffe [14]. The measured electromotive force V_{emf} can be written as

$$V_{\text{emf}} = RJ_{\text{dif}} + V_p. \tag{17}$$

The diffusion current J_{dif} is determined by the carrier concentration gradient ($J_{\text{dif}} = -D\,\text{grad}\,n$) and does not depend on whether the material is polarized or not; i.e., the first term in Eq. (17) produces the same contribution as in a nonpolar material, with the thermopower taking on its traditional form (5). If the second term in Eq. (17) is dominant, it is this term that will determine the form of $S(T)$.

A decrease in material density, i.e., in the number of polarizable particles per unit volume, with increasing temperature may affect, albeit insignificantly, the temperature dependence of polarizability χ or of dielectric permittivity ε [$\chi = (\varepsilon - 1)/4\pi$] of ionic materials (the permittivity ε is decreased). More important, however, may be that the distances between ions increase with increasing temperature and their interaction weakens because of the decreasing elastic coupling coefficient. If the elastic ionic polarization predominates, the dielectric permittivity and the polarization increase with temperature as a result of a decreasing elastic coupling coefficient [15]. According to Eq. (15), the increase in polarization P with increasing temperature brings about a decrease in the field F_{in} acting on each carrier, i.e., a decrease in the drift current J_{drift}. Since the balance between the diffusion and drift currents should persist, this process causes thermopower (16) to increase.

The increase in thermopower with increasing temperature may become manifest within a certain temperature interval in ionic materials with conductivity of the polaron type. As already mentioned, the polaron well depth is given by Eq. (7). Formation of a polaron well reduces the energy of the system by an amount W_p [1]. Therefore, the increase in polarizability and, hence, in thermopower with increasing temperature may be expected to occur at temperatures lower than

$$T_c = W_p/k = e^2/\varepsilon_p r_0 k. \tag{18}$$

Above this temperature, according to Eq. (5), the thermopower should decrease with increasing T, as follows from most models developed for charge transfer in semiconductors.

The amount by which the thermopower can grow with increasing temperature is determined by the magnitude of the static dielectric permittivity ε. The dielectric permittivity ε for materials with ionic or partially ionic bonding is typically ~4–10 [15]. In addition, the variation of the elastic coupling constant with temperature also plays an important role. Although we have no data on this variation in high-boron compounds at our disposal, the complexity of the structure and the looseness characteristic of these materials suggest that the coupling constant may vary considerably (by a few times) with temperature in the range 300–1000 K.

We note one more factor capable of affecting possible small polaron formation. If a carrier moves fast enough, the time it spends near an ion, $\tau \approx r_0/v_{\text{drift}}$, may turn out to be insufficient for the polaron well to form. As a result, $\varepsilon_\infty = \varepsilon$ and no polaron-mediated conduction will exist. The magnitude of τ decreases with increasing temperature, which may decrease the temperature range within which the polaron effects are essential. On the other hand, the time τ grows, as a rule, with increasing disorder in the material. As a result, polaron effects may manifest themselves more clearly with increasing disorder in the material [8].

The temperature dependence of thermopower, as well as that of conductivity, provides important information on the mechanism of charge transfer in semiconductors. It turns out that in all cases where the conductivity is described by an activation law, the thermopower behaves in a universal pattern as described by

Eq. (5). The various types of charge transfer mechanisms differ only in the activation energy E_a.

Unlike metals, the thermopower in semiconductors always decreases with increasing temperature. A slight increase in thermopower with temperature appears only under some assumptions in the case of variable-range hopping charge transfer at the Fermi level. In its very nature, this mechanism of charge transfer can prevail only at low temperatures. Experiments performed on polar materials sometimes reveal a fairly strong increase in thermopower at high temperatures (500–1000°C). Calculations made within the model of Fritzsche [2], i.e., using Eqs. (1)–(3), for various transfer mechanisms do not provide an explanation for this behavior of thermopower. Calculations of the conductivity mediated by small polarons carried out in terms of earlier models [5, 6] likewise fail in accounting for the growth of thermopower at high temperatures. The polaron conductivity model proposed in [12] satisfactorily describes the temperature dependence of conductivity over a broad temperature range for a large number of disordered ionic materials. However, thermopower calculations made within the Fritzsche model also yield a temperature dependence of the kind of Eq. (5) and, therefore, do not explain the growth of thermopower at high T.

The unusual behavior of thermopower can be understood if one takes into account the temperature dependence of polarization (or polarization emf) in polar materials. In these materials, polarization of the elastic ionic type typically prevails. In contrast to the electronic polarization, which is responsible for the behavior of the high-frequency dielectric permittivity ε_∞, the elastic ionic polarization (which is dominant in ionic materials) determines the static dielectric permittivity ε and, in ionic materials, can increase at high temperatures. An increase in the polarization emf brings about a decrease in the mean internal field F_{in} and, hence, in the drift current. To maintain the balance between the diffusion and drift currents, the (experimentally measured) thermopower also increases. The thermopower grows up to temperatures where the polarization energy becomes of the order of kT.

Thus, strong electron–phonon coupling in polar materials may give rise both to the formation of small polarons and polaron-mediated conductivity and to specific features in the temperature dependence of thermopower associated with the temperature dependence of the elastic coupling constant or polarizability.

ACKNOWLEDGMENTS

This study was supported by the Russian Foundation for Basic Research, project no. 99-02-16697.

REFERENCES

1. N. F. Mott and E. A. Davis, *Electronic Processes in Non-Crystalline Materials* (Clarendon, Oxford, 1979; Mir, Moscow, 1983), Vols. 1, 2.
2. H. Fritzsche, Solid State Commun. **9**, 1813 (1971).
3. V. L. Bonch-Bruevich, I. P. Zvyagin, R. Kaĭper, A. G. Mironov, R. Énderlaĭn, and B. Esser, *Electron Theory of Disordered Semiconductors* (Nauka, Moscow, 1981).
4. C. Wood and D. Emin, Phys. Rev. B **29** (8), 4582 (1984).
5. D. Emin, G. Samara, and L. Azevedo, J. Less-Common Met. **117**, 415 (1986).
6. D. Emin, Phys. Today **40** (1), 55 (1987).
7. P. Nagels, in *Amorphous Semiconductors*, Ed. by M. H. Brodsky (Springer, New York, 1979; Mir, Moscow, 1982).
8. O. A. Gudaev and V. K. Malinovskiĭ, Fiz. Tverd. Tela (St. Petersburg) **44** (5), 805 (2002) [Phys. Solid State **44**, 837 (2002)].
9. O. A. Golikova, Phys. Status Solidi A **101**, 277 (1987).
10. O. A. Golikova, Usp. Fiz. Nauk **158** (4), 581 (1989) [Sov. Phys. Usp. **32**, 665 (1989)].
11. O. A. Gudaev and V. K. Malinovskiĭ, Fiz. Tverd. Tela (St. Petersburg) **37** (1), 79 (1995) [Phys. Solid State **37**, 41 (1995)].
12. O. A. Gudaev and V. K. Malinovskiĭ, Fiz. Tverd. Tela (St. Petersburg) **34** (2), 548 (1992) [Sov. Phys. Solid State **34**, 293 (1992)].
13. O. A. Gudaev and V. K. Malinovskiĭ, Fiz. Khim. Stekla **26** (4), 522 (2000).
14. A. F. Ioffe, *Electrical Properties of Solids* (Lenizdat, Leningrad, 1947).
15. M. P. Bogoroditskiĭ, Yu. M. Volokobinskiĭ, A. A. Vorob’ev, and B. M. Tareev, *Theory of Dielectrics* (Énergiya, Moscow, 1965).

Translated by G. Skrebtsov

Physics of the Solid State, Vol. 44, No. 12, 2002, pp. 2224–2231. Translated from Fizika Tverdogo Tela, Vol. 44, No. 12, 2002, pp. 2125–2132.
Original Russian Text Copyright © 2002 by Aliev, Golubev, Dukin, Kurdyukov, Medvedev, Pevtsov, Sorokin, Hutchison.

SEMICONDUCTORS AND DIELECTRICS

Structural, Photonic Band-Gap, and Luminescence Properties of the Opal–Erbium Composite

G. N. Aliev*, V. G. Golubev*, A. A. Dukin*, D. A. Kurdyukov*, A. V. Medvedev*, A. B. Pevtsov*, L. M. Sorokin*, and J. L. Hutchison**

** Ioffe Physicotechnical Institute, Russian Academy of Sciences, Politekhnicheskaya ul. 26, St. Petersburg, 194021 Russia*
e-mail: dookin@gvg.ioffe.rssi.ru
*** Materials Science Division, Oxford University, OXI 3PH Oxford, Great Britain*

Received January 31, 2002

Abstract—Erbium oxide and silicates were embedded in the pores of synthetic opal by using the chemical bath deposition technique. Electron-microscopic images showed the synthesized compounds to be deposited predominantly in a thin uniform layer on the inner surface of the pores. An analysis of the transmittance spectra suggested that the opal–erbium composite thus obtained retained the photonic band-gap properties of the original ordered opal matrix. The Er^{3+} ions in the composite emitted light at several wavelengths in the visible and near-IR regions (550, 860, 980, 1240, 1530 nm) at 80 K.© *2002 MAIK “Nauka/Interperiodica”.*

1. INTRODUCTION

According to Fermi’s golden rule, the total probability of a spontaneous radiative transition in an atom per unit time is proportional to the density of photonic states at the transition frequency (see, e.g., [1]). By properly modifying the density of modes in comparison with their uniform distribution in free space, one can control (suppress or enhance) spontaneous emission [2, 3]. In transparent periodic dielectric media with a period on the order of the radiation wavelength, which are called photonic crystals, Bragg diffraction gives rise to the formation of a photonic band gap (PBG) [3, 4], i.e., of a spectral region in which the photon mode density is zero. At the edges of the PBG, photon dispersion differs strongly from the typical linear relation. As a result, the density of photonic states substantially increases near the PBG edges, which, in turn, brings about an increase in the radiative transition probability and an enhancement of the spontaneous emission of an ensemble of radiating centers embedded in the photonic crystal [5–7].

Synthetic opals can be used as suitable three-dimensional photonic crystals for studying the effect of PBG on spontaneous emission. Synthetic opals have an fcc lattice formed by close-packed spheres of amorphous SiO_2 (a-SiO_2) [8–12]. By choosing the diameter of monodisperse spheres in the range 100–1000 nm, one can vary the PBG position over a broad wavelength region, from the UV to near IR. An opal has a system of octahedral and tetrahedral pores which, when the spheres are in point contact, make up to 26% of its total volume. The pores are connected through channels and form a regular sublattice, which can be filled by other substances, for instance, by materials efficiently emitting light.

In the present study, the trivalent erbium ion Er^{3+} was chosen as an emitting center to be embedded in an opal matrix. Erbium-containing materials enjoy broad application in telecommunications and optoelectronics [13]. The wavelength of the main Er^{3+} ground-state transition, 1.54 μm, coincides with the standard wavelength in use in optical telecommunication systems determined by the quartz waveguide transparency window. The Er^{3+} ion can also efficiently emit light at other discrete wavelengths in the visible and near-IR spectral regions determined by the structure of the excited states of this ion [13]. It is essential that the optical transitions occur in the $4f^{11}$ inner shell of the Er^{3+} ion, which is screened by the outer electronic shells; therefore, the spectral widths of the corresponding emission lines are narrower than the opal PBG width. Thus, the development of an Er-containing opal-based composite would make it possible to investigate the spontaneous emission of Er^{3+} ions (its suppression or enhancement) as a function of the energy position of the erbium emission line relative to the spectrum of electromagnetic modes in a photonic crystal [14]. In what follows, we shall call such a composite the “opal–erbium composite.” Development of this composite presupposes the solution of a number of fundamental problems. First, an Er-containing material has to be introduced into the opal pores in such a way as to preserve the periodicity of the dielectric-permittivity modulation and not to degrade the photonic properties of the opal. Second, the Er^{3+} ion embedded in the composite must efficiently luminesce at several wavelengths in the visible and near-IR spectral regions. Therefore, this ion should be introduced into an opal matrix as a component of a material in which the probability of nonradiative excited-state relaxation of the Er^{3+} ion is as low as possible. Third,

1063-7834/02/4412-2224$22.00 © 2002 MAIK “Nauka/Interperiodica”

the parameters of the composite (the size of the spheres, the dielectric permittivity of the pore filler, etc.) should be chosen such as to provide the possibility of spectral overlap of the Er^{3+} luminescence line with the PBG of the composite. The present study deals with solving these problems.

Note that in order for this composite to be of practical use, it has to provide the possibility of controlling the Er^{3+} spontaneous emission by properly varying (in real time) the spectral position and width of the PBG relative to the position of the ion emission lines. This can be done, for instance, if specific materials, such as liquid crystals [15, 16] or vanadium dioxide [17], which change their dielectric permittivity under the action of an external factor (temperature or an electric field) are introduced into the unfilled volume of the opal–erbium composite pores.

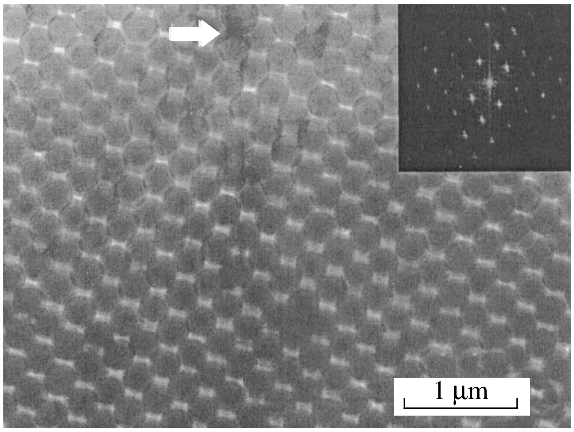

Fig. 1. Electron microscope image of the opal–erbium composite. The arrow identifies a pore filled completely with Er_2O_3. Inset: Fourier transform of this image.

2. EXPERIMENT

We chose synthetic opals with a polydomain structure as the starting matrices. The size of a domain with a highly ordered a-SiO_2 sphere arrangement was 30–100 μm. Samples were platelets 5 × 5 × 0.1 mm in size cut parallel to the opal (111) plane. The SiO_2 sphere diameter was 230 ± 5 nm. The dimensions of interconnected octahedral and tetrahedral pores were roughly 90 and 45 nm, respectively. The opal pores were initially filled with erbium nitrate in the form of a water solution at room temperature. Subsequent thermal decomposition of the erbium nitrate (at 500°C over 1 h) [18] produced erbium oxide Er_2O_3 in the pores. The volume fraction of filled opal pores was determined gravimetrically to be approximately 11% of the total pore volume.

Because of the use of a water solution, the Er_2O_3 formed in pores contained a large amount of hydroxyl groups, which are strong quenchers of erbium photoluminescence (PL) [13]. To reduce the concentration of hydroxyl groups and increase the PL intensity, the samples were annealed in air at 850°C for 1 h.

The microstructure of the composite was studied with the use of a JEM4000EXII electron microscope with a built-in EDX attachment provided with a Si(Li) detector having an ultrathin window. The studies were performed in the high-resolution, diffraction-contrast mode. Elemental analysis was carried out on a sample ~3 nm in size. The technique of sample preparation for electron-microstructural analysis used by us was employed earlier for opal–Si and opal–Pt–Si composites and is described in considerable detail in [19].

To reveal the photonic band-gap properties of the composite, transmittance spectra in the visible were investigated. The measurements were conducted at liquid-nitrogen temperature on a computerized spectrometer based on an MDR-3 monochromator. The spectra were measured with a PM tube (500–800 nm) and an InGaAs photodiode (800–1700 nm) in the lock-in detection regime. To reduce the effect of the sample polydomain structure on the shape of transmittance spectra [20], the measurements were carried out with collimated beams.

To study the emitting properties of the opal–erbium composite, PL spectra were measured at 80 K in the visible and near-IR ranges. The Er^{3+} photoluminescence was excited with an Ar^+ laser at a wavelength of 488 nm (in the vicinity of the $^4I_{15/2} \longrightarrow {}^4F_{7/2}$ transition in the $4f^{11}$ shell of the Er^{3+} ion). The laser beam was focused on the sample to a spot 0.5 mm in diameter. The incident power density did not exceed 5 W/cm^2.

3. RESULTS AND DISCUSSION

Figure 1 shows a part of the composite revealing a clearly pronounced ordered “crystalline” structure with closely packed a-SiO_2 spheres in the (110) plane. The dark-contrast circles in the image are projections of the a-SiO_2 spheres, and the bright spots separating the spheres are the pores. In this image, the arrow identifies one of the pores that is filled completely by Er_2O_3 and has dark contrast. As seen from Fig. 1, the number of such pores is small, which is in accord with the degree of pore filling indicated above. From the high-resolution images presented below, it can be seen that in most pores, Er_2O_3 is deposited in the form of a very thin (~3 nm) coating on the surface of the a-SiO_2 spheres, which is not seen in Fig. 1 due to an insufficiently high magnification.

The inset to Fig. 1 shows a two-dimensional Fourier transform of the image. The regular array of dots (quasi-reflections) in the inset indicates the existence of long-range order in the composite lattice, which is not affected noticeably by the pore filling, by defects in the composite lattice (sphere displacements, “point

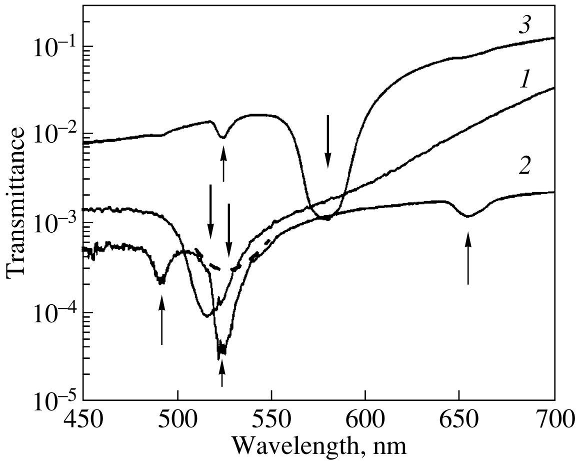

Fig. 2. Transmittance spectra of the (*1*) original opal, (*2*) opal–erbium composite, and (*3*) opal–erbium composite with pores filled completely with glycerol. The down-arrows show the position of the Bragg transmittance minimum corresponding to the photonic band gap. The up-arrows specify the Er^{3+} absorption lines corresponding to the transitions $^4I_{15/2} \longrightarrow {}^4F_{7/2}$ (490 nm), $^4I_{15/2} \longrightarrow {}^2H_{11/2}$ (524 nm), and $^4I_{15/2} \longrightarrow {}^4F_{9/2}$ (655 nm).

defects”), or by size dispersion of the silica spheres. The quasi-reflection array correlates in symmetry with the silica sphere arrangement in Fig. 1, which corresponds to the (110) plane of the fcc lattice.

Figure 2 presents experimental transmittance spectra [obtained under normal incidence on the (111) plane] of bare opal, of the opal–erbium composite, and of the opal–erbium–glycerol composite. Curve *1* is the transmittance spectrum of the starting unfilled opal. The broad dip with a minimum at 516 nm is a result of Bragg diffraction from the opal fcc lattice and is due to the existence of a PBG. The spectral position of the minimum in transmittance under normal incidence of light is given by the relation $\lambda_m = 2d_{(111)}\sqrt{\langle\varepsilon\rangle}$, where $d_{(111)}$ is the interplanar distance in the composite fcc lattice in the [111] direction, which is related to the diameter D of the a-SiO_2 spheres through $d_{(111)} = \sqrt{2/3}\,D$, and $\langle\varepsilon\rangle$ is the average dielectric permittivity of the composite, $\langle\varepsilon\rangle = \sum_i \varepsilon_i f_i$, with ε_i and f_i being the dielectric permittivity and the volume fraction of the ith component of the composite, respectively [21, 22]. In the unfilled opal, we have $\langle\varepsilon\rangle = 0.26\varepsilon_{\text{air}} + 0.74\varepsilon_{SiO_2}$.

Curve *2* is the transmittance spectrum of the opal–erbium composite. The spectrum contains three absorption lines located at 490, 524, and 655 nm (specified by up-arrows), which are identified as belonging to Er and correspond to the following transitions in the $4f^{11}$ shell of the Er^{3+} ion: $^4I_{15/2} \longrightarrow {}^4F_{7/2}$, $^4I_{15/2} \longrightarrow {}^2H_{11/2}$, and $^4I_{15/2} \longrightarrow {}^4F_{9/2}$ [23]. Observation of these lines provides an independent argument for Er being embedded in the composite. Because of the pores being partially filled with an erbium-containing compound, the value of $\langle\varepsilon\rangle$ increases compared with that of the unfilled opal, as a result of which the Bragg transmittance minimum shifts to approximately 525 nm. The strong erbium absorption line peaking at 524 nm in spectrum *2* masks the Bragg absorption line (schematically shown by a dashed line).

To reveal the Bragg absorption line in the transmittance spectrum separately, the pore volume that remained free (89% of the total pore volume) was filled with glycerol. The change in $\langle\varepsilon\rangle$ caused by the glycerol filling shifted the Bragg transmittance line to the 580-nm region (spectrum *3*). The erbium absorption line at 524 nm is seen now as a separate band.

We note that the transmittance of the opal–erbium composite in the wavelength region outside the Bragg absorption line is smaller than that of the starting opal. At the same time, the transmittance of the opal–erbium composite filled by glycerol is higher than that of the unfilled opal. Transmitted light undergoes Bragg diffraction by the fcc lattice of the composite. Part of the incident light undergoes diffuse scattering from various lattice defects, such as vacancies, dislocations, and stacking faults. An increase in optical contrast $\eta = \sqrt{\varepsilon_v/\varepsilon_s}$ (ε_s and ε_v are the volume refraction indices of the SiO_2 spheres and outside them, respectively) results in an enhancement of diffuse light scattering in all directions and, accordingly, in a decrease in diffracted intensity [24], which was measured within a solid angle ~7°. The dielectric permittivities of glycerol, Er_2O_3 [25], and a-SiO_2 in the opal spheres are 2.16, 3.84, and 1.88, respectively. As shown by estimates, the optical contrast in the starting unfilled opal matrix is smaller than that in the opal–erbium composite but larger than that in the opal–erbium–glycerol composite; this is what accounts for the difference in transmittance outside the Bragg absorption region.

The appearance of a clearly pronounced Bragg absorption line in the transmittance spectrum and the possibility of varying its spectral position by introducing, into the opal pores, a filler with a dielectric permittivity different from that of the a-SiO_2 spheres are evidence of the existence of a distinct photonic band-gap structure in the synthesized composite. The presence of a small amount of completely filled pores does not noticeably degrade the periodicity in varying the dielectric permittivity.

Figure 3 presents the PL spectrum of the opal–erbium composite in the visible and near-IR regions measured at $T = 80$ K. One clearly sees five narrow PL peaks (at 550, 860, 980, 1240, 1530 nm) denoted by the numbers *1*–*5*, respectively. The peaks were assigned to emission lines corresponding to the following transitions in the $4f^{11}$ shell of the Er^{3+} ion: $^4S_{3/2} \longrightarrow {}^4I_{15/2}$, $^4S_{3/2} \longrightarrow {}^4I_{13/2}$, $^4I_{11/2} \longrightarrow {}^4I_{15/2}$, $^4S_{3/2} \longrightarrow {}^4I_{11/2}$, and

$^4I_{13/2} \longrightarrow {}^4I_{15/2}$ [23]. The Er^{3+} level diagram and the experimentally observed transitions are shown schematically in Fig. 4. Thus, Er^{3+} ions embedded in the synthesized composite demonstrate strong emission in the visible and near-IR regions. These spectra were not corrected for the spectral sensitivity of the radiation detectors used. Because of a drop in the sensitivity of the InGaAs photodiode in the region 700–940 nm, the true amplitude of the 860-nm peak is a few times larger. The weak broad PL band centered at a wavelength of about 1100 nm and the broad band in the region 600–700 nm are possibly associated with light-emitting defects in the opal matrix.

Note that the PBG of the sample studied lies at ~520 nm (spectrum *2* in Fig. 2) and does not overlap with any of the observed Er^{3+} emitting transitions. The effect of the PBG on spontaneous emission of Er^{3+} in the opal–erbium composite in the case where the PBG coincides in position with a specific Er^{3+} emission line will be considered in our next publication.

The presence of the lines at 550, 860, 980, and 1240 nm in the PL spectra shows that there is no erbium inside the a-SiO_2 spheres. Er^{3+} embedded in the a-SiO_2 matrix would emit only one line ($^4I_{13/2} \longrightarrow {}^4I_{15/2}$) in the 1.5-μm region [13], because the energy of optical phonons in a-SiO_2 is high (1100 cm^{-1}) and, therefore, the probability of nonradiative multiphonon relaxation (MPR) for all excited states, except $^4I_{13/2}$, far exceeds that of radiative transitions. In a phenomenological MPR model [26], a nonradiative transition is assumed to involve the emission of several phonons of only one frequency that interact efficiently with the Er^{3+} ion and have the maximum possible energy $\hbar\omega$. The smallest number of phonons that can be emitted is $n = \Delta E/\hbar\omega$. Experimentally, the MPR probability is given by the relation $W_{MPR} = C\exp(-\alpha\Delta E)$, where C and α are positive constants characterizing the material in which the rare-earth ion is embedded and ΔE is the energy between the radiating and the next lower (closest-in-energy) ion level [27]. The energy ΔE for the excited states $^4S_{3/2}$, $^4I_{11/2}$, and $^4I_{13/2}$ is roughly 3000, 3600, and 6500 cm^{-1}, respectively. The MPR probability decreases exponentially with increasing number of phonons n involved in this process. If the number of phonons is $n \le 3$, radiative recombination is completely suppressed by nonradiative recombination. For $n \ge 10$, the MPR probability is very small [28]. For an optical phonon energy of ~1100 cm^{-1}, the relaxation of the $^4S_{3/2}$ and $^4I_{11/2}$ excited states involves three phonons and the relaxation of $^4I_{13/2}$ involves six phonons. Therefore, the population of the $^4S_{3/2}$ and $^4I_{11/2}$ excited states of Er^{3+} in a-SiO_2 is low and no luminescence corresponding to transitions from these levels is observed.

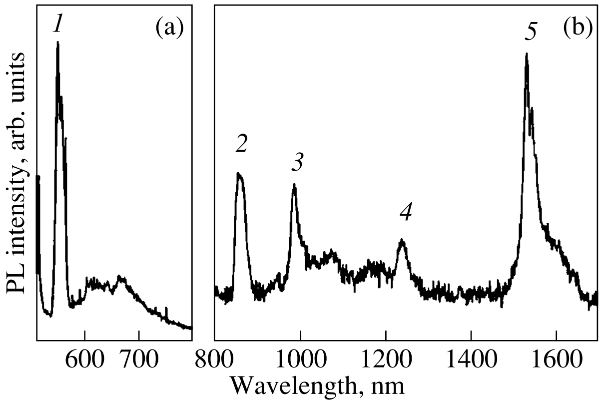

Fig. 3. Photoluminescence spectrum of the opal–erbium composite obtained at T = 80 K in the (a) visible and (b) near-IR region. The sample was annealed in air at T = 850°C for 1 h. Peaks *1*–*5* are Er^{3+} photoluminescence lines corresponding to the transitions $^4S_{3/2} \longrightarrow {}^4I_{15/2}$ (550 nm), $^4S_{3/2} \longrightarrow {}^4I_{13/2}$ (860 nm), $^4I_{11/2} \longrightarrow {}^4I_{15/2}$ (980 nm), $^4S_{3/2} \longrightarrow {}^4I_{11/2}$ (1240 nm), and $^4I_{13/2} \longrightarrow {}^4I_{15/2}$ (1530 nm), respectively.

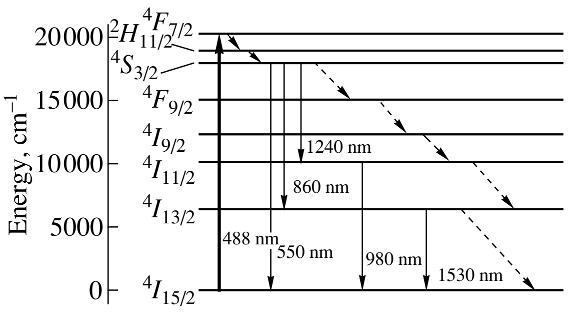

Fig. 4. Energy level diagram of the Er^{3+} ion. Solid down-arrows specify radiative transitions between Er^{3+} levels observed in the composite photoluminescence spectra. The up-arrow shows the transition used to excite the photoluminescence. Dashed arrows identify the transitions occurring in nonradiative multiphonon relaxation.

Consider in more detail the shape of the $^4S_{3/2} \longrightarrow {}^4I_{15/2}$ PL transition line (550 nm) of the composite (spectrum *1* in Fig. 5). For comparison, Fig. 5 also shows the spectrum of a reference Er_2O_3 sample (curve *2*). The reference sample was an Er_2O_3 film on a sapphire substrate prepared employing the technology used by us to synthesize erbium oxide in opal pores and subsequently annealed, as the opal–erbium composite, in air at a temperature of 850°C for 1 h. The spectrum of the $^4S_{3/2} \longrightarrow {}^4I_{15/2}$ transition in the reference sample represents a discrete set of narrow lines. The assignment of the PL spectra of the reference sample attempted using the known Er^{3+} energy levels in crystalline Er_2O_3 [29] suggests that it is indeed crystalline Er_2O_3 that formed on the substrate.

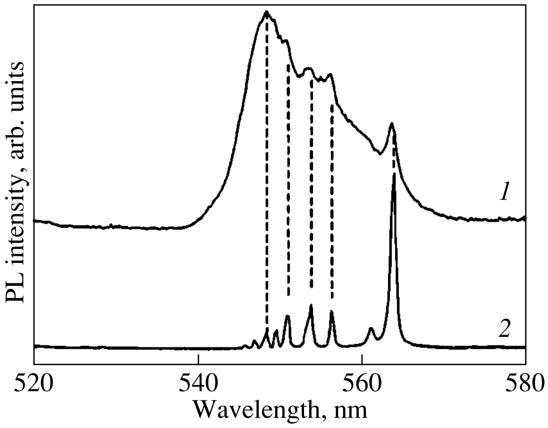

Fig. 5. Photoluminescence line corresponding to the $^4S_{3/2} \longrightarrow {}^4I_{15/2}$ radiative transition of the Er^{3+} ion in the (*1*) opal–erbium composite and (*2*) Er_2O_3 crystalline film.

The line of the $^4S_{3/2} \longrightarrow {}^4I_{15/2}$ transition observed in the Er^{3+} PL spectrum of the composite (spectrum *1* in Fig. 5) has a broad profile with a very weak structure consisting of several low-amplitude narrow peaks. The peak at 564 nm practically coincides in both position and width with the strongest Stark line in the Er_2O_3 spectrum. The weaker peaks in spectrum *1* (at 556, 553, 551, 548 nm) also coincide in position with the other, weaker Er_2O_3 lines (shown by dashed lines). Hence, spectrum *1* is actually a sum of the PL spectra of Er^{3+} ions in the amorphous matrix (broad profile) and in crystalline Er_2O_3 (narrow peaks). The PL intensity maximum in spectrum *1* is shifted strongly toward shorter wavelengths as compared with the position of the strongest luminescence line of crystalline Er_2O_3 (spectrum *2*). Thus, the Er-containing emitting amorphous material cannot be amorphous Er_2O_3, because in the Er^{3+} PL spectrum of amorphous Er_2O_3 all Stark components of the $^4S_{3/2} \longrightarrow {}^4I_{15/2}$ transition would be inhomogeneously broadened while the PL maximum would remain in the position of the strongest Stark line, namely, in the 564-nm region.

Let us turn now to the Er distribution in composite pores found using transmission electron microscopy. Figure 6a presents an enlarged image of a sphere surrounded by six pores. The image was made in a region of the composite with completely filled pores (similar to that identified with an arrow in Fig. 1). The three bottom pores and the pore at the top left of Fig. 6a are partially filled, while the remaining two are empty. Partially filled pores typically have a thin dark-contrast layer (~3 nm) on the sphere surface, which shows that this layer has a component (an element with a large atomic number *z*) with a higher electron absorption

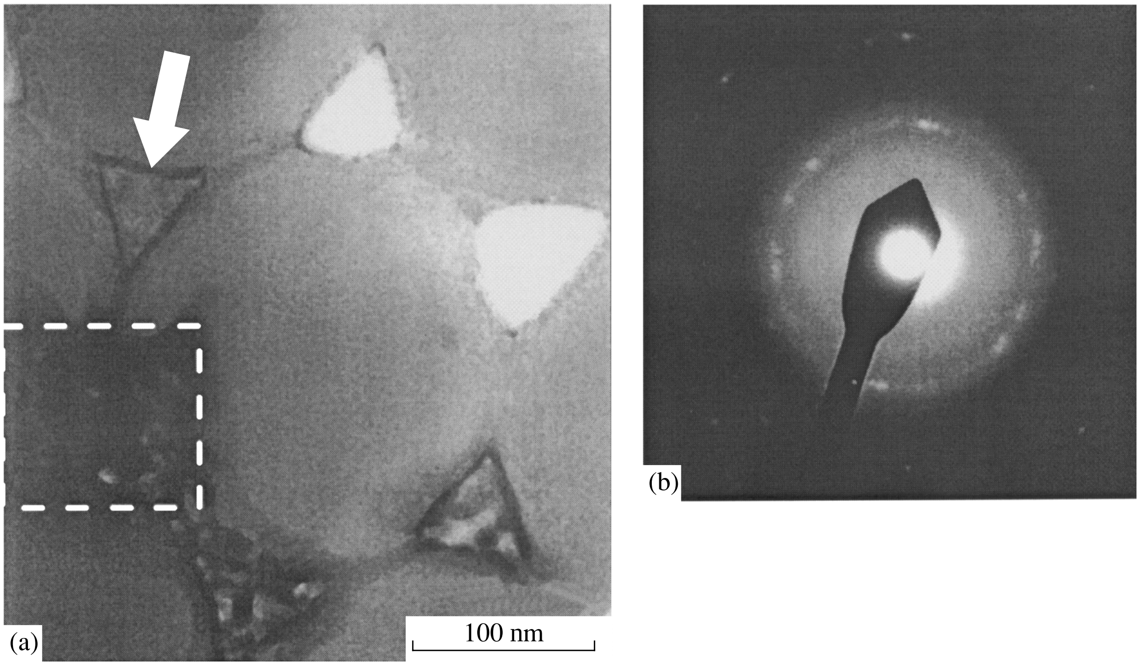

Fig. 6. (a) Electron microscope image of an *a*-SiO_2 sphere surrounded by six pores in the opal–erbium composite. The photograph shows the region of the sample having both pores filled completely with Er_2O_3 (one such pore is enclosed in the dashed rectangle) and pores in which the erbium-containing substance (presumably $Er_2Si_2O_7$) is deposited in a thin uniform layer (specified by the arrow) on the pore surface. (b) Electron diffraction pattern from a filled pore specified by the dashed rectangle in Fig. 6a.

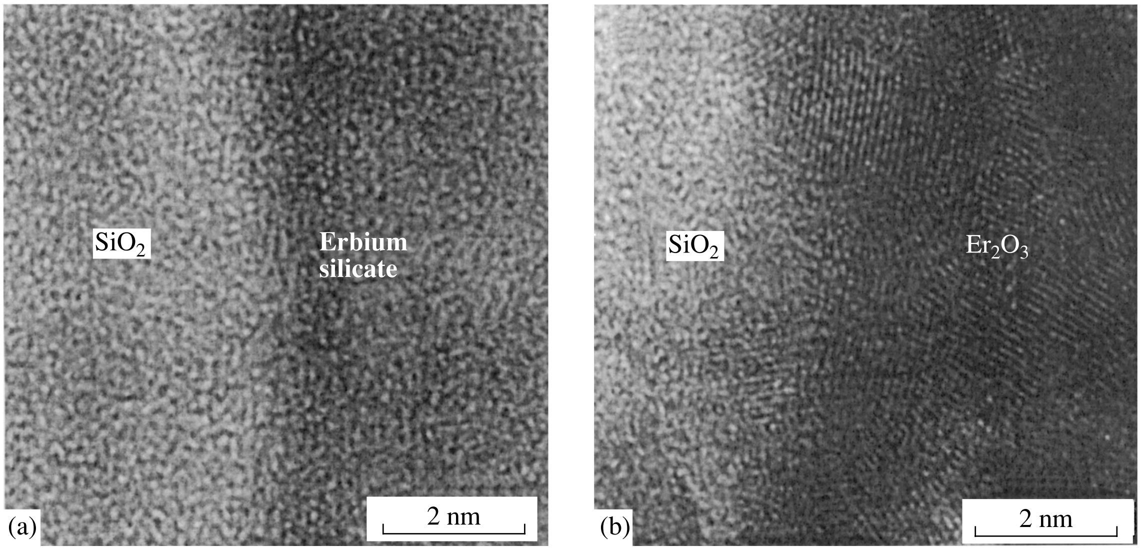

Fig. 7. High-resolution electron microscope image of (a) the interface between an a-SiO_2 sphere and an Er-containing amorphous layer and (b) the interface between an a-SiO_2 sphere and a pore filled completely with polycrystalline Er_2O_3.

than that of the silicate sphere ($z = 14$). In empty pores, the sphere surface also exhibits traces of a layer (with not as distinct a boundary) with a darker contrast than that of a sphere. This may indicate the beginning of filler deposition on the surface of the sphere or of chemical interaction between the filler and the sphere. The technology of filler introduction used in this experiment permits one to suggest that the layer is enriched in erbium ($z = 68$). The four filled pores reveal, in addition to a thin layer on the sphere surface, dark-contrast crystallites.

Figure 7a displays an electron microscope image, obtained in the high-resolution regime, of the region of the boundary between an a-SiO_2 sphere (bright contrast) and a layer on its surface (dark contrast). The dark-contrast layer, as well as the region of the silica sphere, does not exhibit indications of an ordered (crystalline) structure. This permits one to maintain that the material in the near-surface layer of the silica sphere is in the amorphous state. Figure 7b is an image of the boundary between an a-SiO_2 sphere and the material completely filling a pore (dark contrast). The material in the pore has a polycrystalline structure. The alternation of spots of darker and brighter contrast is associated with nonuniform thickness of the cluster (material in the pore). The darker contrast is due to a superposition of crystallites. The erbium-enriched amorphous layer on the sphere surface is less distinct, because its dark contrast, due to strong absorption, is close to that of the material in the pore. The crystallites near the sphere surface become superposed on the amorphous layer and mask its image.

An electron diffraction pattern (Fig. 6b) obtained from a completely filled pore (identified by a dashed square) contains Debye rings with separate reflections distributed over a ring. Such electron diffraction patterns are characteristic of a polycrystalline object in which not all crystallite orientations are equally probable. In addition, this pattern has a diffuse halo near its central part, close to the spot produced by the primary electron beam. An analysis of this electron diffraction pattern (determination of interplanar distances from the Debye rings) provides unambiguous evidence of the formation of polycrystalline erbium oxide Er_2O_3 in opal pores. As for the diffuse halo, it can be due to scattering either from amorphous silicate spheres or from the thin amorphous dark-contrast layer present on the surface of the spheres. Nevertheless, a combined analysis of our optical and structural studies permits us to conclude that erbium enters both the amorphous and crystalline phases forming in the resultant composite.

It is known that Er dissolves poorly in SiO_2. The Er solubility limit in SiO_2 is 0.1 mol % [30]. It is highly probable that Er_2O_3 deposited initially on the sphere surface starts to react under annealing with a-SiO_2 to produce erbium silicates. There are several types of erbium silicates: oxoorthosilicate Er_2SiO_5, orthosilicate $Er_4(SiO_4)_3$, and pyrosilicate $Er_2Si_2O_7$ [31]. At the annealing temperature of 800°C, only Er_2SiO_5 and $Er_2Si_2O_7$ can form [32]. In accordance with the phase diagram of the Er_2O_3–SiO_2 system [32], interaction of Er_2O_3 with excess SiO_2 produces a mixture of $Er_2Si_2O_7$ with SiO_2. An excess of Er_2O_3 results in the formation of a mixture of Er_2SiO_5 with Er_2O_3. In the intermediate case, a mixture of $Er_2Si_2O_7$ and Er_2SiO_5 forms. In this experiment, the smaller volume of the thin Er_2O_3 layer on the surface of a silicate sphere in comparison with the volume of the sphere corresponds to the first case. In the stage of formation, the silicate resides apparently in the amorphous state and can crystallize only in subsequent annealing. For instance, an ErO_x film 25 nm thick surrounded on both sides by SiO_x layers was annealed at 800°C for 2 h [33]. As a result of the annealing, $Er_2Si_2O_7$ formed in the film.

The dimensions of the pores in the opal matrix used (45 and 90 nm) exceed the thickness of the layer revealed on the surface of the spheres by more than an order of magnitude. As a result of the surface–material ratio being smaller, the interaction of Er_2O_3 with SiO_2 in completely filled pores does not produce silicates throughout the pore volume. When annealing such pores, silicates will possibly form only at the interface between the sphere and the filler, with polycrystalline Er_2O_3 remaining far away from the sphere surface. Near the interface between a sphere and the filler, a mixture of silicates can, in principle, form. For instance, the mixture can become enriched in $Er_2Si_2O_7$ on the side of the a-SiO_2 sphere and in Er_2SiO_2 on the side of the Er_2O_3-filled pore. The absence of reflections corresponding to the interplanar distance of the silicate phases in the electron diffractogram suggests that the silicates are in the amorphous state. This provides an indirect argument for the earlier conclusion that the PL signal is contributed by both the Er^{3+} ions in the opal matrix (a thin amorphous layer of presumably $Er_2Si_2O_7$ on the surface of a-SiO_2 spheres) and Er^{3+} in crystalline Er_2O_3 (crystallites in completely filled pores).

4. CONCLUSIONS

Thus, we produced an opal–erbium composite by using the chemical bath deposition technique. It has been shown that erbium is contained in two phases, one of which is amorphous, in the form of a layer on the surface of silica spheres, and the other is polycrystalline, in filled pores whose fraction is small. Electron microscope studies revealed that Er is deposited on the pore surface as a thin amorphous coating (presumably, $Er_2Si_2O_7$) in practically all pores. This permits one to maintain that it is this phase that erbium predominantly enters. Only a small fraction of pores is filled completely with polycrystalline Er_2O_3. Optical measurements showed that the synthesized opal–erbium composite retains the photonic band-gap properties of the original opal matrix. When pumped resonantly at a wavelength of 488 nm ($^4I_{15/2} \longrightarrow {}^4F_{7/2}$ transition), erbium in the composite efficiently emits light in the visible and near IR regions at several discrete wavelengths corresponding to the radiative transitions $^4S_{3/2} \longrightarrow {}^4I_{15/2}$ (550 nm), $^4S_{3/2} \longrightarrow {}^4I_{13/2}$ (860 nm), $^4I_{11/2} \longrightarrow {}^4I_{15/2}$ (980 nm), $^4S_{3/2} \longrightarrow {}^4I_{11/2}$ (1240 nm), and $^4I_{13/2} \longrightarrow {}^4I_{15/2}$ (1530 nm). Thus, the synthesized opal–erbium composite combines the photonic band-gap properties of opal with the luminescence of erbium and can serve as a model object to study the effect of the photonic band gap on the spontaneous emission of radiating centers.

ACKNOWLEDGMENTS

This study was supported by of the Russian Foundation for Basic Research (project no. 02-02-16502a), Ministry of Science and Industry of the Russian Federation (project “Physics of Solid-State Nanostructures”), and NATO (grant no. PST.CLG.978079).

REFERENCES

1. R. Loudon, *The Quantum Theory of Light* (Clarendon, Oxford, 1973; Mir, Moscow, 1976).
2. E. M. Purcell, Phys. Rev. **69** (11–12), 681 (1946).
3. E. Yablonovitch, Phys. Rev. Lett. **58** (20), 2059 (1987).
4. S. John, Phys. Rev. Lett. **58** (23), 2486 (1987).
5. J. P. Dowling and C. M. Bowden, Phys. Rev. A **46** (1), 612 (1992).
6. S. John and T. Quang, Phys. Rev. Lett. **74** (17), 3419 (1995).
7. W. L. Vos and A. Polman, MRS Bull. **26** (8), 642 (2001).
8. V. N. Astratov, V. N. Bogomolov, A. A. Kaplyanskii, *et al.*, Nuovo Cimento D **17** (11–12), 1349 (1995).
9. V. N. Bogomolov, S. V. Gaponenko, A. M. Kapitonov, *et al.*, Appl. Phys. A **63** (6), 613 (1996).
10. A. van Blaaderen, R. Ruel, and P. Wiltzius, Nature **385** (6614), 321 (1997).
11. H. Miguez, C. López, F. Meseguer, *et al.*, Appl. Phys. Lett. **71**, 1148 (1997).
12. Y. N. Xia, B. Gates, Y. D. Yin, and Y. Lu, Adv. Mater. **12** (10), 693 (2000).
13. A. Polman, J. Appl. Phys. **82** (1), 1 (1997).
14. S. John and T. Quang, Phys. Rev. A **50** (2), 1764 (1994).
15. K. Busch and S. John, Phys. Rev. Lett. **83** (5), 967 (1999).
16. D. Kang, J. E. Maclennan, N. A. Clark, *et al.*, Phys. Rev. Lett. **86** (18), 4052 (2001).
17. V. G. Golubev, V. Yu. Davydov, N. F. Kartenko, *et al.*, Appl. Phys. Lett. **79** (14), 2127 (2001).
18. L. N. Komissarova, V. M. Shatskiĭ, G. Ya. Pushkina, L. G. Shcherbakova, L. G. Mamsurova, and G. E. Sukhanova, *Compounds of Rare-Earth Elements: Carbonates, Oxalates, Nitrates, and Titanates* (Nauka, Moscow, 1984).
19. N. A. Feoktistov, V. G. Golubev, J. L. Hutchison, *et al.*, Semicond. Sci. Technol. **16** (12), 955 (2001).
20. Yu. A. Vlasov, V. N. Astratov, A. V. Baryshev, *et al.*, Phys. Rev. E **61** (5), 5784 (2000).
21. H. Miguez, A. Blanco, F. Meseguer, *et al.*, Phys. Rev. B **59** (3), 1563 (1999).
22. V. G. Golubev, V. A. Kosobukin, D. A. Kurdyukov, *et al.*, Fiz. Tekh. Poluprovodn. (St. Petersburg) **35** (6), 710 (2001) [Semiconductors **35**, 680 (2001)].
23. M. J. Weber, Phys. Rev. **157** (2), 262 (1967).
24. Yu. A. Vlasov, V. N. Astratov, O. Z. Karimov, *et al.*, Phys. Rev. B **55** (20), R13357 (1997).

25. W. F. Krupke, Phys. Rev. **145** (1), 325 (1966).
26. L. A. Riseberg and H. W. Moos, Phys. Rev. **174** (2), 429 (1968).
27. L. A. Riseberg and M. J. Weber, in *Progress in Optics*, Ed. by E. Wolf (Elsevier, New York, 1976), Vol. 14, p. 89.
28. M. D. Shinn, W. A. Sibley, M. G. Drexhage, *et al.*, Phys. Rev. B **27** (11), 6635 (1983).
29. J. B. Gruber, J. R. Henderson, M. Muramoro, *et al.*, J. Chem. Phys. **45** (2), 477 (1966).
30. M. J. Weber, in *Ultrastructure Processing of Advanced Materials*, Ed. by D. R. Uhlmann and D. R. Ulrich (Wiley, New York, 1992), p. 447.
31. I. A. Bondar’, N. V. Vinogradova, L. N. Dem’yanets, Zh. A. Ezhova, V. V. Ilyukhin, V. Yu. Kara-Ushanov, L. N. Komissarova, E. V. Lazarevskiĭ, B. N. Livitin, P. P. Mel’nikov, D. A. Murashov, V. P. Orlovskiĭ, K. K. Palkina, M. A. Petrova, I. A. Rozanov, N. N. Chudinova, and A. A. Fotiev, *Compounds of Rare-Earth Elements: Silicates, Germanates, Phosphates, Arsenates, and Vanadates* (Nauka, Moscow, 1983).
32. N. A. Toropov, F. Ya. Galakhov, and S. F. Konovalova, Izv. Akad. Nauk SSSR, Ser. Khim., No. 8, 1365 (1961).
33. K. Hafidi, Y. Ijdiyaou, M. Azizan, *et al.*, Appl. Surf. Sci. **108** (2), 251 (1997).

Translated by G. Skrebtsov

Physics of the Solid State, Vol. 44, No. 12, 2002, pp. 2232–2234. Translated from Fizika Tverdogo Tela, Vol. 44, No. 12, 2002, pp. 2133–2134.
Original Russian Text Copyright © 2002 by Domoratsk, Rizak, Sadovskaya.

SEMICONDUCTORS AND DIELECTRICS

Thermal Conductivity of Bismuth Tellurite

K. V. Domoratsky*, V. M. Rizak, and L. Ya. Sadovskaya***
** Dnepropetrovsk State University, Dnepropetrovsk, 49050 Ukraine*
*** Uzhgorod State University, ul. Podgornaya 46, Uzhgorod, 88000 Ukraine*
e-mail: elf@ff.dsu.dp.ua

Received October 23, 2001; in final form, February 4, 2002

Abstract—This paper reports on the results of investigations of the thermal conductivity along the three crystallographic directions in bismuth tellurite crystals. It is found that bismuth tellurite exhibits a low thermal conductivity inherent in glasses and disordered solid solutions. At temperatures below the Debye temperature, the thermal conductivity coefficients depend on the temperature as $\sqrt{T}$, which is characteristic of disordered solid solutions. The temperature dependence of the thermal conductivity of bismuth tellurite is calculated in the framework of the Debye model. © *2002 MAIK “Nauka/Interperiodica”.*

1. INTRODUCTION

Thermal conductivity is directly associated with the anharmonicity of lattice vibrations. The study of thermal conductivity is an efficient method of investigating phonon processes in crystals. This paper reports on the results of investigations into the thermal conductivity of bismuth tellurite crystals. To the best of our knowledge, information on the thermal conductivity of these crystals has hitherto been unavailable.

2. SAMPLE PREPARATION AND EXPERIMENTAL TECHNIQUE

Single crystals of Bi_2TeO_5 were grown by the Czochralski method [1]. A single crystal of bismuth tellurite at room temperature has orthorhombic symmetry with the unit cell parameters $a = 11.602$ Å, $b = 16.461$ Å, and $c = 5.523$ Å [2]. All three thermal conductivity coefficients were studied using a single-crystal sample in the form of a parallelepiped ($5 \times 7 \times 9$ mm in size) with its faces corresponding to the three principal crystallographic directions. The thermal conductivity was measured using the method of a stationary longitudinal heat flux. The measurements were performed in the temperature range 100–370 K on a TAU-2 automated setup [3] designed in NPO VNIIFTRI. The software of the computer measuring system included the IR operating system and the DCANN instrument-module control program [4].

3. RESULTS AND DISCUSSION

Figure 1 shows the measured temperature dependences of the thermal conductivity coefficients λ_i ($i = 1, 2, 3$) of bismuth tellurite in the temperature range 100–370 K for the three principal crystallographic directions. At temperatures $T < 250$ K, all the obtained dependences $\lambda(T)$ are governed by the law T^{3-n}, where the value of $n = 3.5$ is smaller than that in the case of phonon scattering by point defects ($n = 4$) and larger than that in the case of scattering by cylindrical defects ($n = 3$) [5]. At temperatures below 250 K, the small magnitudes and temperature dependences of the thermal conductivity coefficients along the studied directions in the Bi_2TeO_5 single crystal are consistent with the magnitudes and behavior of the thermal conductivity coefficients of the disordered solid solutions. In our recent paper [6], we noted that the possibility exists of structural disordering occurring in bismuth tellurite due to a random orientation of the lone electron pair. It can be assumed that this mechanism is responsible for the specific features in the thermal conduction of Bi_2TeO_5 single crystals.

In the temperature range $T > 250$ K, the temperature dependence of the thermal conductivity coefficient of

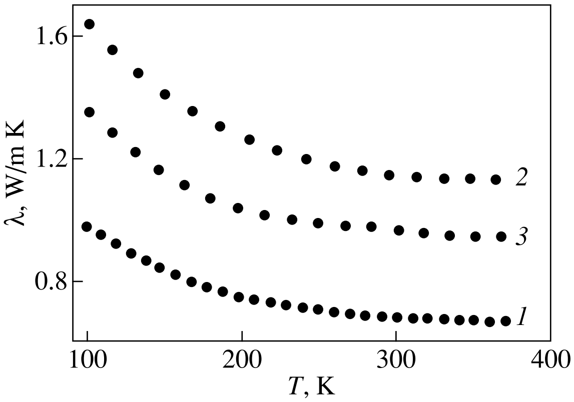

Fig. 1. Temperature dependences of the thermal conductivity coefficient of single-crystal bismuth tellurite for the crystallographic directions (*1*) [100], (*2*) [010], and (*3*) [001].

the Bi_2TeO_5 single crystal is represented by a more flattened curve that smoothly transforms into a portion in which λ weakly depends on the temperature up to the highest temperature under investigation. According to Ioffe [7], the weak temperature dependence of the thermal conductivity in solids with low values of λ can be associated with the strong anharmonicity, which is responsible for close values of the phonon mean free path l and the unit cell dimensions. This recalls the behavior of the thermal conductivity coefficients in amorphous solids when the mean free path is limited by the mean distance between atoms or molecules.

As can be seen from Fig. 1, the thermal conductivity of Bi_2TeO_5 exhibits a weak anisotropy in magnitude which is virtually independent of temperature. In the structure of bismuth tellurite, the heavy metal atoms are located at sites of the cubic fluorite-like lattice [2]. It should be noted that, at temperatures higher than the Debye temperature, the mean free path l is commensurate (~3 Å) to the distance between these atoms. Hence, the mean free path can be assumed to be isotropic. According to the experimental data obtained in [8], the mean velocities of propagation of elastic waves in the [100], [010], and [001] directions, which were determined by taking into account both the longitudinal and transverse components, are equal to 2113, 2294, and 2257 m/s, respectively. Therefore, it can be assumed that the anisotropy of the thermal conductivity of bismuth tellurite is determined primarily by the anisotropy of the mean velocities of sound, whereas the low degree of anisotropy in this case is caused by the isotropy of the phonon mean free path.

In order to describe theoretically the temperature dependence of the thermal conductivity on the basis of the Debye model [9]

$$\lambda(T) = \frac{1}{2\pi^2 \nu} \int_0^{\nu_{\max}} h\nu^3 \tau_0 \frac{(h\nu/kT^2)\exp(h\nu/kT)}{[\exp(h\nu/kT)-1]^2} d\nu, \quad (1)$$

we calculated the dependence $\lambda(T)$. Here, τ_0 is the relaxation time, $\nu_{\max} = k\Theta_D/h$, and Θ_D is the Debye temperature (≈250 K [10]).

Within this approximation, the relaxation time is determined by phonon scattering due to lattice anharmonicity τ_a, phonon scattering by defects τ_d, and phonon scattering by boundaries of the sample τ_b [9]; that is,

$$\tau_0^{-1} = \tau_a^{-1} + \tau_d^{-1} + \tau_b^{-1}. \quad (2)$$

A similar estimate of these phonon relaxation times is given in [11]:

$$\tau_0^{-1} = DT\nu^2 \exp(-c/T), \quad (3)$$

where D and c are constants.

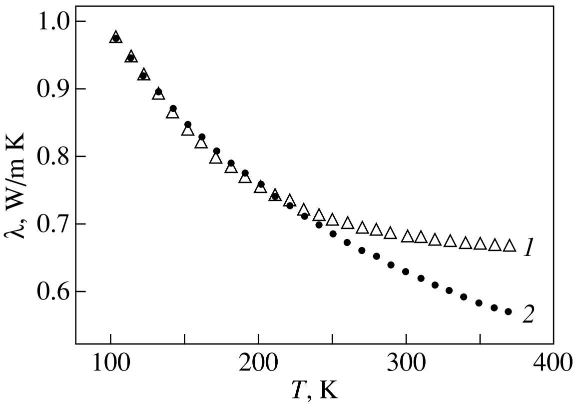

Fig. 2. (*1*) Experimental and (*2*) calculated temperature dependences of the thermal conductivity coefficient of a dielectric crystal. Curve *2* is calculated according to formula (6) with the parameters of Bi_2TeO_5 in the crystallographic direction [100].

In the presence of defects, the relaxation time component τ_d^{-1}, according to [12], can be estimated as

$$\tau_d^{-1} = A\nu^4, \quad (4)$$

where A is a constant dependent on the specific volume (per atom in the unit cell of the crystal), the Debye velocity of sound in the crystal, and the defect concentration.

In the case when the phonons are scattered by boundaries of the crystal, τ_b^{-1} does not depend on the temperature [12]; that is,

$$\tau_b^{-1} = B = \text{const.} \quad (5)$$

By using formulas (1)–(5), we obtain

$$\lambda(T) = \frac{1}{2\pi^2 \nu} \int_0^{\nu_{\max}} h\nu^3 \frac{(h\nu/kT^2)\exp(h\nu/kT)}{[\exp(h\nu/kT)-1]^2} \times \frac{1}{A\nu^4 + B + DT\nu^2 \exp(-c/T)} d\nu, \quad (6)$$

where $A = 2.1 \times 10^{-40}$ s^3, $B = 5.1 \times 10^8$ s^{-1}, $C = 0.2$ K, and $D = 8 \times 10^{-18}$ s/K are the fitting parameters.

Figure 2 depicts the theoretical dependence $\lambda(T)$, which was obtained by numerical simulation using formula (6). It can be seen from Fig. 2 that the calculated curve coincides with the experimental temperature dependence of the thermal conductivity of bismuth telluride at low temperatures. A noticeable difference is observed in the temperature range above 250 K, in which the measured thermal conductivity coefficient weakly depends on the temperature (Fig. 2). This can be due to a short mean free path of short-wavelength acoustic phonons as compared to the unit cell dimensions and indicates a deviation from the phonon mechanism of heat transfer [13].

REFERENCES

1. K. V. Domoratsky, A. Yu. Kudzin, L. Ja. Sadovskaya, and G. Ch. Sokolynskii, Ferroelectrics **214**, 191 (1998).
2. D. Mercurio, M. El. Farissi, B. Frit, and P. Goursat, Mater. Chem. Phys. **9**, 467 (1983).
3. V. V. Sviridenko, V. A. Medvedev, N. P. Rybnik, and V. G. Gorbunova, Izmer. Tekh., No. 5, 34 (1987).
4. K. Aström and B. Wittenmark, *Computer Controller Systems* (Prentice-Hall, Englewood Cliffs, 1984; Mir, Moscow, 1987).
5. P. G. Klemens, in *Physical Acoustics: Principles and Methods*, Vol. 3, Part B: *Lattice Dynamics*, Ed. by W. P. Mason (Academic, New York, 1965; Mir, Moscow, 1968).
6. K. V. Domoratskiĭ, V. I. Pastukhov, A. Yu. Kudzin, *et al.*, Fiz. Tverd. Tela (St. Petersburg) **42** (8), 1404 (2000) [Phys. Solid State **42**, 1443 (2000)].
7. A. F. Ioffe, Fiz. Tverd. Tela (Leningrad) **1** (1), 160 (1959) [Sov. Phys. Solid State **1**, 141 (1959)].
8. A. M. Antonenko, K. V. Domoratsky, A. Yu. Kudzin, and L. Ya. Sadovskaya, Condens. Matter Phys. **2** (4), 721 (1999).
9. R. Berman, *Thermal Conduction in Solids* (Clarendon, Oxford, 1976; Mir, Moscow, 1979).
10. K. V. Domoratskiĭ, V. M. Rizak, L. Ya. Sadovskaya, and V. A. Stefanovich, Fiz. Tverd. Tela (St. Petersburg) **41** (4), 629 (1999) [Phys. Solid State **41**, 565 (1999)].
11. V. I. Al'tukhov, Author's Abstract of Doctoral Dissertation (Checheno-Ingushskiĭ Univ., 1982).
12. I. M. Rizak, V. M. Rizak, S. I. Perechinskiĭ, *et al.*, in *Proceedings of the XII Conference on Physics of Ferroelectrics, Tver, 1992*, Vol. 1, p. 26.
13. V. M. Rizak, Doctoral Dissertation (Uzhgorod, 1996).

Translated by O. Moskalev

Physics of the Solid State, Vol. 44, No. 12, 2002, pp. 2235–2239. Translated from Fizika Tverdogo Tela, Vol. 44, No. 12, 2002, pp. 2135–2138.
Original Russian Text Copyright © 2002 by Lisitsyna, Korepanov, Lisitsyn.

SEMICONDUCTORS AND DIELECTRICS

A Comparative Analysis of the Spectral Characteristics of Triplet Self-Trapped Excitons and F_2 Centers in Alkali Halide Crystals

L. A. Lisitsyna*, V. I. Korepanov, and V. M. Lisitsyn****
** Tomsk State Civil Engineering University, Solyanaya pl. 2, Tomsk, 634003 Russia*
*** Tomsk Polytechnical University, Tomsk, 634034 Russia*
e-mail: lisitsyn@list.epd.tpu.edu.ru

Received November 22, 2001; in final form, February 15, 2002

Abstract—A comparative analysis of the spectral characteristics of self-trapped excitons (STE) and F_2 centers in the states with the same spin multiplicity is carried out. Based on the analysis, a criterion for the separation of the triplet–triplet (*T*–*T*) absorptive transitions in the electronic and hole components of the STE in any alkali halide crystal is proposed. It is concluded that inhomogeneities in the form of a homological cation or anion impurity in the nearest coordination shells of the spatial position of the STE, rather than hole, affect the spectral position of the *T*–*T* transitions in the electron component of the STE. *© 2002 MAIK “Nauka/Interperiodica”.*

A two-halide, self-trapped exciton (STE) in alkali halide crystals is an $(X_2^{2-})^*$ excimer ($X \equiv$ Hal). Depending on the crystal, the core of the excimer (X_2^- molecule) occupies two halide sites (the on-type STE, D_{2h} point symmetry), one halide site (the off-type STE, C_{2v} symmetry), or an intermediate noncentrosymmetric position in the vicinity of a nucleating anion vacancy (Fig. 1) [1–5].

Kan'no proposed a criterion for the determination of the type of an STE in any alkali halide crystal [5]. The criterion is based on the value of the Stokes shift (Fig. 2) characterizing the difference between the minimal energy required to create an STE and the energy emitted by the STE. In crystals with a large value of the Rabin–Klick parameter (≥0.4), off-type self-trapped excitons (type III, according to Kan'no) characterized by a large Stokes shift are formed. In crystals characterized by a small value of the Rabin–Klick parameter (<0.4), on-type self-trapped excitons (type I, according to Kan'no) with a small Stokes shift are formed. In type-II STEs, the core occupies an intermediate position between the positions corresponding to one- and two-site localization. (The Rabin–Klick parameter characterizes the compactness of the crystal lattice; in the series of alkali halide crystals, this parameter changes from 0.18 (NaI) to 1.1 (KF) and is equal to the ratio *S*/*D*, where *S* is the distance between the nearest neighbor halides along the ⟨110⟩ axis and *D* is the diameter of a halide atom [6].)

Nowadays, the assumption of the existence of different self-trapped excitons is used to explain the generation of point defects during the decay of electron excitations and to interpret the evolution of the initial defects in alkali halide crystals with temperature and time [7–9]. The main experimental verifications of the

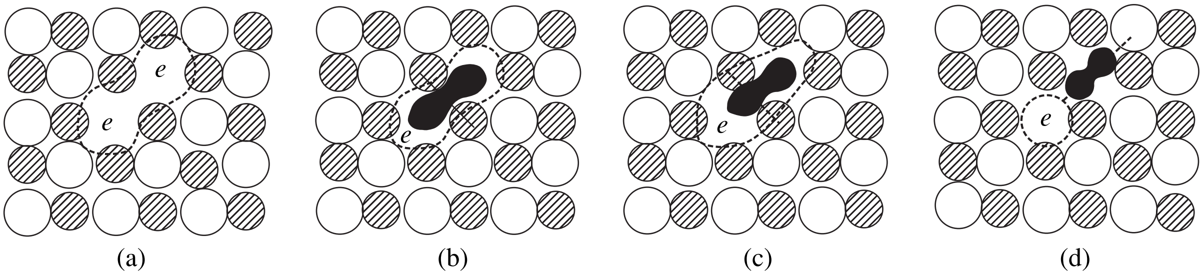

Fig. 1. Model of (a) the F_2 center and (b–d) two-halide self-trapped excitons of different types in alkali halide crystals: (b) type-I (on-type) exciton, (c) type-II exciton, and (d) type-III (off-type) exciton; open and cross-hatched circles are halogen and alkali-metal ions, respectively.

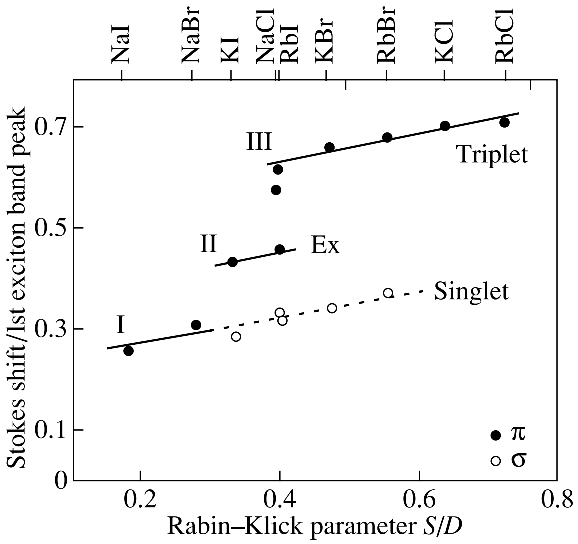

Fig. 2. Dependence of the ratio between the Stokes shift of the triplet radiative transition of the STE and the energy of the lowest absorptive transition of the exciton on the Rabin–Klick parameter (according to [5]).

off-center position of the STE core in some alkali halide crystals have been obtained from Raman spectra [10] and the spectra of double electron–nuclear resonance [11]. An increase in the STE lifetime with increasing Rabin–Klick parameter of the crystal is also indirect evidence of the off-center position of the STE core [2].

However, an analysis of the absorption spectra of the triplet–triplet (*T*–*T*) transitions of the STE in eleven alkali halides and a comparison of these spectra with theoretically calculated spectral positions of these transitions do not lead to the unambiguous conclusion that the STE structure in different alkali halide crystals is different.

It is well known that the spectrum of the *T*–*T* absorptive transitions of the STE in alkali halide crystals is in the range 0.5–5 eV and consists of a number of bands (see table). These bands are due to π-polarized transitions of the electronic component of the STE at energies below 3 eV and to transitions in the hole component of the STE at 3–5 eV, with the shortest wavelength transitions in the hole component being σ-polarized [21] (see table; the electron transitions in the hole component of the STE are italicized). In chlorides, the spectral position of short-wavelength absorptive transitions in the hole component of the STE coincides with the *H* band, which can be treated as a verification of the single-site position of the X_2^- molecule and, therefore, of the existence of type-III STEs (according to Kan'no) in these crystals (Fig. 2). In all iodides, however, the spectral position of absorptive transitions in the hole component of the STE coincides with the position of the absorption bands of V_k centers,[1] whereas, according to Kan'no, there are type-I STEs in NaI, type-II STEs in KI, and type-III STEs in RbI (Fig. 2).

It is well known that the calculated spectral positions of the *T*–*T* absorptive transitions in the electronic component of the STE in different alkali halide crystals do not coincide with those found experimentally. According to theoretical estimates [4, 22, 23], the spectral position of the longest wavelength transition in the on-type STE is in the range 0.1–1.3 eV, whereas experimentally, this transition is observed at an energy above 1 eV (in the range of the *F* absorption band) in all known alkali halide crystals except for NaBr and NaI. The discrepancy between the calculated and experimental data is taken as evidence of the existence of the off-type STE in all alkali halide crystals except NaBr and NaI. In contrast to the on-type STE, the electron wave function of an off-type self-trapped exciton is virtually localized at the anion vacancy. Therefore, the transitions in the electronic component of these STEs occur in the spectral range close to the *F* absorption band [24, 25]. However, this conclusion is based on the assumption that the spectral position of the *T*–*T* transitions in the electronic component of the STE is determined by the spatial position of the STE core [5]. In our opinion, there is no experimental verification of this conclusion; moreover, it contradicts the experimental data.

In order to investigate the influence of the core structure on the spectral kinetic parameters of the STE, we carried out a comparative analysis of the properties of the STE and F_2 centers in the same crystal. The structure of these centers differs in the type of the core if the outer molecular orbital is the same.

It is known that in alkali halide crystals, the F_2 center consists of two electrons, which are trapped by the field of two neighboring anion vacancies (Fig. 1a). The center results from the capture of an electron by an F_2^+ center,

$$F_2^* \equiv (F_2^+ + e)^*$$

(the F_2^+ center consists of two neighboring anion vacancies with one electron localized on them), and possesses D_{2h} point symmetry in the triplet state.

The on-type STE (Fig. 1b) also possesses D_{2h} point symmetry in the triplet state; this STE results from the capture of an electron by a V_k center and can be represented as

$$\mathrm{STE}^* \equiv (X_2^- + e)^*.$$

---

[1] The V_k center is an X_2^- molecule occupying two neighboring halide sites.

Characteristics of the F_2 centers and self-trapped excitons in alkali halide crystals: the lifetime in the singlet (τ_σ) and triplet (τ_π) radiative states, the spectral positions of the singlet (E_σ) and triplet (E_π) radiative transitions, the spectrum of the triplet–triplet absorptive transitions (*T*–*T*), the position *E* of absorptive transitions of the V_k and *H* centers, and the Rabin–Klick parameter *S*/*D* of the crystals

Compound	τ_σ, ns	τ_π, s	E_σ, eV	*T*–*T*, eV		τ_σ, ns	τ_π, 10^{-6} s	E_σ, eV	E_π, eV	*E*, eV		*S*/*D*
	F_2	F_2	F_2	F_2	STE	STE	STE	STE	STE	V_k	*H*	
KI		6	0.8	1.4	1.4	2.3	4.4	4.13	3.34	1.08	2.8	0.33
		[13]	[14]	[13]	1.6	[18]	[1]	[19]	[19]	1.55	2.23	[6]
					2.2					2.12	[19]	
					3.2					3.10		
					[17]					[20]		
KBr		14	1	1.6	1.58	3.3	130	4.4	2.44			0.45
		[13]	[14]	1.8	1.76	[18]	[1]	[19]	[19]	1.38		[6]
				2.24	2.24					1.65	3.26	
				[15]	3.3					3.22	[19]	
					[17]					[20]		
KCl	28	100	1.1	1.8	1.87		5000		2.54			0.6
	[12]	[13]	[14]	2.1	2.12		[1]		[19]			[6]
				2.45	2.45					1.65		
				[15]	3.7					3.4	3.69	
					[17]					[20]	[19]	
NaCl	26		1.2	2.1	2.08	2.8	300	5.47	3.47			0.38
	[12]		[14]	[16]	3.2	[18]	[1]	[19]	[19]	3.28	3.9	[6]
					3.9					[20]	[19]	
					[17]							

Note: The absorption spectra are given at 10 K.

In contrast to the F_2^* center, the two anion vacancies in the STE are occupied by the two-halide X_2^- molecule.

From the data listed in the table, it follows that the spectral kinetic parameters of the STE and F_2 centers in the same crystal are significantly different. In contrast to the F_2 center, the STE contains a molecular core; therefore, the STE absorption spectrum is determined by *T*–*T* absorptive transitions not only in the electronic component but also in the hole component (in the X_2^- molecule).

The presence of the molecular core in the STE also leads to an increase in the energies E_σ and E_π of the singlet and triplet radiative transitions; depending on the crystal, the increase is 3–4 and approximately 2 eV, respectively. In addition, the presence of the molecular core in the STE gives rise to a decrease in the lifetime of the excited singlet and triplet radiative states by an order and roughly five orders of magnitude, respectively.

However, the tendency of the lifetime of the STE in the triplet state to increase with increasing Rabin–Klick parameter in the series of potassium halides holds for both STE and F_2 centers (see table). For the STE, this tendency is explained by the change in the point symmetry of the center [1, 5], but it is quite obvious that this explanation is not valid for the F_2 centers, because their point symmetry is the same in all crystals.

A comparison of the *T*–*T* absorption spectra of the STE and F_2 centers in the same crystal (see table) indicates that, in the range 1–3 eV, the spectrum of transitions in the KCl, KBr, and NaCl crystals is the same for both centers. The position of the longest wavelength band in the multiband spectrum of the STE in the KI crystal coincides with the position of the only band in the spectrum of the F_2 center. As mentioned above, the absorption spectrum of the triplet STE contains the bands corresponding to transitions in both electron and hole components, whereas the absorption spectrum of the triplet F_2 center contains the bands corresponding to transitions in the electronic component alone. Therefore, it can be argued that the spectra of *T*–*T* transitions in the electronic component of the F_2 center and STE coincide in each crystal listed in the table [26].

The comparative analysis of the spectral characteristics of the STE and F_2 center in the triplet state in the same crystal and in the series of alkali halide crystals makes it possible to draw the following conclusions.

(1) The coincidence of the spectra of *T*–*T* absorptive transitions in the electronic components of the STE and F_2 centers in KI, NaCl, KCl, and KBr indicates that the differences between the core structures of these centers do not affect the spectral position of these transitions. Indeed, the core of the F_2 center in all the crystals is two free anion vacancies, while the STE core is an X_2^- molecule, which is partially displaced from the centrosymmetrical position and situated in the vicinity of the nucleating vacancy (in KI and NaCl crystals) or occupies an anion site near an anion vacancy (in KCl and KBr crystals).

(2) The presence of transitions in the hole component of the STE (in addition to those in the electronic component) is the fundamental difference between the spectra of *T*–*T* absorptive transitions in the STE and F_2 centers. This difference can be used as a criterion for the separation of the transitions in the electronic and hole components of the STE in any crystal if the *T*–*T* transition spectra of the STE and F_2 centers are known.

The problem of the separation of the transitions is of particular interest in the analysis of the STE spectra in iodides, in which the transition in the hole component of the STE coincides with the transition in the V_k center. It is well known that the configurational and spin–orbit interactions lead to an additional splitting and mixing of the Π and Σ^+ states in the V_k center of these crystals, which results in the appearance of additional transitions at energies below 3 eV whose spectral position and polarization can coincide with transitions in the electronic component [20].

We propose the following criterion for the separation of the transitions in the electronic and hole components of the STE: the coincidence of the bands in the *T*–*T* absorption spectra for the STE and F_2 center corresponds to transitions in the electronic component. For example, by comparing the spectra of *T*–*T* transitions in the F_2 center and STE in the KI crystal, one can see that there is only one band (1.4 eV) corresponding to transitions in the electronic component, whereas the other bands correspond to transitions in the hole component of the STE (see table). The presence of such transitions in the I_2^- molecule is direct confirmation of the validity of this conclusion [20].

(3) The coincidence of the spectra of *T*–*T* transitions in the electronic component of the STE and F_2 centers indicates that the structure of the nearest coordination shells of these centers is the same.

It is known that in a crystal doped with heavy anion or light cation homologs, irradiation leads to the formation of STEs whose spectral kinetic parameters differ from those of the STE in the regular lattice. Changes in the lifetime and spectral position of the radiative transitions, as well as in the spectrum of *T*–*T* absorptive transitions, are observed to occur only in the electronic component of the STE. In KCl–Na crystals, for example, the spectrum of *T*–*T* transitions in the electronic component of the STE at 80 K consists of a wide nonuniform band at 2 eV [27, 28], in contrast to the spectrum of the pure crystal, which contains one band at 2.2 eV. The spectrum of *T*–*T* transitions in the electronic component of the STE in RbCl and RbCl–I crystals at 10 K consists of bands at 1.7, 1.95, 2.25 and 1.5, 1.7, 1.85 eV, respectively [29]; in KCl and KCl–I crystals, bands are observed at 2.0 and 1.65 eV, respectively [30]; and in KBr and KBr–I crystals, at 1.7 and 1.13 eV, respectively [31] (in the latter two cases, the STE spectra are observed at 80 K).

We proved in [31, 32] that the introduction of halide impurities leads to the creation of a near-impurity STE (which consists of a homohalide core and the impurity ion in the nearest coordination shell) rather than of a heterohalide STE, as assumed, for example, in [29]. Since a long-wavelength shift of the positions of the bands in the *T*–*T* absorption spectrum of the electronic component of the STE is observed upon the introduction of both the cation and anion homologs, there is obviously a common reason behind this shift. In our opinion, this reason is the presence of an impurity in the nearest surrounding of the STE in a doped crystal. The comparative analysis of the absorption spectra of the STE in different alkali halide crystals which we performed in this paper also indicates that the spectral position of *T*–*T* transitions in the electronic component of the STE is determined by the state of the nearest neighbor surrounding rather than by the structure of the STE core. An analysis of the optically detected electron paramagnetic resonance spectrum of the STE in KCl crystals also suggests that the electronic component of the STE strongly interacts with the ligand cores and only weakly interacts with the STE core [33].

ACKNOWLEDGMENTS

This work was supported by the state program “Physics of Quantum and Wave Processes.”

REFERENCES

1. K. Song and L. Chen, J. Phys. Soc. Jpn. **58** (8), 3022 (1989).
2. C. H. Leung, G. Brunet, and K. S. Song, J. Phys. C **18**, 4459 (1985).
3. K. Song, C. Leung, and R. Williams, J. Phys.: Condens. Matter **1**, 683 (1989).
4. K. Song and C. Leung, J. Phys.: Condens. Matter **1**, 8425 (1989).
5. K. S. Song and R. T. Williams, *Self-Trapped Excitons* (Springer, Berlin, 1993).

6. H. Rabin and C. Klick, Phys. Rev. **117**, 1005 (1960).
7. R. T. Williams, H. Lui, G. P. Willams, and K. J. Platt, Phys. Rev. Lett. **66** (16), 2140 (1991).
8. L. A. Lisitsyna, E. V. Grechkina, V. I. Korepanov, and V. M. Lisitsyn, Fiz. Tverd. Tela (St. Petersburg) **43** (9), 1613 (2001) [Phys. Solid State **43**, 1680 (2001)].
9. V. M. Lisitsyn, in *High-Current Pulsed Electron Beams in Technology*, Ed. by G. A. Mesyats (Nauka, Novosibirsk, 1983), pp. 61–72.
10. T. Suzuki, K. Tanimura, and N. Itoh, Phys. Rev. B **49** (11), 7233 (1994).
11. D. Block, F. Wasiela, and Y. M. d’Aubinge, J. Phys. C **11**, 4201 (1978).
12. L. Bosi, C. Bussolati, and S. Cova, Phys. Status Solidi **50** (1), 311 (1972).
13. I. Schneider and M. Caspari, Phys. Rev. **133**, A1193 (1964).
14. H. J. Hoffman, J. Phys. (Paris) **41**, 359 (1980).
15. M. Ikezawa and M. Ueta, J. Phys. Soc. Jpn. **18**, 145 (1963); M. Ikezawa, J. Phys. Soc. Jpn. **19** (4), 529 (1964).
16. W. Compton and C. Klick, Phys. Rev. **112**, 1620 (1958).
17. R. Williams and M. Kabler, Phys. Rev. B **9** (4), 1897 (1974).
18. I. M. Blair, D. Pooley, and D. Smith, J. Phys. C **5**, 1537 (1972).
19. Ch. B. Lushchik and A. Ch. Lushchik, *Decay of Electron Excitations with Defect Formation in Solids* (Nauka, Moscow, 1989).
20. *Point Defects in Solids*, Ed. by J. H. Crawford and L. M. Slifkin (Plenum, New York, 1972), Vol. 1.
21. K. Tanimura, K. Soda, and N. Itoh, Solid State Commun. **36**, 745 (1980).
22. K. Song, A. Stoneham, and A. Harker, J. Phys. C **8**, 1125 (1975).
23. N. Itoh, A. Stoneham, and A. Harker, J. Phys. C **10**, 4197 (1977).
24. K. Edamatsu, M. Sumita, S. Hirota, and M. Hirai, Phys. Rev. B **47** (11), 6747 (1993).
25. S. Hirota, K. Edamatsu, and M. Hirai, Phys. Rev. Lett. **67** (23), 3283 (1991).
26. L. A. Lisitsyna, Izv. Vyssh. Uchebn. Zaved., Fiz. **38** (8), 115 (1995).
27. K. Nanimura, N. Nurakami, and N. Itoh, J. Phys. Soc. Jpn. **51** (3), 888 (1982).
28. Y. Hirano and N. Itoh, Phys. Lett. A **60A** (5), 465 (1977).
29. O. Arimoto, K. Sasaki, K. Kan’no, and Y. Nakai, J. Phys. Soc. Jpn. **54** (8), 3188 (1985).
30. V. M. Lisitsyn, A. A. Malyshev, and V. Yu. Yakovlev, Fiz. Tverd. Tela (Leningrad) **25** (11), 3356 (1983) [Sov. Phys. Solid State **25**, 1932 (1983)].
31. M. F. Kuznetsov and V. I. Korepanov, Opt. Spektrosk. **64**, 960 (1988) [Opt. Spectrosc. **64**, 573 (1988)].
32. V. I. Korepanov, V. M. Lisitsyn, and L. A. Lisitsyna, Izv. Vyssh. Uchebn. Zaved., Fiz. **39** (11), 94 (1996).
33. P. G. Baranov, Izv. Akad. Nauk SSSR, Ser. Fiz. **45**, 254 (1981).

Translated by A. Poushnov

Physics of the Solid State, Vol. 44, No. 12, 2002, pp. 2240–2250. Translated from Fizika Tverdogo Tela, Vol. 44, No. 12, 2002, pp. 2139–2148.
Original Russian Text Copyright © 2002 by Bert, Kolesnikova, Romanov, Chaldyshev.

Elastic Behavior of a Spherical Inclusion with a Given Uniaxial Dilatation

N. A. Bert*, A. L. Kolesnikova, A. E. Romanov*, and V. V. Chaldyshev***

** Ioffe Physicotechnical Institute, Russian Academy of Sciences,*
Politekhnicheskaya ul. 26, St. Petersburg, 194021 Russia
e-mail: aer@mail.ioffe.ru
*** Institute of Problems in Machine Science, Russian Academy of Sciences,*
Vasil'evskiĭ ostrov, Bol'shoĭ pr. 61, St. Petersburg, 199178 Russia

Received January 22, 2002

Abstract—The elastic behavior of a spherical inclusion with a uniaxial dilatation is considered. As an example, the experimental data on stressed nanoclusters in doped semiconductors (As–Sb clusters in GaAs) are presented. The fields of displacements, elastic strains, and stresses are determined for spherical inclusions with uniaxial dilatation, and the specific features of these fields are revealed. The elastic energy of a uniaxial spheroid is calculated and compared with that for a triaxial spheroid. The relaxation mechanisms for the elastic field of the inclusion associated with the formation of prismatic dislocation loops are considered. *© 2002 MAIK “Nauka/Interperiodica”.*

1. INTRODUCTION

The determination of elastic stresses created by a second-phase inclusion is a classical problem in the physics, as well as mechanics, of solids [1–4]. On the one hand, a certain isolated region in a solid may experience a change in shape, resulting in the emergence of elastic strains and stresses in this region and in the surrounding matrix. The change in shape can be caused by a local plastic deformation (e.g., twinning), the separation of a new chemical phase (e.g., precipitates), a phase transformation in the material (e.g., martensite transformation), a nonuniform thermal expansion, etc. On the other hand, the presence of inhomogeneities in the material modifies the existing strain and stress fields created by external sources. In this case, the inhomogeneity is a stress concentrator. The simplest examples of such inhomogeneities are a pore or a region in a material with changed elastic moduli.

In general, an inclusion can have an arbitrary shape and volume. However, for many applications, it is sufficient to investigate an inclusion of the simplest spherical or ellipsoidal shape. The solutions for such inclusions are of practical value (see classical publications [2, 3]), are simple, and can be determined in a closed analytical form. Among other things, it has been proved that elastic strains and stresses are constant in an ellipsoidal inclusion the material of which is subjected to a uniform eigenstrain [2]. Elastic fields outside inclusions have a more complex form determined by the nature of transformations of the material in the inclusion.

At the present time, the theory of elastic inclusions has found a new application in the description of the properties of nanoclusters, viz., quantum dots in semiconducting materials [5–9]. By simulating quantum dots as inclusions with a prescribed change in volume, it is possible, for example, to estimate the effect of elastic fields generated by clusters on the electronic properties of the material inside and in the immediate vicinity of a quantum dot [6, 10–12]. In addition, the elastic interaction between quantum dots leads to their vertical ordering (along the direction of growth) [5, 13, 14], while the interaction with external sources of elastic stresses may also result in ordering in the horizontal plane (parallel to the growth surface) [15].

Arsenic clusters in gallium arsenide layers grown using molecular-beam epitaxy at a low temperature (LT-GaAs) and subjected to post-growth annealing are an important example of nanosize inclusions in a crystalline semiconducting matrix [16, 17]. It was found that such a material possesses an ultrashort lifetime of charge carriers and a high resistivity, which is extremely attractive for a number of ultrahigh-speed electronic, optical, and optoelectronic device applications [18]. As a result of recent investigations, the atomic structure of As clusters in a GaAs matrix was determined and methods for controlling the size, concentration, and spatial arrangement of the clusters were developed [19]. It was found that As clusters create relatively weak anisotropic strains in the surrounding GaAs matrix such that the LT-GaAs lattice is crystallographically perfect and contains no extended defects (dislocations, stacking faults, etc.) and its lattice param-

1063-7834/02/4412-2240$22.00 © 2002 MAIK “Nauka/Interperiodica”

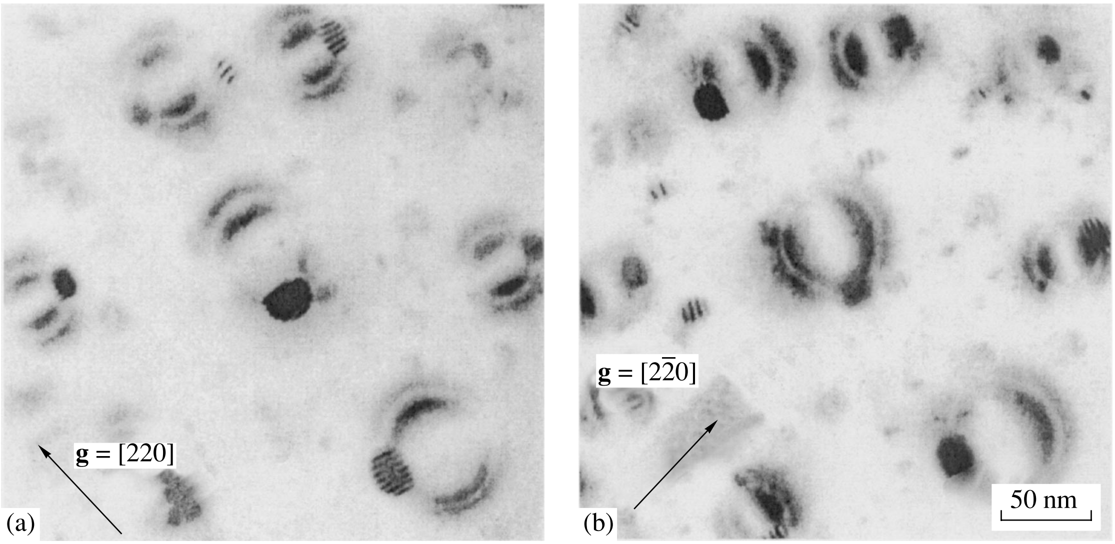

Fig. 1. Bright-field TEM images of an LT-GaAs film δ-doped with antimony and annealed at 600°C. Large inclusions exhibit a Moiré pattern and are associated with dislocation loops. The diffraction vector **g** is directed (a) along [220] and (b) along [2$\bar{2}$0].

eter is close to the value typical of conventional cluster-free gallium arsenide [17, 20–22].

It has been found recently that clusters of an As–Sb alloy with a considerable antimony concentration (20–30 at. %) can be created in a GaAs matrix [23]. In contrast to pure As clusters, such clusters produce considerable deformations in the surrounding GaAs matrix and are characterized by a high growth rate [23, 24]. In order to use such clusters in nanotechnologies, it is essential to determine the origin and relaxation mechanisms for mechanical stresses induced by the clusters. The possibility of using local mechanical stresses to induce self-organization of a cluster system is of considerable interest.

In this study, we investigate the elastic field of a spherical inclusion experiencing uniform deformation along the sphere diameter (uniaxial dilatation). The dilatation along three mutually perpendicular diameters (triaxial dilatation) corresponds to the well-studied case of a spherical inclusion with a prescribed change in volume [25]. The study of the inclusion with uniaxial dilatation was motivated by the above-mentioned observations of stressed clusters in doped semiconductors. In this connection, we present in Section 2 the experimental data on inclusions with uniaxial dilatation. In Section 3, a formal procedure of formation of an elastic inclusion with uniaxial dilatation is considered and the plastic distortion of such an inclusion is determined. Section 4 contains the results of calculations of the elastic fields and energy of an inclusion with uniaxial dilatation; the results and their possible application in simulating the relaxation processes that proceed in the vicinity of nanoclusters in doped semiconductors are discussed in Section 5.

2. EXPERIMENTAL OBSERVATION OF SPHERICAL INCLUSIONS WITH UNIAXIAL PLASTIC DILATATION IN ANTIMONY-DOPED GALLIUM ARSENIDE

Spherical clusters with uniaxial dilatation (plastic distortion) were detected when examining the microscopic structure of GaAs films grown by molecular-beam epitaxy at a low temperature (200°C) (LT-GaAs); these films were δ-doped with antimony and annealed at 500–600°C (the growth and processing technology of such films are described in more detail in [23, 24]). In contrast to the well-studied As clusters [17, 21, 22], As–Sb clusters generated at the antimony δ-layers induced considerable local elastic stresses in the surrounding matrix [23, 24]. Figure 1 shows bright-field transmission electron-microscopic (TEM) images of an LT-GaAs film δ-doped with antimony and annealed at 600°C.

The microstructure of a cluster was found to be rhombohedral; this structure is usually described as hexagonal, with the *c* axis being along one of the ⟨111⟩ directions in the GaAs matrix [21, 22]. Spheroids with large diameters ($D_{sp} > 8$ nm) demonstrated a pronounced Moiré pattern with fringes perpendicular to the diffraction vector (Fig. 1). A meticulous analysis of the cluster images proved that the Moiré pattern emerges due to double electron diffraction from the (210) atomic planes of the clusters and from the (220) planes of the matrix; these planes are parallel to one

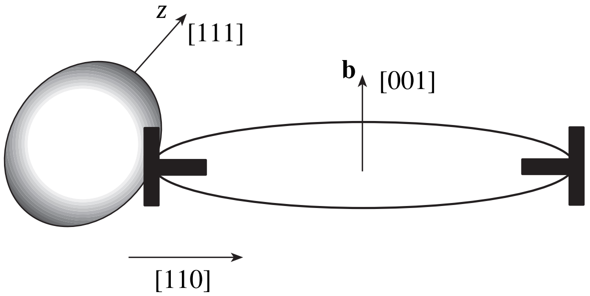

Fig. 2. Schematic diagram of a prismatic dislocation loop associated with a spherical cluster. The direction of uniaxial dilatation (z) in an As–Sb cluster coincides with the hexagonal axis c of the cluster and lies along the [111] direction of the zinc blende structure of GaAs. The Burgers vector of the loop is perpendicular to the (001) plane.

another. The period of the Moiré pattern was about 4 nm. This period is much larger than that for As clusters in conventional LT-GaAs [21, 22]. Obviously, antimony doping increases the distance between the (210) planes of the spheroids and makes them closer to the distances between the (220) planes of the matrix. Since Sb atoms are larger than As atoms and mutual solubility of Sb and As is unlimited, this increase may be due to Sb segregation in As clusters. The antimony concentration in the clusters was estimated, using the Vegard rule, to be 20–30 at. %, while its concentration in the GaAs matrix was estimated to be 1 at. %. The introduction of antimony improves the matching between the (210) planes of the inclusion and the (220) planes of the matrix but increases the mismatching in the transverse direction, i.e., along the c axis of the spheroid and along the [111] direction in the matrix. As a result, these spheroids are subjected to strongly anisotropic stresses that are higher, the larger the cluster size. The elastic fields of such spheroids were calculated using the uniaxial plastic deformation model.

Dislocation loops were observed in the vicinity of spheroids with the diameter larger than 7–8 nm. The loops touched the clusters, the loop diameter depended on the diameter of the accompanied cluster (Fig. 1). It should be noted that such dislocation loops have never been observed in antimony-free LT-GaAs [17, 21, 22]. All loops lay in the (001) planes, i.e., were arranged along δ layers. The centers of the loops were always arranged in one of the two orthogonal $\langle 110\rangle$ directions relative to the clusters with which the loops were associated. There was no clearly manifested correlation between the two loop–cluster mutual orientations and between the two possible projections of the c axis of the cluster onto the (001) plane.

The orientation of the Burgers vector of a dislocation loop was determined with the help of analysis of TEM images under two-beam diffraction conditions. The two TEM micrographs presented in Fig. 1 were obtained for the same loops but for different diffraction vectors, $\mathbf{g}_1 = [220]$ and $\mathbf{g}_2 = [2\bar{2}0]$. In both cases, the contrast associated with the loop disappeared partly when the diffraction vector was parallel to the plane of the loop. Since the contrast vanishes when $\mathbf{g}\cdot\mathbf{b} = 0$ and $\mathbf{g}\cdot(\mathbf{b}\times\mathbf{l}) = 0$ (vector $\mathbf{l}$ is oriented along the dislocation line) [26], we can conclude that the Burgers vector of a dislocation loop must be perpendicular to both diffraction vectors $\mathbf{g}_1$ and $\mathbf{g}_2$, i.e., that the Burgers vector must be perpendicular to the plane of the loop and directed along the [001] axis. Thus, it was found that the observed loops are prismatic. The application of the $\pm\mathbf{g}$ bright–dark-field method of imaging showed that these loops are of interstitial type. The orientation correlation between a spheroid and its dislocation loop is illustrated in Fig. 2.

The threshold diameter of a cluster required for the formation of loops was 7–8 nm. The correlation between the cluster diameter and the loop diameter was investigated in [23]. It should be noted that variation of the annealing temperature did not affect the threshold value of the cluster diameter and the nonlinear behavior of the loop diameter d as a function of the cluster diameter D_{sp}. The obvious effect of the elevation of the annealing temperature was an increase in the diameter and a decrease in the density of both a cluster and its dislocation loop.

Since the correlation between the diameters of a cluster and its loop is obvious and reproducible (at least for various annealing conditions), we can assume that a cluster and its dislocation loop are in equilibrium at each stage of growth and that the interaction between the cluster and the loop plays a certain role. The formation of a loop in the vicinity of a cluster is apparently a factor that reduces the elastic stresses localized near the cluster and the elastic energy of the system as a whole. It should be noted that loops free of clusters were not observed in such materials.

Thus, we can conclude that GaAs matrices doped with Sb contain nanoclusters with uniaxial dilatation along the $\langle 111\rangle$ direction in GaAs. These clusters possess considerable elastic fields, which may lead to the formation of dislocation loops during relaxation.

3. ESHELBY PROCEDURE FOR A SPHERICAL DEFECT WITH UNIAXIAL DILATATION

Let us first consider the general principle of describing an arbitrary volume defect with a prescribed plastic distortion (i.e., variation of shape) using a spherical defect as an example [2]. We first create a spherical cut in an elastic material, separate the lower and upper banks of the cut, and deform the obtained sphere plastically [i.e., insert (or remove) the material of the sphere in accordance with a rule selected by us or shift the banks of the cut]. In this way, we set a plastic distortion β^*_{ij} inside the sphere. Then, by applying a surface load, we elastically deform the object obtained from the

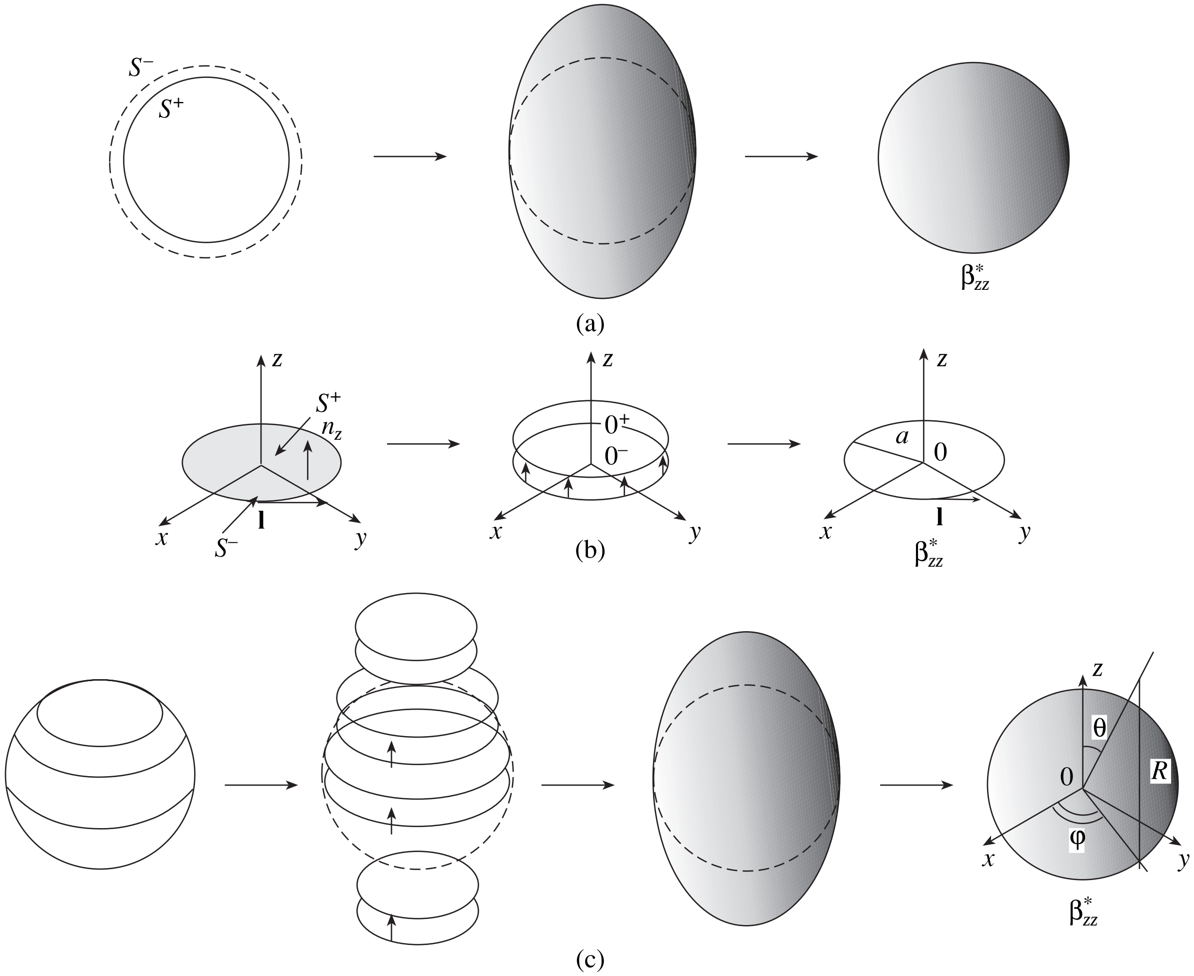

Fig. 3. Model of formation of a spherical inclusion with uniaxial plastic dilatation. (a) The Eshelby procedure of the formation of a spherical inclusion, (b) the Volterra procedure of the formation of a prismatic dislocation loop, and (c) the formation of a spherical inclusion as a sum of prismatic loops.

sphere until it acquires the original shape and insert it into the initial spherical cavity. Finally, we glue the banks of the cut and remove the applied external surface load. As a result of such a procedure (which can be referred to as the Eshelby procedure [2, 3]), we obtain a spherical defect of radius R_{sp} which possesses an elastic field. This field can be calculated on the basis of the prescribed plastic distortion. A classical example of such a defect is a spherical dilatation center [25].

A realization of the above procedure for a spherical inclusion with a uniaxial dilatation is presented schematically in Fig. 3a. In this case, due to uniaxial plastic distortion (deformation), the initial sphere is transformed into a uniaxial spheroid (ellipsoid), one of whose diameters is larger than the other two. The latter two diameters remain unchanged, i.e., equal to the diameter of the initial sphere.

Such a defect can be simulated by a continuous distribution of circular prismatic dislocation loops over the sphere, which enables us to calculate the plastic distortion of the volume defect and determine its elastic field on this basis. We will carry out the Volterra procedure [27] (which is an analogue of the Eshelby procedure in the case of a linear defect) for a circular prismatic dislocation loop (Fig. 3b) and determine its plastic distortion. The procedure of the formation of a linear defect (dislocation, disclination, or Somigliana dislocation) can be presented, in general, as follows: we make a cut S_i over the surface bounded by the line of the defect, then displace the upper bank S_i^+ of the cut relative to the lower bank S_i^- by an amount $[u_j]$, and add (remove) the material in order to eliminate the discontinuities (overlaps) formed. Subsequent gluing of the cut banks leads to the formation of a linear defect with distortion [4, 27]:

$$\beta^*_{ij} = \delta_i(S)[u_j], \tag{1}$$

where $\delta_i(S) = \int_{S_i} \delta(\mathbf{r} - \mathbf{r}')dS'_i$ and $\delta(\mathbf{r} - \mathbf{r}')$ is the three-dimensional delta function; the normal $\mathbf{n}_i$ to the cut surface is connected with the vector **l** of the defect line (which is set arbitrarily) through the right-hand screw rule.

The plastic distortion of a circular prismatic dislocation loop with an infinitesimal Burgers vector $d\mathbf{b} = -db \cdot \mathbf{e}_z$ and radius a, which lies in the plane with normal $\mathbf{n}_z$ and coordinate z_0 (Fig. 3b), is given by [4, 28]

$$\beta^*_{zz}(z_0) = dbH\left(1-\frac{r}{a}\right)\delta(z-z_0), \tag{2}$$

where the subscript zz indicates that the plastic distortion is defined on an area element with normal $\mathbf{n}_z$ in the direction of the z axis, $H\left(1-\frac{r}{a}\right) = \begin{cases}1, & r \le a\\ 0, & r > a\end{cases}$ is the Heaviside function, and $\delta(z-z_0)$ is the Dirac delta function. Assuming that the radius of each of the loops distributed over the sphere surface is $a = \sqrt{R_{\text{sp}}^2 - z_0^2}$ (R_{sp} is the radius of the sphere) and that the distribution density $\rho(z_0)$ is arbitrary in the general case, we find the plastic distortion of the spherical defect (Fig. 3c):

$$\begin{aligned}\beta^*_{zz} &= \int_{-R_{\text{sp}}}^{R_{\text{sp}}} db\rho(z_0)H\left(1-\frac{r}{\sqrt{R_{\text{sp}}^2-z_0^2}}\right)\delta(z-z_0)dz_0\\ &= db\rho(z)H\left(1-\frac{r}{\sqrt{R_{\text{sp}}^2-z^2}}\right)H\left(1-\frac{|z|}{R_{\text{sp}}}\right)\\ &= db\rho(z)H\left(1-\frac{R}{R_{\text{sp}}}\right),\end{aligned} \tag{3}$$

where R is the radial spherical coordinate.

We assume that the loop distribution density is constant: $\rho(z) = \rho$. We denote the dimensionless quantity ρdb by symbol ε^* and write the obtained plastic distortion of the spheroid in the form

$$\beta^*_{zz} = \begin{cases}\varepsilon^*, & R \le R_{\text{sp}},\\ 0, & R > R_{\text{sp}}.\end{cases} \tag{4}$$

In order to elucidate the physical meaning of the parameter ε^*, we express, for the sake of simplicity, the density ρ in the framework of the discrete model as $\rho = \frac{N}{D_{\text{sp}}}$ (N is the number of loops on the sphere diameter $D_{\text{sp}} = 2R_{\text{sp}}$). In this case, we have $\varepsilon^* = \frac{dbN}{2R_{\text{sp}}} = \frac{\Delta R_{\text{sp}}}{R_{\text{sp}}}$. Thus, ε^* is the plastic strain, i.e., the linear dilatation defined within the spheroid of radius R_{sp} and directed along the z axis on an area element with normal $\mathbf{n}_z$. Such a defect will be referred to as a uniaxial spheroid of dilatation type.

4. ELASTIC FIELDS AND ENERGY OF A UNIAXIAL SPHEROID OF DILATATION TYPE

In order to determine the elastic fields of a spheroid, we make use of the relation connecting the plastic distortion of the defect with its field of total displacements in the Cartesian system of coordinates [4]:

$$\begin{aligned}u^t_m(x,y,z) &= -i\int_{-\infty}^{\infty}\int_{-\infty}^{\infty}\int_{-\infty}^{\infty}\xi_l C_{jikl}L_{mk}\hat{\beta}^*_{ij}\\ &\times \exp[i(\xi_x x+\xi_y y+\xi_z z)]d\xi_x d\xi_y d\xi_z,\end{aligned} \tag{5}$$

where L_{mk} and $\hat{\beta}^*_{ij}$ are the Fourier transforms of the Green's function of the medium G_{mk} and of the plastic distortion β^*_{ij}, respectively; C_{jikl} are the elastic moduli of the medium; and (x, y, z) and (ξ_x, ξ_y, ξ_z) are the Cartesian coordinates in the direct and reciprocal spaces, respectively. For an isotropic medium, we have

$$L_{mk} = \frac{1}{(\sqrt{2\pi})^3}\frac{2(1-\nu)\xi^2\delta_{mk}-\xi_m\xi_k}{2(1-\nu)G\xi^4},$$

$$C_{jikl} = \frac{2G\nu}{1-2\nu}\delta_{ji}\delta_{kl} + G(\delta_{ik}\delta_{jl}+\delta_{il}\delta_{ik}),$$

where G is the shear modulus, ν is the Poisson ratio, δ_{mk} is the Kronecker delta, and $\xi^2 = \xi_x^2 + \xi_y^2 + \xi_z^2$.

Let us calculate the Fourier transform of the plastic distortion (4) of the defect and then determine the components of the total-displacement field on the basis of Eq. (5). We find elastic distortions and elastic strains and stresses using general relations from the theory of elasticity and the theory of defects. The Fourier transform of a plastic distortion in the Cartesian system of coordinates has the form

$$\begin{aligned}\hat{\beta}^*_{zz} &= \frac{1}{(\sqrt{2\pi})^3}\int_{-\infty}^{\infty}\int_{-\infty}^{\infty}\int_{-\infty}^{\infty}\beta^*_{zz}(x,y,z)\\ &\times \exp[-i(\xi_x x+\xi_y y+\xi_z z)]dxdydz.\end{aligned} \tag{6}$$

Using relation (4) and passing to spherical coordinates, we obtain

$$\begin{aligned}\hat{\beta}^*_{zz} &= \frac{\varepsilon^*}{(\sqrt{2\pi})^3}\int_0^{R_{\text{sp}}}R^2dR\int_0^{\pi}\sin\theta\\ &\times \exp[-iR\xi_R\cos\theta\cos\xi_\theta]d\theta\int_0^{2\pi}\exp[-iR\xi_R\sin\theta\\ &\times \sin\xi_\theta(\cos\varphi\cos\xi_\varphi+\sin\varphi\sin\xi_\varphi)]d\varphi.\end{aligned} \tag{7}$$

Here, (R, θ, φ) and $(\xi_R, \xi_\theta, \xi_\varphi)$ are the spherical coordinates in the direct and reciprocal spaces, respectively.

Finally, the Fourier transform of the plastic distortion has the form

$$\hat{\beta}^*_{zz} = \frac{4\pi\varepsilon^*}{(\sqrt{2\pi})^3}\frac{1}{\xi_R^3}[\sin(R_{\mathrm{sp}}\xi_R) - R_{\mathrm{sp}}\xi_R\cos(R_{\mathrm{sp}}\xi_R)], \tag{8}$$

where ε^* is the relative plastic dilatation and R_{sp} is the radius of the spheroid.

On the basis of Eqs. (5) and (8), we find the field of total displacements u_k^t of the defect in the framework of the elasticity theory for isotropic media.

1. In the cylindrical system of coordinates (r, φ, z) (Fig. 3c), outside the inclusion [superscript (out)], we have

$$u_r^{t(\mathrm{out})} = \frac{\varepsilon^* R_{\mathrm{sp}}\tilde{r}}{30(1-\nu)\tilde{R}^7}(3\tilde{r}^2 - 5\tilde{r}^4 + 10\nu\tilde{r}^4 + 5\tilde{r}^2\tilde{z}^2$$
$$+ 20\nu\tilde{r}^2\tilde{z}^2 - 12\tilde{z}^2 + 10\tilde{z}^4 + 10\nu\tilde{z}^4),$$
$$u_\varphi^{t(\mathrm{out})} = 0, \tag{9a}$$
$$u_z^{t(\mathrm{out})} = \frac{\varepsilon^* R_{\mathrm{sp}}\tilde{z}}{30(1-\nu)\tilde{R}^7}(9\tilde{r}^2 + 5\tilde{r}^4 - 10\nu\tilde{r}^4 + 25\tilde{r}^2\tilde{z}^2$$
$$- 20\nu\tilde{r}^2\tilde{z}^2 - 6\tilde{z}^2 + 20\tilde{z}^4 - 10\nu\tilde{z}^4),$$

while inside the inclusion [superscript (in)], we have

$$u_r^{t(\mathrm{in})} = \frac{\varepsilon^* R_{\mathrm{sp}}\tilde{r}}{15(1-\nu)}(5\nu - 1),$$
$$u_\varphi^{t(\mathrm{in})} = 0, \tag{9b}$$
$$u_z^{t(\mathrm{in})} = \frac{\varepsilon^* R_{\mathrm{sp}}\tilde{z}}{15(1-\nu)}(7 - 5\nu),$$

where $\tilde{r} = \frac{r}{R_{\mathrm{sp}}}$, $\tilde{z} = \frac{z}{R_{\mathrm{sp}}}$, $\tilde{R} = \frac{R}{R_{\mathrm{sp}}}$, $R^2 = r^2 + z^2$, and R_{sp} is the sphere radius.

2. In the spherical system of coordinates (R, θ, φ) $(0 \le \theta \le \pi)$ (Fig. 3c), outside of the inclusion, we have

$$u_R^{t(\mathrm{out})} = \frac{\varepsilon^* R_{\mathrm{sp}}}{60(1-\nu)\tilde{R}^4}$$
$$\times[-3 + 15\tilde{R}^2 - (9 - 25\tilde{R}^2 + 20\nu\tilde{R}^2)\cos 2\theta],$$
$$u_\theta^{t(\mathrm{out})} = \frac{\varepsilon^* R_{\mathrm{sp}}}{30(1-\nu)\tilde{R}^4}[-3 - 5\tilde{R}^2 + 10\nu\tilde{R}^2]\sin 2\theta, \tag{10a}$$
$$u_\varphi^{t(\mathrm{out})} = 0,$$

while inside the inclusion, we have

$$u_R^{t(\mathrm{in})} = \frac{\varepsilon^* R_{\mathrm{sp}}\tilde{R}}{15(1-\nu)}[3 + (4 - 5\nu)\cos 2\theta],$$
$$u_\theta^{t(\mathrm{in})} = -\frac{\varepsilon^* R_{\mathrm{sp}}\tilde{R}}{15(1-\nu)}(4 - 5\nu)\sin 2\theta, \tag{10b}$$
$$u_\varphi^{t(\mathrm{in})} = 0.$$

Here, the notation is the same as in Eqs. (9). Obviously, the components of total displacements are continuous upon a transition through the defect boundary $R = R_{\mathrm{sp}}$ irrespective of the coordinate system.

The field of elastic distortions β_{pq} can be defined as the difference between the total distortion and the given plastic distortion (4):

$$\beta_{pq} = \beta_{pq}^t - \beta_{pq}^*, \tag{11}$$

where the total distortion is defined as $\beta_{pq}^t = \frac{\partial u_q^t}{\partial p}$ $(p, q = x, y, z)$ in the Cartesian system of coordinates and

$$\beta_{rr}^t = \frac{\partial u_r^t}{\partial r}, \quad \beta_{r\varphi}^t = \frac{\partial u_\varphi^t}{\partial r}, \quad \beta_{rz}^t = \frac{\partial u_z^t}{\partial r},$$
$$\beta_{\varphi\varphi}^t = \frac{\partial u_\varphi^t}{\partial\varphi}\frac{1}{r} + \frac{u_r^t}{r}, \quad \beta_{\varphi r}^t = \frac{\partial u_r^t}{\partial\varphi}\frac{1}{r} - \frac{u_\varphi^t}{r},$$
$$\beta_{\varphi z}^t = \frac{\partial u_z^t}{\partial\varphi}\frac{1}{r}, \quad \beta_{zz}^t = \frac{\partial u_z^t}{\partial z}, \quad \beta_{zr}^t = \frac{\partial u_r^t}{\partial z}, \quad \beta_{z\varphi}^t = \frac{\partial u_\varphi^t}{\partial z}$$

in the cylindrical system of coordinates. It should be noted that in the case of a volume defect with a plastic distortion independent of the spatial coordinates, we can decompose not only the distortion but also the total displacement into elastic and plastic components: $u_k^t = u_k + u_k^*$ (this decomposition cannot be done for linear defects [27]). Symmetrizing the elastic distortion tensor gives the field of elastic strains of the inclusion.

1. In the cylindrical system of coordinates (r, φ, z), outside of the inclusion, we have

$$\varepsilon_{rr}^{(\mathrm{out})} = \frac{\varepsilon^*}{30(1-\nu)\tilde{R}^9}(-12\tilde{r}^4 + 10\tilde{r}^6 - 20\nu\tilde{r}^6$$
$$- 45\tilde{r}^4\tilde{z}^2 - 30\nu\tilde{r}^4\tilde{z}^2 + 81\tilde{r}^2\tilde{z}^2$$
$$- 45\tilde{r}^2\tilde{z}^4 - 12\tilde{z}^4 + 10\tilde{z}^6 + 10\nu\tilde{z}^6),$$
$$\varepsilon_{\varphi\varphi}^{(\mathrm{out})} = \frac{\varepsilon^*}{30(1-\nu)\tilde{R}^7}(3\tilde{r}^2 - 5\tilde{r}^4 + 10\nu\tilde{r}^4 + 5\tilde{r}^2\tilde{z}^2$$
$$+ 20\nu\tilde{r}^2\tilde{z}^2 - 12\tilde{z}^2 + 10\tilde{z}^4 + 10\nu\tilde{z}^4), \tag{12a}$$
$$\varepsilon_{zz}^{(\mathrm{out})} = \frac{\varepsilon^*}{30(1-\nu)\tilde{R}^9}(9\tilde{r}^4 + 5\tilde{r}^6 - 10\nu\tilde{r}^6 + 45\tilde{r}^4\tilde{z}^2$$
$$- 72\tilde{r}^2\tilde{z}^2 + 30\nu\tilde{r}^2\tilde{z}^4 + 24\tilde{z}^4 - 40\tilde{z}^6 + 20\nu\tilde{z}^6),$$

$$\varepsilon_{rz}^{(\mathrm{out})} = \frac{\varepsilon^*}{2(1-\nu)\tilde{R}^9}\tilde{r}\tilde{z}(-3\tilde{r}^2 + \tilde{r}^4 - 3\tilde{r}^2\tilde{z}^2 + 4\tilde{z}^2 - 4\tilde{z}^4),$$

$$\varepsilon_{r\varphi}^{(\mathrm{out})} = \varepsilon_{z\varphi}^{(\mathrm{out})} = 0,$$

while inside the inclusion, we have

$$\begin{aligned}
\varepsilon_{rr}^{(\mathrm{in})} &= \frac{\varepsilon^*}{15(1-\nu)}(5\nu - 1),\\
\varepsilon_{\varphi\varphi}^{(\mathrm{in})} &= \frac{\varepsilon^*}{15(1-\nu)}(5\nu - 1),\\
\varepsilon_{zz}^{(\mathrm{in})} &= \frac{2\varepsilon^*}{15(1-\nu)}(5\nu - 4),\\
\varepsilon_{rz}^{(\mathrm{in})} &= \varepsilon_{r\varphi}^{(\mathrm{in})} = \varepsilon_{z\varphi}^{(\mathrm{in})} = 0.
\end{aligned}\tag{12b}$$

2. In the spherical system of coordinates (R, θ, φ), outside of the inclusion, we have

$$\begin{aligned}
\varepsilon_{RR}^{(\mathrm{out})} &= \frac{\varepsilon^*}{30(1-\nu)\tilde{R}^5}\\
&\times[6 - 15\tilde{R}^2 + (18 - 25\tilde{R}^2 + 20\nu\tilde{R}^2)\cos 2\theta],\\
\varepsilon_{\theta\theta}^{(\mathrm{out})} &= \frac{\varepsilon^*}{60(1-\nu)\tilde{R}^5}[-3 + 15\tilde{R}^2\\
&- (21 - 5\tilde{R}^2 - 20\nu\tilde{R}^2)\cos 2\theta],\\
\varepsilon_{\varphi\varphi}^{(\mathrm{out})} &= \frac{\varepsilon^*}{60(1-\nu)\tilde{R}^5}[-9 + 5\tilde{R}^2 + 20\nu\tilde{R}^2\\
&+ 15(-1 + \tilde{R}^2)\cos 2\theta],\\
\varepsilon_{R\theta}^{(\mathrm{out})} &= \frac{\varepsilon^*}{30(1-\nu)\tilde{R}^5}(12 - 5\tilde{R}^2 - 5\nu\tilde{R}^2)\sin 2\theta,\\
\varepsilon_{R\varphi}^{(\mathrm{out})} &= \varepsilon_{\theta\varphi}^{(\mathrm{out})} = 0,
\end{aligned}\tag{13a}$$

while inside the inclusion, we have

$$\begin{aligned}
\varepsilon_{RR}^{(\mathrm{in})} &= \frac{\varepsilon^*}{30(1-\nu)}[-9 + 15\nu - (7 - 5\nu)\cos 2\theta],\\
\varepsilon_{\theta\theta}^{(\mathrm{in})} &= \frac{\varepsilon^*}{30(1-\nu)}[-9 + 15\nu + (7 - 5\nu)\cos 2\theta],\\
\varepsilon_{\varphi\varphi}^{(\mathrm{in})} &= \frac{\varepsilon^*}{15(1-\nu)}(5\nu - 1),\\
\varepsilon_{R\theta}^{(\mathrm{in})} &= \frac{\varepsilon^*}{30(1-\nu)}(7 - 5\nu)\sin 2\theta,\\
\varepsilon_{R\varphi}^{(\mathrm{in})} &= \varepsilon_{\theta\varphi}^{(\mathrm{in})} = 0.
\end{aligned}\tag{13b}$$

The field of elastic stresses in the framework of the elasticity theory for isotropic media has the following form.

1. In the cylindrical system of coordinates (r, φ, z), outside of the inclusion, we have

$$\begin{aligned}
\sigma_{rr}^{(\mathrm{out})} &= \frac{G\varepsilon^*}{15(1-\nu)\tilde{R}^9}(-12\tilde{r}^4 + 10\tilde{r}^6 - 10\nu\tilde{r}^6\\
&+ 81\tilde{r}^2\tilde{z}^2 - 45\tilde{r}^4\tilde{z}^2 - 30\nu\tilde{r}^4\tilde{z}^2 - 12\tilde{z}^4\\
&+ 10\tilde{z}^6 - 10\nu\tilde{z}^6 - 45\tilde{z}^4\tilde{r}^2 - 30\nu\tilde{z}^4\tilde{r}^2),\\
\sigma_{\varphi\varphi}^{(\mathrm{out})} &= \frac{G\varepsilon^*}{15(1-\nu)\tilde{R}^7}(3\tilde{r}^2 - 5\tilde{r}^4 + 20\nu\tilde{r}^4 + 5\tilde{r}^2\tilde{z}^2\\
&+ 10\nu\tilde{r}^2\tilde{z}^2 - 12\tilde{z}^2 + 10\tilde{z}^4 - 10\nu\tilde{z}^4),\\
\sigma_{zz}^{(\mathrm{out})} &= \frac{G\varepsilon^*}{15(1-\nu)\tilde{R}^9}(9\tilde{r}^4 + 5\tilde{r}^6 - 72\tilde{r}^2\tilde{z}^2\\
&+ 45\tilde{r}^4\tilde{z}^2 + 24\tilde{z}^4 - 40\tilde{z}^6),\\
\sigma_{rz}^{(\mathrm{out})} &= \frac{G\varepsilon^*}{(1-\nu)\tilde{R}^9}\tilde{r}\tilde{z}(-3\tilde{r}^2 + \tilde{r}^4 - 3\tilde{r}^2\tilde{z}^2 + 4\tilde{z}^2 - 4\tilde{z}^4),\\
\sigma_{r\varphi}^{(\mathrm{out})} &= \sigma_{z\varphi}^{(\mathrm{out})} = 0,
\end{aligned}\tag{14a}$$

while within the inclusion, we have

$$\begin{aligned}
\sigma_{rr}^{(\mathrm{in})} &= -\frac{2G\varepsilon^*}{15(1-\nu)}(5\nu + 1),\\
\sigma_{\varphi\varphi}^{(\mathrm{in})} &= -\frac{2G\varepsilon^*}{15(1-\nu)}(5\nu + 1),\\
\sigma_{zz}^{(\mathrm{in})} &= -\frac{16G\varepsilon^*}{15(1-\nu)},\\
\sigma_{rz}^{(\mathrm{in})} &= \sigma_{r\varphi}^{(\mathrm{in})} = \sigma_{z\varphi}^{(\mathrm{in})} = 0.
\end{aligned}\tag{14b}$$

2. In the spherical system of coordinates (R, θ, φ), outside of the inclusion, we have

$$\begin{aligned}
\sigma_{RR}^{(\mathrm{out})} &= \frac{G\varepsilon^*}{15(1-\nu)\tilde{R}^5}[6 - 15\tilde{R}^2 - 5\nu\tilde{R}^2\\
&+ (18 - 25\tilde{R}^2 + 5\nu\tilde{R}^2)\cos 2\theta],\\
\sigma_{\theta\theta}^{(\mathrm{out})} &= \frac{G\varepsilon^*}{30(1-\nu)\tilde{R}^5}[-3 + 15\tilde{R}^2 - 10\nu\tilde{R}^2\\
&- (21 - 5\tilde{R}^2 + 10\nu\tilde{R}^2)\cos 2\theta],\\
\sigma_{\varphi\varphi}^{(\mathrm{out})} &= \frac{G\varepsilon^*}{30(1-\nu)\tilde{R}^5}[-9 + 5\tilde{R}^2 + 10\nu\tilde{R}^2\\
&- 15(1 - \tilde{R}^2 + 2\nu\tilde{R}^2)\cos 2\theta],\\
\sigma_{R\theta}^{(\mathrm{out})} &= \frac{G\varepsilon^*}{15(1-\nu)\tilde{R}^5}(12 - 5\tilde{R}^2 - 5\nu\tilde{R}^2)\sin 2\theta,\\
\sigma_{R\varphi}^{(\mathrm{out})} &= \sigma_{\theta\varphi}^{(\mathrm{out})} = 0,
\end{aligned}\tag{15a}$$

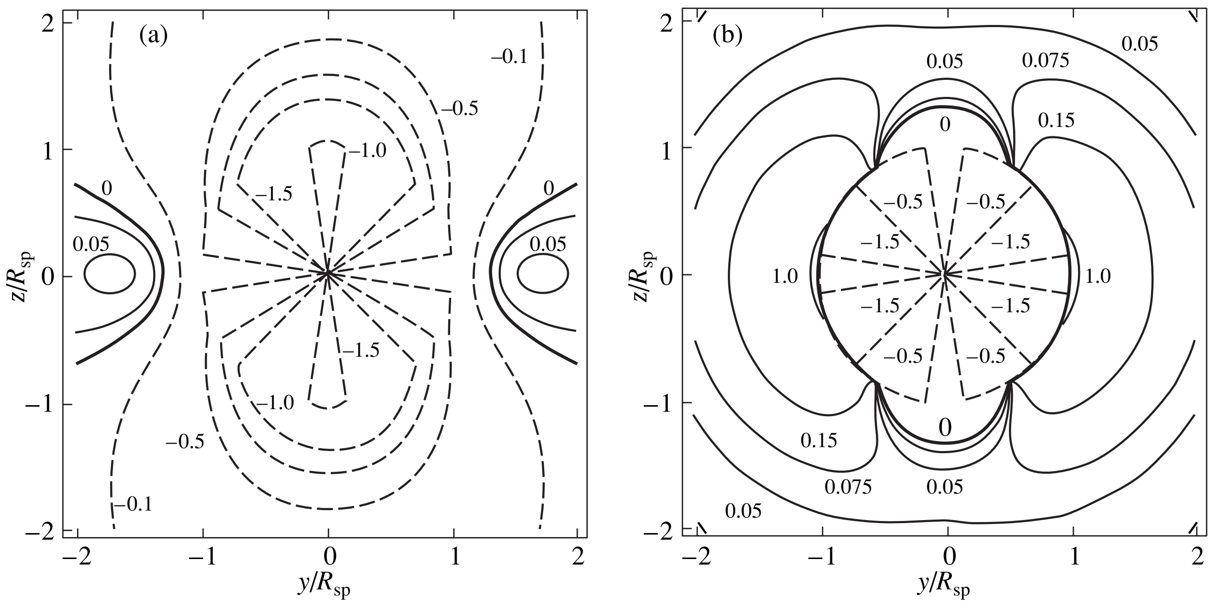

Fig. 4. Maps of (a) σ_{RR} and (b) $\sigma_{\theta\theta}$ stress isolines in the vicinity of a spheroid with uniaxial plastic distortion. Stresses are given in units of $\varepsilon^* G$; ε^* is the relative uniaxial dilatation, G is the shear modulus, and R_{sp} is the radius of the sphere. The Poisson ratio is $\nu = 0.3$.

while inside the inclusion, we have

$$\sigma_{RR}^{(\text{in})} = \frac{G\varepsilon^*}{15(1-\nu)}[-9-5\nu-(7-5\nu)\cos 2\theta],$$

$$\sigma_{\theta\theta}^{(\text{in})} = \frac{G\varepsilon^*}{15(1-\nu)}[-9-5\nu+(7-5\nu)\cos 2\theta],$$

$$\sigma_{\varphi\varphi}^{(\text{in})} = -\frac{2G\varepsilon^*}{15(1-\nu)}(5\nu+1), \tag{15b}$$

$$\sigma_{R\theta}^{(\text{in})} = \frac{G\varepsilon^*}{15(1-\nu)}(7-5\nu)\sin 2\theta,$$

$$\sigma_{R\varphi}^{(\text{in})} = \sigma_{\theta\varphi}^{(\text{in})} = 0.$$

The notation used in Eqs. (14) and (15) is the same as that in Eqs. (9) and (10). It should be noted that the above fields for a uniaxial spheroid satisfy the equilibrium conditions and the stress components σ_{RR} and $\sigma_{R\theta}$ normal to the surface of the spheroid are continuous:

$$\sigma_{RR}^{(\text{out})}\Big|_{R=R_{\text{sp}}} = \sigma_{RR}^{(\text{in})}\Big|_{R=R_{\text{sp}}}, \quad \sigma_{R\theta}^{(\text{out})}\Big|_{R=R_{\text{sp}}} = \sigma_{R\theta}^{(\text{in})}\Big|_{R=R_{\text{sp}}}.$$

By simply summing the fields of three uniaxial spheroids with plastic distortions β_{xx}^*, β_{yy}^*, and β_{zz}^*, respectively, we obtain the field of a triaxial spheroid or a spherical dilatation center, which completely coincides with the well-known formulas (see, e.g., [25]): the field of total displacements is

$$\begin{aligned} u_R^{t(\text{out})} &= \frac{\varepsilon^*(1+\nu)}{3(1-\nu)}\frac{R_{\text{sp}}}{\tilde{R}^2}, \\ u_R^{t(\text{in})} &= \frac{\varepsilon^*(1+\nu)}{3(1-\nu)}R_{\text{sp}}\tilde{R}; \end{aligned} \tag{16}$$

the field of elastic displacements of the spheroid is

$$\begin{aligned} u_R^{(\text{out})} &= \frac{\varepsilon^*(1+\nu)}{3(1-\nu)}\frac{R_{\text{sp}}}{\tilde{R}^2}, \\ u_R^{(\text{in})} &= -\frac{2\varepsilon^*(1-2\nu)}{3(1-\nu)}R_{\text{sp}}\tilde{R}; \end{aligned} \tag{17}$$

the field of elastic strains is

$$\begin{aligned} \varepsilon_{RR}^{(\text{out})} &= -\frac{2\varepsilon^*(1+\nu)}{3(1-\nu)}\frac{1}{\tilde{R}^3}, \\ \varepsilon_{\varphi\varphi}^{(\text{out})} = \varepsilon_{\theta\theta}^{(\text{out})} &= \frac{\varepsilon^*(1+\nu)}{3(1-\nu)}\frac{1}{\tilde{R}^3}, \\ \varepsilon_{RR}^{(\text{in})} = \varepsilon_{\varphi\varphi}^{(\text{in})} = \varepsilon_{\theta\theta}^{(\text{in})} &= -\frac{2\varepsilon^*(1-2\nu)}{3(1-\nu)}; \end{aligned} \tag{18}$$

and the field of elastic stresses is

$$\sigma_{RR}^{(\text{out})} = -\frac{4G\varepsilon^*(1+\nu)}{3(1-\nu)}\frac{1}{\tilde{R}^3},$$

$$\sigma_{\varphi\varphi}^{(\text{out})} = \sigma_{\theta\theta}^{(\text{out})} = \frac{2G\varepsilon^*(1+\nu)}{3(1-\nu)}\frac{1}{\tilde{R}^3}, \tag{19}$$

$$\sigma_{RR}^{(\text{in})} = \sigma_{\varphi\varphi}^{(\text{in})} = \sigma_{\theta\theta}^{(\text{in})} = -\frac{4G\varepsilon^*(1+\nu)}{3(1-\nu)}.$$

Figure 4 shows the maps for the distribution of the stress components σ_{RR} and $\sigma_{\theta\theta}$ for a uniaxial spheroid in a plane passing through the z axis (due to the symmetry of the problem, the elastic fields in the planes passing through the z axis are obviously identical). The stresses are given in units of $G\varepsilon^*$, and the Poisson ratio is $\nu = 0.3$. Obviously, the stress distribution for a uniaxial spheroid exhibits typical features, such as the existence of domains of stresses of different sign outside the spheroid, the dependence of the value of stresses on the angle of inclination to the plastic dilatation axis z inside and outside the spheroid, and indeterminacy of stresses at the center of the spheroid.

It would be interesting to compare the elastic self-energies of a uniaxial and a triaxial spheroid. Using the expression for the energy of a volume defect, $E = -\frac{1}{2}\int_{V_{\text{def}}}\beta_{ij}^*\sigma_{ij}^{(\text{in})}dV'$ (V_{def} is the defect volume) [4], we find the elastic energies of the uniaxial spheroid (superscript I),

$$E^{\text{I}} = \frac{32\pi}{45(1-\nu)}G\varepsilon^{*2}R_{\text{sp}}^3, \tag{20}$$

and of the triaxial spheroid (superscript III),

$$E^{\text{III}} = \frac{8\pi(1+\nu)}{3(1-\nu)}G\varepsilon^{*2}R_{\text{sp}}^3. \tag{21}$$

An estimation of the energies for $\nu = 0.3$ gives $E^{\text{I}} = 3.19G\varepsilon^{*2}R_{\text{sp}}^3$ and $E^{\text{III}} = 15.56G\varepsilon^{*2}R_{\text{sp}}^3$. For identical preset parameters, the elastic energy of an inclusion with uniaxial dilatation is lower than the energy of an inclusion with a triaxial (bulk) dilatation but is comparable to it.

5. RELAXATION OF ELASTIC FIELDS OF A STRESSED SPHEROID

The calculated elastic fields and energies of inclusions with uniaxial dilatation can be used to analyze relaxation processes occurring in the vicinity of stressed clusters in doped semiconductors [23]. We will briefly consider a model of formation of a dislocation loop near a cluster in the geometry shown in Fig. 2. In this case, the coordinate z axis lies along the hexagonal axis c (i.e., in the direction of the uniaxial dilatation).

The elastic energy E of the spheroid–loop system includes the following components: the elastic self-energy of the cluster E^{I} (20), the self-energy of the loop E_l, and the their interaction energy W:

$$E = E^{\text{I}} + E_l + W. \tag{22}$$

The self-energy of a prismatic loop is given by [29]

$$E_l = \frac{Gb^2d}{4(1-\nu)}\left(\ln\frac{4d}{R_{\text{core}}} - 2\right), \tag{23}$$

where b is the value of the Burgers vector, d is the diameter of the loop, and R_{core} is the radius of the loop core.

The interaction energy can be determined as the integral over the area S_l of the dislocation loop:

$$W = -b\int_{S_l}\sigma_{bb}(r,\varphi,z)dS, \tag{24}$$

where σ_{bb} are the stresses acting in the plane of the loop in the direction of the normal to this plane. The stress σ_{bb} has a complex spatial dependence, which contains contributions from practically all the components defined by Eqs. (15a). However, for a qualitative analysis, we can consider only the stress $\sigma_{\theta\theta}^{(\text{out})}$ (Fig. 4b) coinciding with σ_{bb} for $\varphi = 0$. Obviously, outside the inclusion, there is a region with tensile stresses $\sigma_{\theta\theta}^{(\text{out})} > 0$ in which the formation of a prismatic dislocation loop is advantageous from the energy point of view. In particular, this region also embraces the plane (001) in which the experimentally observed dislocation loops are located (Figs. 1, 2).

Let us consider the change in the energy of the system, $\Delta E = E_l + W$, upon the introduction of a loop, with the cluster energy remaining unchanged (E^{I} = const). An analysis shows [23] that in the case when a prismatic dislocation loop touches a tilted inclusion with one-dimensional distortion, there exists a critical loop diameter below which the energy obviously decreases. The critical diameter is determined from the condition $\Delta E(d_c) = 0$. Another important quantity, viz., the optimal diameter d_0 of the dislocation loop, can be determined from the condition of the maximum decrease in energy $\Delta E(d_0) = \Delta E_{\min} < 0$. The dependences of d_c and d_0 on the cluster diameter D_{sp} match the experimental data for the following model parameters: $b = \frac{1}{2}a_{\text{GaAs}} = 0.28$ nm, $\nu = 0.3$, and $\varepsilon^* = 0.5$ [23]. Obviously, the obtained value of the uniaxial dilatation ε^* is exaggerated. For values $\varepsilon^* \le 0.05$, the interaction energy W does not play a decisive role in the energy balance of the spheroid–loop system. In this case, we must take into account the change in the self-energy of the cluster as a result of formation of a dislocation loop. This question will be considered in a separate publication.

In any case, the gain in energy is a necessary condition for the nucleation of external dislocation loops; however, this process occurs only due to a strong supersaturation with arsenic interstitials. Their extremely high concentration in the LT-GaAs films δ-doped with Sb was confirmed recently by an analysis of enhanced Sb–As intermixing [30]. These point defects are also important for a high rate of growth and decrease in the density of As–Sb clusters. Thus, interstitial As atoms, as well as substitutional As atoms and Ga vacancies, play a key role in all structural transformations in LT-GaAs. The growth rate of large As–Sb clusters can increase additionally due to rapid diffusion along dislocation lines.

An analysis of dislocation loops formed at phosphorus inclusions in Ge crystals [31, 32] revealed an empirical relation between the diameters of a cluster (D_{cl}) and a loop (d_l); this relation was based on the law of conservation of matter in the cluster–loop system:

$$d_l = \sqrt{\frac{2}{3}\frac{D_{\text{cl}}^3}{b}\frac{\Delta V}{V}}, \tag{25}$$

where $\frac{\Delta V}{V}$ is the relative change in atomic volumes in the inclusion and in the matrix and b is the Burgers vector of the loop. Obviously, a relation of the type of Eq. (25) should be used as an additional relation in analyzing the energy balance in a spheroid–loop system.

Another elastic-energy relaxation channel in a system of clusters with a uniaxial dilatation may be associated with orientation ordering of the clusters when a correlation exists for the orientations of the z axes of the clusters. An estimate of the interaction energy of two clusters shows, however, that such an interaction is significant when the separation between the clusters does not exceed their mean diameter. In actual practice, clusters are always separated by larger distances, which allows us to disregard their interaction.

6. CONCLUSIONS

Thus, we have demonstrated experimentally that nanoclusters in LT-GaAs doped with antimony possess considerable elastic fields. These clusters contain up to 30 at. % Sb and exhibit dilatation along the c axis of the transformed hexagonal lattice. An adequate model for such clusters is an inclusion with uniaxial dilatation. This model has been constructed, and the plastic distortion of such an inclusion has been determined. The displacements, elastic strains, and stresses have been calculated analytically for the inner and outer regions of the inclusion with uniaxial dilatation. The maps of elastic stresses in the vicinity of the inclusion were considered. The elastic energy of the inclusion with uniaxial dilatation has been found to be comparable with the energy of an inclusion with triaxial dilatation. Relaxation processes associated with the nucleation of dislocation loops in the vicinity of stressed clusters (inclusions) in doped semiconductors were considered.

The above analysis leads to the following conclusions.

(i) The elastic fields and energies of an inclusion with uniaxial dilatation in an isotropic medium can be determined in a closed analytical form containing only elementary functions.

(ii) The change in the inclusion self-energy must play a significant role in relaxation of the stored elastic energy of the inclusion through the formation of an accompanying prismatic dislocation loop.

(iii) The interaction energy of elastic inclusions with uniaxial dilatation cannot be responsible for their ordering for the experimentally observed (e.g., in LT-GaAs) distances between nanoclusters.

ACKNOWLEDGMENTS

This study was supported by the Russian Foundation for Basic Research (project no. 98-02-17617) and INTAS (grant no. 97-30930), as well as by the programs “Physics of Solid-State Nanostructures” and “Fullerenes and Atomic Clusters” of the Ministry of Industry of the Russian Federation.

REFERENCES

1. E. Kroner, Acta Mater. **2**, 301 (1954).
2. J. D. Eshelby, Proc. R. Soc. London, Ser. A **221**, 376 (1957).
3. J. D. Eshelby, Proc. R. Soc. London, Ser. A **252**, 561 (1959).
4. T. Mura, *Micromechanics of Defects in Solids* (Martinus Nijhoff, Boston, 1987).
5. D. Bimberg, M. Grundmann, and N. N. Ledentsev, MRS Bull. **23**, 31 (1998).
6. J. H. Davis, J. Appl. Phys. **84**, 1358 (1998).
7. A. D. Andreev, J. R. Downes, D. A. Faux, and E. P. O’Reilly, J. Appl. Phys. **86**, 297 (1999).
8. G. S. Pearson and D. A. Faux, J. Appl. Phys. **88**, 730 (2000).
9. A. E. Romanov, G. E. Beltz, W. T. Fisher, *et al.*, J. Appl. Phys. **89**, 4523 (2001).
10. M. Grundmann, O. Stier, and D. Bimberg, Phys. Rev. B **52**, 11969 (1995).
11. J. A. Barker and E. P. O’Reilly, Phys. Rev. B **61**, 13840 (2000).
12. O. V. Konstantinov, E. Yu. Kotel’nikov, A. V. Matveentsev, and A. E. Romanov, Pis’ma Zh. Tekh. Fiz. **27** (16), 40 (2001) [Tech. Phys. Lett. **27**, 683 (2001)].
13. J. Tersoff, C. Teichert, and M. G. Lagally, Phys. Rev. Lett. **76**, 1675 (1996).
14. V. A. Shchukin, D. Bimberg, V. G. Malyshkin, and N. N. Ledentsov, Phys. Rev. B **57**, 12262 (1998).
15. A. E. Romanov, P. M. Petroff, and J. S. Speck, Appl. Phys. Lett. **74**, 2280 (1999).
16. M. R. Melloch, N. Otsuka, J. M. Woodall, *et al.*, Appl. Phys. Lett. **57**, 1531 (1990).
17. N. A. Bert, A. I. Veĭnger, M. D. Vilisova, *et al.*, Fiz. Tverd. Tela (St. Petersburg) **35**, 2609 (1993) [Phys. Solid State **35**, 1289 (1993)].
18. D. D. Nolte, J. Appl. Phys. **85**, 6259 (1999).
19. V. V. Chaldyshev, Mater. Sci. Eng. B **88**, 85 (2002).

20. X. Liu, A. Prasad, J. Nishio, *et al.*, Appl. Phys. Lett. **67**, 279 (1995).
21. Z. Liliental-Weber, A. Claverie, J. Washburn, *et al.*, Appl. Phys. A: Solids Surf. **53**, 141 (1991).
22. N. A. Bert and V. V. Chaldyshev, Fiz. Tekh. Poluprovodn. (St. Petersburg) **30**, 1889 (1996) [Semiconductors **30**, 988 (1996)].
23. V. V. Chaldyshev, N. A. Bert, A. E. Romanov, *et al.*, Appl. Phys. Lett. **80**, 377 (2002).
24. N. A. Bert, V. V. Chaldyshev, A. A. Suvorova, *et al.*, Appl. Phys. Lett. **74**, 1588 (1999).
25. C. Teodosiu, *Elastic Models of Crystal Defects* (Springer, Berlin, 1982; Mir, Moscow, 1985).
26. S. Nakahara, S. N. Chu, and R. A. Stall, Philos. Mag. A **53**, 403 (1986).
27. R. de Wit, in *Fundamental Aspects of Dislocation*, Ed. by J. A. Simmons, R. de Wit, and R. Bullough (National Bureau of Standards, Washington, 1970), Vol. 1, pp. 651–673; J. Res. Natl. Bur. Stand., Sect. A **77** (1), 49 (1973); **77** (3), 359 (1973); **77**, 607 (1973).
28. A. L. Kolesnikova and A. E. Romanov, Preprint No. 1019, Fiz.-Tekh. Inst. im. A. F. Ioffe Akad. Nauk SSSR (Ioffe Physicotechnical Institute, Academy of Sciences of USSR, Leningrad, 1986).
29. J. Dundurs and N. J. Salamon, Phys. Status Solidi B **50**, 125 (1972).
30. V. V. Chaldyshev, N. A. Bert, Yu. G. Musikhin, *et al.*, Appl. Phys. Lett. **79**, 1294 (2001).
31. N. D. Zakharov, V. N. Rozhanskiĭ, and R. L. Korchazhkina, Fiz. Tverd. Tela (Leningrad) **16**, 1444 (1974) [Sov. Phys. Solid State **16**, 926 (1974)].
32. N. D. Zakharov, V. Noĭman, and V. N. Rozhanskiĭ, Fiz. Tverd. Tela (Leningrad) **16**, 2775 (1974) [Sov. Phys. Solid State **16**, 1800 (1974)].

Translated by N. Wadhwa

Physics of the Solid State, Vol. 44, No. 12, 2002, pp. 2251–2256. Translated from Fizika Tverdogo Tela, Vol. 44, No. 12, 2002, pp. 2149–2154.

Mobility of Dislocations with Spontaneous Rearrangement of Core States and Anomalous Plasticity of Crystalline Materials

B. V. Petukhov

Shubnikov Institute of Crystallography, Russian Academy of Sciences, Leninskiĭ pr. 59, Moscow, 117333 Russia

Received January 29, 2002

Abstract—The ensemble-averaged effective velocity of dislocations experiencing spontaneous transitions between mobile and low-mobility states of their cores is calculated. It is found that the dependence of the averaged kinetics of dislocations on stress and temperature is modified considerably as compared to ordinary slip. The description of macroscopic plastic deformation on the basis of the proposed model demonstrates the presence of an anomalous peak in the deforming stress in the elevated temperature region. A thermoactivation procedure is proposed for analysis of experimental data in the region of anomalous growth in the deforming stress upon an increase in temperature. The theoretically predicted dependence of the position of the peak (on the temperature scale) on the strain rate is compared with experimental data for β-CuZn. *© 2002 MAIK “Nauka/Interperiodica”.*

1. INTRODUCTION

The plasticity of crystalline materials is determined in many cases by the mobility of dislocations. The features of the structure of dislocations and the state of their cores can considerably affect the temperature and strain-rate dependence of the flow stress of the material. Most materials become more ductile upon heating, and their deforming stress becomes lower; this property is described qualitatively (and quantitatively in many cases) by the Arrhenius law of motion of dislocations:

$$V = V_0 \exp\left\{-\frac{E_0(\sigma)}{kT}\right\}. \tag{1}$$

Here, V is the velocity of dislocations, $E_0(\sigma)$ is the activation energy for the motion of dislocation, σ is the stress, and V_0 is a preexponential factor, whose dependence on σ and T can usually be disregarded as compared to the dependence of the exponent. Using the Orowan relation $\dot{\varepsilon} = \rho b V$, we can relate the mobility characteristics of individual dislocations to the macroscopic parameters of plastic deformation:

$$\ln\frac{\dot{\varepsilon}_0}{\dot{\varepsilon}} = \frac{E_0(\sigma)}{kT} = -T\frac{\partial\sigma/\partial T}{\partial\sigma/\partial\ln\dot{\varepsilon}}. \tag{2}$$

Here, $\dot{\varepsilon}$ is the plastic-flow rate, $\dot{\varepsilon}_0 = \rho b V_0$, ρ is the density of mobile dislocations, and b is the magnitude of their Burgers vector. The right-hand side of Eq. (2) contains a combination of directly measurable parameters of plastic deformation; therefore, this relation (if it is applicable) makes it possible to determine the activation energy for the motion of dislocations from the results of macroscopic experiments. We can also determine another important microscopic parameter, the so-called activation volume $A = -dE_0/d\sigma$, from the experimentally measurable value of the strain-rate sensitivity of the deforming stress:

$$A = \frac{kT}{d\sigma/d\ln\dot{\varepsilon}}. \tag{3}$$

Practical realization of the analysis of experimental data on the basis of relations (2) and (3) has attained a high level, especially for materials in which the dislocation mobility is controlled by overcoming the Peierls–Nabarro relief and which are characterized by a strong temperature dependence of the plastic-flow rate (see, e.g., [1]).

However, there exists a large class of materials for which the behavior of deforming stress cannot be described by either the above relations or only in the region of relatively low temperatures. Such materials include simple metals of the Be type, ordered alloys, and intermetallides. For these materials, the temperature dependence of deforming stress has an additional peak in the higher temperature region, which is known as an anomaly in the flow stress since, contrary to traditional expectations, the deforming stress increases with temperature in a certain interval. This phenomenon attracts considerable attention from researchers in view of the possible practical application of such materials at elevated temperatures, as well as in connection with the study of new fundamental mechanisms of dislocation dynamics (see the series of reviews in [2]).

The anomalous behavior is attributed to the possible spontaneous transformation of dislocation cores from the mobile to a low-mobility (sessile) state. In most cases, this occurs as a result of a transverse slip or

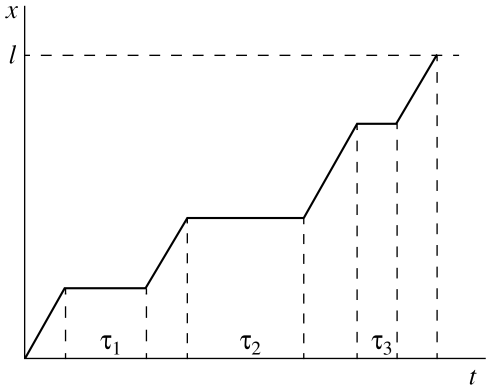

Fig. 1. Typical kinetics of displacements of a dislocation in the presence of spontaneous locking–delocking processes. A realization with three random delays in motion by the times τ_1, τ_2, and τ_3 is shown.

creeping with a change from a planar configuration of a dislocation to a 3D configuration (e.g., Kir–Wilsdorf locking), but other mechanisms are also possible [3–5]. A simple model describing the dislocation dynamics in the presence of spontaneous transitions from mobile to low-mobility states of dislocations and *vice versa* was proposed in [6, 7]. Here, this model is improved significantly by taking into account explicitly the statistics of delay times in sessile states. The modified model is then used to extend relations (2) and (3) to the neighborhood of the anomalous peak to obtain a description of the observed mechanisms and to work out a procedure for determining microstructural parameters of dislocation dynamics from the experimental data on macroscopic plastic deformation.

2. DYNAMICS OF DISLOCATION JUMPS

The jumpwise motion of dislocations observed through an electron microscope in *in situ* experiments [8, 9] calls for a modification of the conventional scheme of description of dislocation motion. This implies time scales much longer than the time of an elementary act of surmounting an individual obstacle when conventional slip appears as continuous. The statistics of dislocation delays as a result of spontaneous self-locking must be taken into account appropriately. In this section, the conventional scheme of description of dislocation slip is generalized with minimal essential complication of the model through the simplest inclusion of dislocation delay in the sessile states.

We take into account the fact that, in addition to slip of dislocations with a velocity V in a mobile state, spontaneous transitions to a sessile state at a rate of J_- (per unit time), as well as the reverse transitions to the mobile state at a rate J_+, are possible. These transitions lead to delays in motion in time intervals of $\tau_1, \tau_2, \ldots$. As a result, the time required to traverse a path l is equal to the sum of the time of motion l/V and all delay times τ_i in sessile states: $t = l/V + \sum\tau_i$ (Fig. 1).

The effective velocity of motion V_{eff} in this case is given by

$$V_{\text{eff}} = l/t = \frac{l}{l/V + \sum\tau_i}. \tag{4}$$

Let us calculate the effective velocity $\langle V_{\text{eff}}\rangle$ averaged over the dislocation ensemble.

The probability that the duration of a delay lies between τ_i and $\tau_i + d\tau_i$ is equal to $\exp(-J_+\tau_i)J_+d\tau_i$. All delays are independent; therefore, the probability of encountering a set of delays in the corresponding time intervals is equal to the product of individual probabilities. Consequently, the averaging procedure can be written in the form

$$\begin{aligned}\langle V_{\text{eff}}\rangle &= \sum_{n=0}^{\infty} P_n \left\langle \frac{l}{\dfrac{l}{V} + \sum\limits_{i=0}^{n}\tau_i} \right\rangle \\ &= \sum_{n=0}^{\infty} P_n \int \frac{l}{\dfrac{l}{V} + \sum\limits_{i=0}^{n}\tau_i} \prod_{i=1}^{n} \exp(-J_+\tau_i) J_+ d\tau_i.\end{aligned} \tag{5}$$

Here, P_n is the probability that n delays occur during the time of motion l/V and $\tau_0 \equiv 0$. The average number of delays over the time interval l/V is equal to J_-l/V, while the probability of n delays is given, in accordance with the Poisson law, by

$$P_n = \frac{1}{n!}\left(\frac{lJ_-}{V}\right)^n \exp\left(-\frac{lJ_-}{V}\right). \tag{6}$$

We will use the representation

$$\frac{1}{l/V + \sum\tau_i} = \int_0^{\infty} dz \exp[-z(l/V + \sum\tau_i)], \tag{7}$$

which allows us to reduce the integration with respect to $\{\tau_i\}$ to the product of n identical integrals:

$$\begin{aligned}\left\langle \exp\left(-z\sum_{i=1}^{n}\tau_i\right)\right\rangle &= \prod_{i=1}^{n}\int_0^{\infty} \exp(-z\tau_i - J_-\tau_i)d\tau_i \\ &= \left(\frac{J_+}{z + J_+}\right)^n.\end{aligned} \tag{8}$$

Substituting Eqs. (6) and (8) into Eq. (5) and using the sum rule $\sum\limits_{n=0}^{\infty}\dfrac{x^n}{n!} = e^x$, we obtain

$$\langle V_{\text{eff}}\rangle = lJ_+\int_0^{\infty} dz \exp\left\{-\frac{J_+l}{V}z - \frac{J_-l}{V}\frac{z}{z+1}\right\}. \tag{9}$$

It can easily be seen from Eq. (9) that, as expected, $\langle V_{\text{eff}} \rangle \longrightarrow V$ for a small locking rate $J_- \longrightarrow 0$. We are interested, however, in the other limiting case when the locking rate is quite large, $J_- > V/l$, so that locking acts will occur over the path l with an appreciable probability. In this case, we obtain from relation (9) the following approximate expression for $\langle V_{\text{eff}} \rangle$:

$$\langle V_{\text{eff}} \rangle \approx V\left\{ \exp\left(-\frac{J_- l}{V}\right) + \frac{J_+}{J_-} \right\}. \tag{10}$$

This result demonstrates that the relations for averaged dislocation kinetics in the presence of spontaneous locking–delocking processes differ in many respects from those characteristic of usual slip. We can mention, for example, the dependence of $\langle V_{\text{eff}} \rangle$ on the path length l, which generally requires a more accurate formulation of the problem. The time dependence of the mean free path was found in [6] to be nonlinear, which correlates with the dependence of $\langle V_{\text{eff}} \rangle$ on l obtained here. The formulation of the problem in [6] is in better agreement with experiments on the motion of dislocations over a fixed time of sample loading, similar to those described in [10]. In this work, we are interested primarily in the application of the results to the description of plastic deformation in the case when the time of experiments is much longer than the lifetime of individual dislocations while their total mean free paths remain approximately identical.

3. THERMOACTIVATION ANALYSIS OF THE ANOMALOUS TEMPERATURE DEPENDENCE OF DEFORMING STRESS

Substituting Eq. (10) for $\langle V_{\text{eff}} \rangle$ into the Orowan relation, we obtain an equation for determining the dependence of the deforming stress on the strain rate $\dot{\varepsilon}$ and on other parameters of the problem, which is modified in comparison with Eq. (2). Of special interest is the temperature dependence of deforming stress, which can be determined only after specifying the rearrangement rate $J_\pm$.

Assuming that the rearrangement of the state of a dislocation core occurs under the action of thermal fluctuations, we will describe the temperature dependence of $J_\pm$ using the Arrhenius law $J_\pm = J_{\pm 0}\exp(-E_\pm/kT)$. As a result, we obtain, instead of Eq. (2),

$$\begin{aligned} &\exp\left\{ -\lambda \exp\left(\frac{E_0(\sigma) - E_-}{kT} \right) \right\} \\ &+ \frac{J_{+0}}{J_{-0}} \exp\left(\frac{E_- - E_+}{kT} \right) = \frac{\dot{\varepsilon}}{\dot{\varepsilon}_0} \exp\left\{ \frac{E_0(\sigma)}{kT} \right\}. \end{aligned} \tag{11}$$

Here, $\lambda = lJ_{-0}/V_0$ is the dimensionless total mean free path of dislocations.

Equation (11), which is a relation between strongly varying exponential functions of temperature, has two branches of solutions for $E_0(\sigma)$ with an abrupt transition between the branches. It can easily be seen that the branch corresponding to the dominance of the second term on the left-hand side of Eq. (11) describes a normal dependence of type (2) with renormalized activation energies $E_0(\sigma) \longrightarrow E_0(\sigma) + E_+ - E_-$ and with the preexponential factor $\dot{\varepsilon}_0 \longrightarrow \dot{\varepsilon}_0 J_{-0}/J_{+0}$. This corresponds to back-and-forth motion of dislocations with a large number of rearrangements, which is equivalent, on the average, to a slip with increased barrier heights at elevated temperatures. The branch with the first term on the left-hand side of Eq. (11) dominating has another form; the equation for this branch can be approximately written in the form

$$\lambda \exp\left\{ \frac{E_0(\sigma) - E_-}{kT} \right\} \approx \ln\frac{\dot{\varepsilon}_0}{\dot{\varepsilon}} - \frac{E_0(\sigma)}{kT}. \tag{12}$$

The driving force for a rearrangement of the dislocation core to a sessile state is associated with a decrease in the self-energy of the core rather than with an external stress as in the case of slip. Consequently, we can assume that the dependence of E_- on σ is less significant as compared to $E_0(\sigma)$ and neglect it here, assuming that E_- is a certain constant. We will also neglect the temperature dependence of the total dislocation mean free path λ against the background of exponential Arrhenius dependences. Let us verify that Eq. (12) describes an anomalous temperature dependence of deforming stress. For this purpose, we reduce Eq. (12) to a form convenient for iterations by taking the logarithm of this relation:

$$E_0(\sigma) = E_- kT \ln\left(\frac{\lambda}{\ln(\dot{\varepsilon}_0/\dot{\varepsilon}) - E_0(\sigma)/kT} \right). \tag{13}$$

Assuming, as a zeroth approximation, that $E_0(\sigma) = 0$ on the right-hand side of Eq. (13), we obtain the first iteration, $E_0(\sigma) \approx E_- kT\ln[\lambda/\ln(\dot{\varepsilon}_0/\dot{\varepsilon})]$. Substituting this iteration into the right-hand side of Eq. (13) gives a refined result:

$$\begin{aligned} E_0(\sigma) &\approx E_- - kT \\ &\times \ln\left\{ \frac{\lambda}{\ln(\dot{\varepsilon}_0/\dot{\varepsilon}) + \ln[\lambda/\ln(\dot{\varepsilon}_0/\dot{\varepsilon})] - E_-/kT} \right\}. \end{aligned} \tag{14}$$

A comparison of this approximation with a numerical solution to Eq. (13) shows that it is quite effective, and we confine our analysis to this approximation. The logarithmic factor on the right-hand side of Eq. (14) is positive and depends on temperature only weakly. Thus, in accordance with Eq. (14), $E_0(\sigma)$ decreases with heating, which corresponds to an increase in σ, i.e., to the anomalous temperature behavior of the deforming stress.

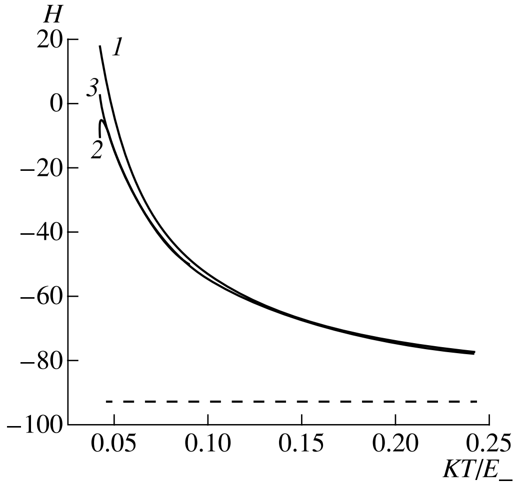

Fig. 2. Temperature behavior of the experimentally measurable parameter $H = -(\partial\sigma/\partial T)/(\partial\sigma/\partial\ln\dot{\varepsilon})$ calculated by using different approximations for $E_0(\sigma)$: (*1*) the first iteration of Eq. (13), (*2*) second iteration, and (*3*) numerical solution. The dashed line corresponds to the asymptotic value for $T \longrightarrow 0$; $\ln(\dot{\varepsilon}_0/\dot{\varepsilon}) = 20$, $\lambda = 1000$.

Given the stress dependence of the activation energy $E_0(\sigma)$, expression (14) makes it possible to calculate the temperature dependence of the deforming stress $\sigma(T)$. The inverse problem (reconstruction of $E_0(\sigma)$ from the experimental data on the macroscopic ductility of the material) is also of interest. The possibility of solving this problem in principle will be discussed below.

The proposed model predicts some relations between the quantities measured experimentally during mechanical tests. These relations allow us to determine the microscopic parameters of dislocation dynamics from a comparison with experimental data, as is done with the help of Eqs. (2) and (3) in the case of a normal plastic deformation. Let us consider such relations for active loading of samples ($\dot{\varepsilon}$ = const) in the anomalous region.

Let us determine the temperature and strain-rate sensitivities predicted by the proposed model of an anomalous flow. Differentiating relation (12) with respect to temperature, we obtain

$$\frac{dE_0}{dT} = \frac{dE_0}{d\sigma}\frac{\partial\sigma}{\partial T} = \frac{-k\left(\ln\frac{\dot{\varepsilon}_0}{\dot{\varepsilon}} - \frac{E_0}{kT}\right)\ln\frac{\lambda}{\ln(\dot{\varepsilon}_0/\dot{\varepsilon}) - E_0/kT} + \frac{E_0}{T}}{\ln(\dot{\varepsilon}_0/\dot{\varepsilon}) - E_0/kT + 1}. \tag{15}$$

Differentiation of relation (12) with respect to $\ln\dot{\varepsilon}$ gives

$$\frac{dE_0}{d\ln\dot{\varepsilon}} = \frac{dE_0}{d\sigma}\frac{d\sigma}{d\ln\dot{\varepsilon}} = -\frac{kT}{\ln(\dot{\varepsilon}_0/\dot{\varepsilon}) - E_0/kT + 1}. \tag{16}$$

Dividing Eq. (15) by Eq. (16), we eliminate the activation volume $A = -dE_0/d\sigma$ on the left-hand side of the equations and retain only the experimentally measurable quantities. Thus, we arrive at the relation

$$\begin{aligned} H &= -T\frac{\partial\sigma/\partial T}{\partial\sigma/\partial\ln\dot{\varepsilon}} \\ &= -\left(\ln\frac{\dot{\varepsilon}_0}{\dot{\varepsilon}} - \frac{E_0}{kT}\right)\ln\frac{\lambda}{\ln(\dot{\varepsilon}_0/\dot{\varepsilon}) - E_0/kT} + \frac{E_0}{T}. \end{aligned} \tag{17}$$

It should be noted that, in the limit $E_0/kT \longrightarrow \ln(\dot{\varepsilon}_0/\dot{\varepsilon})$, Eqs. (15)–(17) lead to the conventional laws (2) and (3) for a normal plastic flow. The inequality $E_0/kT < \ln(\dot{\varepsilon}_0/\dot{\varepsilon})$ holds for anomalous deformation occurring at elevated temperatures. In order to obtain order-of-magnitude estimates, it is expedient to consider the limit $E_0/kT \ll \ln(\dot{\varepsilon}_0/\dot{\varepsilon})$. In this case, we have

$$A\frac{\partial\sigma}{\partial T} \approx k\ln\frac{\lambda}{\ln(\dot{\varepsilon}_0/\dot{\varepsilon})} \tag{18}$$

instead of Eq. (15) and

$$A\frac{\partial\sigma}{\partial\ln\dot{\varepsilon}} \approx \frac{kT}{\ln(\dot{\varepsilon}_0/\dot{\varepsilon})} \tag{19}$$

instead of Eq. (16).

It can be seen from Eq. (18) that the temperature sensitivity $\partial\sigma/\partial T$ is positive in the range under investigation. It is also interesting to note that the strain-rate sensitivity described by Eq. (19) is lower by a factor of $\ln(\dot{\varepsilon}_0/\dot{\varepsilon})$ than in the normal case. For typical values of $\ln(\dot{\varepsilon}_0/\dot{\varepsilon}) \sim 10$–30, the sensitivities differ by more than an order of magnitude and, hence, the value of $kT/(\partial\sigma/\partial\ln\dot{\varepsilon})$ differs significantly in this case from the microscopic activation volume, regardless of its being proportional to this volume.

More accurate results can be obtained by using a numerical or iterative solution to Eq. (13) for $E_0(\sigma)$. Substituting this solution into Eq. (17), we obtain the curve depicted in Fig. 2. It can be seen from Fig. 2 that the iterative approximation is quite good everywhere except in a narrow region of transition to the normal behavior at low temperatures. In view of the roughness of the model itself, even the first iteration appears to be quite satisfactory. In this approximation, an explicit analytical expression for H has the form

$$\begin{aligned} H &= -T\frac{\partial\sigma/\partial T}{\partial\sigma/\partial\ln\dot{\varepsilon}} \approx -\ln\left(\frac{\lambda}{\ln(\dot{\varepsilon}_0/\dot{\varepsilon})}\right) + \frac{E_-}{kT} \\ &- \left[\ln\frac{\dot{\varepsilon}_0}{\dot{\varepsilon}} + \ln\left(\frac{\lambda}{\ln(\dot{\varepsilon}_0/\dot{\varepsilon})}\right) - \frac{E_-}{kT}\right] \\ &\times \ln\left\{\frac{\lambda}{\ln\frac{\dot{\varepsilon}_0}{\dot{\varepsilon}} + \ln\left(\frac{\lambda}{\ln(\dot{\varepsilon}_0/\dot{\varepsilon})}\right) - \frac{E_-}{kT}}\right\}. \end{aligned} \tag{20}$$

The quantity H depends on the temperature and strain rate, which offers an opportunity to make a comparison with experimental data. Since the left-hand side of Eq. (20) contains an experimentally measurable quantity, this relation makes it possible in principle to verify the proposed model and to determine, by fitting, the following parameters of the problem: $\ln(\dot{\varepsilon}_0/\dot{\varepsilon})$, the dislocation mean free path λ, and the locking energy E_-. Knowing these parameters, one can reconstruct, using Eq. (14), the microscopic stress dependence of the barrier height E_0 controlling the slip of dislocations. The practical realization of this procedure of analyzing the available experimental data for a number of specific materials will be described in a separate publication.

4. POSITION OF THE PEAK ON THE TEMPERATURE SCALE

The temperature interval on which an elevated deforming stress is observed is of practical importance. It is also interesting to analyze the dependence of the position of the peak on various parameters; the knowledge of this dependence makes it possible to control the peak position. Let us consider these questions.

The deforming stress on the anomalous branch increases with temperature until this branch is replaced by the normal high-temperature branch described earlier. Thus, in view of the above-mentioned strongly exponential behavior, the position of the deforming-stress peak on the temperature scale is determined by the point of intersection of the above two branches of the solution to Eq. (11). It can easily be verified by comparing the two solutions that this point of intersection corresponds to the temperature T_m approximately given by

$$T_m \approx \frac{E_+/k}{\ln\frac{\dot{\varepsilon}_0}{\dot{\varepsilon}} + \ln\left\{\frac{\lambda}{\ln(\dot{\varepsilon}_0/\dot{\varepsilon})}\right\}}. \qquad (21)$$

This expression predicts a noticeable dependence of the peak position on the plastic strain rate. Such a dependence is indeed observed in experiments (this is shown in Fig. 3 using the data obtained in [11] for β-CuZn). Figure 3 illustrates the temperature variation of the deforming stress in the vicinity of the anomalous peak for three different values of the strain rate. It can be seen from Fig. 3 that the curves are quite close in the region where σ increases with temperature, which corresponds to a low strain-rate sensitivity of the deforming stress in the anomaly region predicted by the theory. At the same time, the positions of the maximum points of the peaks differ significantly for different values of $\dot{\varepsilon}$.

In order to compare the theoretical results with experimental data, we must specify the stress dependence of the delocking energy E_+. We can assume that delocking is the process of escape of a dislocation from a linear potential well under the action of thermal fluctuations and stress. This process is similar to the detachment of a dislocation from a linear chain of pinning centers; for this latter process, Friedel proposed a stress dependence of the activation energy of the form $E_+ \sim 1/\sigma$ [12]. In this case, in accordance with Eq. (21), the dependence of the quantity $1/(T_m\sigma_m)$ on $\ln\dot{\varepsilon}$ must be close to linear. The inset to Fig. 3 shows that this is actually true, and fitting of the proportionality factors makes it possible to find the delocking energy in the corresponding stress range (Fig. 4).

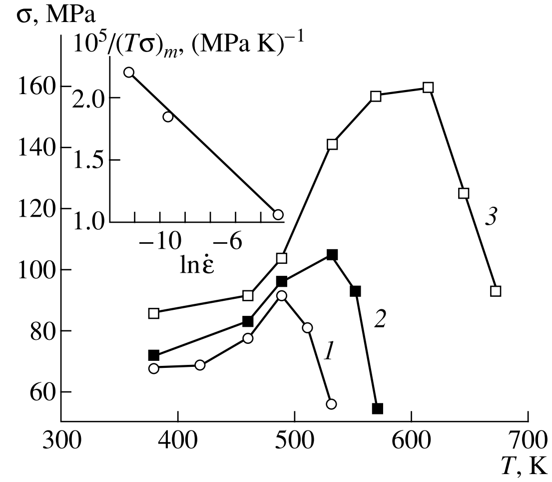

Fig. 3. Strain-rate dependence of the position of the anomalous peak of the deforming stress in β-CuZn according to the data presented in [11]. Curves *1–3* were obtained for the strain rates $\dot{\varepsilon}_1 = 10^{-5}$ s^{-1}, $\dot{\varepsilon}_2 = 10^{-4}$ s^{-1} and $\dot{\varepsilon}_3 = 5.2 \times 10^{-2}$ s^{-1}, respectively. The inset shows the dependence of the quantity $1/(T\sigma)_m$ corresponding to the peak maximum on $\ln\dot{\varepsilon}$.

Numerous theoretical investigations of anomalous plasticity are based on microscopic mechanisms or a mesoscopic simulation of the dislocation dynamics [2–5, 13, 14]. Although such calculations make it possible in principle to solve any specific problem, representation of the results of such calculations is rather complicated. Considerable inconvenience is associated with the absence of analytical formulas that could be compared with the experimental results. For this reason, it would be useful to have a simple phenomenological model for the phenomenon under investigation for discussing qualitative dependences on all significant parameters. Such a model is developed in this study.

The starting point of the theory proposed here is the proposition concerning the existence of spontaneous locking and delocking processes for dislocations, which is confirmed by the results of *in situ* electron microscopic experiments [8, 9]. Averaging over the statistical distribution of delay times in sessile states leads to an anomalous contribution to the effective velocity of dislocations. This contribution considerably modifies

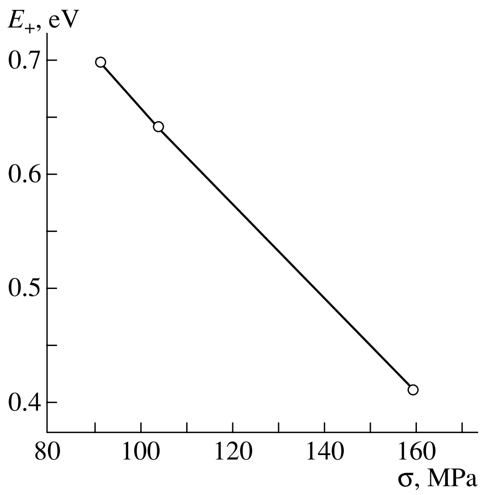

Fig. 4. Stress dependence of the delocking energy E_+ obtained by fitting Eq. (21) to the data presented in Fig. 3.

the dependence of the averaged mobility of dislocations on temperature and stress. The results of the corresponding calculations show that the mobility of dislocations in the presence of spontaneous self-locking cannot be described by the simple Arrhenius law, in contrast to the case of simple slip. For this reason, the conventional scheme of thermoactivation analysis turns out to be incorrect. This may explain, in particular, considerable discrepancies in the order of magnitude of the activation volume determined from the macroscopic plasticity using traditional methods ($A \sim 1000b^3$) and from the motion of individual dislocations ($A \sim 100b^3$) in Ni_3Al [10]. The relations derived by us here provide a basis for developing a new procedure of thermoactivation analysis.

5. CONCLUSIONS

The generalization of the conventional dislocation slip model by taking into account thermally activated transitions between the slip and sessile states of dislocation cores carried out in this study has made it possible to qualitatively explain the anomalous increase in the deforming stress upon heating and its low strain-rate sensitivity. The developed model also makes it possible, in principle, to quantitatively process experimental data in the region of the anomaly in the deforming stress with a view to determine the microscopic parameters of dislocation dynamics.

Previously, experimental data only demonstrated the very fact of the anomaly and certain tendencies (probably, due to the absence of a substantiated procedure for comparison with theoretical predictions). The model proposed here is in accord with these qualitative tendencies; hopefully, this model will stimulate further related experimental studies. Meticulous comparison of the proposed theory with experimental data requires detailed information on the temperature dependence of the deforming stress combined with data on its strain-rate dependence, which unfortunately are not available at present. The available results on the dependence of the position of the deforming-stress peak (on the temperature scale) on the strain rate for β-CuZn [11] are described satisfactorily by the proposed theory.

REFERENCES

1. T. Suzuki and S. Takeuchi, in *Crystal Lattice Defects and Dislocation Dynamics*, Ed. by R. A. Vardanian (Nova Science, Huntington, 2000), p. 1.
2. *Dislocations in Solids*, Ed. by F. R. N. Nabarro (North-Holland, Amsterdam, 1996), Vol. 10.
3. M. J. Mills, in *Multiscale Phenomena in Plasticity: From Experiments to Phenomenology, Modeling and Materials Engineering*, Ed. by J. Lepinoux, D. Maziere, V. Pontikis, and G. Saada (Kluwer, Dordrecht, 2000), NATO Science Series, Ser. E: Applied Sciences, Vol. 367, p. 469.
4. B. A. Grinberg and M. A. Ivanov, Fiz. Met. Metalloved. **78** (3), 3 (1994).
5. D. Caillard, Acta Mater. **44** (7), 2773 (1996).
6. B. V. Petukhov, Fiz. Tverd. Tela (St. Petersburg) **43** (5), 813 (2001) [Phys. Solid State **43**, 845 (2001)].
7. B. V. Petukhov, Kristallografiya **46** (3), 525 (2001) [Crystallogr. Rep. **46**, 474 (2001)].
8. S. Farenc and A. Couret, Mater. Res. Soc. Symp. Proc. **288**, 965 (1993).
9. D. Haussler, M. Bartsch, M. Aindow, *et al.*, Philos. Mag. A **79** (5), 1045 (1999).
10. E. M. Nadgorny and Yu. L. Iunin, Mater. Res. Soc. Symp. Proc. **364**, 707 (1995).
11. K. A. Lee and C. S. Lee, Scr. Mater. **39** (9), 1289 (1998).
12. J. Friedel, *Dislocations* (Pergamon, Oxford, 1964; Mir, Moscow, 1967).
13. D. Caillard and V. Paidar, Acta Mater. **44** (7), 2759 (1996).
14. B. Devincre, P. Veyssiere, L. P. Kubin, and G. Saada, Philos. Mag. A **75** (5), 1263 (1997).

Translated by N. Wadhwa

Physics of the Solid State, Vol. 44, No. 12, 2002, pp. 2257–2259. Translated from Fizika Tverdogo Tela, Vol. 44, No. 12, 2002, pp. 2155–2157.
Original Russian Text Copyright © 2002 by Korovkin, Lebedkina.

Influence of Plastic Deformation on IR Photoconduction Stimulated by *F*-Center-Exciting Light in Colored NaCl Crystals

E. V. Korovkin and T. A. Lebedkina

Institute of Solid-State Physics, Russian Academy of Sciences,
Chernogolovka, Moscow oblast, 142432 Russia
e-mail: korovkin@issp.ac.ru, tlebyod@issp.ac.ru

Received January 8, 2002; in final form, March 14, 2002

Abstract—Plastic deformation of NaCl crystals colored by irradiation with gamma rays was found to lead to the occurrence of a band in the spectrum of IR photoconductivity stimulated by *F*-center-exciting light. This band corresponds to photon energies lying in the range from 0.65 to 1.11 eV and higher and has two distinct peaks, at 0.74 and 0.88 eV. The position of the former peak correlates well with the spectrum of IR quenching of the photoplastic effect, which suggests that this peak is associated with a dislocation electronic level. *© 2002 MAIK “Nauka/Interperiodica”.*

1. The photoplastic effect (increase in the deforming stress caused by illumination of the crystal) was discovered in colored alkali-halide crystals (AHCs) in 1964 [1] and has been studied intensively since then [2–13]. Studies of the photoplastic effect in AHCs by using the dislocation internal-friction method [2, 3] have revealed that this effect is due to a rearrangement of point defects and creation of photoinduced pinning centers (PIPC). At the same time, results of many investigations [2, 3, 7–9] indicate that there are two different mechanisms of the formation of PIPC. First, the electrons that are released from *F* centers under the action of light can be recaptured by the corresponding point defects in the illuminated volume of the sample. The PIPC thus formed will pin moving dislocations and give rise to an increase in the stress required for the dislocations to move further. The other mechanism operates as follows. Electrons released from *F* centers are captured by dislocations. Moving along the dislocations and, together with them, through the crystal, the electrons encounter point defects of the type mentioned above and form PIPC. This mechanism is more efficient, because the PIPC are created on dislocation lines. In 1971, Ermakov and Nadgornyĭ [4] discovered the IR quenching of the photoplastic effect in AHCs; the peak of the IR quenching was found to correspond to an IR-photon energy equal to roughly 0.7 eV, which was assumed (in accordance with the model of IR quenching of the photoplastic effect developed in [4]) to be the energy depth of a dislocation electronic level. Of course, one could have assumed that IR radiation acts not on an electron located on a dislocation but directly on the PIPC and destroys them; however, it was shown in [3] that the PIPC are destroyed by orange light (620 nm) rather than by infrared light.

An attempt to investigate the dislocation electronic level by using the photoconduction (PC) method was made by us in 1987. When a crystal was exposed to IR radiation, we observed the expected increase in photoconductivity and the IR photoconduction stimulated by *F*-center-exciting light (*F*-light). However, it was found that those effects were associated not with dislocations but with specific electron traps of the polaron type, which were present in the AHCs studied by us (NaCl, KCl, KBr) and were investigated in [14–16]. Those investigations stimulated us to considerably improve the PC method as applied to AHCs and other insulating crystals. In this paper, a second attempt is made to detect and investigate the dislocation electronic level in NaCl using the PC method.

2. It is anticipated that the presence of the dislocation electronic level can give rise to IR photoconduction stimulated by *F*-light for photon energies close to 0.7 eV in crystals containing a large number of dislocations. From the results presented in [15], it follows that observations of this effect should be made at $T > 90$ K (for NaCl), because the traps detected earlier hinder such observations at lower temperatures. At $T > 90$ K, the lifetime of these traps in NaCl is so short that by the time the IR photoconduction was observed (more than 1 s after the prior exposure to *F*-light), the traps had been thermally emptied. At the same time, in the vicinity of room temperature, our measurements revealed currents associated with the emptying of traps other than those investigated earlier, as well as currents due to the reorientation of electric dipoles in the crystal. For this reason, we carried out the investigation only in the temperature range 100–200 K.

We investigated NaCl crystals (cross section 4×4 mm, length 11–12 mm) colored by irradiation with

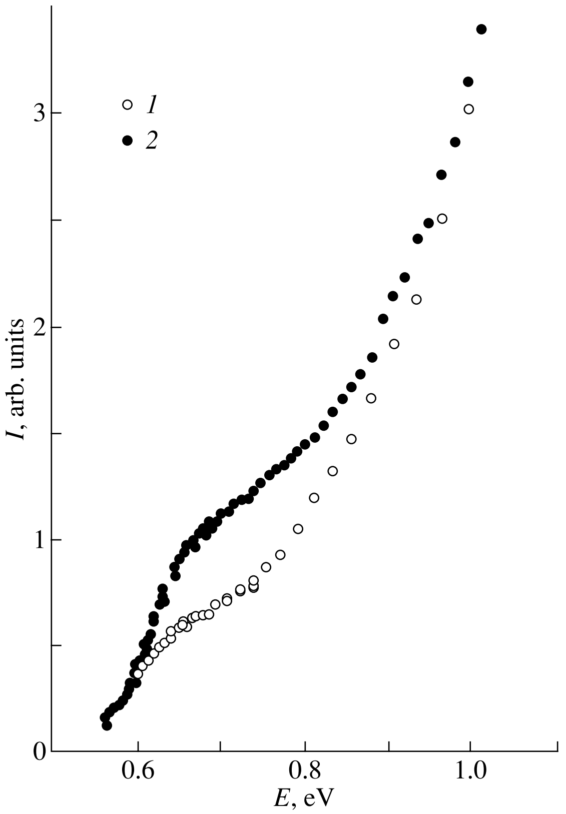

Fig. 1. Spectra of *F*-light-stimulated IR photoconductivity for (*1*) an undeformed NaCl sample and (*2*) the same sample subjected to plastic deformation in compression (ε = 10%).

gamma rays to a dose of up to 10^7 rad. The samples were deformed (compressed) plastically along their length by using an Instron test machine at a strain rate of 20 μm/min up to a deformation of 10–15% at room temperature. Figure 1 shows the spectra of *F*-light-stimulated IR photoconductivity of samples with a high dislocation density (plastic strain 10%) and of samples without dislocations (not subjected to plastic deformation). The spectra were measured at $T = 140$ K following a usual procedure [16]. For each measurement, the procedure consisted of (i) illuminating a sample with *F*-light (SI-8 tungsten lamp, SS-8 and SZS-25 filters) for 10 s, (ii) recording an IR-photoconduction signal (monochromatic light, photon energy range 0.6–1.2 eV) for 7 s, and (iii) illuminating with intense IR radiation (SI-8 lamp, IKS-1 filter) for 5 s in order to empty the electronic levels that remained occupied. It can be seen from Fig. 1 that the spectrum of a deformed sample exhibits a feature at a photon energy of 0.7 eV; this feature is a peak against the background of the sharply increasing signal with increasing photon energy. A similar sharp increase is also observed in the spectrum of an undeformed sample. We conjectured that this increase is due to electron traps with energy levels lying in the orange, red, and near-infrared spectral regions and attempted to reduce the concentration of such traps in order to make the peak more pronounced.

For this purpose, after each illumination of a sample with *F*-light, we additionally illuminated it with the appropriate light in order to empty the unwanted traps. In addition, the measuring procedure was optimized by choosing the appropriate temperature and spectra and durations of both exciting light (instead of *F*-light) and additional illumination. The spectrum of the exciting light was broadened toward longer wavelengths (to 690 nm at the 50% transmission level and 740 nm at the 10% transmission level) by substituting an SZS-25 filter 5 mm thick for combined SS-8 and SZS-25 filters in order not only to excite *F* centers but also to destroy unwanted traps. In this case, it is desirable that the transmission decrease sharply in the range 800–1000 nm and, hence, the states under study in the infrared spectral region not be destroyed. However, there are no filters that are transparent in the visible region and exhibit a sharper transmission band edge in the spectral range indicated above than that of an SZS-25 filter.

The spectrum of the additional illumination was formed by adding an OS-14 light filter to the SZS-25 light filter, which prevented the transmission of light with a wavelength shorter than 580 nm and, hence, the liberation of electrons from *F* centers. Since our automated setup did not allow more than two sets of light filters to be changed (the excitation by *F*-light, additional illumination, and the emptying of traps by illumination were performed using the same SI-8 lamp with different light filters), we could not empty the traps after each measurement. It was found in a separate experiment that this last trap-emptying procedure did not affect the measurement data, at least in the spectral range of interest (0.6–1.2 eV). This fact indicates that the concentration of the occupied states of interest after prolonged exposure of a sample to *F*-light (for 30 s) is virtually independent of their initial concentration, which remained after the preceding measurement.

Since the duration of the measurement of the entire spectrum was long, the optimization of the measuring procedure was made by measuring the signal only at two points of the spectrum, 0.75 and 0.94 eV. The parameters were adjusted so that the slope of the spectral curve was minimum in this range and the magnitude of the signal itself was sufficiently large. The latter was very important, because the sensitivity could not be increased further: we used the maximum-sensitivity scale of the electrometer (the upper limit of its range was 10^{-12} A) and the maximum supply voltage (500 V).

The optimum duration of exposure to *F*-light was found to be 30 s. Small variations (±5 s) in this quantity did not affect the slope of the spectral curve but caused the signal to change in magnitude (the signal increased with increasing duration of excitation). However, when the excitation duration exceeded 30 s, the signal increased slowly. For this reason, we chose this value lest the duration of the entire measurement cycle be

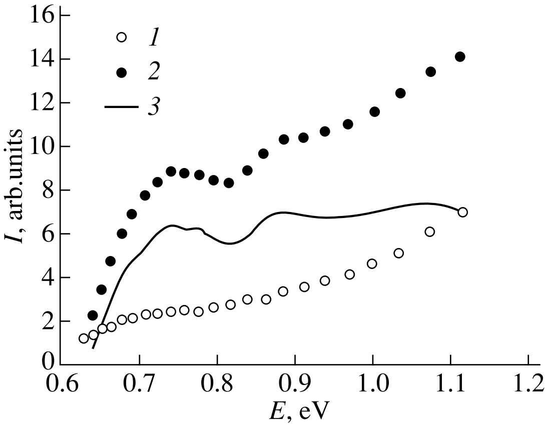

Fig. 2. Spectra of *F*-light-stimulated photoconductivity measured on a sample additionally illuminated with orange light. (*1*) An undeformed NaCl sample, (*2*) the same sample subjected to plastic deformation (14.65%) in compression, and (*3*) the difference of spectra *2* and *1*.

very long. The optimum duration of the additional illumination was found to be 20 s.

Variations in temperature within the range 100–400 K virtually did not affect the slope of the spectral curve, but the magnitude of the signal was affected: the signal decreased when the temperature deviated from its optimum value, 113 K.

3. Figure 2 shows spectra measured on one sample. The sample was first investigated at $T = 113$ K (where it was undeformed, curve *1*), then warmed to room temperature and removed from the cryostat; then, the sample was deformed plastically at a strain rate of 20 μm/min to a strain of 14.65% and again investigated at the same temperature following the same procedure (curve *2*). The measurements made on many other samples are virtually identical to those presented in Fig. 2, especially over the range 0.6–0.95 eV. The data presented in Fig. 2 were obtained for the width of the monochromator slit being 1 mm. As a monochromator, we used an IKS-21 spectrometer with an LiF prism. Spectra measured on deformed samples with the width of the monochromator being 0.6 and 2 mm were similar over the range 0.6–0.95 eV, and only at higher photon energies (0.95–1.2 eV) were deviations observed: with the wider slit, the photocurrent rose more steeply with increasing photon energy. Thus, the spectral curves presented in Fig. 2 are correct in the range 0.6–0.95 eV; that is, these curves are independent of the width of the monochromator slit used in the measurements.

It can be seen from Fig. 2 that there are two maxima (at the photon energies 0.74 and 0.88 eV) in the spectrum of the plastically deformed sample. If we assume that the peak at 0.74 eV corresponds to a certain electronic state whose contribution to the photoconductivity spectrum can be described by a more or less symmetric bell-shaped curve, then we can estimate the half-width of this peak using the fact that its low-energy slope is clearly defined. The half-width is found to be 0.15 eV.

4. It is well known that plastic deformation leads to the creation of a great quantity of point defects and their complexes, many of which can act as electron traps. For example, the conventional photoconductivity in the *F* band falls off in a plastically deformed sample in comparison with that in an undeformed sample, because the mean free path of an electron is decreased when additional traps arise in great numbers. Therefore, we cannot state with assurance that the peaks of the IR photoconductivity detected by us are associated with dislocation electronic levels rather than with such traps. However, the fact that the position of one of these peaks correlates well with the spectrum of IR quenching of the photoplastic effect [4] allows one to conjecture that this peak is related to a dislocation electronic level.

REFERENCES

1. J. Nedeau, J. Appl. Phys. **35**, 669 (1964).
2. G. A. Ermakov, E. V. Korovkin, and Ya. M. Soĭfer, Fiz. Tverd. Tela (Leningrad) **16**, 697 (1974) [Sov. Phys. Solid State **16**, 457 (1974)].
3. G. A. Ermakov, E. V. Korovkin, and Ya. M. Soĭfer, Fiz. Tverd. Tela (Leningrad) **16**, 1756 (1974) [Sov. Phys. Solid State **16**, 1139 (1974)].
4. G. A. Ermakov and É. M. Nadgornyĭ, Pis'ma Zh. Éksp. Teor. Fiz. **14**, 45 (1971) [JETP Lett. **14**, 29 (1971)].
5. J. Deputat and Z. Pawlowski, Bull. Acad. Pol. Sci., Ser. Sci. Tech. **13**, 69 (1965).
6. J. M. Cabrera and F. Agullo-Lopez, J. Appl. Phys. **45**, 1013 (1974).
7. E. V. Korovkin, Fiz. Tverd. Tela (Leningrad) **21**, 1785 (1979) [Sov. Phys. Solid State **21**, 1021 (1979)].
8. E. V. Korovkin, Fiz. Tverd. Tela (Leningrad) **23**, 2545 (1981) [Sov. Phys. Solid State **23**, 1493 (1981)].
9. E. V. Korovkin, Fiz. Tverd. Tela (Leningrad) **24**, 524 (1982) [Sov. Phys. Solid State **24**, 294 (1982)].
10. E. V. Korovkin, Pis'ma Zh. Éksp. Teor. Fiz. **35**, 481 (1982) [JETP Lett. **35**, 595 (1982)].
11. T. Kataoka and T. Jamada, in *Proceedings of the IX Yamada Conference on Dislocations in Solids, Tokyo, 1984*, p. 467.
12. T. Higihara and T. Okada, in *Proceedings of the IX Yamada Conference on Dislocations in Solids, Tokyo, 1984*, p. 471.
13. T. Higihara, Y. Hayashiuchi, and T. Okada, in *Proceedings of the IX Yamada Conference on Dislocations in Solids, Tokyo, 1984*, p. 475.
14. E. V. Korovkin and T. A. Lebedkina, Fiz. Tverd. Tela (Leningrad) **33**, 2483 (1991) [Sov. Phys. Solid State **33**, 1400 (1991)].
15. E. V. Korovkin and T. A. Lebedkina, Fiz. Tverd. Tela (Leningrad) **33**, 2822 (1991) [Sov. Phys. Solid State **33**, 1595 (1991)].
16. E. V. Korovkin and T. A. Lebedkina, Fiz. Tverd. Tela (Leningrad) **42**, 1412 (2000) [Phys. Solid State **42**, 1451 (2000)].

Translated by Yu. Epifanov

Physics of the Solid State, Vol. 44, No. 12, 2002, pp. 2260–2265. Translated from Fizika Tverdogo Tela, Vol. 44, No. 12, 2002, pp. 2158–2163.
Original Russian Text Copyright © 2002 by Krivtsov, Morozov.

DEFECTS, DISLOCATIONS, AND PHYSICS OF STRENGTH

On Mechanical Characteristics of Nanocrystals

A. M. Krivtsov and N. F. Morozov

Institute of Problems in Machine Science, Russian Academy of Sciences,
Vasil'evskiĭ ostrov, Bol'shoĭ pr. 61, St. Petersburg, 199178 Russia
e-mail: krivtsov@AK5744.spb.edu

Received January 11, 2002

Abstract—The dependence of the elastic moduli of a nanocrystal on its size is investigated theoretically with reference to a two-dimensional single-crystal strip. It is shown that the uncertainty (of a fundamental nature) in the size of a nanocrystal causes the determination of many of its mechanical characteristics to be ambiguous. It is found that the Cauchy–Green relations are modified and the elastic-constant tensor ceases to be symmetric; the size and shape of a nanocrystal render its mechanical properties more anisotropic. For a single-crystal strip, the Poisson ratio decreases and the Young modulus increases with decreasing thickness of the strip; in the case of a very thin crystal film (two atomic layers thick), these elastic moduli can differ from their macroscopic values by a factor of two. The size effects which make the continuum elasticity theory inapplicable to nanocrystals are estimated. The size effects that occur when the molecular dynamics method is applied for modeling macroscopic objects are also discussed. *© 2002 MAIK "Nauka/Interperiodica".*

1. INTRODUCTION

The recent rapid development of nanotechnologies has generated a need for analytical models that can adequately describe the physical-mechanical properties of nanometer-sized objects. In most existing models, the main mechanical characteristics of nanocrystals are assumed to be identical to those measured for macroscopic crystals. However, when a structure consists of only a few atomic layers, discordance between its evident discreteness and the continuum models applied for describing the structure should manifest itself. The discrepancy between the values of the elastic moduli measured for microscopic and macroscopic samples has been pointed out by many investigators [1–3]. Unfortunately, direct measurements of the elastic characteristics of a nanometer-sized object are impossible; one is forced to use indirect methods [2, 4, 5]. One of the methods used for determining the elastic characteristics of such objects is the study of the microrelief that forms when a sample covered with an ultrathin film is stretched [2, 5, 6]. By solving the corresponding continuum problem on the stability of the thin-walled construction, one can determine the Poisson ratio and the Young modulus of the covering film from such experiments [1, 6, 7]. However, the values of the elastic characteristics determined in this way differ essentially from the corresponding macroscopic values. This discrepancy may be due to both the specific internal structure of the sputtered film and the discreteness of the film on a nanometer scale. This paper is devoted to studying the influence of the discreteness of a film on its elastic moduli and is a continuation of the study performed in [8].

To investigate the size effect for the mechanical characteristics of a material, we take, as a model, a two-dimensional strip of a single crystal with hexagonal closely packed (hcp) structure (triangle lattice). The atoms are assumed to interact via a pairwise potential. The main results are obtained by including only the nearest neighbor interaction; the effect of more distant neighbor atoms is estimated in Section 4. In determining the elastic moduli, we restrict our consideration to the case of tension and compression of a single crystal; the case of shear strain is not discussed in this paper.

2. DETERMINATION OF ELASTIC MODULI

We consider a two-dimensional single crystal (Fig. 1) infinitely long (along the x axis) and $N \geq 2$ atomic layers thick (along the y axis). Each atom interacts only with nearest neighbor atoms, as shown in

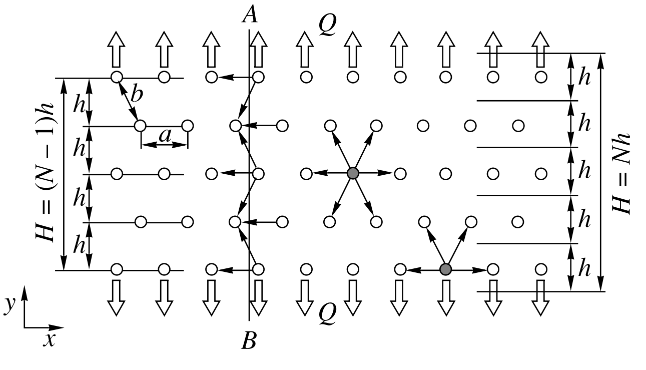

Fig. 1. Model under study: two-dimensional single-crystal strip (schematic).

Fig. 1. Constant tensile forces Q are applied to the atoms situated at the ends of the crystal. The deformed state of the crystal is fully determined by the distance a between neighboring atoms in each layer and the distance h between adjacent layers. The distance between the nearest neighbor atoms belonging to adjacent layers is b (Fig. 1). Obviously, we have $b^2 = a^2/4 + h^2$. In the undeformed state, the lattice consists of equilateral triangles with sides $a = b = a_0$ and the load applied to the ends is zero ($Q = 0$). Let $F(r)$ be the interaction force between two atoms separated by a distance r (the attractive force is considered to be positive). Then, the equilibrium condition (along the y axis) for an atom situated at the crystal surface has the form

$$Q = 2\frac{h}{b}F(b) \longrightarrow \sigma_2 \overset{\text{def}}{=} \frac{Q}{a} = 2\frac{h}{ab}F(b). \tag{1}$$

Here, σ_2 is the normal stress applied along the y axis. Let us mentally cut the crystal along the vertical straight line AB (Fig. 1). The total normal force exerted on one part of the crystal by the other is

$$H\sigma_1 = NF(a) + (N-1)\frac{a}{2b}F(b). \tag{2}$$

Here, σ_1 is the normal stress applied along the x axis; and H is the crystal thickness (along the y axis). The value of H cannot be determined unambiguously. For example, if the thickness is defined as the spacing between the layers lying at opposite ends of the crystal (Fig. 1), then $H = (N-1)h$. On the other hand, it is reasonable to define the crystal thickness as the product of the thickness of one layer multiplied by the number of layers, which gives $H = Nh$. For this reason, we define the thickness as

$$H \overset{\text{def}}{=} N_* h, \quad N - 1 \le N_* \le N, \tag{3}$$

where the quantity N_* reflects the ambiguity of the definition of H. Since the strains are small, the forces acting in the crystal can be approximately written in the form

$$F(a) = C\Delta a, \quad F(b) = C\Delta b, \quad C \overset{\text{def}}{=} F'(a_0) > 0, \tag{4}$$

where C is the atomic-bond stiffness and the symbol Δ indicates the deviation of a quantity from its corresponding value for an undeformed crystal. Let us denote the strains of the crystal along the x and y axes by ε_1 and ε_2, respectively. We have

$$\varepsilon_1 \overset{\text{def}}{=} \Delta a/a_0, \quad \varepsilon_2 \overset{\text{def}}{=} \Delta h/h_0, \quad h_0 \overset{\text{def}}{=} \sqrt{3}a_0/2. \tag{5}$$

Substituting Eqs. (3)–(5) into Eqs. (1) and (2) yields the elasticity relations

$$\sigma_1 = C_{11}\varepsilon_1 + C_{12}\varepsilon_2, \quad \sigma_2 = C_{21}\varepsilon_1 + C_{22}\varepsilon_2, \tag{6}$$

where the stiffness coefficients C_{kn} are given by

$$\begin{gathered} C_{11} = \frac{3\sqrt{3}}{4}\frac{N-\frac{1}{9}}{N_*}C, \quad C_{12} = \frac{\sqrt{3}}{4}\frac{N-1}{N_*}C, \\ C_{21} = \frac{\sqrt{3}}{4}C, \quad C_{22} = \frac{3\sqrt{3}}{4}C. \end{gathered} \tag{7}$$

It follows from Eq. (7) that the crystal under study is anisotropic. It will be recalled that an infinite two-dimensional hcp crystal is isotropic. Therefore, the anisotropy of the crystal under study is a size effect. Let us introduce the notation

$$\begin{gathered} \nu_1 \overset{\text{def}}{=} -\frac{\varepsilon_2}{\varepsilon_1}\bigg|_{\sigma_2 = 0}, \quad E_1 \overset{\text{def}}{=} -\frac{\sigma_1}{\varepsilon_1}\bigg|_{\sigma_2 = 0}, \\ \nu_2 \overset{\text{def}}{=} -\frac{\varepsilon_1}{\varepsilon_2}\bigg|_{\sigma_1 = 0}, \quad E_2 \overset{\text{def}}{=} -\frac{\sigma_2}{\varepsilon_2}\bigg|_{\sigma_1 = 0}. \end{gathered}$$

Here, ν_1 and E_1 are the Poisson ratio and the Young modulus, respectively, characterizing the tension along the x axis and ν_2 and E_2 are the respective quantities characterizing the tension along the y axis. Using Eqs. (6), we obtain

$$\begin{gathered} \nu_1 = \frac{C_{21}}{C_{22}}, \quad E_1 = C_{11} - \nu_1 C_{12} = \frac{D}{C_{22}}, \\ \nu_2 = \frac{C_{12}}{C_{11}}, \quad E_2 = C_{22} - \nu_2 C_{21} = \frac{D}{C_{11}}, \\ D \overset{\text{def}}{=} C_{11}C_{22} - C_{12}C_{21}. \end{gathered} \tag{8}$$

Substituting Eqs. (7) into Eqs. (8) yields the required expressions for the elastic moduli:

$$\begin{gathered} \nu_1 = \nu_\infty, \quad E_1 = \frac{N}{N_*}E_\infty, \\ \nu_2 = \frac{N-1}{N-\frac{1}{9}}\nu_\infty, \quad E_2 = \frac{N}{N-\frac{1}{9}}E_\infty. \end{gathered} \tag{9}$$

Here, $E_\infty = 2C/\sqrt{3}$ and $\nu_\infty = 1/3$ are the values of the Young modulus and Poisson ratio corresponding to the infinite crystal, respectively [9, 10]. Let us discuss the formulas derived above.

When the crystal is stretched along the atomic layers, the Young modulus E_1 essentially depends on the quantity N_*, i.e., on the definition of the thickness of the nanometer-sized crystal strip. If we put $N_* = N$ (the maximum value of N_*), then the Poisson ratio and Young modulus for tension along atomic layers will be independent of the number of layers. This is due to the fact that the crystal is infinite in the longitudinal direction. The Young modulus $E_1^{\max}$ corresponding to the

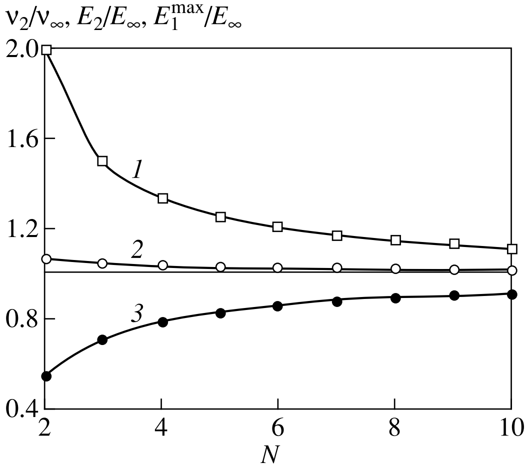

Fig. 2. Dependences of the Young modulus and Poisson ratio on the number of atomic layers. (*1*, *2*) Young modulus in the longitudinal ($E_1^{\max}/E_\infty$) and transverse (E_2/E_∞) directions, respectively, and (*3*) the relative Poisson ratio (ν_2/ν_∞) for stresses applied along the transverse direction.

minimum value $N_* = N - 1$ is not a constant; it increases with decreasing number of atomic layers, so that at $N = 2$, this Young modulus becomes twice as large as E_∞ (Fig. 2). Therefore, the ambiguity of the definition of the Young modulus is essential in the case of small values of N.

When the crystal is stretched transversely to the atomic layers, both the Poisson ratio and the Young modulus vary with N; namely, the Poisson ratio decreases and the Young modulus increases with decreasing number of layers (Fig. 2). It can be seen from Fig. 2 that the Poisson ratio ν_2 depends on N more heavily than does the Young modulus E_2. For example, at $N = 2$, the deviation of the Young modulus from E_∞ does not exceed 6%, whereas the Poisson ratio in this case is nearly half as large as ν_∞.

As $N \longrightarrow \infty$, the elastic moduli approach their values for an infinite crystal; these values do not depend on the direction of the applied stress. It should be noted that when the macroscopic values of the elastic moduli are used, the maximum relative error is roughly $\frac{100\%}{N}$. For example, at $N = 10$, the deviation of $E_1^{\max}$ and ν_2 from their respective macroscopic values is 11%, whereas at $N = 100$, this deviation is as small as 1% (Table 1).

Table 1. Dependence of the elastic moduli of a nanocrystal on the number of atomic layers

N	$E_1^{\max}/E_\infty$	ν_2	ν_2/ν_∞	E_2/E_∞
2	2.00	0.18	0.53	1.06
3	1.50	0.23	0.69	1.04
4	1.33	0.26	0.77	1.03
5	1.25	0.27	0.82	1.02
10	1.11	0.30	0.91	1.01
20	1.05	0.32	0.96	1.01
50	1.02	0.33	0.98	1.00
100	1.01	0.33	0.99	1.00

Note: $E_1^{\max}$, E_2, and E_∞ are the Young moduli for a strip (in the longitudinal and transverse directions) and for an infinite crystal, respectively; ν_2 and ν_∞ are the Poisson ratios for a strip (in the transverse direction) and an infinite crystal, respectively.

3. STRAIN ENERGY

Let us discuss the elasticity relations (6). According to the macroscopic elasticity theory, the stresses σ_k and the elastic moduli C_{kn} are related to the specific strain energy through the Cauchy–Green equations

$$\sigma_k = \frac{\partial U}{\partial \varepsilon_k}, \quad C_{kn} \overset{\text{def}}{=} \frac{\partial \sigma_k}{\partial \varepsilon_n} = \frac{\partial^2 U}{\partial \varepsilon_k \partial \varepsilon_n}, \tag{10}$$

where U is the strain energy per unit volume. As before, we consider only the case of linear elasticity. From Eq. (10), it follows that $C_{kn} = C_{nk}$. Let us elucidate whether this relation holds for a nanocrystal. According to Eq. (7), we have

$$\frac{C_{12}}{C_{21}} = \frac{N-1}{N_*}. \tag{11}$$

Therefore, in the case of $N_* = N$, which is shown in Section 2 to be the most preferable, we have $C_{12} \neq C_{21}$. Does this result contradict the energy considerations? In order to clarify this issue, we consider the case where the crystal is stretched transversely to the atomic layers and find the change in the potential energy of a crystal domain with a fairly large length along the atomic layers. We have

$$dE_\Pi = N_x Q dy, \tag{12}$$

where E_Π is the total potential energy of the crystal, Q is the external force acting on an atom at the crystal surface (Fig. 1), dy is a small displacement of the upper surface of the crystal (the lower surface is assumed to be fixed), and N_x is the number of forces Q applied to the upper face of the crystal domain in question. We assume that N_x is sufficiently large for the size effects due to the finiteness of this domain to be negligible. The specific potential energy (per unit volume) is defined as

$$U \overset{\text{def}}{=} E_\Pi/(N_x a_0 N_* h_0). \tag{13}$$

The quantity in parentheses is the entire volume of the crystal domain, with $N_x a_0$ being its dimension along the x axis and $N_* h_0$ being the domain dimension (thickness) along the y axis. As indicated in Section 2, the latter quantity cannot be determined unambiguously; this ambiguity also manifests itself in the definition of the specific internal energy. The quantities Q and dy are related to the stress and strain of the crystal through the equations

$$\begin{aligned} Q &= \sigma_2 a \approx \sigma_2 a_0, \\ dy &= (N-1)dh = (N-1)h_0 d\varepsilon_2. \end{aligned} \tag{14}$$

Substituting Eqs. (13) and (14) into Eq. (12) yields

$$\sigma_2 = \frac{N-1}{N_*}\frac{\partial U}{\partial \varepsilon_2}. \tag{15}$$

Thus, the macroscopic Cauchy–Green relations (10) do not hold in the case of finite values of N. Of course, Eq. (15) can be reduced to Eq. (10) by putting $N_* = N - 1$. In this case, as follows from Eq. (11), the condition $C_{12} = C_{21}$ is satisfied. However, it will be recalled that the Young modulus E_1 essentially depends on N in this case, in contrast to the case of $N_* = N$ [see Eq. (9)]. This situation also lends support to the fundamental conclusion that the size of a nanocrystal, as well as the quantities that depend on this size, can be defined differently. A definition appropriate in one case proves to be unsuitable in another. Thus, we find that the Cauchy–Green relations (10) in the case in question have to be modified as follows:

$$\sigma_1 = \frac{\partial U}{\partial \varepsilon_1}, \quad \sigma_2 = \frac{N-1}{N_*}\frac{\partial U}{\partial \varepsilon_2}, \quad C_{kn} = \frac{\partial \sigma_k}{\partial \varepsilon_n}. \tag{16}$$

The formula for σ_1 in Eq. (16) is identical to that for a macroscopic crystal, because the crystal under study is infinite along the x axis.

Directly calculating the number of atomic bonds per unit length of the single-crystal strip, we find an explicit formula for the specific interaction energy U:

$$U = \frac{1}{N_* a_0 h_0}[N\Pi(a) + 2(N-1)\Pi(b)], \tag{17}$$

where $\Pi(r)$ is the potential energy of interaction between two atoms separated by a distance r. The stiffness coefficients C_{kn} as calculated from Eqs. (16) with the specific energy given by Eq. (17) are identical to those calculated in Section 2 [see Eq. (7)].

4. ALLOWANCE FOR INTERACTION WITH ATOMS OF THE SECOND COORDINATION SHELL

In the previous sections, we considered the interaction of an atom only with its nearest neighbor atoms (the first coordination shell). Including the interactions with more distant atoms highly complicates the calculation of the elastic moduli, because surface effects in this case distort the crystal lattice in the equilibrium state; these effects not only complicate the algebra but also increase the ambiguity in defining the nanocrystal dimensions (because there is no certain lattice spacing). The latter circumstance, in turn, leads to an additional ambiguity in determining all quantities that depend on the nanocrystal size (such as the Young modulus). Another difficulty is associated with the fact that when the interaction with more distant atoms is included, the mechanical characteristics become strongly dependent on the functional form of the interaction potential (in the case where only the interaction with nearest neighbor atoms is taken into account, the Poisson ratio is independent of the form of the interatomic interaction and the Young modulus depends only on one characteristic of the interaction, the bond stiffness). All the difficulties indicated above make exact analytical solution of the problem at hand impossible. However, if the interatomic interaction decays fairly rapidly with distance, one can advantageously make use of approximate methods in which the effect of more distant atoms is treated as a perturbation on the situation considered in the previous sections. A detailed discussion of these problems is beyond the scope of this paper. We consider only one particular case, which allows one to appreciate how the inclusion of atoms of the second coordination shell affects the results obtained above.

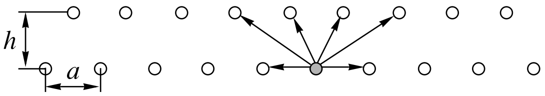

Fig. 3. Two-layered crystal (schematic).

Let us calculate the Poisson ratio with allowance for the atoms of the second coordination shell by considering the stresses applied along the atomic layers. For the sake of simplicity, we restrict ourselves to the case of a crystal consisting of two atomic layers (Fig. 3; the arrows indicate the atoms with which a given atom interacts). The specific potential energy of the crystal can be written as

$$U = \frac{1}{V_0}\left[P(a^2) + P\left(\frac{1}{4}a^2 + h^2\right) + P\left(\frac{9}{4}a^2 + h^2\right)\right], \tag{18}$$

where $P(r^2) \overset{\text{def}}{=} \Pi(r)$ is the potential energy of interatomic interaction (as a function of distance squared) and V_0 is the crystal volume per atom. The value of V_0 cannot be defined unambiguously, but this value is not used in what follows. The last term in Eq. (18) [not included in Eq. (17)] describes the interaction with atoms of the second coordination shell. The Poisson ratio for stresses applied along the x axis can be calculated from Eqs. (8) and (16) to be

$$\nu_1 = -\frac{C_{21}}{C_{22}} = -\frac{\partial^2 U}{\partial \varepsilon_1 \partial \varepsilon_2}\left(\frac{\partial^2 U}{\partial \varepsilon_2 \partial \varepsilon_2}\right)^{-1}. \tag{19}$$

Table 2. Calculated Poisson ratio for the case where stresses are applied along the atomic layers

	Allowance for atoms of the first coordination shell alone	Allowance for atoms of the second coordination shell	
		approximate	exact
Poisson ratio	0.333	0.320	0.318
Deviation from ν_∞, %	0	4.1	4.5
Computing formulas	(9)	(22)	(20), (21)

Substituting Eq. (18) into Eq. (19) yields

$$\nu_1 = -\frac{a^2}{4h^2}\frac{P''\left(\frac{1}{4}a^2+h^2\right)+9P''\left(\frac{9}{4}a^2+h^2\right)}{P''\left(\frac{1}{4}a^2+h^2\right)+P''\left(\frac{9}{4}a^2+h^2\right)}. \tag{20}$$

The quantities a and h should be determined from the equilibrium conditions $\partial U/\partial a = \partial U/\partial h = 0$. Using Eq. (18), these conditions can be represented in the form

$$\begin{gathered} P'(a^2)+2P'\left(\frac{1}{4}a^2+h^2\right) = 0, \\ P'\left(\frac{1}{4}a^2+h^2\right)+P'\left(\frac{9}{4}a^2+h^2\right) = 0. \end{gathered} \tag{21}$$

Solving the set of equations (21) and substituting the obtained values of a and b into Eq. (20) yields the Poisson ratio. If the interaction potential decays fairly rapidly with distance, we can use an approximate expression,

$$\nu_1 \approx \frac{1}{3}\left(1+8\frac{P''(3a_0^2)}{P''(a_0^2)}\right), \tag{22}$$

which is obtained from Eq. (20) by replacing a and h by their values for the undeformed lattice and expanding the result in powers of the small parameter $P''(3a_0^2)/P''(a_0^2)$.

Let us discuss Eq. (22). It will be recalled that in the case of the interaction with nearest neighbor atoms alone, the Poisson ratio ν_1 was shown to be independent of the number of atomic layers and exactly equal to its macroscopic value, 1/3. It follows from Eq. (22) that the allowance for the interaction with atoms of the second coordination shell leads to a deviation of the value of ν_1 from 1/3; however, this deviation is small if the interaction potential decays rapidly with distance. For example, in the case of the Lennard–Jones potential

$$\Pi(r) = P(r^2) = \Pi_*\left[\left(\frac{a_0}{r}\right)^{12}-2\left(\frac{a_0}{r}\right)^6\right]$$

(where a_0 is the equilibrium spacing in a system of two atoms and Π_* is the binding energy), the value of $P''(3a_0^2)$ can be as small as 0.5% of $P''(a_0^2)$. Substituting this value into Eq. (22), we find that the Poisson ratio changes by 4% when the interaction with atoms of the second coordination shell is included. The numerically calculated values of the Poisson ratio from exact formulas (20) and (21) and from the approximate expression (22) are listed in Table 2.

Thus, allowance for the interaction with atoms of more distant coordination shells leads to changes in the elastic moduli, but these changes are insignificant if the interaction potentials decay rapidly with distance. It should be noted that we made calculations for the case of $N = 2$, where the size effect is the most pronounced; for larger values of N, the influence of the second coordination shell is even less noticeable. However, in a three-dimensional nanocrystal, the effect may be stronger. For example, for an fcc lattice, the distance to the second coordination shell is $\sqrt{2}a_0$ (instead of $\sqrt{3}a_0$ as in the two-dimensional case) and the corresponding value of $P''(2a_0^2)$ for the Lennard–Jones potential is equal to 3% of $P''(a_0^2)$ (instead of 0.5% in the two-dimensional case).

5. DISCUSSION

In the previous sections, we considered the case of a two-dimensional crystal with an hcp lattice infinite in one direction and having a finite number of atomic layers in the other. Now, we will discuss the obtained results and their possible application to crystals of other types.

We established above that there is an ambiguity (of a fundamental nature) in determining the size of a nanocrystal, which leads to uncertainties in many macroscopic characteristics, such as the applied stress, Young modulus, and specific volume strain energy. There is no way to define the nanocrystal size unambiguously; if the size definition is such that the elastic moduli are as close to their macroscopic values as possible, then the Cauchy–Green relations are modified and the elastic constant tensor of the crystal ceases to be symmetric. If, conversely, the Cauchy–Green relations are assumed to be valid, the size effect is enhanced considerably. We note that the ambiguity under discussion does not manifest itself in the values of quantities (such as the Poisson ratio and the strain energy per unit mass) that are independent of the way in which the nanocrystal size is defined.

From the results of our study, it also follows that the anisotropy of the elastic properties depends on the shape and size of the nanocrystal. The mechanical properties of an infinite crystal lattice, as a rule, are anisotropic; however, in the case of a nanocrystal, the anisotropy associated with the structure of the crystal lattice is combined with the anisotropy related to the shape and size of the nanocrystal.

In the case considered in this paper, the Poisson ratio decreases and the Young modulus increases with decreasing thickness of the nanocrystal. For very thin crystal films, these elastic moduli can differ from their macroscopic values by a factor of two. This conclusion correlates well with the values of the elastic moduli determined from the experimental data from [1], according to which the Young modulus of a thin film increases with decreasing film thickness. However, it should be verified whether or not this conclusion is applicable to crystal lattices of other types (above all, three-dimensional ones).

We also found that if the interaction with atoms of the first coordination shell alone is taken into account, the Poisson ratio is independent of the character of the atomic interaction and the Young modulus depends only on one parameter of this interaction, the bond stiffness. Allowance for the interaction with atoms of the second coordination shell leads to enhancement of the size effect (especially in the three-dimensional case). The elastic moduli become strongly dependent on the functional form of the atomic interaction. These properties are exhibited by both two- and three-dimensional simple crystal lattices. However, if the atomic interaction decays rapidly with distance, the allowance for the interaction with atoms of the second coordination shell leads only to a negligible correction.

Thus, the results of this study allow us to conclude that the continuum mechanics, including the continuum elasticity theory, should be applied to nanocrystals with a great deal of caution. Allowance should be made for the change in the mechanical characteristics when crystals are nanometer sized. This conclusion is especially true for the characteristics (such as the Young modulus) that can be defined differently on a nanometer scale. When such characteristics are used, their definition should be clearly indicated in the case of nanometer-sized objects. However, we do not argue that the classical elasticity theory is completely inapplicable on a nanometer scale. Rather, this theory should be used with allowance for the size effects and the adequacy of the continuum approximation should be verified in each specific case. We note that, according to the calculations presented above, the size effect is more significant when a nanocrystal consists of a few atomic layers; the size effect is small in the case of several tens of atomic layers and is negligible for crystals with hundreds of atomic layers.

The question of how the discreteness of the atomic structure affects the mechanical characteristics is also of importance in the following respect. The molecular dynamics method is presently used widely for modeling macroscopic processes in solids [11–15], and the question arises of how many particles should be taken into account in calculations in order to obtain the required accuracy. According to our results, the error caused by the replacement of a continuous medium by its discrete atomic analog is roughly $1/N$, where N is the ratio of the characteristic linear dimension of the model to the average interatomic distance. Therefore, for the error to be 1%, we should take 100 particles in one-dimensional modeling, 10^4 particles in the two-dimensional case, and 10^6 particles in the three-dimensional case. Calculations for such systems can be easily carried out on a modern computer. Therefore, in principle, the molecular dynamics method can be used for modeling the processes in a macroscopic solid.

ACKNOWLEDGMENTS

This study was supported by the Russian Foundation for Basic Research, project nos. 99-07-90443 and 00-01-00489.

REFERENCES

1. D. L. Bykov and D. N. Konovalov, in *Proceedings of the XXXVI International Workshop "Topical Problems of Strength," Vitebsk, 2000,* p. 428.
2. Yu. P. Baĭdarovtsev, G. N. Savenkov, and V. A. Tarasenko, Vysokomol. Soedin., Ser. A **41** (8), 1302 (1999).
3. J. J. Kim, H. A. Marzouk, C. C. Eloi, and J. D. Robertson, J. Appl. Phys. **78** (1), 245 (1995).
4. V. I. Nikolaev, V. V. Shpeĭzman, and B. I. Smirnov, Fiz. Tverd. Tela (St. Petersburg) **42** (3), 428 (2000) [Phys. Solid State **42**, 437 (2000)].
5. A. L. Volynskiĭ, I. V. Chernov, and N. F. Bakeev, Dokl. Akad. Nauk **355** (4), 491 (1997).
6. S. L. Bazhenov, A. L. Volynskiĭ, E. E. Voronina, and N. F. Bakeev, Dokl. Akad. Nauk **367** (1), 75 (1999).
7. D. L. Bykov and D. N. Konovalov, Vestn. Tambov. Univ. **5** (2–3), 224 (2000).
8. A. M. Krivtsov and N. F. Morozov, Dokl. Akad. Nauk **381** (3), 825 (2001) [Dokl. Phys. **46**, 825 (2001)].
9. A. M. Krivtsov, Tr. St.-Peterburg. Gos. Tekh. Univ. **443**, 9 (1992).
10. A. M. Krivtsov, Z. Angew. Math. Mech. **79** (S2), 419 (1999).
11. I. F. Golovnev, E. I. Golovneva, A. A. Konev, and V. M. Fomin, Fiz. Mezomekh. **2**, 21 (1998).
12. V. A. Lagunov and A. B. Sinani, Fiz. Tverd. Tela (St. Petersburg) **43** (4), 644 (2001) [Phys. Solid State **43**, 670 (2001)].
13. F. F. Abraham, D. Brodbeck, W. E. Rudge, *et al.*, Modell. Simul. Mater. Sci. Eng. **6** (5), 639 (1998).
14. B. L. Holian and P. S. Lomdahl, Science **280** (5372), 2085 (1998).
15. A. M. Krivtsov, Int. J. Impact Eng. **23** (1), 477 (1999).

Translated by Yu. Epifanov

Physics of the Solid State, Vol. 44, No. 12, 2002, pp. 2266–2270. Translated from Fizika Tverdogo Tela, Vol. 44, No. 12, 2002, pp. 2164–2168.
Original Russian Text Copyright © 2002 by Troyanchuk, Mantytskaya, Chobot.

Magnetic Phase Diagram of the $Bi_{1-x}Ca_xMnO_3$ Manganites

I. O. Troyanchuk, O. S. Mantytskaya, and A. N. Chobot
Institute of Solid-State and Semiconductor Physics, National Academy of Sciences of Belarus, Minsk, 220076 Belarus
e-mail: troyan@ifttp.bas-net.by

Received January 8, 2002

Abstract—The magnetic and elastic properties of the $Bi_{1-x}Ca_xMnO_3$ manganites are studied. The phase transformations revealed are ferromagnet–spin glass ($x \geq 0.15$) and spin glass–charge-ordered antiferromagnet ($x \geq 0.25$). The ferromagnetic state is characterized by ordering of the Mn^{3+} $d_{x^2-y^2}$ orbitals. It is suggested that the spin glass state originates from local static Jahn–Teller distortions. The antiferromagnetic charge-ordered and the spin-glass disordered phases coexist in samples with $0.25 < x < 0.32$, which may be due to the charge order–disorder phase transformation being martensitic in character. The magnetic phase diagram is constructed. *© 2002 MAIK “Nauka/Interperiodica”.*

1. INTRODUCTION

Manganites of the type $Ln_{1-x}A_xMnO_3$ (with Ln standing for a lanthanide and A, for an alkaline-earth element) exhibit a clearly pronounced relation between their electrical and magnetic properties. Some compounds of this class are charge- and orbitally ordered, which makes them convenient subjects for investigating the interaction between the orbital, charge, and spin types of states. The bismuth manganite is known to differ strongly in its magnetic properties from rare-earth-based manganites [1–7]. Rare-earth manganites are antiferromagnets with an orthorhombically distorted unit cell [8]. The bismuth manganite is a ferromagnet with a Curie temperature of 105 K. The unit cell has triclinic symmetry [1, 2]. Despite differences in the magnetic properties and crystal structure, the bismuth manganite, like the rare-earth manganites, is a dielectric. It was conjectured that this behavior is due to a specific type of orbital ordering, which is different from the orbital ordering in rare-earth manganites [4]. Recent structural studies support this conjecture [9].

Another very interesting property of strontium-doped bismuth manganite is the very high charge-ordering temperature (T_{CO}), about 550 K, which was found for $Bi_{0.5}Sr_{0.5}(Mn^{3+}_{0.5}Mn^{4+}_{0.5})O_3$ [10, 11]. The characteristic temperature for rare-earth manganites of the type $Ln_{0.5}A_{0.5}MnO_3$ lies in the interval 180–250 K [12]. While the charge-ordering temperature for the $Bi_{0.5}Ca_{0.5}MnO_3$ composition is lower than that for the strontium series, it is still fairly high (T_{CO} = 325 K) [13]. These differences are apparently due to the Bi^{3+} ions participating more actively in the formation of covalent chemical bonding compared to rare-earth ions. It should be pointed out that bismuth manganite can be obtained only at high pressures. Therefore, preparation of high-quality samples is a complicated problem. $Bi_{1-x}Ca_xMnO_3$-type compositions with a Ca content above 70% have been studied fairly well due to the possibility of single-crystal growth [14]. The antiferromagnetic phase of the G type ($x = 1$) was shown to transfer to the C-type antiferromagnetic one ($x = 0.85$) through an intermediate inhomogeneous ferromagnetic state [15, 16]. Rare-earth manganites with $x > 0.7$ exhibit practically the same behavior [17]. The bismuth manganites reveal specific features at lower calcium contents. It is well known that with increasing calcium concentration, manganites of the type $La_{1-x}Ca_xMnO_3$ undergo a sequence of transitions: from an orbitally ordered antiferromagnet to a ferromagnet and then to a charge-ordered antiferromagnet, whereas in bismuth manganites, the ferromagnetic state transfers to antiferromagnetic as calcium ions are substituted by bismuth. The purpose of this study was to establish the mechanism underlying the concentration-driven ferromagnet–antiferromagnet and charge disorder–order phase transformations in the $Bi_{1-x}Ca_xMnO_3$ system.

2. EXPERIMENT

$Bi_{1-x}Ca_xMnO_3$ compositions with $x \leq 0.15$ were fabricated at a high pressure (P = 4 GPa, T = 800°C) from the oxides Bi_2O_3, MnO_2, Mn_2O_3, and $Ca(OH)_2$ mixed in stoichiometric ratios. The compositions with $x \geq 0.2$ were obtained by solid-phase reactions in air. As the calcium content was increased, the temperature of synthesis in air was raised from T = 900°C ($x = 0.25$) to 1150°C ($x = 0.6$). The samples were cooled slowly in a furnace (100°C/h).

X-ray structural analysis, which was carried out on a DRON-3 diffractometer with Cr K_α radiation, showed all the compositions to be single-phase perovskites. The magnetic measurements were performed on a Foner magnetometer. The elastic properties were stud-

1063-7834/02/4412-2266$22.00 © 2002 MAIK “Nauka/Interperiodica”

ied by measuring the temperature dependence of the resonance frequency $\nu^2(T)$ of mechanical vibrations of the sample. The resonance frequency squared is known to vary in proportion to Young's modulus. The temperature variation rate was 2–3°C/min. The studies were made on cylinder-shaped samples 50-mm long and 6 mm in diameter. The electrical conductivity was measured using the standard four-probe method (with ultrasonically deposited indium contacts).

3. DISCUSSION OF RESULTS

X-ray characterization showed the $Bi_{1-x}Ca_xMnO_3$ samples to have monoclinic symmetry in the interval $0 \le x \le 0.6$. The unit cell volume decreased gradually with increasing calcium content because of part of the trivalent manganese ions being transferred to quadrivalent manganese, which has a substantially smaller ionic radius. The $BiMnO_3$ compound obtained by us has a Curie temperature of 104 K and a magnetic moment, as derived from field dependences of magnetization, of about 3.3 μ_B/Mn^{3+}, which is in accord with literature data. Substitutions of Bi^{3+} by Ca^{2+} ions to a small extent weaken the ferromagnetic exchange interactions strongly and stabilize the antiferromagnetic part of exchange interactions. This behavior stands in sharp contrast with the properties of the rare-earth manganites $Ln_{1-x}Ca_xMnO_3$ (Ln = La, Pr, Nd, Sm, Eu), where replacement of a small part of the Ln ions by ions of calcium (10%) stabilizes the ferromagnetic state [18]. The $Bi_{0.9}Ca_{0.1}MnO_3$ composition has a Curie temperature of 70 K and a magnetic moment of about 2.0 μ_B/Mn^{3+}. The magnetization does not reach saturation in fields of up to 16 kOe; this feature is characteristic of nonuniform ferromagnets. The long-range ferromagnetic order in compositions with $0.15 \le x \le 0.25$ is apparently destroyed. This follows from the magnetization measured as a function of temperature, $M(T)$, and field, $M(H)$, after cooling in various regimes. Figure 1 plots the magnetization of a $Bi_{0.75}Ca_{0.25}MnO_3$ sample measured under warming in a field of 100 Oe following zero-field cooling (ZFC) or field cooling (FC). The ZFC curve passes through a maximum near T = 40 K. At this temperature, the FC magnetization exhibits a break. Above 40 K, the ZFC and FC curves almost coincide. Such a dependence is typical of spin glasses. This conjecture is supported by the fact that the magnetization in a field H = 15 kOe is far from saturation (Fig. 2). Another feature worthy of mentioning is the fairly large increase in the magnetic susceptibility at a temperature close to 90 K (Fig. 3). We consider this fact as supportive evidence of the formation of superparamagnetic clusters with a short-range magnetic order characteristic of $BiMnO_3$.

The magnetic properties of the x = 0.32 composition resemble in some aspects those of the x = 0.25 sample. The FC and ZFC magnetizations likewise diverge at 40 K, the temperature at which the ZFC curve has a maximum (Fig. 1). However, the magnetic susceptibility decreases strongly and the $M(H)$ dependence becomes closer to linear (Fig. 2). Another interesting observation is the appearance of a weakly pronounced anomaly in magnetization near the Néel temperature T_N = 160 K (Fig. 3). In the x = 0.4 sample, this anomaly transforms to a distinct maximum, which shifts gradually toward lower temperatures with increasing calcium

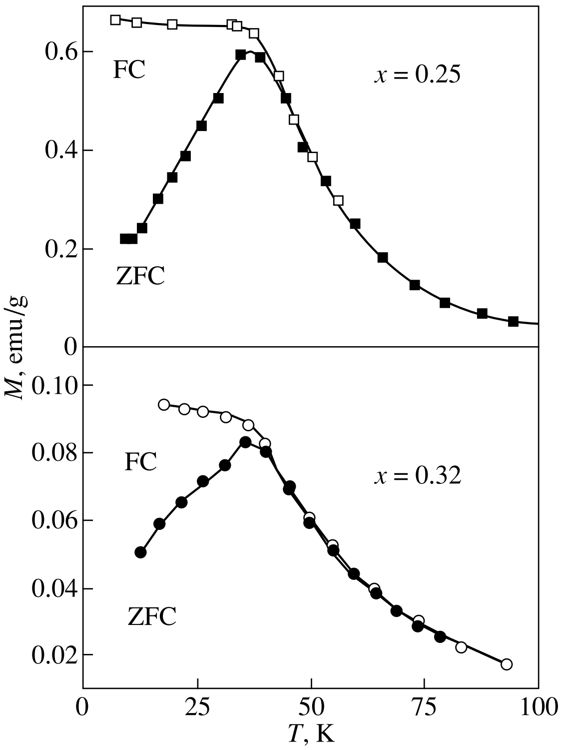

Fig. 1. ZFC and FC magnetizations plotted as a function of temperature for the x = 0.25 and 0.32 compositions.

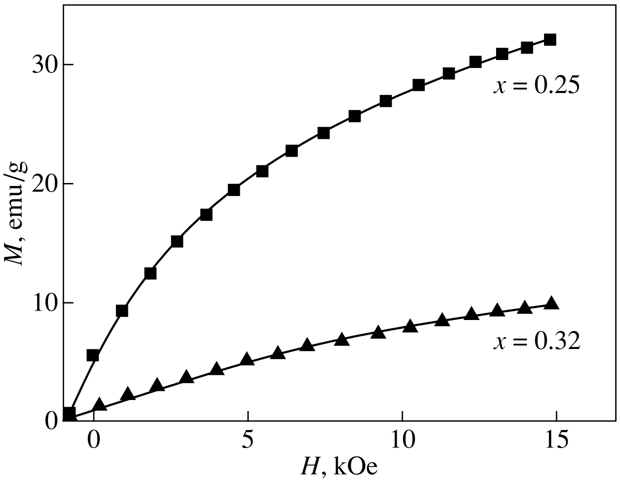

Fig. 2. Field dependences of magnetization for the x = 0.25 and 0.32 compositions measured at T = 5 K.

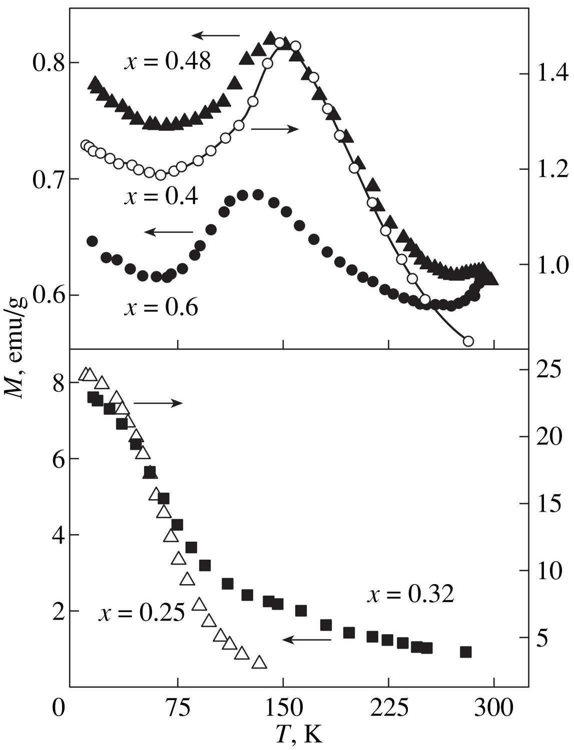

Fig. 3. Temperature dependence of magnetization obtained for the $x = 0.25$, 0.32, 0.4, 0.48, and 0.6 compositions in a field $H = 10$ kOe.

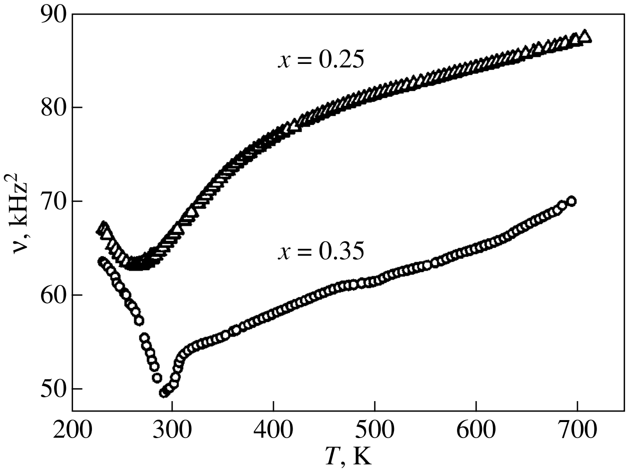

Fig. 4. Temperature dependence of squared resonance frequency for the $x = 0.25$ and 0.32 compositions.

content. It appears natural to relate this maximum to the antiferromagnetic ordering temperature. It should be pointed out, however, that the anomalous behavior of magnetization caused by antiferromagnetic ordering is much less pronounced in the $Ln_{1-x}Ca_xMnO_3$ rare-earth manganites [19]. This is apparently due to the magnetic ordering in bismuth and rare-earth manganites occurring in different conditions. In samples with $x = 0.48$ and 0.6, the magnetic susceptibility again begins to grow as one approaches room temperature, which indicates the onset of another phase transformation slightly above room temperature.

Additional information was gained from a study of the elastic properties (Fig. 4). For all samples with concentrations in the interval $0.25 \leq x \leq 0.6$, the $\nu^2(T)$ curve exhibited a minimum in the Young modulus near which the damping increased strongly. This anomalous behavior can be associated with the onset of a structural phase transformation. The temperature of this phase transformation increased smoothly with increasing calcium content from $T_{CO} = 267$ K ($x = 0.25$) to 325 K ($x = 0.6$). After this, the temperature at which the Young modulus reached a minimum decreased rapidly.

The temperature dependences of electrical resistivity indicated the conduction to have a semiconducting character. While the electrical conductivity revealed a jump near the temperatures of the Young modulus minimum for compositions $0.48 \leq x \leq 0.6$, the conduction in the high-temperature phase retained a semiconducting character.

It is well known that substitution of chromium for manganese in charge-ordered manganites can bring about a breakdown of charge ordering and a transition from the antiferromagnetic to ferromagnetic state [20]. Therefore, we turned to a study of the $Bi_{0.5}Ca_{0.5}(Mn_{1-y}Cr_y)O_3$ system. However, x-ray diffractograms of the samples with $y > 0.05$ revealed additional lines originating from impurity phases. One may thus conclude that, in contrast to the rare-earth manganites, the bismuth-based compounds do not form solid solutions of the type of $Bi_{0.5}Ca_{0.5}(Mn_{1-x}Cr_x)O_3$.

Figure 5 presents a magnetic phase diagram of the $Bi_{1-x}Ca_xMnO_3$ manganites based on the above studies. As the calcium content in the $Bi_{1-x}Ca_xMnO_3$ system increases, the latter passes through three different magnetic states, namely, ferromagnetic ($x \leq 0.1$), spin-glass ($0.15 \leq x \leq 0.25$), and antiferromagnetic ($x > 0.25$). In the case of antiferromagnetic compositions, the magnetic-ordering and structural-transformation temperatures vary only weakly within the concentration interval from $x = 0.25$ to 0.6. The ferromagnetic ordering in $BiMnO_3$ is most likely due to cooperative ordering of the $d_{x^2-y^2}$ orbitals [4, 9]. With orbital ordering of this type, according to the Goodenough–Kanamori rules, ferromagnetic ordering becomes more energetically favorable than antiferromagnetic ordering. We may recall that rare-earth manganites exhibit orbital ordering of the d_{z^2} type, which stabilizes the *A*-type antiferromagnetic structure [21]. Orbital disorder in $BiMnO_3$ sets in, apparently, at a fairly high temperature, near 760 K. It is at this temperature that liberation of the latent heat of transformation was observed to occur [7].

Replacement of bismuth ions by calcium results in the formation of quadrivalent manganese ions, which should be accompanied by destruction of orbital ordering due to the appearance of non-Jahn–Teller Mn^{4+} ions in the lattice. However, according to Goodenough [21], the orbitally disordered phase in manganites should be ferromagnetic, whereas we observed a state of the spin-glass type. A direct transition from the antiferromagnetic to the spin-glass phase without passing through the ferromagnetic state was observed to occur in the rare-earth manganites $Sm_{1-x}Ba_xMnO_3$ and $Y_{1-x}Ca_xMnO_3$ ($x \sim 0.12$) [22, 23]. It should be pointed out that at approximately this concentration of rare-earth ions, the ferromagnetic–spin glass transition takes place in $Bi_{1-x}Ca_xMnO_3$.

There is more than one opinion on the nature of exchange interactions in manganites [4, 21]. The antiferromagnetic state certainly forms through oxygen-mediated superexchange interactions of the type Mn–O–Mn. Most researchers believe that the ferromagnetic state in manganites is created through double exchange, i.e., via direct carrier transfer between various lattice sites. In order for such an exchange mechanism to operate, manganese ions in different valence states must be present and the electrical conductivity must be high. The presence of manganese ions of different valencies is not a sufficient condition for high electrical conductivity; indeed, the 3*d* orbitals of manganese and the 2*p* orbitals of oxygen should also overlap strongly. It is believed that this parameter is controlled by the Mn–O–Mn bond angle [4, 21]. The larger the lanthanide ion, the larger should be the Mn–O–Mn angle, the wider the 3*d* band, and, accordingly, the higher the magnetic ordering temperature and the electrical conductivity. It was observed that the magnetic state of the manganites also depends on the difference between the ionic radii of the rare-earth and the lanthanide ions. A large difference between the radii lowers, as a rule, the magnetic ordering temperature as a result of competition between various exchange interactions characterized by a large difference in the Mn–O–Mn angles. This is why the spin-glass state sets in in the $Sm_{1-x}Ba_xMnO_3$ system, wherein the average radius of the Sm and Ba ions is far larger than that between the Y and Ca cations in the $Y_{1-x}Ca_xMnO_3$ system [22, 23]. However, in all rare-earth manganites, the Mn^{3+}–O–Mn^{4+} exchange coupling in the orbitally disordered phase is apparently ferromagnetic. The Mn–O–Mn angles in bismuth-based manganites are fairly large, which is supported by structural studies [9] and the quite high Curie temperature of $BiMnO_3$. Hence, in the case of an orbitally disordered phase, one can expect the ferromagnetic part of exchange interactions to be dominant, which is at odds with experiment. Therefore, we believe that, in contrast to the rare-earth manganites, no orbitally disordered phase forms in the $BiMnO_3$ system in the concentration interval $0.1 \le x \le 0.3$. The spin-glass state forms in the $Bi_{1-x}Ca_xMnO_3$ system most likely as a result of competition between ferromagnetic interactions in $BiMnO_3$-type clusters and antiferromagnetic coupling in clusters in which the Mn^{3+} orbitals are frozen in random orientations. As the Ca^{2+} concentration increases, a new type of antiferromagnetic clusters, apparently due to charge ordering, appears. The existence in $Bi_{0.75}Ca_{0.25}MnO_3$ of large clusters, charge-ordered in a similar way to those in $Bi_{0.5}Ca_{0.5}MnO_3$, is suggested in studies of its elastic properties (Fig. 5). Despite the presence of the spin-glass-type ground state, there is a certain fraction of states characterized by short-range order of the type of a charge-ordered phase, which is indicated by the fact that the Young modulus minima for the $x = 0.25$ and 0.35 compositions are close in temperature. We believe that the extremely high stability of the orbitally and charge-ordered states in bismuth-based manganites derives from the strongly anisotropic character of the Bi–O covalent bonding.

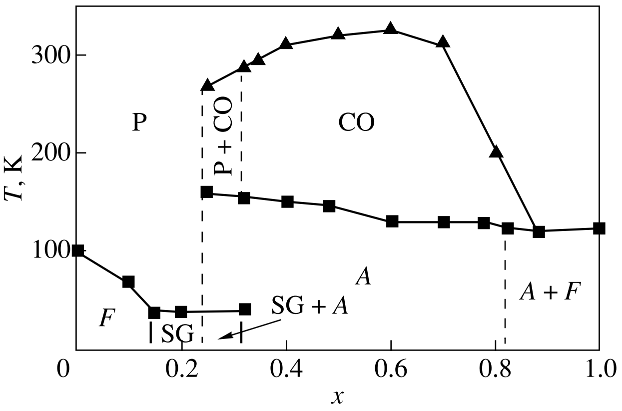

Fig. 5. Magnetic phase diagram of the $Bi_{1-x}Ca_xMnO_3$ manganites: phase *F* is ferromagnetic, P is paramagnetic, CO is charge-ordered, *A* is antiferromagnetic, and SG is the spin glass.

Another point worthy of mentioning is the disagreement between the results of our studies of the elastic properties and the structural measurements reported in [24]. According to [24], $Bi_{1-x}Ca_xMnO_3$ compounds with concentrations $0.2 \le x \le 0.4$ undergo a structural phase transformation with a change in symmetry above room temperature. We observed, however, only the low-temperature phase transformation, which is undoubtedly associated with the formation of a charge-ordered phase.

In conclusion, we consider the nature of inhomogeneous states in manganites close to concentration-driven phase transformations. There are two views on this problem, namely, that the inhomogeneous magnetic states form through electron phase separation [25] or as a result of chemical inhomogeneities. In the former case, clusters of the ferromagnetic phase must be very small because this type of phase separation is associated with an increase in the energy of electrostatic repulsion between charge carriers of like sign.

Electron microscopy and neutron diffraction studies revealed the coexistence of phases with characteristic sizes over 1000 Å [26]. Spectroscopic measurements indicate a high chemical homogeneity of the compositions [27]. We believe that inhomogeneous phase states that arise near boundaries of the concentration-driven phase transformations may actually be a consequence of the martensitic nature of the phase transformations. If this is the case, then both phases should differ in chemical composition and carrier concentration only weakly. This conjecture is corroborated by experiments indicating the orbital and charge ordering in manganites to be martensitic phase transformations [27, 28]. To each type of orbital and charge order corresponds a specific magnetic structure [4, 21].

ACKNOWLEDGMENTS

This study was supported by the Belarussin Foundation for Basic Research, project no. F99-261.

REFERENCES

1. Yu. Ya. Tomashpol'skiĭ, E. V. Zubova, K. P. Burdina, and Yu. N. Venevtsev, Izv. Akad. Nauk SSSR, Neorg. Mater. **3** (11), 2132 (1967).
2. F. Sugawara, S. Iida, and Y. Syono, J. Phys. Soc. Jpn. **20**, 1529 (1965).
3. V. A. Bokov, N. A. Myl'nikova, S. A. Kizhaev, *et al.*, Fiz. Tverd. Tela (Leningrad) **7** (12), 3695 (1965) [Sov. Phys. Solid State **7**, 2993 (1965)].
4. I. O. Troyanchuk, N. V. Kasper, O. S. Mantytskaya, and S. P. Pastushonok, Zh. Éksp. Teor. Fiz. **105** (2), 239 (1994) [JETP **78**, 212 (1994)].
5. I. O. Troyanchuk, N. V. Samsonenko, and E. F. Shapovalova, J. Phys.: Condens. Matter **8**, 11205 (1996).
6. I. O. Troyanchuk and V. N. Derkachenko, Fiz. Tverd. Tela (St. Petersburg) **32** (8), 2474 (1990) [Sov. Phys. Solid State **32**, 1436 (1990)].
7. H. Chiba, T. Atou, and Y. Syono, J. Solid State Chem. **132**, 139 (1997).
8. S. Quezel-Ambrunaz, Bull. Soc. Fr. Mineral. Crystallogr. **91**, 339 (1968).
9. T. Atou, H. Chiba, K. Ohoyama, *et al.*, J. Solid State Chem. **145** (2), 639 (1999).
10. C. Frontera, J. L. García-Muñoz, A. Llobet, *et al.*, J. Phys.: Condens. Matter **13**, 1071 (2001).
11. J. L. García-Muñoz, C. Frontera, M. A. G. Aramda, *et al.*, Phys. Rev. B **63**, 64415 (2001).
12. H. Kuwahara, Y. Tomioka, A. Asamitsu, *et al.*, Science **270**, 961 (1995).
13. H. Woo, T. A. Tyson, M. Croft, *et al.*, Phys. Rev. B **63**, 134412 (2001).
14. Y. Murakami and D. Shindo, Phys. Rev. B **55** (22), 15043 (1997).
15. P. N. Santhosh, J. Goldberger, P. M. Woodward, *et al.*, Phys. Rev. B **62** (22), 14928 (2000).
16. H. Chiba, M. Kikuchi, K. Kusaba, *et al.*, Solid State Commun. **99** (7), 499 (1996).
17. J. J. Neumeier and J. L. Cohn, Phys. Rev. B **61** (21), 14319 (2000).
18. I. O. Troyanchuk, N. V. Samsonenko, H. Szymczak, and A. Nabialek, J. Solid State Chem. **131**, 144 (1997).
19. Y. Tokura and Y. Tomioka, J. Magn. Magn. Mater. **200**, 1 (1999).
20. B. Raveau, A. Maignan, and C. Martin, J. Solid State Chem. **130**, 162 (1997).
21. J. B. Goodenough, A. Wold, and R. J. Arnott, Phys. Rev. **124**, 373 (1961).
22. I. O. Troyanchuk, D. D. Khalyavin, S. V. Trukhanov, and H. Szymczak, J. Phys.: Condens. Matter **11**, 8707 (1999).
23. R. Mathieu, P. Nordblad, D. N. H. Nam, *et al.*, Phys. Rev. B **63**, 174405 (2001).
24. V. A. Bokov, N. A. Grigoryan, and M. E. Bryzhina, Phys. Status Solidi **20**, 745 (1967).
25. É. L. Nagaev, Usp. Fiz. Nauk **166**, 833 (1996) [Phys. Usp. **39**, 781 (1996)].
26. C. Martin, M. Maignan, M. Hervieu, and B. Raveau, J. Magn. Magn. Mater. **205**, 184 (1999).
27. V. Podzorov, B. G. Kim, V. Kiryukhin, *et al.*, Phys. Rev. B **64**, 140406 (2001).
28. I. O. Troyanchuk, A. I. Akimov, L. A. Bliznjuk, and N. V. Kasper, J. Alloys Compd. **228**, 83 (1995).

Translated by G. Skrebtsov

Physics of the Solid State, Vol. 44, No. 12, 2002, pp. 2271–2275. Translated from Fizika Tverdogo Tela, Vol. 44, No. 12, 2002, pp. 2169–2173.
Original Russian Text Copyright © 2002 by Dunaevskiĭ, Deriglazov.

MAGNETISM AND FERROELECTRICITY

Effect of Orbital Degeneracy on the Magnetic Phases of Manganites in the Electron Doping Region

S. M. Dunaevskiĭ and V. V. Deriglazov
Konstantinov St. Petersburg Nuclear Physics Institute, Russian Academy of Sciences,
Gatchina, Leningrad oblast, 188350 Russia
e-mail: dunaevsk@mail.pnpi.spb.ru

Received January 11, 2002

Abstract—The carrier electronic spectrum $E(\mathbf{k})$ calculated with inclusion of orbital degeneracy of the manganese e_g band for the main types (A, G, and C) of antiferromagnetic ordering in La$_{1-y}$Ca$_y$MnO$_3$ was employed to derive the total energies of various magnetic configurations for the electron doping region $y > 0.5$. To find the magnetic configuration with the minimum total energy, this energy was minimized with respect to the angle between the spins of Mn^{4+} ions belonging to two different magnetic sublattices. The manganite phase diagrams obtained in this way for $T = 0$ K depend on the Heisenberg interatomic exchange parameter J_{AF} and the intraatomic Hund exchange J_{H} and fit correctly to the available experimental data. The calculations show that if the e_g-level splitting is taken into account, there is no magnetic-sublattice canting for equilibrium A and C phases in the region of realistic values of the parameters $0.012 < J_{\mathrm{AF}}/t < 0.02$ and $J_{\mathrm{H}}/t = 1.7$. Transition to the ferromagnetic state through the double-exchange mechanism is energetically favorable only for the G phase with increasing electron concentration. However, already for $x \le 0.1$, the collinear phase C becomes dominant and this transition does not occur. *© 2002 MAIK “Nauka/Interperiodica”.*

1. INTRODUCTION

A problem in the physics of the La$_{1-y}$Ca$_y$MnO$_3$ manganites (y = 0–1) that is still awaiting solution is the observed asymmetry of their phase diagrams relative to the value $y = 0.5$ [1, 2], as its nature remains unclear. It was pointed out in [3] that one of the reasons for the asymmetry in the properties is the difference in the $E(\mathbf{k})$ carrier spectra between the A, G, and C antiferromagnetic phases, which arises when the orbital degeneracy of the e_g level is taken into account in the double-exchange model. Indeed, the band spectrum of holes near the valence band top of LaMnO$_3$ ($y = 0$), which is a compound with layered antiferromagnetic A structure, differs very strongly from the electronic spectrum in CaMnO$_3$ ($y = 1$), which is a G-type antiferromagnet; this is due to the different types of orbital ordering in these compounds.

We will show that taking into account orbital degeneracy leads not only to a difference in the carrier spectrum $E(\mathbf{k})$ between different magnetic phases but also affects the conditions favoring the formation of the collinear or canted (A, G, C, and F) magnetic structures corresponding to the minimum of total energy. To find the total energy of a magnetic structure, one needs to know the corresponding electronic spectrum $E(\mathbf{k})$ of carriers (electrons or holes) in manganites. In most of the recent studies [4–7], the energies of the A, G, and C antiferromagnetic phases were calculated using the $E(\mathbf{k})$ spectrum derived for the ferromagnetic (F) type of magnetic ordering [4]. To calculate the spectra of all the antiferromagnetic phases, one has to take into account the increase in the number of inequivalent atoms in a unit cell and consider matrices of an order twice as large as that of matrices employed with ferromagnets [3].

2. METHOD OF CALCULATION

This study deals with a calculation of equilibrium magnetic phases of electron-doped manganites (large y) at $T = 0$ K based on $E(\mathbf{k})$ dispersion relations obtained by one of the present authors (see [3]) for the main types of antiferromagnetic ordering (A, C, G) in manganites and takes into account the orbital degeneracy of the manganese e_g level. By choosing the region of large Ca concentrations, y = 0.6–1 (small number of electrons in the conduction band), one can disregard, as a first approximation, the Coulomb interactions.

We make use of an effective manganite Hamiltonian consisting of the double-exchange Hamiltonian [8], which takes into account strong intraatomic Hund interaction and the orbital degeneracy of the manganese e_g level, and the t_{2g}-electron Heisenberg Hamiltonian, which describes the interaction of local magnetic moments $\mathbf{S}_i$ with one another:

$$H = H_{DE} + H_H,$$

$$H_{DE} = \sum_{i\alpha\sigma} \varepsilon_{i\alpha\sigma} d^+_{i\alpha\sigma} d_{i\alpha\sigma} + \sum_{ij\alpha\beta\sigma'\sigma} t^{\sigma\sigma'}_{ij\alpha\beta}\left(\frac{\theta_{ij}}{2}\right) d^+_{i\alpha\sigma} d_{j\beta\sigma'},$$

$$H_H = \sum J_{ij}\mathbf{S}_i\mathbf{S}_j, \qquad (1)$$

$$t^{\sigma\sigma'}_{ij\alpha\beta}\left(\frac{\theta_{ij}}{2}\right) = \begin{cases} t_{ij\alpha\beta}\cos\left(\frac{\theta_{ij}}{2}\right) & (\sigma = \sigma') \\ \pm t_{ij\alpha\beta}\sin\left(\frac{\theta_{ij}}{2}\right) & (\sigma \neq \sigma'). \end{cases}$$

The indices α and β in Eq. (1) label degenerate atomic e_g orbitals $|1\rangle = |z^2\rangle$ and $|2\rangle = |x^2 - y^2\rangle$; indices *i*, *j* label the atoms; $\varepsilon_{i\alpha\uparrow} = \varepsilon_{d\alpha} - J_{\mathrm{H}}S$ and $\varepsilon_{i\alpha\downarrow} = \varepsilon_{d\alpha} + J_{\mathrm{H}}(S + 1)$, with $\varepsilon_{d\alpha}$ being the energy of the unperturbed α-type *d* level of the Mn^{4+} ion and J_{H} being the intraatomic Hund integral (its value for Mn^{3+} was found to be 0.25 eV [3]); $d^{+}_{i\sigma}(d_{i\sigma})$ are the creation (annihilation) operators for an e_g electron at site *i*; σ is the spin index; J_{ij} are the exchange integrals in the Heisenberg model of localized t_{2g} electrons; and $t_{ij\alpha\beta}$ are the corresponding transfer integrals between manganese ions:

$$t_{ij\alpha\beta} \equiv t^{\alpha\beta}_{ij} = \begin{cases} -t\begin{pmatrix} \frac{1}{4} & \frac{-\sqrt{3}}{4} \\ \frac{-\sqrt{3}}{4} & \frac{3}{4} \end{pmatrix} & \text{along the } x \text{ axis} \\ -t\begin{pmatrix} \frac{1}{4} & \frac{\sqrt{3}}{4} \\ \frac{\sqrt{3}}{4} & \frac{3}{4} \end{pmatrix} & \text{along the } y \text{ axis} \\ -t\begin{pmatrix} 1 & 0 \\ 0 & 0 \end{pmatrix} & \text{along the } z \text{ axis,} \end{cases} \qquad (2)$$

where $\alpha, \beta = |1\rangle = |z^2\rangle, |2\rangle = |x^2 - y^2\rangle$, $t = \frac{V^2_{pd\sigma}}{E_d - E_p}$, and $V_{pd\sigma}$ is the transfer integral (Koster–Slater parameter) between the *d* orbital of manganese and *p* orbital of oxygen.

In the double-exchange model, the transfer integral $t_{ij\alpha\beta}$ depends on half the angle $(\theta_{ij}/2)$ between local magnetic moments of the nearest neighbor Mn ions and the value of *t* for the manganites lies in the interval 0.15–0.3 eV [3]. In the *G* phase, $\theta_{ij} = \pi$ for the nearest neighbors. In the *C* phase, the Mn ion spins form ferromagnetic chains perpendicular to the *xy* plane. In this plane, $\theta_{ij} = \theta_{xy} = \pi$, and in a chain, we have $\theta_{ij} = \theta_z = 0$. In the *A* phase, the neighboring ferromagnetic planes in which $\theta_{ij} = \theta_{xy} = 0$ are antiferromagnetically ordered with respect to one another: i.e., $\theta_{ij} = \theta_z = \pi$ if the atoms labeled *i* and *j* belong to neighboring planes. In the *F* phase, we always have $\theta_{ij} = 0$. For all antiferromagnetic phases, only one angle θ_{ij} is other than zero.

One can also use Hamiltonian (1) to consider the effect of e_g level splitting on the electronic part of the total energy of the system. It is known that an experimental study of the $(\mathrm{La{-}Nd})_{1-y}\mathrm{Sr}_y\mathrm{MnO}_3$ compound with *y* = 0.52–0.62 revealed an antiferromagnetic *A* phase with a predominant occupation of orbitals of the $|2\rangle = |x^2 - y^2\rangle$ type [9]. There are also certain theoretical grounds for maintaining that in the *A* phase, we have $\varepsilon_{d1} - \varepsilon_{d2} > 0$ (except the case of $y = 0$) [7, 10]. For the *C* phase, the splitting has the opposite sign (see [10]), and for the *G* and *F* phases, the e_g level is not split at all. Therefore, we considered various cases of splitting of the e_g level under electron doping of CaMnO_3. In the first case, the e_g level splitting was zero for all the phases, and in the second, the splitting for the *A* and *C* phases was chosen to be proportional to $x = 1 - y$ in such a way as to obtain $|\varepsilon_{d1} - \varepsilon_{d2}| = 0.3$–0.5 eV [11] for the *A* phase of LaMnO_3 in the limiting case $y = 0$. For the *G* and *F* phases, the e_g level in the second case was again unsplit.

As follows from the form of the Hamiltonian, in the presence of free carriers, there is always competition in the system between the ferromagnetic and antiferromagnetic types of ordering. The onset of ferromagnetism is favored by the double-exchange kinetic energy, whereas the antiferromagnetic ordering is taken into account by the Heisenberg part of the Hamiltonian. In the simplest case (i.e., without the inclusion of orbital degeneracy), there exist at least two possibilities of reaching a compromise between these trends. One of them is the de Gennes canted antiferromagnetism [12], where the angle θ_{ij} between the spins of the nearest neighbor manganese ions is other than π. The other possibility consists in the onset of electron phase separation, with the carriers (electrons or holes) distributed nonuniformly in space to form enriched ferromagnetic regions embedded in an antiferromagnetic background [13].

In the case of orbital degeneracy and in the $y \longrightarrow 1$ limit, it can easily be shown analytically (using the spectrum near the conduction-band bottom, $\mathbf{k} = (0, 0, 0)$, obtained in [3]) that, in accordance with [12], the trend to magnetic sublattice canting is fully retained only for the *G* phase, whereas for the *A* and *C* phases, this trend is strongly suppressed because of the heavily anisotropic character of the transfer integral and of the type of electronic states near the conduction-band bottom. To verify this point, we carried out numerical calculation of the total energies (in units of *t*) per manganese atom for all collinear and canted magnetic configurations. The calculations were performed for various electron concentrations $x = 1 - y$ and sets of the parameters J_{H}/t and J_{AF}/t, where J_{AF} is the exchange coupling parameter for the *G* phase, which exists in the system under study with no doping, CaMnO_3 ($J_{\mathrm{AF}} = 1.5$ meV,

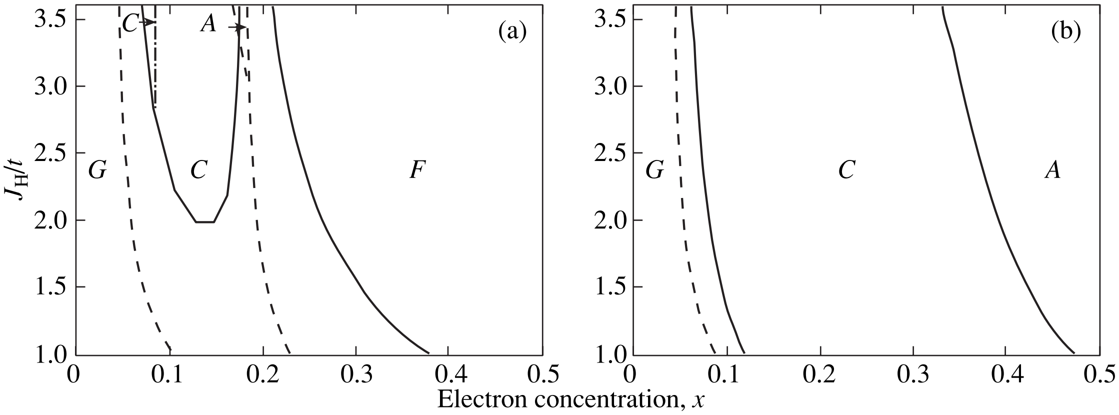

Fig. 1. Phase diagram of manganites in the electron concentration range x = 0–0.5 obtained by minimization of the total energies of antiferromagnetic configurations with respect to the angle θ within the formalism of Hamiltonian (1). Dashed lines show phase boundaries obtained without minimization of total energies with respect to the angle θ. (a) Splitting of the e_g level is not included. The phase diagram is constructed in the (x, J_H/t) coordinates for the exchange parameter of the Heisenberg model $J_{AF}/t = 0.15$. The equilibrium *A*, *C*, and *F* phases are uncanted. Only the equilibrium *G* and *C*' phases are canted. (b) Splitting of the e_g level is included. The calculated *G*–*C*–*A* phase alternation agrees with experiment throughout the J_H/t variation region.

T_N = 141 K). The results obtained do not cover the case of $x = 0.5$, because the magnetic *CE* phase related to the charge-ordering effect was not considered here. For all antiferromagnetic configurations, the total energies were minimized with respect to the corresponding angle θ, thus yielding the equilibrium magnetic configuration for each value of $x < 0.5$.

The energy per manganese atom in the *G* phase was calculated as

$$E_G\left(x, \frac{\theta}{2}\right) = 3J_{AF}S^2\cos\theta/t + \int\limits_{-\infty}^{\varepsilon_F}\varepsilon n_G\left(\varepsilon, \cos\frac{\theta}{2}\right)d\varepsilon, \quad (3)$$

where $S = 3/2$, ε_F is the Fermi level, $n_G(\varepsilon, \cos\theta/2)$ is the normalized *G*-phase density of states, and J_{AF} is the exchange parameter of the Heisenberg model for the nearest neighbors. The density of states was found by summing over the corresponding Brillouin zone of the $E(\mathbf{k}, \cos\theta/2)$ spectrum calculated using diagonalization of the *G*-phase Hamiltonian matrix, which is given in an explicit form in [3]. For all the other magnetic structures, the total energies were calculated in the same way. The first term in Eq. (3) was $J_{AF}S^2(2\cos\theta + 1)/t$ for the *G* phase, $J_{AF}S^2(\cos\theta + 2)/t$ for the *A* phase, and $3J_{AF}S^2\cos\theta/t$ for the *F* phase. Obviously enough, this formalism also allows calculation of orbital ordering in the magnetic structures under study. The problem effectively reduces to diagonalization of the same matrices from [3] but with a parameter $t_{ij\alpha\beta}(\Omega)$ depending on the angle Ω in the configuration space [14] with respect to which the total energy has to be minimized. The present study does not, however, cover this problem.

3. RESULTS AND DISCUSSION

In the absence of free electrons, the magnetic phases are arranged in order of increasing magnetic energy as *G*, *C*, *A*, and *F*. As x increases, competition between the kinetic and magnetic energies of the system brings about the realization of one of the possible magnetic states. Plotted in the (x, J_H/t) coordinates in Fig. 1a is the phase diagram of the $La_{1-y}Ca_yMnO_3$ system for x = 0–0.5 without the e_g level splitting and in Fig. 1b, with splitting for the value $J_{AF}/t = 0.015$ characteristic of $CaMnO_3$ at $t = 0.1$ eV. Figure 1a and 1b each present two phase diagrams. The dashed lines specify the phase boundaries obtained in the approximation of collinear magnetic sublattices, and the solid lines are the phase boundaries found by minimizing the total energy with respect to the angle θ. The splitting was assumed to be proportional to the electron concentration such that at $x = 1$, it is equal to the value typical of the Jahn–Teller splitting in $LaMnO_3$, namely, $\varepsilon_{d\alpha} = \pm1.5tx$ for the *A* phase and $\varepsilon_{d\alpha} = -(\pm1.5tx)$ for the *C* phase. The upper sign corresponded to the $|z^2\rangle$ orbital; the lower sign, to the $|x^2 - y^2\rangle$ orbital. Thus, the predominantly occupied orbital is $|x^2 - y^2\rangle$ in the *A* phase and $|z^2\rangle$ in the *C* phase. This suggestion is corroborated by an experimental observation of static tetragonal distortions of the cubic structure in the $Nd_{1-y}Sr_yMnO_3$ system (y = 0.5–0.75) and by the sign of these distortions being dependent on the type of antiferromagnetic ordering [15]. Obviously enough, such splitting does not lift the level degeneracy completely within the x variation interval studied. For the *G* and *F* phases, the e_g-level splitting was assumed to be zero ($\varepsilon_{d1(2)} = 0$). If the e_g-level splitting is neglected, the collinear phase *A* exists only within a narrow electron concentration region near $x = 0.18$ and for a very large value of the parameter J_H/t (Fig. 1a).

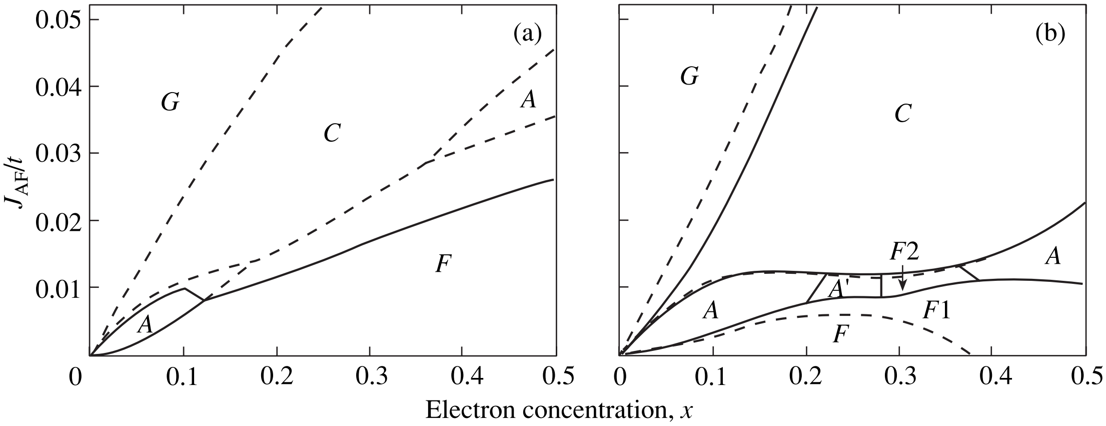

Fig. 2. Phase diagram of manganites plotted in the (x, J_{AF}/t) coordinates. The solid line separates the $F(A)$ and G phases and is found by minimizing the total energy with respect to the angle θ. Dashed lines specify the phase boundaries obtained without minimization of the total energies with respect to θ. (a) Splitting of the e_g level is not included, $J_H = 1.7t$. (b) Splitting of the e_g level is included, $J_H = 1.7t$. Within a narrow region $x = 0.21$–0.28, the canted A phase, denoted by A', is the equilibrium magnetic configuration. The ferromagnetic phase $F2$ forms from the split phase A, and the ferromagnetic phase $F1$ forms from the split phase C. Phases C and A are uncanted, and phase G is canted.

Canting of the magnetic sublattices changes the pattern of the phase diagram qualitatively. Phase A disappears, and the region of existence of the collinear phase C decreases noticeably. Near $x = 0.09$ and for $J_H/t > 2.9$, a canted C phase with a canting angle of 12° forms (identified in Fig. 1a by C'). The corresponding canting angles for the G structure are approximately proportional to x and reach 180° at the G–F boundary.

Taking the e_g-level splitting into account modifies the pattern of the phase diagram very strongly. The main change consists in the disappearance of the ferromagnetic region, which is usually not revealed in experiment. In its place, the energy is minimum for the collinear C phase if $x \cong 0.1$–0.4 and for the collinear A phase if $x \geq 0.4$. The corresponding canting angles for the G phase are approximately proportional to x and reach 50° at the G–C boundary. Thus, numerical calculations support the qualitative conclusion (made above) that the A and C phases are collinear phases in the region of their existence. Neutron scattering experiments made in the A phase of $Nd_{1-y}Sr_yMnO_3$ ($y > 0.52$) likewise do not reveal any deviations from collinearity [16]. The fact that the magnetic sublattices of the A and C phases are not canted also indicates that these phases do not show a tendency to electron phase separation.

Figure 2 displays phase diagrams of the system under study calculated for the cases illustrated in Fig. 1 and constructed in the (x, J_{AF}/t) coordinates for $J_H = 1.7t$ [3]. The solid line is the boundary between the $F(A)$ and G phases obtained by minimizing total energy with respect to the angle θ. The calculations show that the G–C–A-phase alternation, experimentally observed to occur with increasing x [15], is possible only within a fairly narrow interval $0.033 < J_{AF}/t < 0.043$ corresponding to very large J_{AF}. The canting of the sublattices only aggravates the situation, because now only the G, F, and A phases are left in the diagram, with the A phase being retained only for small values of x and J_{AF}/t. Above $J_{AF}/t = 0.025$, only the canted G phase exists. As before, the corresponding canting angles are approximately proportional to x and reach 180° at the G–F boundary. The phase diagram calculated for the case of e_g-level splitting (Fig. 2b) is of great interest. Taking splitting into account permits one to obtain the "correct" phase alternation within realistic values of the parameter $0.012 < J_{AF}/t < 0.02$ already in the collinear approximation. While inclusion of canting does bring about the appearance of a region of the noncollinear A' phase within the region of the A phase, the collinear A phase persists for $J_{AF}/t > 0.012$. Furthermore, minimization with respect to the angle θ makes the canted A phase as A' (denoted in Fig. 2) an equilibrium magnetic configuration within a narrow interval $x = 0.21$–0.28 and for small values $0.006 < J_{AF}/t < 0.01$. As x increases, this phase transforms into the ferromagnetic phase $F2$ created by the splitting of the A phase. A ferromagnetic $F1$ phase forming from the split C phase exists slightly below the $F2$ region. In these regions, the total energy of the unsplit ferromagnetic phase F turns out to be larger than that of $F1$ or $F2$. Within the realistic interval $0.012 < J_{AF}/t < 0.02$, the G–C–A magnetic-phase alternation and the position of the phase boundaries agree well with experiment [9, 15]. The canting of the magnetic sublattices does not change the qualitative pattern of the phase diagram while shifting the boundary between the G and C phases.

While the possibility of a partial lifting of e_g degeneracy for low electron doping levels has been admitted by some authors [5, 7], this possibility was not considered because of the low concentration of Mn^{3+} ions. Our calculations reveal a qualitative rearrangement of the phase diagrams when the e_g-level splitting is included, thus yielding the correct *G–C–A* phase alternation with increasing x for realistic values of the parameters J_H/t and J_{AF}/t.

Thus, the phase diagrams obtained by us with inclusion of the e_g-level splitting and of the noncollinearity of the magnetic sublattices fit well enough the available experimental data (alternation of the magnetic structures observed to occur with increasing x) for electron concentrations $x = 0–0.5$ and realistic values of the parameters J_H/t and J_{AF}/t. Interestingly, there is no canting for the equilibrium *A* and *C* phases. As the electron concentration increases, transition to the ferromagnetic state through the double-exchange mechanism becomes energetically favorable only for the *G* phase. However, already for $x \leq 0.1$, the collinear *C* phase becomes dominant and this transition is no longer observed. These observations corroborate the experimental data indicating the absence of electron phase separation in manganites with *n*-type conduction.

ACKNOWLEDGMENTS

This study was supported by the Russian Foundation for Basic Research, project nos. 00-62-16729 and 00-02-81205 Bel2000-a.

REFERENCES

1. S. Mori, C. H. Chen, and S. W. Cheong, Nature (London) **392**, 473 (1998).
2. R. Maezono, S. Ishihara, and N. Nagaosa, Phys. Rev. B **57**, R13993 (1998).
3. S. M. Dunaevskiĭ, Fiz. Tverd. Tela (St. Petersburg) **43** (12), 2166 (2001) [Phys. Solid State **43**, 2257 (2001)].
4. H. Shiba, R. Shina, and A. Takahashi, J. Phys. Soc. Jpn. **66**, 941 (1997).
5. J. van den Brink and D. Khomskii, Phys. Rev. Lett. **82**, 1016 (1999).
6. Liang-Jian Zou, Phys. Rev. B **63**, 155103 (2001).
7. G. Venketeswara Pai, Phys. Rev. B **63**, 064431 (2001).
8. P. W. Anderson and H. Hasegawa, Phys. Rev. **100**, 675 (1955).
9. T. Akimoto, Y. Maruyama, Y. Moritomo, *et al.*, Phys. Rev. B **57**, R5594 (1998).
10. R. Maezono, S. Ishihara, and N. Nagaosa, Phys. Rev. B **58**, 11583 (1998).
11. J. W. Liu, Z. Zeng, Q. Q. Zheng, and H. Q. Lin, Phys. Rev. B **60**, 12968 (1999).
12. P. G. de Gennes, Phys. Rev. **118**, 141 (1960).
13. E. L. Nagaev, Zh. Éksp. Teor. Fiz. **57**, 1274 (1969) [Sov. Phys. JETP **30**, 693 (1970)].
14. K. I. Kugel' and D. I. Khomskiĭ, Usp. Fiz. Nauk **136** (4), 628 (1982) [Sov. Phys. Usp. **25**, 231 (1982)].
15. R. Kajimoto, H. Yoshizawa, H. Kawano, *et al.*, Phys. Rev. B **60**, 9506 (1999).
16. H. Kawano, R. Kajimoto, H. Yoshizawa, *et al.*, Phys. Rev. Lett. **78**, 4253 (1997).

Translated by G. Skrebtsov

Physics of the Solid State, Vol. 44, No. 12, 2002, pp. 2276–2280. Translated from Fizika Tverdogo Tela, Vol. 44, No. 12, 2002, pp. 2174–2177.
Original Russian Text Copyright © 2002 by Kalmykov, Titov.

MAGNETISM AND FERROELECTRICITY

Nonlinear Response of Superparamagnetic Particles with Cubic Anisotropy to a Sudden Change in the Applied Strong Static Magnetic Field

Yu. P. Kalmykov* and S. V. Titov**
** Centre d'Etudes Fondamentales, Université de Perpignan, Perpignan Cedex, 66860 France*
e-mail: kalmykov@univ-perp.fr
*** Institute of Radio Engineering and Electronics, Russian Academy of Sciences,*
pl. Vvedenskogo 1, Fryazino, Moscow oblast, 141190 Russia
e-mail: svt245@ire216.msk.su

Received September 19, 2001; in final form, February 4, 2002

Abstract—The nonlinear response of superparamagnetic particles with cubic anisotropy to a sudden change in an applied strong static magnetic field is analyzed. The relaxation function spectrum and the relaxation time of the magnetization are calculated for typical values of the anisotropy and dissipation parameters. *© 2002 MAIK "Nauka/Interperiodica".*

1. Single-domain ferromagnetic particles are characterized by an anisotropic internal potential with several minima separated by barriers. If the particles are small (~10 nm in diameter), the barriers are relatively low. In this case, the magnetization vector $\mathbf{M}(t)$ can change its orientation by surmounting the barrier with the aid of thermal fluctuations. Thermal instability of the magnetization gives rise to superparamagnetism [1], because each particle behaves as a paramagnetic atom with a magnetic moment of ~10^4–10^5 Bohr magnetons. Since the magnetic dipole moment of a particle is large, the Zeeman energy can be comparable to the thermal energy kT even in a moderate external field $\mathbf{H}_0$. Therefore, when analyzing the magnetization relaxation in external ac fields, nonlinear effects should be taken into account [2–4]. Until recently, only the theory of the linear response of superparamagnetic particles in weak magnetic fields was relatively well developed. Due to its complexity, the theory of nonlinear response was significantly less developed; this partial development was achieved predominantly using perturbation methods (see, e.g., [5–8]). A certain advance in the study of nonlinear effects was made in [9–11]; in [9, 10], the kinetics of particles with uniaxial anisotropy in strong ac fields was considered, while in [11], the nonlinear response of such particles to a momentary change in an external strong static magnetic field was investigated. The objective of this paper is to extend the results obtained in [11] to the case of particles with cubic anisotropy, i.e., to investigate the magnetization kinetics in an external strong static magnetic field when this field is suddenly changed in both magnitude and direction.

2. Let the external static magnetic field applied to the system under study be suddenly changed from $\mathbf{H}_\mathrm{I}$ to $\mathbf{H}_\mathrm{II}$ at time $t = 0$. We consider the relaxation of the magnetization vector $\mathbf{M}(t)$ of a system of noninteracting superparamagnetic particles from equilibrium state I (in the field $\mathbf{H}_\mathrm{I}$), characterized by a distribution function W_I (at $t \le 0$), to equilibrium state II (in the field $\mathbf{H}_\mathrm{II}$) with distribution function W_II (at $t \longrightarrow \infty$). The dynamics of the projection M_r of the magnetization vector $\mathbf{M}(t)$ onto an arbitrary direction specified by a unit vector $\mathbf{r} = (\nu_X, \nu_Y, \nu_Z)$ is described by the normalized relaxation function

$$f(t) = \frac{\langle M_r\rangle(t) - \langle M_r\rangle_\mathrm{II}}{\langle M_r\rangle_\mathrm{I} - \langle M_r\rangle_\mathrm{II}}. \tag{1}$$

Angular brackets with indices I and II indicate the average with respect to the equilibrium distribution functions W_I and W_II, respectively, and angular brackets without any index indicate the average over realizations of the random variable $M_r(t)$. This problem is essentially nonlinear, because the amplitude of the change in the external magnetic field is assumed to be arbitrary.

The relaxation processes in a system of superparamagnetic particles, as a rule, are considered within the diffusion approximation of Brown [2]. For our problem, the nonlinear response of the system in the diffusion approximation can be found by solving the Fokker–Planck equation for the probability density function $W(\mathbf{M}, t)$ of the magnetization [2]:

$$\begin{gathered} 2\tau_N \frac{\partial}{\partial t} W \\ = \Delta W + \beta[\alpha^{-1}\mathbf{u}(\nabla V_\mathrm{II} \times \nabla W) + \nabla(W \nabla V_\mathrm{II})], \\ t > 0, \end{gathered} \tag{2}$$

with the initial condition $W(\mathbf{M}, 0) = W_{\mathrm{I}}$. Here, Δ and ∇ are the Laplacian and gradient operator, respectively, operating on the surface of a unit sphere; $\tau_N = \beta M_s(1 + \alpha^2)/2\gamma\alpha$ is the characteristic (diffusion) time; $\beta = v/kT$; v is the volume of a particle; M_s is the magnetization of the material of a particle; γ is the gyromagnetic ratio; $\alpha = \gamma\eta M_s$ and η are the dimensionless and dimensional dissipation coefficients, respectively, characterizing the intensity of thermal magnetization fluctuations; $\mathbf{u}$ is a unit vector along the magnetization vector $\mathbf{M}(t)$; and V_{II} is the free-energy density of a particle in state II, which has the following form for particles with cubic anisotropy [12]:

$$\beta V_{\mathrm{II}} = \sigma(\sin^4\theta\sin^2 2\varphi + \sin^2 2\theta) - \xi_{\mathrm{II}}\cos\theta. \qquad (3)$$

Here, θ and φ are the polar and azimuth angles, respectively; σ is the dimensionless anisotropy constant; and $\xi_{\mathrm{II}} = \beta M_s H_{\mathrm{II}}$ is a dimensionless field parameter. The Fokker–Planck equation (2) can be derived from the Gilbert equation [2] with a fluctuating field associated with thermal magnetization fluctuations of an individual particle (which, in turn, determine relaxation). The dynamics of the magnetization vector $\mathbf{M}(t)$ of a particle is similar to the inertialess Brownian rotation of a molecule in a liquid, which is described by an analogous Fokker–Planck equation (Smoluchowski equation), with the only difference that this equation does not contain the term proportional to $\sim\alpha^{-1}$ and responsible for precession of the magnetization vector (because the interaction of the electric field with the electric dipole moment of a molecule and the interaction of the magnetic field with the magnetization vector of a superparamagnetic particle are different in nature). A discussion of the range of applicability of the Gilbert and Fokker–Planck equations can be found, e.g., in [2, 13].

The Fokker–Planck equation (2) can be solved formally [14] by expanding the distribution function W in terms of the spherical harmonics $Y_{l,m}(\theta, \varphi)$ [15]. In this case, the problem reduces to solving an infinite set of recurrence equations for the averaged spherical harmonics (moments) [16, 17]. This set of equations can also be derived by averaging the Gilbert equation without recourse to the Fokker–Planck equation [16, 17]. In both cases, the final equation for the relaxation functions $c_{l,m}(t) = \langle Y_{l,m}\rangle(t) - \langle Y_{l,m}\rangle_{\mathrm{II}}$ has the form [11]

$$\frac{d}{dt}c_{l,m}(t) = \sum_{l'}\sum_{s} d_{l',m\pm s,l,m}c_{l',m\pm s}(t) \qquad (4)$$

with the initial conditions $c_{l,m}(0) = \langle Y_{l,m}\rangle_{\mathrm{I}} - \langle Y_{l,m}\rangle_{\mathrm{II}}$. The coefficients $d_{l',m',l,m}$ for the case of cubic anisotropy can be found, e.g., in [12, 18, 19].

The recurrence equation (4) for the nonlinear response has the same structure as in the case of a linear response [12]. Therefore, this equation can be solved using the (matrix) continued-fraction method [12]; namely, Eq. (4) is transformed into a vector recurrence equation with three terms:

$$\tau_N\frac{d}{dt}\mathbf{C}_n(t) = \mathbf{Q}_n^-\mathbf{C}_{n-1}(t) + \mathbf{Q}_n\mathbf{C}_n(t) + \mathbf{Q}_n^+\mathbf{C}_{n+1}(t), \qquad (5)$$
$$n = 1, 2, 3, \ldots,$$

where the matrices $\mathbf{Q}_n$, $\mathbf{Q}_n^+$, and $\mathbf{Q}_n^-$ are defined in [12] and the vectors

$$\mathbf{C}_n(t) = \begin{pmatrix} \mathbf{c}_{4n}(t) \\ \mathbf{c}_{4n-1}(t) \\ \mathbf{c}_{4n-2}(t) \\ \mathbf{c}_{4n-3}(t) \end{pmatrix}$$

(except $\mathbf{C}_0(t) = 0$) consist of four subvectors

$$\mathbf{c}_{4n-i}(t) = \begin{pmatrix} c_{4n-i,-4(n-1+\delta_{i0})}(t) \\ c_{4n-i,-4(n-2+\delta_{i0})}(t) \\ \vdots \\ c_{4n-i,4(n-1+\delta_{i0})}(t) \end{pmatrix}, \quad i \geq 1.$$

Following [20], we take the unilateral Fourier transform of Eq. (5) and express the solution to this equation in terms of matrix continued fractions:

$$\tilde{\mathbf{C}}_1(\omega) = \int_0^\infty \mathbf{C}_1(t)e^{-i\omega t}dt = \tau_N\Delta_1(\omega)$$
$$\times\left\{\mathbf{C}_1(0) + \sum_{n=2}^{\infty}\left(\prod_{k=2}^{n}Q_{k-1}^+\Delta_k(\omega)\right)\mathbf{C}_n(0)\right\}, \qquad (6)$$

where the matrix continued fraction $\Delta_n(\omega)$ is defined as

$$\Delta_n(\omega) = \cfrac{\mathbf{I}}{i\omega\tau_N\mathbf{I} - \mathbf{Q}_n - \mathbf{Q}_n^+\cfrac{\mathbf{I}}{i\omega\tau_N\mathbf{I} - \mathbf{Q}_{n+1} - \mathbf{Q}_{n+1}^+\cfrac{\mathbf{I}}{i\omega\tau_N\mathbf{I} - \mathbf{Q}_{n+2} - \ddots}\mathbf{Q}_{n+2}^-}\mathbf{Q}_{n+1}^-},$$

$$\tilde{f}(\omega) = \frac{\sqrt{2}\nu_Z c_{1,0}(\omega) + (\nu_X + i\nu_Y)\tilde{c}_{1,-1}(\omega) - (\nu_X - i\nu_Y)\tilde{c}_{1,1}(\omega)}{\sqrt{2}\nu_Z c_{1,0}(0) + (\nu_X + i\nu_Y)c_{1,-1}(0) - (\nu_X - i\nu_Y)c_{1,1}(0)}, \qquad (7)$$

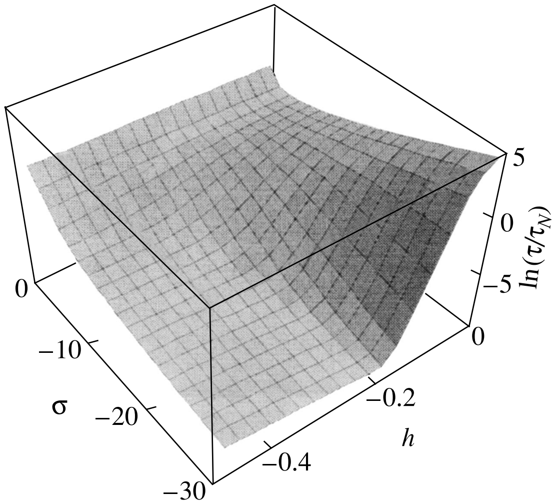

Fig. 1. Dependence of $\ln(\tau/\tau_N)$ on σ (for $\sigma < 0$) and on $h = h_{\mathrm{II}} = h_{\mathrm{I}}/2$ for the case where the external field is suddenly decreased in magnitude by a factor of two.

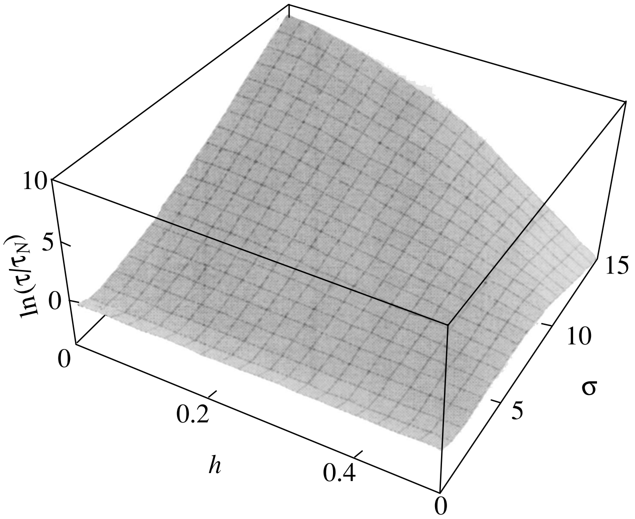

Fig. 2. Dependence of $\ln(\tau/\tau_N)$ on σ (for $\sigma > 0$) and on $h = h_{\mathrm{II}} = h_{\mathrm{I}}/2$ for the case where the external field is suddenly decreased in magnitude by a factor of two.

and the integrated relaxation time is

$$\tau = \int_0^\infty f(t)dt = \tilde{f}(0). \tag{8}$$

3. For the sake of simplicity, we restrict our consideration to the case where the external field is applied along the Z axis of the laboratory coordinate frame. Therefore, we have $\nu_X = \nu_Y = 0$ and $\nu_Z = 1$ and the analysis is significantly simplified, because the response is determined by the relaxation function $c_{1,0}(t)$, which is a component of the vector $\mathbf{C}_1(t)$ in Eq. (6). The function $c_{1,0}(t)$ can be expressed in terms of the eigenvalues λ_k of the Fokker–Planck operator as [14]

$$c_{1,0}(t) = \sum_k c_k e^{-\lambda_k t}.$$

In this case, the relaxation time defined by Eq. (8) is given by

$$\tau = \frac{\sum_k c_k/\lambda_k}{\sum_k c_k}. \tag{9}$$

In general, it is difficult to calculate τ from Eq. (9), because we need to know all λ_k and the weighting factors c_k. In this paper, following [11], we calculate τ from Eq. (8) using the matrix continued fractions rather than λ_k and c_k. However, it has been shown that in many cases, both these approaches lead to identical results for $c_{1,0}(t)$ and τ (see, e.g., [4, 20]). As for the physical interpretation, the method in which the eigenvalues are used is very convenient, because each eigenvalue λ_k corresponds to a certain frequency (mode) characterizing the dynamics of the magnetization vector. In many cases, the relaxation time τ is determined by the slowest, low-frequency mode, corresponding to the smallest eigenvalue λ_1 and characterizing transitions of the magnetization vector from one equilibrium state to another (by passing over a barrier). The behavior of τ is often similar to that of λ_1^{-1} but under certain conditions, as in the case under study here, can be significantly different [20, 21].

4. Our calculations showed that the nonlinear response of particles with cubic anisotropy depends on the dissipation parameter α, which is due to the coupling between longitudinal and transverse (precession) modes. This dependence is qualitatively similar to that in the linear case, which was investigated in detail in [12]. Estimations show that $\alpha \sim 0.01$–0.1. For the sake of definiteness, we performed calculations for $\alpha = 0.1$. The dependence of the relaxation time τ on σ and $h = h_{\mathrm{II}} = h_{\mathrm{I}}/2$ in the case where the external strong field is suddenly decreased in magnitude by a factor of two is shown in Fig. 1 for $\sigma < 0$ and in Fig. 2 for $\sigma > 0$. The dependence of τ on σ and $h = h_{\mathrm{II}} = -h_{\mathrm{I}}$ in the case where the direction of the external field is suddenly reversed is shown in Fig. 3 for $\sigma < 0$. From these results, it can be seen that at small values of h, the dependence of τ on the parameter σ is of an activation character; that is, the relaxation time τ increases exponentially with increasing height of the potential barrier (characterized by σ) between the stable states (free-energy minima) of a particle. However, as h increases further, the relaxation time τ decreases with increasing σ. In other words, when the parameter h exceeds a certain critical value h_c, the dependence of the integrated relaxation time τ on the height of the potential barrier ceases to be of an acti-

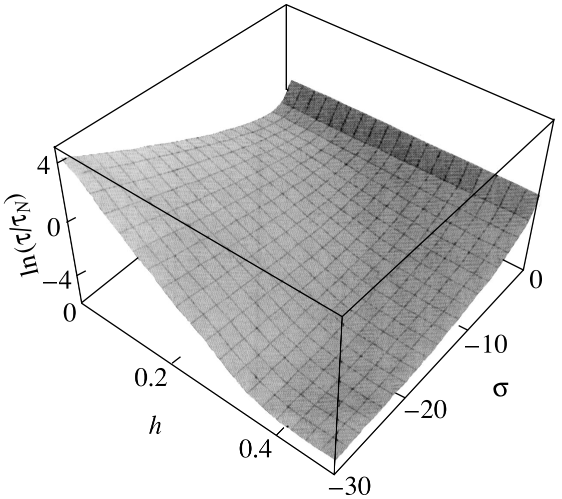

Fig. 3. Dependence of $\ln(\tau/\tau_N)$ on σ (for $\sigma < 0$) and on $h = h_{\mathrm{II}} = -h_{\mathrm{I}}$ for the case where the direction of the external field is suddenly reversed.

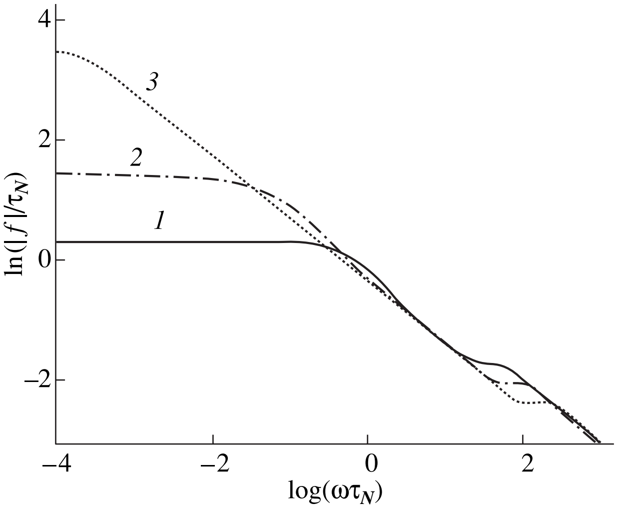

Fig. 4. Dependence of $\ln(|\tilde{f}|/\tau_N)$ on $\log(\omega\tau_N)$ for the case where a strong static magnetic field is suddenly turned on ($h_{\mathrm{I}} = 0$, $h_{\mathrm{II}} = 0.3$) and σ is equal to (*1*) 5, (*2*) 10, and (*3*) 20.

vation character. This effect is typical of Brownian particles passing over the potential barrier between two stable equilibrium states in an external strong static field [21, 22] and is due to a decrease in the population of the upper energy state. As a result, the transitions from the upper energy state to the lower state through the potential barrier no longer determine the relaxation time; the dominating contribution comes from high-frequency intrawell modes in the lower stable state. In the case of the linear response of superparamagnets, this effect has been investigated in detail for both particles with uniaxial anisotropy [4, 21] and particles with cubic anisotropy [12].

The spectrum of the modulus of the relaxation function $|\tilde{f}|$ in the case where an external strong field is suddenly turned on ($h_{\mathrm{I}} = 0$, $h_{\mathrm{II}} = h$) is shown in Fig. 4 for $\sigma > 0$. In this case, there are two bands in the spectrum of $|\tilde{f}|$. The frequency and half-width of the low-frequency band are determined by the mean magnetization lifetime in the upper stable state (λ_1^{-1}). The high-frequency band is associated with intrawell modes, which determine the high-frequency dynamics of the magnetization vector in intermediate local equilibrium states. As in the case of the local response [12], when the dissipation parameter is small ($\alpha \le 0.01$), the spectrum of the nonlinear relaxation function has a band at the frequency of precession of the magnetization vector **M**; with decreasing α, the characteristic frequency of this band increases as α^{-1}.

Using the same method, we can also calculate the linear response of a system of superparamagnetic particles with cubic anisotropy to a small momentary change in the magnitude of the static field $\mathbf{H}_{\mathrm{I}}$. In this case ($h_{\mathrm{II}} = h_{\mathrm{I}} - \varepsilon$, with $\varepsilon \longrightarrow 0$), the relaxation function $f(t)$ is identical to the normalized equilibrium longitudinal correlation function $C_{\parallel}(t)$ in state I:

$$f(t) = C_{\parallel}(t)$$
$$= \frac{\langle\cos\theta(0)\cos\theta(t)\rangle_{\mathrm{I}} - \langle\cos\theta(0)\rangle_{\mathrm{I}}^2}{\langle\cos^2\theta(0)\rangle_{\mathrm{I}} - \langle\cos\theta(0)\rangle_{\mathrm{I}}^2}. \tag{10}$$

According to the linear-response theory, the linear longitudinal susceptibility is

$$\chi_{\parallel}(\omega) \propto C_{\parallel}(0) - i\omega\int_0^{\infty} C_{\parallel}(t)e^{-i\omega t}dt. \tag{11}$$

It should be noted that, as in the case of particles with uniaxial anisotropy [11], the integrated relaxation time for the nonlinear response with a transition from state I to state II can differ significantly from that for the linear response in states I and II.

ACKNOWLEDGMENTS

The authors are grateful to W.T. Coffey (Trinity College, Dublin) for valuable suggestions.

This study was supported by the Russian Foundation for Basic Research, project no. 01-02-16050.

REFERENCES

1. L. Néel, Ann. Geophys. **5** (1), 99 (1949).
2. W. F. Brown, Jr., IEEE Trans. Magn. **15** (5), 1196 (1979).
3. D. A. Garanin, V. V. Ishchenko, and L. V. Panina, Teor. Mat. Fiz. **82** (2), 242 (1990).

4. W. T. Coffey, D. S. F. Crothers, Yu. P. Kalmykov, and J. T. Waldron, Phys. Rev. B **51** (22), 15947 (1995).
5. É. K. Sadykov and A. G. Isavnin, Fiz. Tverd. Tela (St. Petersburg) **38** (7), 2104 (1997) [Phys. Solid State **38**, 1160 (1997)].
6. Yu. L. Raikher and V. I. Stepanov, Phys. Rev. B **55** (22), 15005 (1997).
7. Yu. L. Raikher, V. I. Stepanov, A. N. Grigirenko, and P. I. Nikitin, Phys. Rev. E **56** (6), 6400 (1997).
8. J. L. Garcia-Palacios and P. Svedlindh, Phys. Rev. Lett. **85** (17), 3724 (2000).
9. Yu. L. Raikher and V. I. Stepanov, Phys. Rev. Lett. **86** (10), 1923 (2001).
10. Yu. L. Raĭkher and V. I. Stepanov, Fiz. Tverd. Tela (St. Petersburg) **43** (2), 270 (2001) [Phys. Solid State **43**, 279 (2001)].
11. Yu. P. Kalmykov and S. V. Titov, Fiz. Tverd. Tela (St. Petersburg) **42** (5), 893 (2000) [Phys. Solid State **42**, 918 (2000)].
12. Yu. P. Kalmykov, Phys. Rev. B **61** (9), 6205 (2000).
13. Yu. L. Raikher and M. I. Shliomis, Adv. Chem. Phys. **87**, 595 (1994).
14. L. J. Geoghegan, W. T. Coffey, and B. Mulligan, Adv. Chem. Phys. **100**, 475 (1997).
15. D. A. Varshalovich, A. N. Moskalev, and V. K. Khersonskii, *Quantum Theory of Angular Momentum* (Nauka, Leningrad, 1975; World Scientific, Singapore, 1988).
16. Yu. P. Kalmykov and S. V. Titov, Phys. Rev. Lett. **82** (14), 2967 (1999).
17. Yu. P. Kalmykov and S. V. Titov, Fiz. Tverd. Tela (St. Petersburg) **41** (11), 2020 (1999) [Phys. Solid State **41**, 1854 (1999)].
18. Yu. P. Kalmykov, S. V. Titov, and W. T. Coffey, Phys. Rev. B **58** (6), 3267 (1998).
19. Yu. P. Kalmykov and S. V. Titov, Zh. Éksp. Teor. Fiz. **115** (1), 101 (1999) [JETP **88**, 58 (1999)].
20. W. T. Coffey, Yu. P. Kalmykov, and J. T. Waldron, *The Langevin Equation* (World Scientific, Singapore, 1996).
21. D. A. Garanin, Phys. Rev. E **54** (4), 3250 (1996).
22. Yu. P. Kalmykov, J. L. Déjardin, and W. T. Coffey, Phys. Rev. E **55** (3), 2509 (1997).

Translated by Yu. Epifanov

Physics of the Solid State, Vol. 44, No. 12, 2002, pp. 2281–2286. Translated from Fizika Tverdogo Tela, Vol. 44, No. 12, 2002, pp. 2178–2182.
Original Russian Text Copyright © 2002 by Ryzhkovskiĭ, Glazkov, Goncharov, Kozlenko, Savenko.

MAGNETISM AND FERROELECTRICITY

Neutron Diffraction Investigation of the Magnetic Structure of the Mn_2Sb Pnictide at High Pressures

V. M. Ryzhkovskiĭ*, V. P. Glazkov, V. S. Goncharov*,**
D. P. Kozlenko*, and B. N. Savenko*****

** Institute of Solid-State and Semiconductor Physics, Belarussian Academy of Sciences, ul. Brovki 17, Minsk, 220072 Belarus*
*** Russian Research Centre Kurchatov Institute, pl. Kurchatova 1, Moscow, 123182 Russia*
**** Joint Institute for Nuclear Research, Dubna, Moscow oblast, 141980 Russia*
e-mail: demeshko@ifttp.bas-net.by

Received February 7, 2002

Abstract—This paper reports on the results of investigations into the influence of high pressures (up to 5.3 GPa) at $T = 300$ K on the magnetic structure of the Mn_2Sb pnictide. The crystal and magnetic structures of the Mn_2Sb compound are studied using a direct neutron diffraction method. It is demonstrated that the magnetic ferrimagnet–antiferromagnet phase transition, which is observed in a number of Mn_2Sb-based substitutional solid solutions upon chemical compression of the Mn_2Sb crystal lattice, does not occur in the Mn_2Sb compound under high pressures in the aforementioned range due to an anisotropic pressure-stimulated strain in the Mn_2Sb lattice. At pressures $P \geq 2.8$ GPa, the Mn_2Sb compound is characterized by a spin reorientation with respect to the tetragonal axis and the basal plane of the crystal lattice. © *2002 MAIK “Nauka/Interperiodica”*.

1. INTRODUCTION

The Mn_2Sb pnictide is an intermetallic compound with a tetragonal crystal structure of the Cu_2Sb type (space group *P*4/*nmm*, *C*38). This structure is composed of layered blocks and contains nonequivalent cation sites of two types (*I* and *II*) with different anion environments, namely, the tetrahedral and octahedral anion environments, respectively. The structural motif and interatomic distances in the Mn_2Sb pnictide provide the formation of trilayer blocks (II_a–I–II_b) along the tetragonal axis *c*. In this structure, the intrablock and interblock exchange interactions between magnetically active atoms are competing in character and have proven to be sensitive to variations in the interatomic distances, bond angles, and other structure parameters, which, to a large extent, is responsible for the great variety of magnetic properties of the materials belonging to this structural type [1]. For example, it will suffice to mention that virtually all types of classical magnetic ordering and magnetic structures with specific features are observed in a relatively small series of known compounds with a Cu_2Sb-type structure (Cu_2Sb, Mn_2Sb, Mn_2As, Fe_2As, Cr_2As, MnAlGe, MnGaGe, and MnZnSb).

In the Mn_2Sb structure, trilayer blocks consist of Mn-*I* and Mn-*II* magnetically active atoms whose magnetic moments are different in magnitude and opposite to each other in direction. Consequently, the Mn_2Sb pnictide exhibits ferrimagnetic properties over the entire temperature range of magnetic ordering with the Curie temperature $T_C = 550$ K. For this compound, the magnetic structure and its characteristics under normal conditions have been thoroughly investigated both experimentally and theoretically [2–4]. The specific feature of the magnetic structure of the Mn_2Sb compound is that it experiences spin reorientation with rotation of the atomic magnetic moments from the basal plane of the crystal lattice toward the *c* axis ($\Phi^- \longrightarrow \Phi^+$) as the temperature increases to $T_s = 250$ K. The crystal and magnetic structures of the Mn_2Sb pnictide are shown in Fig. 1.

A number of substitutional solid solutions based on the Mn_2Sb–$Mn_{2-x}A_xSb_{1-y}B_y$ matrix (where *A* is Cr, Cu, Zn, V, or Co and *B* is As, Sn, Ge, or Bi) undergo a first-order magnetic phase transition from a ferrimagnetic (F) state to an antiferromagnetic (AF) state (F $\longrightarrow$ AF). The magnetic structure of these alloys in the antiferromagnetic state is similar to the magnetic structure of the Mn_2As (AF) compound in which the magnetic cell is doubled along the *c* axis as compared to the nuclear cell (Fig. 1).

According to the phenomenological theory (the exchange inversion model) proposed by Kittel [5], the effective exchange interactions occurring in these structures reverse sign at a critical lattice parameter c_{cr}, which can be attained, for example, upon chemical or thermal compression of the crystal lattice of the initial matrix. Reasoning from the Kittel model theory, it can be expected that, in the case when the crystal lattice of Mn_2Sb is compressed to critical sizes under a high pressure, this compound should undergo a phase transition from the ferrimagnetic state to the antiferromagnetic

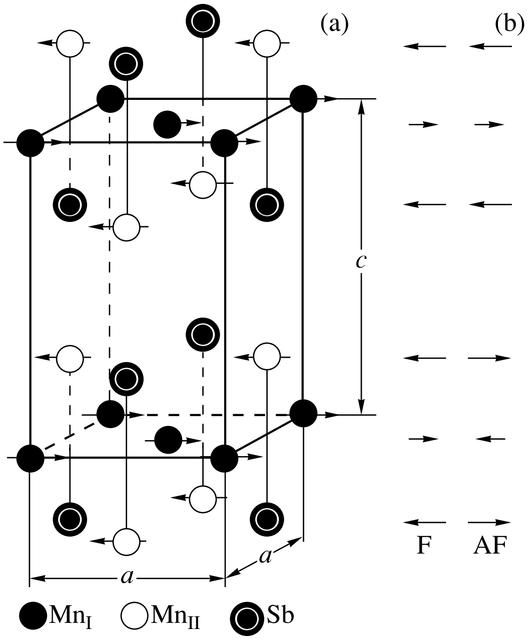

Fig. 1. (a) Crystal and magnetic structures of the Mn_2Sb pnictide ($T < 250$ K, $P = 0$) and (b) schematic diagram of the magnetic structures of the ferrimagnet (F) and antiferromagnet (AF) in solid solutions based on the Mn_2Sb compound.

state. However, until presently, the question as to whether the Mn_2Sb compound undergoes a phase transition from the ferrimagnetic state to the antiferromagnetic state upon compression of the crystal lattice under pressure has remained open. In particular, a number of experiments in which changes in the magnetic state under pressure were studied using an indirect method led to rather contradictory inferences. Kanomata *et al.* [6] performed an x-ray diffraction investigation of the Mn_2Sb compound and revealed substantial changes in the lattice parameters of Mn_2Sb at $P = 3.5$ GPa and $T =$ 300 K. In [6], these changes were attributed to a magnetic phase transition from the ferrimagnetic state to the antiferromagnetic state. As was shown earlier by Bierstedt [7], this transition under normal conditions should occur with a drastic increase in the electrical resistivity. However, our recent electrical measurements in the pressure range up to 8 GPa [8] did not reveal anomalies in the dependence $R = f(P)$. These findings count in favor of the assumption that the magnetic ordering observed in this compound is invariable in character.

Neutron diffraction is one of the most efficient methods for studying variations in the magnetic ordering of the material under investigation. This method makes it possible to determine directly the characteristics of both the atomic and magnetic structures. In particular, the neutron diffraction experiment can provide an unambiguous answer to the question as to whether or not a magnetic phase transition from a ferrimagnetic state to an antiferromagnetic state of the Mn_2Sb compound occurs under pressure, because the ferrimagnetic and antiferromagnetic phases are characterized by qualitatively different neutron diffraction patterns owing to the different dimensions of their magnetic cells [4].

Unfortunately, the potentialities of the neutron diffraction method, as applied to high pressures, were long limited by a relatively narrow pressure range (no higher than $P \sim 2$ GPa). Recent considerable progress achieved in the sapphire-anvil technique and the advent of new special spectrometers designed for high-pressure investigations have provided a means for extending the attainable pressure range to 7–10 GPa in the neutron diffraction experiment. This made it possible to elucidate the influence of high pressure on the magnetic structure of the Mn_2Sb pnictide.

2. SAMPLE PREPARATION AND EXPERIMENTAL TECHNIQUE

Polycrystalline samples of the Mn_2Sb pnictide were prepared through direct alloying of powders (composed of the initial components) in evacuated quartz cells with the use of alundum crucibles according to the procedure described earlier in [9]. Prior to measurements, the prepared samples were examined using x-ray diffraction and neutron diffraction analyses. The diffraction patterns exhibited additional weak reflections from the concomitant manganese antimonide phase MnSb, which is characteristic of both the Mn_2Sb compound and Mn_2Sb-based solid solutions [10].

The neutron diffraction measurements at pressures up to 5.3 GPa were performed on an IBR-2 pulsed high-flux reactor (Frank Laboratory of Neutron Physics, Joint Institute for Nuclear Research, Dubna) with the use of a DN-12 spectrometer [11] and high-pressure chambers with sapphire anvils [12]. In this case, the volume V of the studied samples was approximately equal to 2 mm^3. The diffraction spectra were recorded at the scattering angle $2\theta = 45.5°$. For this scattering angle and the wavelength $\lambda = 2$ Å, the resolution of the diffractometer $\Delta d/d$ was 0.022. The characteristic time taken for one diffraction spectrum to be measured was equal to 20 h. The pressure in the chamber was measured from the shift of the ruby luminescence line. The sample pressure was taken as the averaged pressure for several points on the sample surface. All the measurements were performed at room temperature.

3. RESULTS AND DISCUSSION

Figure 2 shows fragments of the diffraction spectra of the Mn_2Sb pnictide at pressures $P = 0$ and 2.8 GPa. It can be seen from Fig. 2 that, at a pressure of 2.8 GPa, the intensities of a number of reflections, specifically of the (110) and (001) reflections, change significantly. However, additional superstructure reflections that can be expected in the case of a magnetic phase transition

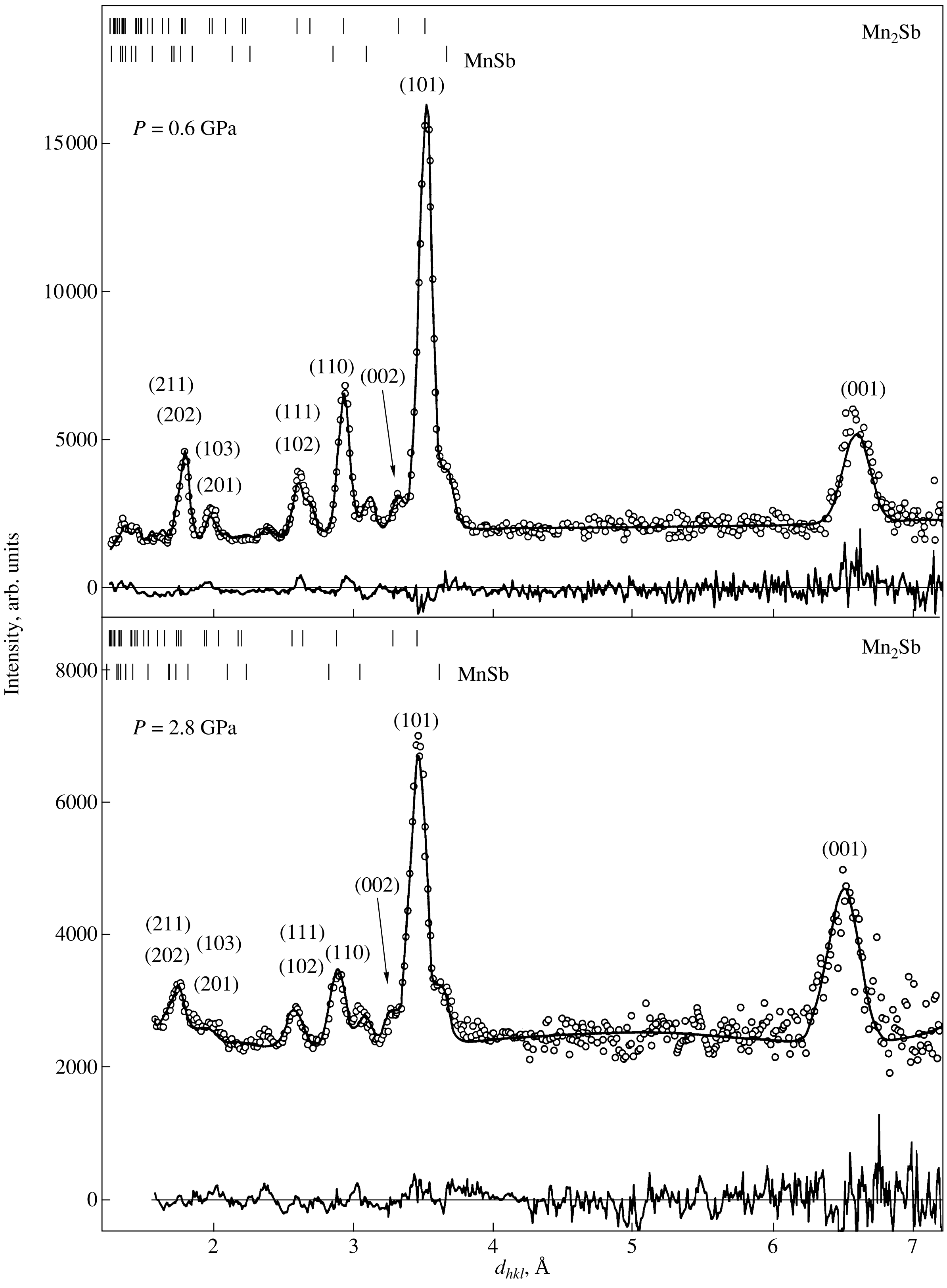

Fig. 2. Fragments of the diffraction spectra of the Mn$_2$Sb pnictide at pressures $P = 0$ and 2.8 GPa. Points are the experimental data, the upper solid lines represent the calculated profiles, and the lower solid lines are the difference curves. The upper and lower tic marks indicate the positions of diffraction peaks for the main and impurity (MnSb) phases, respectively. Measurements are performed on a DN-12 spectrometer.

Structural and magnetic parameters of the Mn_2Sb pnictide at pressures $P = 0$ and 2.8 GPa

Parameter	P, GPa		
	0	0 [3]	2.8
a, Å	4.078(5)	4.08	4.031(5)
c, Å	6.557(6)	6.56	6.519(6)
Mn (z_1)	0.32(1)	0.2897(6)	0.29(1)
Sb (z_2)	0.71(1)	0.2707(2)	0.70(1)
μ_{Mn}, μ_B	$\mu_{Mn\text{-}I} = 1.5(1)$ $\mu_{Mn\text{-}II} = -2.7(1)$	$\mu_{Mn\text{-}I} = 1.48(15)$ $\mu_{Mn\text{-}II} = -2.66(15)$	$\mu_{Mn\text{-}I} = 1.5(1)$ $\mu_{Mn\text{-}II} = -2.7(1)$
φ, deg	0	0	40(5)
R_b, %	9.6	–	7.41
R_{mag}, %	4.0	–	9.06

from the ferrimagnetic state to the antiferromagnetic state do not appear. Similar neutron diffraction patterns are also observed at pressures $P = 4.3$ and 5.3 GPa. This indicates that an increase in the pressure does not affect the initial ferrimagnetic structure of the Mn_2Sb pnictide. The redistribution of the intensities of the (001) and (110) reflections can be associated with the spin reorientation of manganese atomic magnetic moments with respect to the crystallographic axes of the Mn_2Sb lattice (see below).

Thus, the direct neutron diffraction measurements unambiguously demonstrate that, under pressures up to 5.3 GPa, the Mn_2Sb pnictide does not experience a spin rearrangement in the form of a phase transition from the ferrimagnetic state to the antiferromagnetic state.

Analysis of the neutron diffraction data was carried out using the Rietveld method with the MRIA [13] (atomic structure) and Fullprof [14] (atomic and magnetic structures) program packages in the framework of the known structural model [2]. According to this model, the manganese atoms occupy the positions 2*a* (0, 0, 0) (type *I*) and 2*c* (0, 1/2, z_1) (type *II*) and the antimony atoms are located at the positions 2*c* (0, 1/2, z_2) with space group *P*4/*nmm*. For the diffraction spectrum measured at $P = 0$, we refined the lattice parameters, the positional parameters of the manganese and antimony atoms, and the magnetic moments of the manganese atoms located at positions of types *I* and *II*. For the diffraction spectra measured at high pressures, we refined the lattice parameters, the positional parameters of the manganese and antimony atoms, and the angles φ of deviation of the manganese atomic magnetic moments from the *c* axis toward the basal plane. It was assumed that, as the pressure increases, the magnetic moments of manganese atoms located at different-type positions only slightly vary in magnitude and remain opposite to each other in direction. In our calculations, the thermal parameters of manganese and antimony atoms were taken to be $B_{Mn} = B_{Sb} = 1$ Å^2. It turned out that, in the studied range of interplanar distances, variations in the thermal parameters over a wide range affect the structure parameters insignificantly. The contribution of the MnSb impurity phase was also taken into account in these computations. The table presents the calculated structure parameters of the Mn_2Sb pnictide at pressures $P = 0$ and 2.8 GPa and also the discrepancy factors *R*. The positional parameters and magnetic moments obtained are in agreement with the results reported in [2, 3].

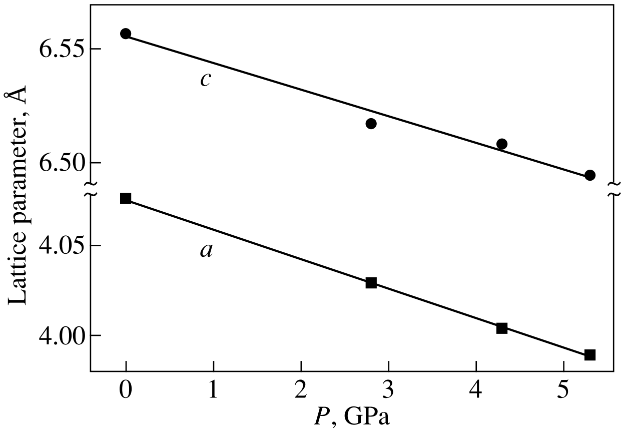

Fig. 3. Pressure dependences of the lattice parameter of the Mn_2Sb pnictide and their linear interpolation.

As can be seen from Fig. 3, the experimental dependences of the lattice parameters *a* and *c* on the pressure exhibit a linear behavior without jumps that should be observed in the case of a magnetic phase transition from the ferrimagnetic state to the antiferromagnetic state.

Recent analysis [15] of the variations observed in the effective exchange interactions occurring in the $Mn_{2-x}A_xSb_{1-y}B_y$ system (where *A* is a 3*d* metal and *B* is As or Sn) has demonstrated that no magnetic phase transition from the ferrimagnetic state to the antiferromagnetic state of Mn_2Sb can occur upon chemical, thermal, or pressure-stimulated compression of the crystal lattice of the initial matrix in the case of its anisotropic strain. This can be associated primarily with the changes in the angles between the interatomic exchange bonds, which are ignored in the Kittel exchange inversion model applied to the description of the phase transition from the ferrimagnetic state to the antiferromagnetic state.

It is known that the linear compression coefficients along the crystallographic axes a and c in the Mn_2Sb compound are significantly different in magnitude [6, 16]. We estimated the linear compression coefficients β_a and β_c from our neutron diffraction data ($\beta_a = a_0^{-1}\, da/dP$ and $\beta_c = c_0^{-1}\, dc/dP$) and obtained the following values: $\beta_a = 4 \times 10^{-5}$ GPa and $\beta_c = 1.8 \times 10^{-5}$ GPa. Although the data available in the literature on the compressibility of Mn_2Sb, according to different authors, have a small quantitative scatter, they show a common tendency; namely, the linear compression coefficient β_a substantially exceeds the coefficient β_c. In our opinion, it is this anisotropic pressure-induced lattice strain that is responsible for the invariability of the initial ferrimagnetic structure of the Mn_2Sb pnictide under high pressures. It is worth noting that there occurs a similar thermal compression of the crystal lattice of the studied compound [17]. As the temperature decreases, this compression brings about the stabilization rather than disturbance of ferrimagnetic ordering in this compound [18].

The neutron diffraction patterns measured at pressures $P \geq 2.8$ GPa are characterized by a redistribution of intensities of the observed reflections. This suggests a reorientation of the atomic magnetic moments with respect to the crystallographic axes of the lattice under the conditions when the initial ferrimagnetic structure remains unchanged. This effect is especially pronounced for the intensities of the (001) and (110) reflections, whose magnetic components are most sensitive to spin reorientation with respect to the basal plane and the tetragonal axis of the crystal lattice. Under normal conditions, the spin reorientation in the Mn_2Sb compound is observed at $T_s = 250$ K. According to different authors [19, 20], the pressure coefficient of the spin-reorientation transition is estimated as $dT_s/dP \simeq +0.2$ K/GPa; i.e., in the case when the pressure dependence of the temperature T_s shows a linear behavior, the spin reorientation at room temperature should be expected at a pressure of approximately 2 GPa. This reorientation of the magnetic moments is in qualitative agreement with the intensity redistribution observed for the (001) and (110) reflections (due to variations in their magnetic components) in the neutron diffraction patterns recorded at $P \geq 2.8$ GPa as compared to that in the neutron diffraction pattern measured at $P = 0$. However, the Rietveld analysis of the neutron diffraction patterns and the quantitative estimate made for the (001) reflection associated with the nuclear magnetic characteristics demonstrate a disagreement between the calculated and experimental results and, hence, disprove a complete reorientation of the magnetic moments with respect to the tetragonal axis and the basal plane of the crystal lattice ($\varphi \simeq 40°$). A further increase in the pressure to 5.3 GPa does not lead to a noticeable redistribution in the intensities of the observed reflections, which indicates the absence of further spin reorientation. This result is of fundamental interest and calls for additional, more detailed investigation.

4. CONCLUSIONS

Thus, the direct neutron diffraction investigation has demonstrated that, under high pressures up to 5.3 GPa, the type of magnetic ordering in the Mn_2Sb pnictide at $T = 300$ K remains unchanged. The ferrimagnetic structure is retained over the entire pressure range studied. At pressures $P \geq 2.8$ GPa, the ferrimagnetic structure of the Mn_2Sb pnictide is characterized by a spin reorientation with respect to the crystallographic axes of the lattice. The result obtained is important for the elucidation of the mechanism of the magnetic phase transition from the ferrimagnetic state to the antiferromagnetic state in the materials belonging to the Cu_2Sb structural type and, especially, for the refinement of the applicability of the Kittel exchange inversion model to the description of this transition.

ACKNOWLEDGMENTS

This work was supported by the Russian Foundation for Basic Research (project nos. 00-02-17077 and 00-15-96778), the State Scientific and Technical Program “Topical Directions in the Physics of Condensed Matter: Neutron Investigations of Condensed Matter,” and in part by the Belarussian Foundation for Basic Research.

REFERENCES

1. J. B. Goodenough, *Magnetism and the Chemical Bond* (Interscience, New York, 1963; Metallurgiya, Moscow, 1968).
2. M. Wilkinson, N. Gingrich, and C. Shull, J. Phys. Chem. Solids **2** (4), 289 (1957).
3. H. A. Alperin, P. J. Brown, and R. Nathans, J. Appl. Phys. **34** (4), 1201 (1963).
4. N. N. Sirota and V. M. Ryzhkovskiĭ, Dokl. Akad. Nauk SSSR **203** (6), 1275 (1972) [Sov. Phys. Dokl. **17**, 370 (1972)].
5. G. Kittel, Phys. Rev. **120** (2), 335 (1960).
6. T. Kanomata, T. Kawashima, T. Kaneko, *et al.*, Jpn. J. Appl. Phys. **30** (3), 541 (1991).
7. P. Bierstedt, Phys. Rev. **132** (2), 669 (1963).
8. V. M. Ryzhkovskiĭ, Fiz. Tverd. Tela (St. Petersburg) **37** (10), 3108 (1995) [Phys. Solid State **37**, 1713 (1995)].

9. V. M. Ryzhkovskiĭ, N. D. Zhigadlo, and Z. L. Erofeenko, Izv. Akad. Nauk BSSR, Ser. Fiz.-Mat. Nauk **2**, 79 (1988).
10. J. D. Wolf and J. E. Hanlon, J. Appl. Phys. **32** (12), 2584 (1961).
11. V. L. Aksenov, A. M. Balagurov, V. P. Glazkov, *et al.*, Physica B (Amsterdam) **265**, 258 (1999).
12. V. P. Glazkov and I. N. Goncharenko, Fiz. Tekh. Vys. Davleniĭ **1**, 56 (1991).
13. V. B. Zlokazov and V. V. Chernyshev, J. Appl. Crystallogr. **25**, 447 (1992).
14. J. Rodriguez-Carvajal, Physica B (Amsterdam) **192**, 55 (1993).
15. V. M. Ryzhkovskiĭ, Metally **3**, 59 (2001).
16. V. M. Ryzhkovskiĭ, Dokl. Akad. Nauk Belarusi **37** (3), 39 (1993).
17. L. Heaton and N. Gingrich, Acta Crystallogr. **8**, 207 (1955).
18. S. Funahashi, J. Magn. Magn. Mater. **31–34**, 595 (1983).
19. T. Kanomata, Y. Masebe, T. Ito, *et al.*, J. Appl. Phys. **69** (8), 4642 (1991).
20. N. N. Sirota, É. A. Vasil’ev, G. I. Makovetskiĭ, *et al.*, in *Proceedings of the International Conference on Magnetism, 1973*, Vol. 3, p. 497.

Translated by O. Borovik-Romanova

Physics of the Solid State, Vol. 44, No. 12, 2002, pp. 2287–2292. Translated from Fizika Tverdogo Tela, Vol. 44, No. 12, 2002, pp. 2183–2188.
Original Russian Text Copyright © 2002 by Babushkin, Buchel'nikov, Bychkov.

MAGNETISM AND FERROELECTRICITY

Reflection of Electromagnetic Waves from the Surface of a Cubic Ferrite

A. V. Babushkin, V. D. Buchel'nikov, and I. V. Bychkov
Chelyabinsk State University, Chelyabinsk, 454021 Russia
e-mail: buche@csu.ru

Received September 27, 2001; in final form, March 20, 2002

Abstract—The reflectivity of electromagnetic waves incident on the surface of a semi-infinite nonconducting cubic ferrite was found both analytically and numerically with inclusion of spin-wave damping. The frequency and field dependences of the reflectivity were found for various values of the damping parameter and the anisotropy and magnetostriction constants in a region far from the point of the orientational phase transition and at this point. It is shown that the reflectivity has peaks near the frequencies of ferromagnetic, magnetoacoustic, and magnetostatic resonances. The peak amplitude decreases with increasing spin-wave damping. At frequencies below the magnetoelastic gap, the reflectivity can take on anomalously small (down to zero) and anomalously large (up to unity) values. These frequencies can lie in the microwave range. *© 2002 MAIK “Nauka/Interperiodica”.*

The problem of controlling the reflectivity of electromagnetic waves incident on surfaces of various substances has not lost its acute interest. This interest is maintained by the need in science and technology for both highly reflecting and nonreflecting materials.

The reflectivity R for electromagnetic waves incident normally from vacuum onto the boundary of a medium possessing nonzero dielectric permittivity ε and magnetic permeability μ is given by the relation [1]

$$R = \left|\frac{\sqrt{\varepsilon} - \sqrt{\mu}}{\sqrt{\varepsilon} + \sqrt{\mu}}\right|^2. \quad (1)$$

This relation is valid only in the cases where ε and μ can be considered constant. In the microwave range, which is of most interest from the standpoint of potential application, the dielectric permittivity of solids is frequency independent. For substances that are not magnetically ordered, the magnetic permeability in the microwave range can be set equal to unity in Eq. (1). Therefore, the electromagnetic-wave reflectivity (EWR) of nonmagnetic solids in this frequency range can be considered constant. In this case, the reflectivity can be increased or decreased by varying ε and μ through proper variation of the composition and structure of the substance, as well as through the development of artificial magnets with a high value of μ (the so-called chiral magnets [2–4]).

The magnetic permeability of magnetically ordered media can increase or decrease anomalously in the region of magnetic-resonance frequencies lying in the microwave range. This behavior of μ finds explanation in its time dispersion [5]. Under these conditions, the EWR of the surface of a magnet can also depend resonantly on frequency. This phenomenon has been observed experimentally [6].

Magnets in which magnetoelastic interaction is noticeable exhibit three resonances, namely, ferromagnetic, magnetoacoustic, and magnetostatic [7]. Near these resonances, anomalies in the magnetic permeability and EWR should also be observed. However, far from orientational phase transitions, these anomalies are small and, furthermore, the three resonances merge because of the effective anisotropy field being large compared to the effective fields of magnetostriction and magnetization. This type of behavior of the EWR was observed experimentally in [6].

A theoretical analysis of the frequency and field dependences of the EWR of surfaces of some ferro- and antiferrodielectrics has been carried out by a number of researchers [8–10]. It was shown that if magnetoelastic interaction is taken into account in the vicinity of the points of orientational phase transitions, the EWR of the surface of semi-infinite ferro- and antiferrodielectrics can reach anomalously large (up to unity) and anomalously small (down to zero) values. In addition, it was pointed out that, by properly varying the applied magnetic field, the EWR can be brought practically to zero over a broad frequency range, up to the gigahertz region. All analytical and numerical calculations in the studies indicated above were made neglecting the spin-wave damping. However, it is well known [5, 11] that this damping affects the dynamic properties of ferro- and antiferromagnets very strongly. It thus appeared to be of interest to study the effect of spin-wave damping on the EWR of the surface of magnetically ordered substances.

1063-7834/02/4412-2287$22.00 © 2002 MAIK “Nauka/Interperiodica”

We present here the results of analytical and numerical calculations of the EWR of the surface of a semi-infinite nonconducting ferrite of cubic symmetry, both far from and close to the orientational phase transition, with spin-wave damping included. It is shown that the EWR depends strongly on the magnetostriction constants, the external magnetic field, and spin-wave damping and can assume anomalously large and anomalously small values within a broad frequency range, including the microwave region.

Our calculation of the reflectivity of the surface of a ferrite of cubic symmetry is based on the theory of coupled electromagnetic and magnetostatic waves. Following [8–10], we consider a ferrite of cubic symmetry occupying a half-space $z > 0$ and having a ground-state magnetization $\mathbf{M} \parallel \mathbf{z} \parallel \mathbf{H}_0$ ($\mathbf{H}_0$ is an external dc magnetic field). Let an electromagnetic wave traveling in vacuum strike the ferrite surface at normal incidence: $h_x = h_0 \exp(ikz - i\omega t)$ and $e_y = -h_0 \exp(ikz - i\omega t)$.

The free-energy density of a cubic ferrite can be written as [12]

$$\begin{aligned} F &= F_{\mathrm{m}} + F_{\mathrm{me}} + F_{\mathrm{e}} - \mathbf{HM}, \\ F_{\mathrm{m}} &= \frac{1}{2}\lambda(\mathbf{M}^2 - M_0^2) + \frac{\alpha}{2}\left(\frac{\partial \mathbf{M}}{\partial x_i}\right)^2 \\ &\quad + K_1(m_x^2 m_y^2 + m_y^2 m_z^2 + m_x^2 m_z^2), \\ F_{\mathrm{me}} &= B_1(m_x^2 u_{xx} + m_y^2 u_{yy} + m_z^2 u_{zz}) \\ &\quad + 2B_2(m_x m_y u_{xy} + m_y m_z u_{yz} + m_x m_z u_{yz}), \\ F_{\mathrm{e}} &= \frac{1}{2}c_{11}(u_{xx}^2 + u_{yy}^2 + u_{zz}^2) \\ &\quad + c_{12}(u_{xx}u_{yy} + u_{yy}u_{zz} + u_{xx}u_{zz}) \\ &\quad + 2c_{44}(u_{xz}^2 + u_{yz}^2 + u_{xy}^2), \end{aligned} \tag{2}$$

where $\mathbf{H} = \mathbf{H}_0 + \mathbf{h}$; λ is the Lagrange factor, which takes into account the constancy of the magnitude of the magnetization vector $\mathbf{M}$; $\mathbf{m} = \mathbf{M}/M_0$; M_0 is the saturation magnetization; α is the exchange constant; K_1 is the first cubic anisotropy constant; B_i are the magnetostriction constants; c_{ij} are the elastic moduli; and u_{ij} is the strain tensor.

Minimizing energy (2) yields the following expressions for the strain tensor and Lagrange factor at equilibrium:

$$\begin{aligned} u_{zz}^0 &= -\frac{B_1(c_{11} + c_{12})}{(c_{11} - c_{12})(c_{11} + 2c_{12})}, \\ u_{yy}^0 &= u_{xx}^0 = \frac{B_1 c_{12}}{(c_{11} - c_{12})(c_{11} + 2c_{12})}, \\ u_{ij}^0 &= 0, \quad i \neq j, \\ \lambda &= H_0/M_0 - 2B_1 u_{zz}^0/M_0^2. \end{aligned} \tag{3}$$

The propagation of coupled spin, elastic, and electromagnetic waves in a ferrite can be described by the coupled equations [5, 11, 12]

$$\begin{aligned} \rho \ddot{u}_i &= \frac{\partial \sigma_{ik}}{\partial x_k}, \quad \sigma_{ik} = \frac{\partial F}{\partial u_{ik}}, \\ \dot{\mathbf{M}} &= g[\mathbf{M}, \mathbf{H}_{\mathrm{ef}}] + \frac{1}{\tau M_0^2}[\mathbf{M}, [\mathbf{M}, \mathbf{H}_{\mathrm{ef}}]], \\ \mathbf{H}_{\mathrm{ef}} &= -\frac{\partial F}{\partial \mathbf{M}} + \frac{\partial}{\partial x_i}\frac{\partial F}{\partial(\partial \mathbf{M}/\partial x_i)}, \\ \mathrm{curl}\mathbf{H} &= \frac{\varepsilon}{c}\frac{\partial \mathbf{E}}{\partial t}, \quad \mathrm{curl}\mathbf{E} = -\frac{1}{c}\frac{\partial \mathbf{B}}{\partial c}, \\ \mathrm{div}\mathbf{B} &= 0, \quad \mathrm{div}\mathbf{E} = 0, \quad \mathbf{B} = \mathbf{H} + 4\pi\mathbf{M}, \end{aligned} \tag{4}$$

where ρ is the density of the material, g is the gyromagnetic ratio, τ is the transverse relaxation time in the spin subsystem, and c is the light velocity in vacuum.

Equations (4) can be solved using the method of small-amplitude oscillations; all parameters of the system are assumed to vary as

$$\mathbf{A} = \mathbf{A}_0 + \mathbf{a}\exp(-i\omega t + ikz), \tag{5}$$

where $\mathbf{A}_0$ are the equilibrium values and $\mathbf{a}$ are small deviations from the latter.

Using Eqs. (2), (3), and (5), we obtain from Eqs. (4) the following linearized system of equations describing the propagation of weak excitations in a ferromagnet:

$$\begin{aligned} (c^2k^2/\varepsilon\omega^2 - \mu_\pm)h_\pm &= 0, \quad m_\pm = \chi_\pm h_\pm/M_0, \\ u_\pm &= -ikB_2\chi_\pm h_\pm/\rho(\omega^2 - \omega_t^2), \\ e_\pm &= \mp ickh_\pm/\varepsilon\omega, \end{aligned} \tag{6}$$

where $a_\pm = a_x \pm ia_y$ are circular components, $\omega_t^2 = c_{44}k^2/\rho$, and $\mu_\pm = 1 + 4\pi\chi_\pm$. The dynamic magnetic susceptibility can be written as

$$\begin{aligned} \chi_\pm &= gM_0(\omega^2 - \omega_t^2)/[(\omega^2 - \omega_t^2) \\ &\quad \times (\omega_{sk} \mp \omega/(1 \mp i\gamma)) + \omega_t^2\omega_{\mathrm{me}}], \end{aligned} \tag{7}$$

where $\omega_{sk} = \omega_0 + \omega_{\mathrm{me}} + g\alpha M_0 k^2$, $\omega_{\mathrm{me}} = gB_2^2/M_0C_{44}$, $\omega_0 = \omega_A + \omega_H$, $\omega_{\mathrm{A}} = 2gK/M_0$, $\omega_H = gH_0$, $K = K_1 + B_1^2/(c_{11} - c_{12}) - B_2^2/2c_{44}$ is the magnetic anisotropy constant renormalized by magnetostriction, and $\gamma = 1/(gM_0\tau)$ is the nondimensional spin-wave damping parameter. The dispersion relation for Eqs. (6) has the form

$$\begin{aligned} (k^2 - k_s^2)(k^2 - k_a^2)(k^2 - k_e^2) - \frac{\zeta}{\alpha}k_a^2(k^2 - k_e^2) \\ - \frac{4\pi}{\alpha}k_e^2(k^2 - k_a^2) = 0, \end{aligned} \tag{8}$$

where $k_s^2 = (\pm\omega - \omega_0)/[g\alpha M_0(1 \mp i\gamma)]$, $k_e = \sqrt{\varepsilon}\omega/c$, and $k_a = \omega/s_t$ are the wave numbers of the noninteracting spin, electromagnetic, and elastic waves, respectively; $s_t^2 = c_{44}/\rho$ is the transverse sound velocity; and $\zeta = B_2^2/\rho s_t^2 M_0^2$ is the nondimensional magnetoelastic-interaction parameter. The constant 4π in Eq. (8) plays the role of the electromagnetic-wave–spin coupling parameter.

Dispersion equation (8) can be solved to yield six values of the wave number corresponding to six coupled waves which can propagate in the ferrite.

The system of boundary conditions for the ferrite includes the conditions of continuity of the tangential components of the electric and magnetic fields, of the continuity of normal components of the electric- and magnetic-induction vectors of these fields, of the absence of stresses, and of the equality of the derivative of the magnetization to zero at the ferromagnet surface [5, 8]. With the different roots of dispersion equation (8), the system of boundary conditions for our geometry can be presented in the form

$$\begin{gathered} h_{0\pm} + h_{R\pm} = \sum_{i=1}^{3} h_{i\pm}, \quad e_{0\pm} + e_{R\pm} = \sum_{i=1}^{3} e_{i\pm}, \\ ic_{44}\sum_{i=1}^{3} k_{i\pm}u_{i\pm} + B_2\sum_{i=1}^{3} m_{i\pm} = 0, \quad \sum_{i=1}^{3} k_{i\pm}m_{i\pm} = 0, \end{gathered} \tag{9}$$

where the fields $h_{R\pm}$ and $e_{R\pm}$ relate to the electromagnetic wave reflected from the surface. Conditions (9) and the starting system of equations (6) permit one to find the EWR of a ferrite surface:

$$R = \frac{1}{2}\left(\left|\frac{\Delta_{R+}}{\Delta_{0+}}\right|^2 + \left|\frac{\Delta_{R-}}{\Delta_{0-}}\right|^2\right), \tag{10}$$

where

$$\begin{aligned} \Delta_{R\pm} = {} & (\sqrt{\varepsilon}k_e + k_{1\pm})(k_{3\pm} - k_{2\pm}) \\ & \times (k_a^2 - k_{3\pm}^2 + k_{2\pm}k_{3\pm} - k_{2\pm}^2) \\ & \times \left[(k_{1\pm}^2 - k_a^2)(k_{1\pm}^2 - k_s^2) - \frac{\zeta}{\alpha}k_a^2\right] \\ & + \text{cyclic permutation}. \end{aligned} \tag{11}$$

The expression for $\Delta_{0\pm}$ is obtained from Eq. (11) by replacing the sum in the first parentheses by the difference.

Far from the point of the orientational phase transition $\omega_0 \neq 0$ (i.e., $2K/M_0 + H \neq 0$) and far from the frequencies of the ferromagnetic (ω_0), magnetoacoustic ($\omega_0 + \omega_{me}$), and magnetostatic ($\omega_0 + \omega_{me} + \omega_M$) resonances (with $\omega_M = 4\pi g M_0$), the expression for R allows for a substantial simplification:

$$R = \frac{1}{2}\left(\left|\frac{\sqrt{\varepsilon} - \sqrt{\mu_+}}{\sqrt{\varepsilon} + \sqrt{\mu_+}}\right|^2 + \left|\frac{\sqrt{\varepsilon} - \sqrt{\mu_-}}{\sqrt{\varepsilon} + \sqrt{\mu_-}}\right|^2\right), \tag{12}$$

where the magnetic permeability is

$$\begin{aligned} \mu_\pm &= 1 + \frac{\omega_M(1+\gamma^2)[\omega_{s0}(1+\gamma^2) \mp \omega + i\gamma\omega]}{(\omega_{s0}(1+\gamma^2) \mp \omega)^2 + \gamma^2\omega^2} \\ &= \mu'_\pm + i\mu''_\pm \end{aligned} \tag{13}$$

and $\omega_{s0} = \omega_0 + \omega_{me}$. We note that the magnetostatic-resonance frequency in metals is called the antiresonance frequency [13]. As follows from Eq. (13), the real part of the magnetic permeability μ'_+ is negative in the region of the ferrite parameters

$$\omega_{s0} < \omega_M[\sqrt{\gamma^2 + 1} - \gamma]/2\gamma \tag{14}$$

and at frequencies

$$\omega_1 < \omega < \omega_2, \tag{15}$$

where

$$\begin{gathered} \omega_{1,2} = \frac{1}{2} \\ \times [2\omega_{s0} + \omega_M \mp \sqrt{\omega_M^2 - 4\gamma^2\omega_{s0}(\omega_{s0} + \omega_M)}]. \end{gathered}$$

If the inequality opposite to (14) holds, the real part of the magnetic permeability μ'_+ is positive for all frequencies. The real part of the magnetic permeability μ'_- is positive for any value of the ferrite parameters and frequencies. If inequalities (14) and (15) hold and $\gamma \ll 1$, Eq. (12) for the EWR can be recast as

$$R = (\varepsilon + \mu_-)/(\sqrt{\varepsilon} + \sqrt{\mu_-})^2.$$

Otherwise, Eq. (12) assumes the form ($\gamma \ll 1$)

$$R = \frac{(\varepsilon - \sqrt{\mu_+\mu_-})^2 + \varepsilon(\sqrt{\mu_+} - \sqrt{\mu_-})^2}{[\varepsilon + \sqrt{\varepsilon}(\sqrt{\mu_+} + \sqrt{\mu_-}) + \sqrt{\mu_+\mu_-}]^2}.$$

We performed a numerical analysis of the behavior of the EWR as a function of frequency, external dc magnetic field, and ferrite parameters. The constants involved are taken to be equal to those typical of ferrites: $M_0 = 500$ Oe, $g = 2 \times 10^7$ s^{-1} Oe^{-1}, $\varepsilon = 10$, $s_t = 3 \times 10^5$ cm/s, and $\rho = 5$ g/cm^3.

Figures 1 and 2 plot the frequency dependence of the EWR in a region far from the orientational phase transition point and at this point.

As follows from Fig. 1, the EWR in a region far from the orientational phase transition exhibits anomalies only within the frequency range determined by Eq. (15), where the real part of the magnetic permeabil-

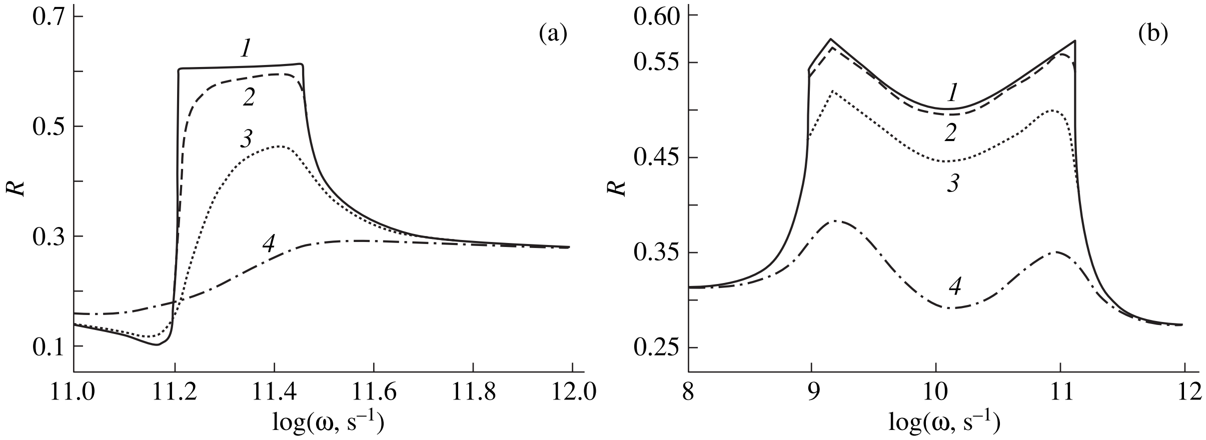

Fig. 1. Frequency dependences of the electromagnetic-wave reflectivity of the surface of a semi-infinite ferrite far away from the orientational phase transition plotted for H = 4050 Oe, $B_2 = 10^7$ erg/cm^3, and K equal to (a) 10^6 and (b) -10^6 erg/cm^3. γ: (*1*) 0, (*2*) 0.01, (*3*) 0.1, and (*4*) 0.5.

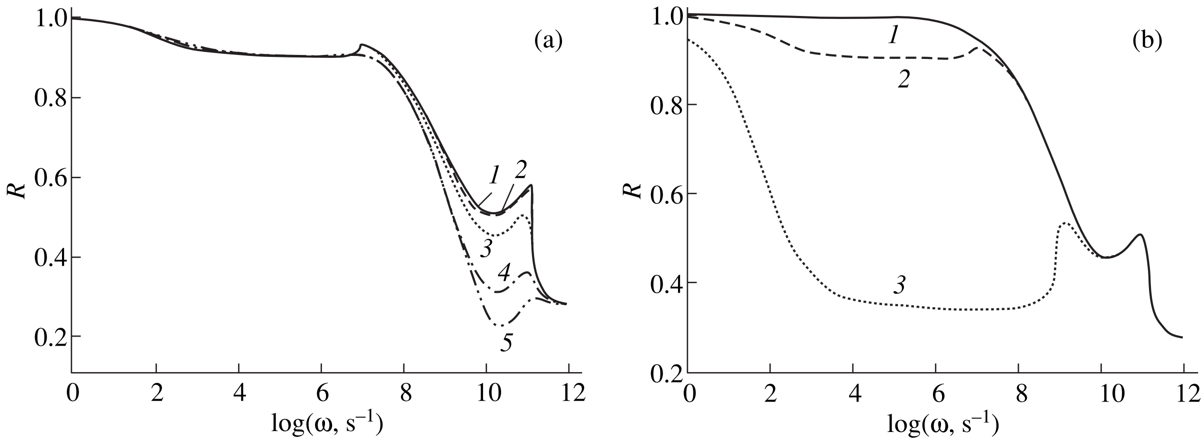

Fig. 2. Frequency dependences of the electromagnetic-wave reflectivity of the surface of a semi-infinite ferrite at the orientational phase transition plotted for H = 400 Oe and $K = -10^6$ erg/cm^3. (a) $B_2 = 10^7$ erg/cm^3 and γ is equal to (*1*) 0, (*2*) 0.01, (*3*) 0.1, (*4*) 0.5, and (*5*) 1; (b) $\gamma = 0.1$ and B_2 is equal to (*1*) 10^6, (*2*) 10^7, and (*3*) 10^8 erg/cm^3.

ity μ'_+ can be negative. For a positive value of the anisotropy constant (Fig. 1a), the peaks corresponding to the ferromagnetic, magnetoacoustic, and magnetostatic resonances are not resolved, because the frequency ω_0 ($\omega_0 \approx \omega_M$) is high compared to the frequency ω_{me} in the region far from the orientational phase transition. For negative μ'_+ and low spin-wave damping, the reflectivity R is sufficiently large and virtually constant. As the spin-wave damping increases, R decreases noticeably in the region of negative μ'_+. In the case of weak spin-wave damping, the pronounced rise in the reflectivity is also preceded by its decrease. This case corresponds to the dynamic magnetic permeability μ'_+ coinciding with the dielectric constant ε. For a negative anisotropy constant and the chosen value of the magnetic field (Fig. 1b), the frequency ω_0 is less than ω_M. As a result, the peaks corresponding to the three resonances indicated above are resolved. The amplitude of the peaks and the value of the reflectivity in the region between the peaks decrease strongly with increasing spin-wave damping. As shown by an analysis of the behavior of the reflectivity as a function of the magnetostriction constant B_2, this dependence is weak in the region far from the orientational phase transition.

At the point of orientational phase transition, R exhibits distinct peaks at all three resonances (Fig. 2). In the vicinity of ferromagnetic and magnetoacoustic resonances, the peak amplitude is considerably larger than that at magnetostatic resonance; at frequencies below the magnetoacoustic-resonance frequency ($\omega < \omega_{\text{me}}$), the value of R may be close to unity. At magnetostatic resonance, the amplitude of the peak depends substantially on the spin-wave damping, whereas in the

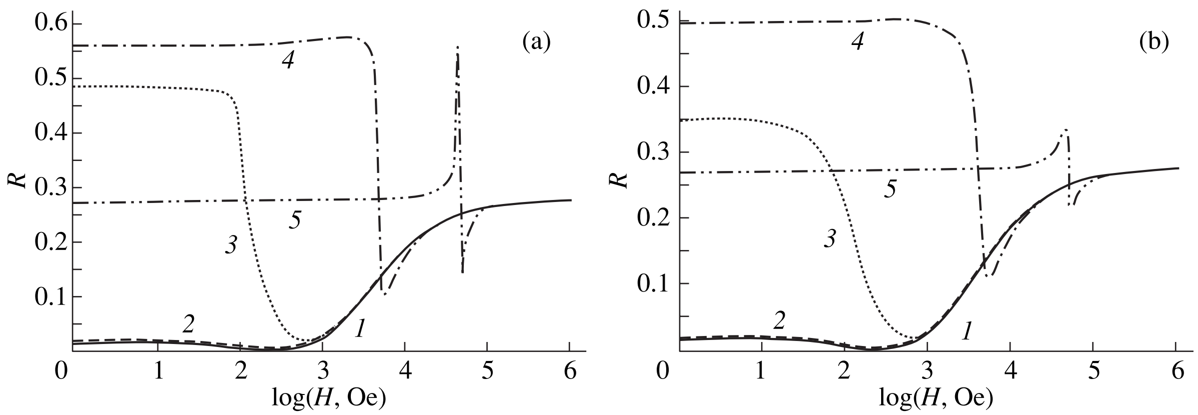

Fig. 3. Field dependences of the electromagnetic-wave reflectivity of the surface of a semi-infinite ferrite plotted for various incident-wave frequencies ω (s^{-1}): (*1*) 1×10^8, (*2*) 1×10^9, (*3*) 1×10^{10}, (*4*) 1×10^{11}, and (*5*) 1×10^{12}. $K = 10^5$ erg/cm^3, $B_2 = 10^7$ erg/cm^3, and γ is equal to (a) 0.01 and (b) 0.1.

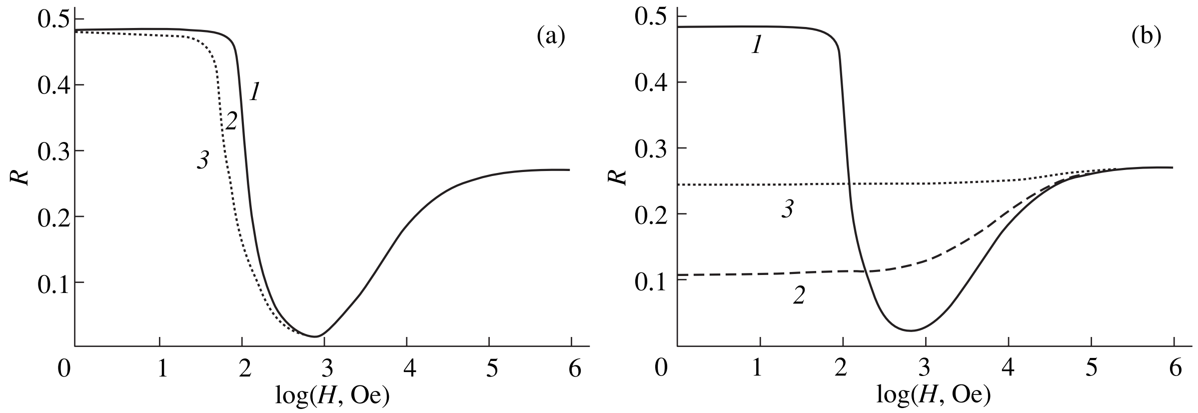

Fig. 4. Field dependences of the electromagnetic-wave reflectivity of the surface of a semi-infinite ferrite plotted for (a) various values of the magnetostriction constant B_2 (erg/cm^3): (*1*) 10^6, (*2*) 10^7, and (*3*) 10^8; $K = 10^5$ erg/cm^3, $\omega = 1 \times 10^{10}$ s^{-1}, and $\gamma = 0.01$. (b) The same plotted various values of the anisotropy constant K (erg/cm^3): (*1*) 10^5, (*2*) 10^6, and (*3*) 10^7; $B_2 = 10^7$ erg/cm^3, $\omega = 1 \times 10^{10}$ s^{-1}, and $\gamma = 0.01$.

region of the other two resonances, this dependence is weak. As seen from Fig. 2b, the EWR depends strongly on the magnitude of the magnetostriction constant. As the magnetostriction increases, the peak amplitude in the region of ferromagnetic and magnetoacoustic resonances decreases. Thus, at the orientational phase transition and for typical values of the magnetostriction constant, the EWR may be close to unity and virtually independent of the spin-wave damping within a broad frequency region.

As follows from Eq. (13), for the dynamic magnetic permeability at frequencies $\omega \ll \omega_0 + \omega_{\text{me}}$, we have $\mu_+ = \mu_- = \mu$, where

$$\mu = 1 + \frac{\omega_M(1+\gamma^2)[\omega_{s0}(1+\gamma^2) + i\gamma\omega]}{\omega_{s0}^2(1+\gamma^2) + \gamma^2\omega^2} = \mu' + i\mu''. \quad (16)$$

In this approximation, for $\varepsilon = \mu'$, the EWR reaches its minimum value:

$$R_{\min} = \frac{\mu''^2}{(\sqrt{\mu' + r} + \sqrt{2\mu'})^2(\mu' + r)}, \quad (17)$$

where $r = \sqrt{\mu'^2 + \mu''^2}$. The condition $\varepsilon = \mu'$ for $\gamma \ll 1$ can be written in the form

$$\omega_A + \omega_H = \frac{\omega_M}{\varepsilon - 1} - \omega_{\text{me}}. \quad (18)$$

It thus follows that the reflectivity can reach the minimum value given by Eq. (17) only in substances with $\omega_M/(\varepsilon - 1) > \omega_{\text{me}}$. This condition is upheld in ferrites almost without exception. Equation (18) also shows that the EWR can be controlled by properly varying either the magnetic field (the term ω_H) or the temperature (the term ω_A). For a ferrite subjected to an elastic

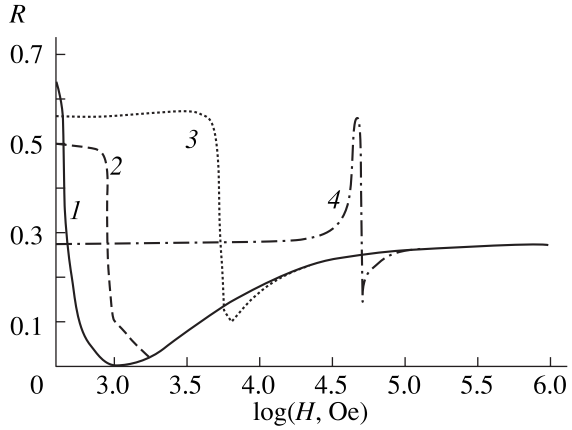

Fig. 5. Field dependences of the electromagnetic-wave reflectivity of the surface of a semi-infinite ferrite plotted for various incident-wave frequencies ω (s^{-1}): (*1*) 1×10^9, (*2*) 1×10^{10}, (*3*) 1×10^{11}, and (*4*) 1×10^{12}; and for a negative anisotropy constant $K = -10^5$ erg/cm^3. $B_2 = 10^7$ erg/cm^3, and $\gamma = 0.01$.

stress, Eq. (18) will contain a term including this stress. In this case, there appears one more possibility of controlling the EWR, namely, by varying the elastic stresses.

Let us estimate, for instance, the magnetic field strength at which $R = R_{\min}$ (for $\omega \ll \omega_0 + \omega_{me}$) for typical values of the ferrite parameters (see above) and $K = -10^6$ erg/cm^3 and $B_2 = 10^6$ erg/cm^3. Substituting these values into Eq. (18) and calculating H, we find that the EWR reaches a minimum in a field $H \approx 4$ kOe. This value is readily accessible in experiments. The condition $\omega \ll \omega_0 + \omega_{me}$ suggests that the frequencies at which a substantial decrease in R can be achieved lie in the interval including the microwave range ($\omega_0 + \omega_{me} \approx 10^{10}$ s^{-1}).

The dependence of the EWR on magnetic field is displayed graphically in Fig. 3 for various frequencies and a positive anisotropy constant. We readily see that at frequencies $\omega \ll \omega_0 + \omega_{me}$ and typical values of the magnetostriction constants, R does indeed decrease anomalously (down to zero). As follows from Eq. (16), for fields $H < \omega_A/g$, the reflectivity in this frequency region is virtually independent of the strength of the dc magnetic field. A comparison of Figs. 3a and 3b shows that spin-wave damping affects the EWR only weakly at frequencies $\omega \ll \omega_0 + \omega_{me}$.

An analysis of the field dependence of the reflectivity as a function of the magnetostriction constant shows that, in the microwave region, R varies within 1–2%, with the magnetoelastic constants varying in the interval $B_2 \sim 1 \times 10^6$–1×10^8 erg/cm^3 (Fig. 4a). The dependence of the reflectivity on the anisotropy constant is stronger (Fig. 4b).

Figure 5 presents the field dependence of the reflectivity for a negative anisotropy constant. We readily see that, at frequencies $\omega \ll \omega_0 + \omega_{me}$, R decreases substantially with decreasing magnetic field before the orientational phase transition, to reach its minimum value (17) if condition (16) is upheld. At the orientational phase transition, on the contrary, the reflection coefficient achieves its maximum value.

Thus, we have demonstrated a simple method for substantially increasing and decreasing the EWR of the surface of a semi-infinite nonconducting ferrite at experimentally accessible frequencies, temperatures, and magnetic fields; this result is important from the standpoint of application. It is shown that spin-wave damping may not affect the anomalous variation of the EWR noticeably.

ACKNOWLEDGMENTS

This study was supported by the Russian Foundation for Basic Research, project Ural no. 01-02-96445.

REFERENCES

1. L. D. Landau and E. M. Lifshitz, *Course of Theoretical Physics*, Vol. 8: *Electrodynamics of Continuous Media* (Nauka, Moscow, 1982; Pergamon, New York, 1984).
2. Yu. N. Kazantsev, M. V. Kostin, G. A. Kraftmakher, and V. V. Shevchenko, Pis'ma Zh. Tekh. Fiz. **17** (22), 19 (1991) [Sov. Tech. Phys. Lett. **17**, 792 (1991)].
3. Yu. N. Kazantsev and G. A. Kraftmakher, Pis'ma Zh. Tekh. Fiz. **19** (20), 74 (1993) [Tech. Phys. Lett. **19**, 665 (1993)].
4. Yu. N. Kazantsev and G. A. Kraftmakher, Pis'ma Zh. Tekh. Fiz. **21** (17), 61 (1995) [Tech. Phys. Lett. **21**, 708 (1995)].
5. A. I. Akhiezer, V. G. Bar'yakhtar, and S. V. Peletminskii, *Spin Waves* (Nauka, Moscow, 1967; North-Holland, Amsterdam, 1968).
6. A. A. Mukhin and A. S. Prokhorov, Tr. Inst. Obshch. Fiz. Akad. Nauk SSSR **25**, 162 (1990).
7. V. D. Buchel'nikov and V. G. Shavrov, Fiz. Tverd. Tela (Leningrad) **33** (11), 3284 (1991) [Sov. Phys. Solid State **33**, 1853 (1991)].
8. V. D. Buchel'nikov, I. V. Bychkov, and V. G. Shavrov, Fiz. Tverd. Tela (St. Petersburg) **34** (11), 3408 (1992) [Sov. Phys. Solid State **34**, 1824 (1992)].
9. V. D. Buchel'nikov, I. V. Bychkov, and V. G. Shavrov, Akust. Zh. **40** (1), 158 (1994) [Acoust. Phys. **40**, 141 (1994)].
10. V. D. Buchel'nikov, I. V. Bychkov, V. S. Romanov, and V. G. Shavrov, Vestn. Chelyab. Univ., Ser. 6: Fiz., No. 1, 96 (1998).
11. A. G. Gurevich and G. A. Melkov, *Magnetic Oscillations and Waves* (Nauka, Moscow, 1994).
12. V. D. Buchel'nikov, I. V. Bychkov, and V. G. Shavrov, Fiz. Met. Metalloved. **66** (2), 222 (1988).
13. M. I. Kaganov, Fiz. Met. Metalloved. **7** (2), 288 (1959).

Translated by G. Skrebtsov

Physics of the Solid State, Vol. 44, No. 12, 2002, pp. 2293–2297. Translated from Fizika Tverdogo Tela, Vol. 44, No. 12, 2002, pp. 2189–2192.
Original Russian Text Copyright © 2002 by Bagautdinov, Novikova.

MAGNETISM AND FERROELECTRICITY

Structural Aspects of the Dielectric Anomaly in $SC(NH_2)_2$ Crystals at 161 K

B. Sh. Bagautdinov* and M. S. Novikova**

* *Institute of Solid-State Physics, Russian Academy of Sciences, Chernogolovka, Moscow oblast, 142432 Russia*
** *Shubnikov Institute of Crystallography, Russian Academy of Sciences, Leninskiĭ pr. 59, Moscow, 117333 Russia*
e-mail: bagautdi@issp.ac.ru

Received January 14, 2002

Abstract—The residual incommensurate modulations in the ferroelectric phase of the $SC(NH_2)_2$ thiourea are investigated using single-crystal x-ray diffractometry. It is found that the structural states of the ferroelectric phase ($T < 169$ K) depend on the thermal prehistory of the crystal in the temperature range of existence of the incommensurate phase (202–169 K). The dielectric anomaly observed at $T_x = 161$ K is justified structurally. *© 2002 MAIK "Nauka/Interperiodica".*

1. INTRODUCTION

Molecular ferroelectric crystals of the $SC(NH_2)_2$ thiourea in the paraphase ($T > 202$ K) and in the ferroelectric phase ($T < 169$ K) are characterized by equitranslational orthorhombic unit cells with symmetries *Pnma* and $P2_1ma$, respectively [1]. The structure revealed in the temperature range between these two phases (i.e., in the range from $T_i = 202$ K to $T_c = 169$ K) is modulated along the **b** axis with the wave vector $\mathbf{q} = \delta\mathbf{b}^*$, where δ is the incommensurability parameter and $\mathbf{b}^*$ is the reciprocal lattice vector of the initial phase. The measured physical properties of the $SC(NH_2)_2$ compound exhibit anomalies at temperatures of 169, 171, 176, 179, and 202 K which are assigned to phase transitions. However, until presently, only the phase transitions occurring at 169, 171, and 202 K had been reliably identified by structural methods. Possibly, the phase transitions at 176 and 179 K have defied identification using x-ray diffraction because the $SC(NH_2)_2$ structure is highly sensitive to x-ray radiation and defects [2, 3]. McKenzie and Dryden [4] revealed an anomaly in the permittivity of $SC(NH_2)_2$ crystals in the ferroelectric phase at $T_x = 161$ K. Although this anomaly at T_x has been intensively examined using different methods [5–7], its nature remains unclear. Yoon *et al.* [5] showed that the intensity and shape of the permittivity peak at 161 K depend on the thermal prehistory of the studied samples. Mashiyama *et al.* [6] performed an x-ray diffraction investigation of the ferroelectric phase ($T < 169$ K) and recorded x-ray diffraction patterns containing Bragg reflections together with their satellite reflections, each shifted toward the main reflection with a decrease in the temperature. In [6], the authors attributed the residual satellite reflections to a quasi-ordered (at $50b$–$100b$ intervals) arrangement of domain walls. Since it had remained unclear how displacements of domain walls could give rise to a sharp permittivity peak at T_x, Hamano *et al.* [7] made the assumption that the number of domain walls anomalously increases in the vicinity of T_x due to 90° domain rotations. However, no hypothetical domain rotation in thiourea crystals was found by Aoyama *et al.* [8] with the use of x-ray topography. In this respect, the aim of the present work was to elucidate the relation between the structural properties and the anomalies observed in the physical properties of thiourea crystals at $T_x = 161$ K. For this purpose, we analyzed how the thermal prehistory of $SC(NH_2)_2$ crystals in the temperature range of existence of the incommensurate phase affects the x-ray diffraction patterns of these crystals in the ferroelectric phase.

2. SAMPLE PREPARATION AND EXPERIMENTAL TECHNIQUE

Single-crystal samples of the $SC(NH_2)_2$ thiourea were grown from a methanol solution at room temperature. Plane-parallel samples $2.0 \times 2.5 \times 0.5$ mm in size were cut normally to the ferroelectric axis **a**. The samples prepared were placed in a cryostat ensuring temperature stabilization with an accuracy of 0.1 K. The measurements were performed on a Siemens D500 x-ray diffractometer (CuK_α radiation) adapted to single-crystal goniometry. The satellite reflections were recorded in the (*hk*0) plane (θ scan mode) and in the undistorted reciprocal lattice along the $\mathbf{b}^*$ axis (**q** scan mode). Diffuse scattering was studied by recording the intensity distribution over wide regions of the reciprocal lattice.

3. RESULTS AND DISCUSSION

Figure 1 shows the temperature dependences of the intensity of the (400) Bragg and (4δ0) satellite reflections over a wide temperature range of structural transformations. Upon cooling of the studied crystal below T_c = 169 K, the intensity of the (400) reflection drastically increases, whereas the intensity of the (4δ0) reflection drastically decreases. The intensity and shape of the observed reflections at temperatures below T_c substantially depend on the thermal prehistory of the crystal in the incommensurate phase. When the crystal is continuously cooled in the temperature range of existence of the incommensurate phase, the intensity of the (400) reflection spontaneously increases in the ferroelectric phase. The subsequent heating leads to a spontaneous decrease in the intensity of this reflection upon phase transition to the incommensurate phase at T_c. Note that, in this case, the temperature hysteresis coincides with the hysteresis ΔT = 1.0 K determined from the jump in the unit cell parameters at T_c [9]. However, the cooling with thermal annealings of the crystal in the temperature range of existence of the incommensurate phase results in a smearing of the phase transition at T_c. Figure 2 depicts the intensity profiles of the (400) reflection in the ferroelectric phase after continuous and stepwise (holding for 30 min at 3-K intervals) cooling in the temperature range of the incommensurate phase. It can be seen that the peak intensity of the (400) reflection upon a stepwise cooling in the temperature range of the incommensurate phase is less than that upon a continuous cooling. Moreover, in the former case, the reflection is broadened along the **b*** direction. In order to elucidate the origin of this effect, we examined in detail the intensity distribution in the vicinity of the (400) reflection. As can be seen from Fig. 3, the positions corresponding to satellite reflections in the incommensurate phase are characterized by diffuse scattering.

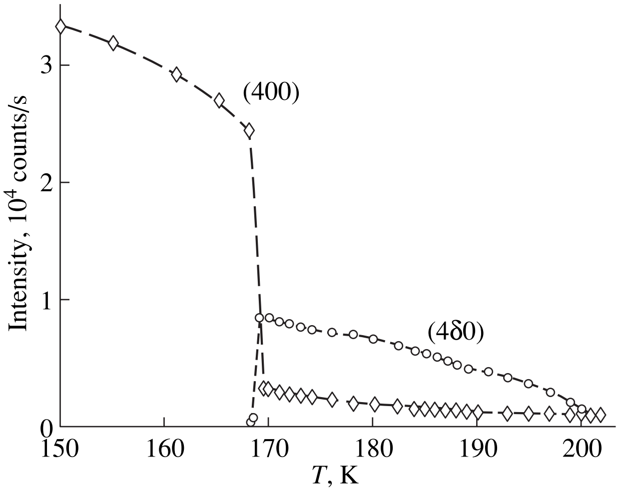

Fig. 1. Temperature dependences of the intensity of the (400) Bragg and (4δ0) satellite reflections upon cooling of the studied sample.

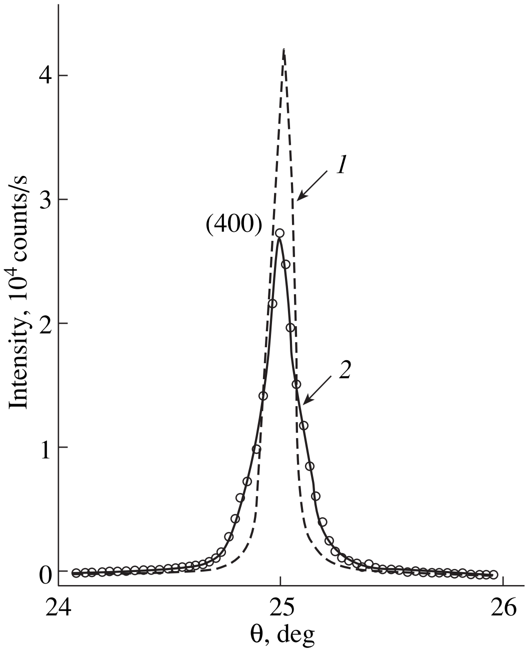

Fig. 2. Profiles of the (400) Bragg reflection at T = 167 K after (*1*) continuous cooling and (*2*) cooling with annealings in the temperature range of existence of the incommensurate phase (θ scanning is performed parallel to the **b*** axis).

In the case where the sample is not cooled below T_x = 161 K, residual satellite reflections are observed over the entire temperature range from 169 to 161 K and the transition from the incommensurate phase to the ferroelectric phase becomes smeared. Upon cooling below 161 K and subsequent heating, satellite reflections are not observed in the range 161–169 K but spontaneously appear in the incommensurate phase at T_c = 169 K. Therefore, the x-ray diffraction data indicate that structural modulations are absent at temperatures below 161 K. For the purpose of examining the structural transformations occurring in the ferroelectric phase in the vicinity of T_x in greater detail, we performed prolonged thermal annealings of the crystal in the temperature range of existence of the incommensurate phase. As is known, thermal annealing in the temperature range of the incommensurate phase brings about the formation of defect density waves [1, 3]. After the preliminary stabilization of the crystal first at T_{st} = 181 K for a day and then at T_{th} = 171 K for 6 h (in the temperature range of existence of the incommensurate phase), the diffraction patterns measured in the temperature range of the ferroelectric phase, apart from the persistent satellite reflections, exhibit additional reflections at the positions corresponding to the wave

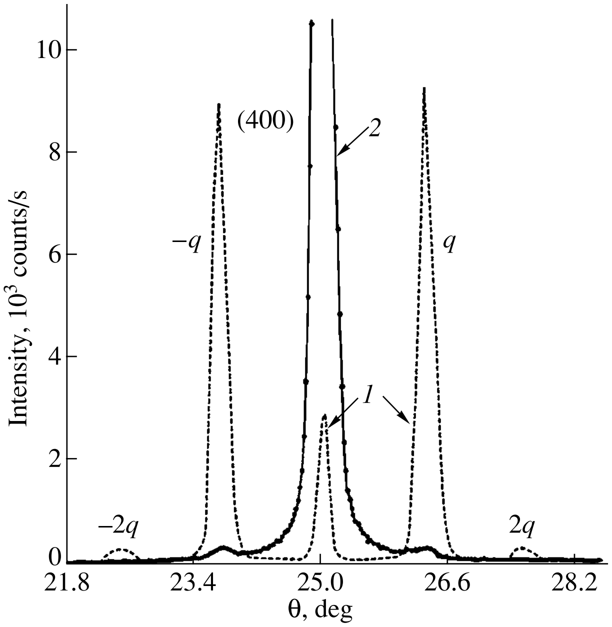

Fig. 3. Intensity distributions in the vicinity of the (400) reflection: (*1*) the incommensurate phase at $T = 172$ K and (*2*) the ferroelectric phase at $T = 166$ K.

vectors ($\mathbf{q}_{st} - \mathbf{q}_{th}$) and $-(\mathbf{q}_{st} - \mathbf{q}_{th})$ (Fig. 4). The reflections observed at the positions corresponding to the sums and differences of the wave vectors suggest the formation of modulations with a superposition of coexisting modulation waves throughout the crystal [3]. A model illustrating the formation of new modulations (beats) due to a superposition of waves with vectors $\mathbf{q}_{st}$ and $\mathbf{q}_{th}$ is depicted in Fig. 5.

It can be seen that, compared to the initial modulations, the modulations formed by their superposition are characterized by larger atomic displacements at the positions with coinciding phases and by smaller atomic displacements at the positions with phases differing in sign. The persistence of the satellite reflections at temperatures below T_c for crystals with defect density waves indicates that ordering of defects in the incommensurate phase induces modulations of the ferroelectric phase. After cooling below T_c, the satellite reflections become metastable and disappear with time or during further cooling (Figs. 6, 7). Upon disordering of defect density waves, the residual satellite reflections transform into diffuse scattering, which (with time and during cooling) shifts toward the nearest Bragg reflection, whereas the intensity of the main reflection increases. The intensity distributions in the vicinity of the (400) reflection at temperatures of 165 and 159 K are shown in Figs. 6 and 7, respectively. At temperatures above T_x, the satellite reflections are retained for a time comparable in length to the stabilization time in the incommensurate phase (Fig. 6). Upon cooling below $T_x = 161$ K, the satellite reflections transform into diffuse scattering (Fig. 7).

It should be noted that the modulations of the incommensurate phase of thiourea crystals, especially in the vicinity of the temperature T_c, bring about the appearance of satellite reflections with orders higher than the first order (first-order and second-order satellite reflections are shown in Figs. 3 and 6). Therefore, in order to describe correctly the shape of an atomic displacement wave, it is necessary to include higher harmonics of wave vectors [1]. These modulations at temperatures in the vicinity of T_c have a domainlike

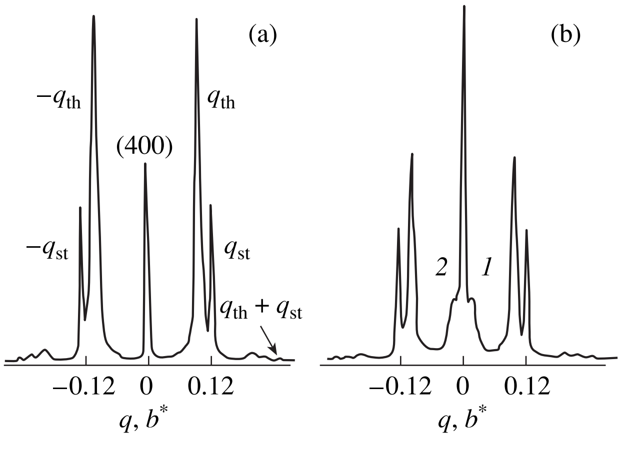

Fig. 4. Intensity distributions in the vicinity of the (400) reflection at temperatures of (a) 171 and (b) 166 K for the crystal with a defect density wave induced through temperature stabilization at $T_{st} = 182$ K for a day and at $T_{th} = 171$ K for 6 h. In the ferroelectric phase, the side peaks in the vicinity of the Bragg reflection correspond to (*1*) ($\mathbf{q}_{st} - \mathbf{q}_{th}$) and (*2*) ($\mathbf{q}_{th} - \mathbf{q}_{st}$) wave vectors.

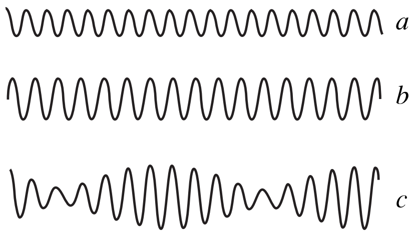

Fig. 5. Atomic displacements due to a superposition of modulations: (*a*) modulations with wave vector $\mathbf{q}_1$ and $y_1 = A_1\sin(q_1x + \varphi_1)$, (*b*) modulations with wave vector $\mathbf{q}_2$ and $y_2 = A_2\sin(q_2x + \varphi_2)$, and (*c*) modulations as a result of superposition of atomic displacements corresponding to the waves y_1 and y_2.

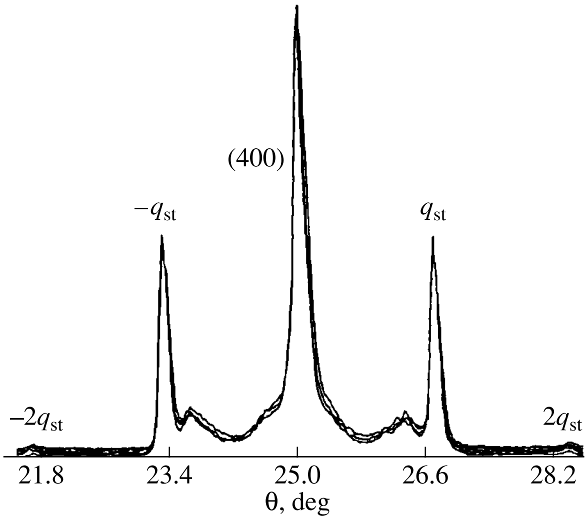

Fig. 6. Distribution of the scattering intensity in the vicinity of the (400) reflection at T = 165 K ($T > T_x$ = 161 K) for the crystal with a defect density wave.

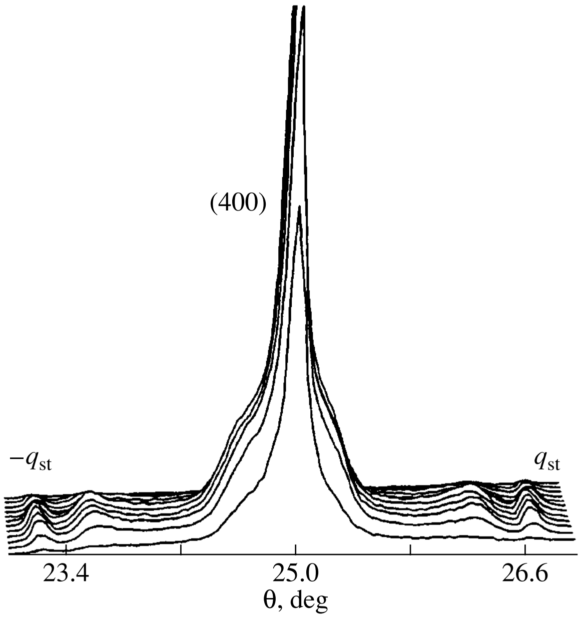

Fig. 7. Distribution of the scattering intensity in the vicinity of the (400) reflection at T = 159 K ($T < T_x$ = 161 K) for the crystal with a defect density wave.

structure, and the phase of modulations is disturbed at domain walls (solitons). In the modulated phase, the solitons are regularly arranged and their planes are perpendicular to the modulation vector **q**. Upon transition to the ferroelectric phase, a number of soliton boundaries are annihilated, whereas the other soliton boundaries transform into walls between ferroelectric domains. The structure of a domain wall depends on the atomic displacements in contiguous domains. If the displacements of atoms are larger than the amplitudes of their thermal vibrations, the structure involves thick domain walls (for elimination of discontinuities in the crystal lattice). As follows from the x-ray diffraction patterns, the domains in the ferroelectric phase of thiourea crystals are perpendicular to the [010] direction and have a thickness of 2000–4000 Å, whereas the thickness of domain walls is approximately equal to 1000 Å [8]. Since the superposition of the modulation waves leads to an increase in the displacement amplitude of in-phase atoms (Fig. 5), it can be assumed that thicker domain walls are formed in the crystal with defect density waves. In the modulated state of the structure with thick domain walls in crystals with defect density waves, the satellite reflections are more stable upon transition to the ferroelectric phase. Unlike the modulations in the incommensurate phase, the modulations of twin boundaries in the ferroelectric phase are affected by electric fields of the domains involved. It is known that the modulations of thiourea crystals disappear in electric fields [10]. We can assume that spontaneous electric fields induced at a temperature of 161 K are critical for residual interdomain modulations in the thiourea crystals. The persistence of the satellite reflections (associated with the modulated state of the structure) upon cooling of the crystal to T_x = 161 K and their disappearance at lower temperatures suggest the occurrence of a phase transition from the modulated structure to a normal structure at a temperature T_x. The intensity distribution of the satellite reflections and their metastable properties at $T < T_c$ demonstrate that the modulations are partly retained in the structure. Therefore, the phase transition at T_x hypothetically occurs in twin boundaries.

4. CONCLUSION

Thus, the specific feature of the $SC(NH_2)_2$ structure in the temperature range of existence of the ferroelectric phase is that its modulations are retained after the transition from the incommensurate phase to the ferroelectric phase at T_c = 169 K and disappear at temperatures below T_x = 161 K. We made the assumption that the transformation of the modulated domain boundaries into normal boundaries at a temperature T_x is responsible for the anomalies in the physical properties observed in [4, 5].

ACKNOWLEDGMENTS

We would like to thank V.K. Magataev for supplying the crystals studied in this work, I.M. Shmyt’ko for furnishing the cryostat used in our measurements, and S.S. Khasanov for his assistance in investigating the $SC(NH_2)_2$ crystals.

REFERENCES

1. H. Z. Cummins, Phys. Rep. **185**, 211 (1990).
2. G. Andre, D. Durand, F. Denoyer, *et al.*, Phys. Rev. B **35**, 2909 (1987).
3. B. Sh. Bagautdinov and I. M. Shmyt'ko, Pis'ma Zh. Éksp. Teor. Fiz. **59** (3), 171 (1994) [JETP Lett. **59**, 182 (1994)].
4. D. R. McKenzie and J. S. Dryden, J. Phys. C **6**, 67 (1973).
5. J. Yoon, Y. J. Kwag, Y. Cho, and S. Kwun, J. Phys. Soc. Jpn. **62**, 327 (1993).
6. H. Mashiyama, M. Sakamoto, H. Nakamura, *et al.*, J. Phys. Soc. Jpn. **60**, 1755 (1991).
7. K. Hamano, T. Sujiyama, and H. Sakata, J. Phys. Soc. Jpn. **59**, 4476 (1990).
8. J. Aoyama, S. Suzuki, and M. Takagi, J. Phys. Soc. Jpn. **61**, 3613 (1992).
9. I. M. Shmyt'ko, B. Sh. Bagautdinov, and V. K. Magataev, Fiz. Tverd. Tela (St. Petersburg) **38** (7), 2223 (1996) [Phys. Solid State **38**, 1224 (1996)].
10. J. P. Jamet, J. Phys. Lett. **42**, 123 (1981).

Translated by O. Borovik-Romanova

Physics of the Solid State, Vol. 44, No. 12, 2002, pp. 2298–2308. Translated from Fizika Tverdogo Tela, Vol. 44, No. 12, 2002, pp. 2193–2203.
Original Russian Text Copyright © 2002 by Kukushkin, Zakharov.

MAGNETISM AND FERROELECTRICITY

Switching Kinetics of Ferroelastic Ferroelectrics

S. A. Kukushkin* and M. A. Zakharov**
** Institute of Problems of Mechanical Engineering, Russian Academy of Sciences, Vasil’evskiĭ ostrov,*
Bol’shoĭ pr. 61, St. Petersburg, 199178 Russia
e-mail: ksa@math.ipme.ru
*** Novgorod State University, Novgorod, 173003 Russia*

Received January 24, 2002

Abstract—Switching kinetics of uniaxial ferroelastic ferroelectrics (FFs) in external electric and stress fields is studied using classical theory of nucleation and growth. The stage in which the polarization and deformation reversal involves the main body of the FF and the final stage (Ostwald ripening) of the FF switching are studied with allowance for the change in the repolarization and redeformation during the phase transition. The time dependences of the repolarization and redeformation are found, and equations are derived from which the polarization current and the deformation flux, as well as their time dependence, can be calculated. The calculated main characteristics of the FF switching are compared with the experimental data for switching of Rochelle salt single crystals. © *2002 MAIK “Nauka/Interperiodica”.*

1. INTRODUCTION

The process of switching of ferroelectrics and related materials placed in an external field is a first-order phase transition (see, e.g., [1]) and can be divided, for convenience, into three characteristic steps [2–4]. In the initial stage, nuclei of the new phase arise as fluctuations; the system as a whole does not respond to the formation of domains whose orientation is different from that of the parent medium, and the thermodynamic parameters of the system remain virtually unchanged. As shown in [2], the main characteristic of the initial stage of switching is the steady-state flux, determining the intensity of the process of nucleation. At the second stage, the switching of structural elements (unit cells) involves the main body of the initial single-domain sample, which causes the internal field of the crystal to change. Finally, at the third, final stage, Ostwald ripening (mergence of fine nuclei with larger ones) occurs and the mean nucleus size increases. The interphase boundary decreases in area due to an energetically favorable decrease in the number of domain spacers, and the free energy of the system decreases.

Such a division of a phase transition into characteristic steps is a crucial point of the theory of nucleation and growth and is justified for phase transitions in metastable condensed systems, including supersaturated solutions and supercooled melts, and for switching of ferroelectrics. The kinetic theory of switching of uniaxial ferroelectric crystals was developed in [2–4], and the thermodynamics and kinetics of switching of uniaxial ferroelastic ferroelectrics (FFs) at its initial stage were considered in [5]. A noticeable advance in the studying of switching of ferroelectrics was made in [6–9].

In this paper, we continue the theoretical study made in [5] into the switching kinetics of uniaxial FFs placed in external electric and stress fields and consider the second and third steps of the switching process. In Section 2, we analyze the stage of mass repolarization and redeformation of a uniaxial FF; the corresponding set of kinetic equations is derived, and its solution is found. In Section 3, the kinetics of the FF switching at its final stage is investigated and the most likely mechanisms of the domain growth are discussed. In Section 4, we determine the polarization current and the deformation flux; the latter quantity is a switching characteristic of ferroelastics alone and is a direct analog of the polarization current in ferroelectrics. According to [10], the deformation flux in ferroelastics arises as a result of generation of stress waves (acoustic emission), which takes place during reversible plastic deformation of a crystal. Finally, in Section 5, the main characteristics of FF switching calculated in this paper are compared with the experimental data for switching of single crystals of Rochelle salt, which is a classical uniaxial FF.

2. KINETICS OF POLARIZATION AND DEFORMATION REVERSAL INVOLVING THE MAIN BODY OF THE FERROELASTIC FERROELECTRIC

Preparatory to discussing the FF switching, we will refresh the reader’s memory with the basic facts employed in this paper, as well as with the terminology and notation used in the preceding paper [5]. It is well known [11] that the order parameter η of the lower symmetry phase of a uniaxial FF transforms like a component of a polar vector and, simultaneously, like a component of a second-rank tensor. This order parameter is proportional to both the spontaneous polarization ($P_x = a_1\eta$) and the spontaneous strain ($U_{yz} = a_2\eta$). Here, the x axis is taken to be along the polar axis of the crystal and a_1 and a_2 are the coefficients of the η–E_x and η–σ_{yz} cross terms, respectively, in the thermodynamic potential describing the FF, where E_x is the x component of the electric field and σ_{yz} is the yz component of the stress field applied to the FF. We note that, in uniaxial FFs, ferroelastic domains coincide with ferroelectric ones; therefore, we will refer to all of them as ferroelastic-ferroelectric domains [5]. Further, the process of repolarization of ferroelectric domains and of redeformation of ferroelastic domains, which proceed simultaneously during switching of a uniaxial FF, will be referred to as repolarization–redeformation. Finally, along with the order parameter η, polarization P_x, and strain U_{yz}, we will use the corresponding (specific) quantities $\eta_\omega = \eta\omega$, $p_x = P_x\omega = a_1\eta_\omega$, and $u_{yz} = U_{yz}\omega = a_2\eta_\omega$ for a unit cell of the crystal (ω is the unit cell volume). In particular, for a ferroelastic-ferroelectric domain of size n, the corresponding values of the order parameter, polarization, and strain are $\eta_n = \eta_\omega n$, $P_{xn} = p_x n = a_1\eta_n$, and $U^n_{yz} = u_{yz}n = a_2\eta_n$, respectively.

In order to describe the switching kinetics of a uniaxial FF in terms of the classical theory of nucleation and growth, we use the Fokker–Planck(Zel'dovich) equation [12]

$$\frac{\partial f(n,t)}{\partial t} + \frac{\partial}{\partial n}[V_n f(n,t)] = \frac{\partial}{\partial n}\left[D_n\frac{\partial f(n,t)}{\partial n}\right], \qquad (1)$$

where $f(n, t)$ is the distribution function of repolarized and redeformed domains in the number of unit cells in them, $V_n = (dn/dt)$ is the growth velocity of a domain of size n in the space of domain sizes, and D_n is the diffusion coefficient of repolarization–redeformation nuclei in the domain-size space.

It is important that Eq. (1) can be treated as a continuity equation in domain-size space; the corresponding flux $J(n, t)$ consists of two parts, “hydrodynamic” $V_nf(n, t)$ and “fluctuation” $D_n[\partial f(n, t)/\partial n]$. The former component of the flux corresponds to the change in the distribution function of repolarized and redeformed domains associated with their growth with velocity V_n, while the latter component describes fluctuations in the domain size.

This kinetic equation is valid at any stage of the FF switching. However, for the stage where the repolarization and redeformation involve the main body of the FF, the evolution equation (1) can be significantly simplified. A distinctive feature of this stage is that the major portion of nuclei have reached the critical size and the spontaneous formation of supercritical nuclei can occur only as a result of a macroscopic (and, hence, very unlikely) fluctuation [12, 13]. In this connection, we note that the fluctuation component of the flux in the Fokker–Planck equation is dominant at the initial stage of the FF switching (studied in [2, 5]), whereas the hydrodynamic component becomes dominant at later stages [14]. Therefore, we can neglect the fluctuation component and write the basic kinetic equation (1) in the form

$$\frac{\partial f(n,t)}{\partial t} + \frac{\partial}{\partial n}[V_n f(n,t)] = 0. \qquad (2)$$

To solve the Fokker–Planck equation (2), we need an explicit expression for the growth velocity V_n of a nucleus in the size space. Such an expression for a nucleus of a ferroelastic-ferroelectric domain in the form of a cylinder was found in [5] to be

$$V_n = 2(\pi H\omega)^{1/2}\beta_0 \times \frac{2\eta_\omega(a_1E_x + a_2\sigma_{yz} - a_1E_{xn} - a_2\sigma^n_{yz})}{k_BT}n^{1/2} \qquad (3)$$
$$= 2(\pi H\omega)^{1/2}\beta_0\frac{2p_x(E_x - E_{xn}) + 2u_{yz}(\sigma_{yz} - \sigma^n_{yz})}{k_BT}n^{1/2},$$

where H is the height of the nucleus, which can be estimated from the formula $H \sim w^{1/3}$; β_0 is the steady-state flux of unit cells; E_{xn} and σ^n_{yz} are the electric and stress components of the internal field for a nucleus of size n; k_B is the Boltzmann constant; and T is the temperature of the crystal.

At the FF switching stage under study, the repolarization and redeformation vary only slightly and are still fairly large [3]. Therefore, the size n of arising and growing nuclei far exceeds the critical value ($n \gg n_c$) and Eq. (3) can be rewritten as

$$V_n = 2C[a_1E_x(t) + a_2\sigma_{yz}(t)]n^{1/2}, \qquad (4)$$

where $C = 2\beta_0(\pi H\omega)^{1/2}\eta_\omega/k_BT$.

A change in the repolarization and redeformation of the FF is due to the formation of a great number of repolarization–redeformation nuclei, which causes the internal field in the parent medium to change. However, the total number of unit cells, which are elementary carriers of the specific order parameter η_ω, specific polarization (dipole moment) p_x, and specific strain u_{yz}, remains unchanged. Therefore, following [3], the kinetic equation (2) should be supplemented by the corresponding balance equation. This latter equation can be written in a differential form as

$$J(E^0_x, \sigma^0_{yz})\frac{\eta_\omega}{\eta_{10}} = \frac{d\xi_\eta}{dt} + \frac{\eta_\omega}{\eta_{10}}\int_0^\infty V_n f(n,t)dn, \qquad (5)$$

where ξ_η is the relative repolarization–redeformation (RR), which is defined in [5]; η_{10} is the equilibrium value of the order parameter; η_ω is the specific order parameter (per unit cell of volume ω); $J(E^0_x, \sigma^0_{yz})\eta_\omega/\eta_{10}$ is the source of the repolarization and redeformation produced by the external electric and stress fields; and

$(\eta_\omega/\eta_{10})\int_0^\infty V_n f(n, t)dn$ is the rate of transformation of polarization and deformation into the new phase.

It should be noted that the balance equation (5) is equivalent to two conservation laws. Indeed, in the case of a uniaxial FF, the relative RR ξ_η is identical to the relative repolarization ξ_P and to the relative redeformation ξ_U [5].

Therefore, Eq. (5) can be rewritten in the form

$$J(E_x^0, \sigma_{yz}^0)\frac{p_x}{P_{x10}} = \frac{d\xi_P}{dt} + \frac{p_x}{P_{x10}}\int_0^\infty V_n f(n, t)dn \qquad (6)$$

or

$$J(E_x^0, \sigma_{yz}^0)\frac{u_{yz}}{U_{yz}^{10}} = \frac{d\xi_U}{dt} + \frac{u_{yz}}{U_{yz}^{10}}\int_0^\infty V_n f(n, t)dt, \qquad (7)$$

where P_{x10} and U_{yz}^{10} are the equilibrium values of the polarization and strain, respectively. Equation (6) is the law of conservation of the total dipole moment of the crystal [3], and Eq. (7) is a direct mechanical analog of this law.

Following [3], we define the source of repolarization–redeformation $J(E_x^0, \sigma_{yz}^0)$ as the number of unit cells of the parent phase (per unit volume) in which the sign of the order parameter η_ω is reversed (in a unit time) under the action of an external field. In other words, this quantity is the number of structural elements of the FF in a unit volume that are switched (i.e., repolarized and redeformed) in a unit time. Using the expressions derived in [2, 5] when calculating the domain growth velocity, we obtain

$$\begin{aligned} J(E_x^0, \sigma_{yz}^0) &= \beta_0''\frac{2\eta_\omega(a_1E_x^0 + a_2\sigma_{yz}^0 - a_1\bar{E}_x - a_2\bar{\sigma}_{yz})}{k_BT} \\ &= \beta_0''\frac{2p_x(E_x^0 - \bar{E}_x) + 2u_{yz}(\sigma_{yz}^0 - \bar{\sigma}_{yz})}{k_BT}, \end{aligned} \qquad (8)$$

where $\beta_0'' = N_V\nu\exp(-V_0/k_BT)$, with V_0 being the height of the potential barrier for the sign reversal of the (specific) order parameter η_ω of a unit cell in a zero external field, N_V being the number of unit cells per unit volume (which can be estimated from the formula $N_V \sim \omega^{-1}$), and ν being the vibration frequency of atoms in a unit cell; E_x^0 and σ_{yz}^0 are the external electric and stress fields of the source at the moment the repolarization–redeformation began to involve the main body of the FF; and $\bar{E}_x$ and $\bar{\sigma}_{yz}$ are the electric and stress field, respectively, that acted on the FF before the source began to operate.

When considering the kinetics of the FF switching at the initial stage in [5], we defined the RR $\Delta\eta = |\eta - \eta_{10}|$ and the relative RR $\xi_n = (\Delta\eta/\eta_{10})$. To describe the FF switching stage under study, we introduce analogous quantities

$$\Delta^0 = \eta^0 - \bar{\eta} = \Delta\eta^0 - \Delta\bar{\eta}, \qquad (9)$$

$$\xi_\eta^0 = \frac{\Delta^0}{\eta_{10}} = \frac{\Delta\eta^0 - \Delta\bar{\eta}}{\eta_{10}}. \qquad (10)$$

In the case where the electric and stress fields applied to the crystal are relatively weak, the RRs $\Delta\eta^0$ and $\Delta\bar{\eta}$ depend on these fields as [5]

$$\Delta\eta^0 = \frac{a_1E_x^0 + a_2\sigma_{yz}^0}{2\alpha(T_c - T)}, \quad \Delta\bar{\eta} = \frac{a_1\bar{E}_x + a_2\bar{\sigma}_{yz}}{2\alpha(T_c - T)}, \qquad (11)$$

where α is the coefficient of the quadratic term η^2 in the expansion of the incomplete thermodynamic potential of the FF in the vicinity of the Curie point T_c.

In this case, substituting Eqs. (8) and (11) into Eq. (10), we find

$$\begin{aligned} \xi_\eta^0 &= \frac{\Delta\eta^0 - \Delta\bar{\eta}}{\eta_{10}} = \frac{1}{\eta_{10}}\frac{a_1E_x^0 + a_2\sigma_{yz}^0 - a_1\bar{E}_x - a_2\bar{\sigma}_{yz}}{2\alpha(T_c - T)} \\ &= \frac{J(E_x^0, \sigma_{yz}^0)\eta_\omega\tau}{\eta_{10}}, \end{aligned} \qquad (12)$$

where

$$\tau = \frac{k_BT}{4\alpha(T_c - T)\beta_0''\eta_\omega^2}. \qquad (13)$$

On the other hand, below the Curie point, according to [11], the dielectric susceptibility is $\chi_{xx}^{T,\sigma_{yz}}\varepsilon_0 = a_1^2/2\alpha(T_c - T)$ (where ε_0 is the permittivity of vacuum) and the elastic compliance is $s_{yzyz}^{T,E_x} = a_2^2/2\alpha(T_c - T)$; therefore, Eq. (13) for the time parameter τ can be represented in two equivalent forms:

$$\tau = \frac{k_BT\chi_{xx}^{T,\sigma_{yz}}\varepsilon_0}{2\beta_0''p_x^2}, \qquad (14)$$

$$\tau = \frac{k_BTs_{yzyz}^{T,E_x}}{2\beta_0''u_{yz}^2}. \qquad (15)$$

Substituting Eq. (12) into the balance equation (5) yields

$$\frac{\xi_\eta^0}{\tau} = \frac{d\xi_0}{dt} + \frac{\eta_\omega}{\eta_{10}}\int_0^\infty V_n f(n, t)dn. \qquad (16)$$

If the time parameter τ is small, the derivative $d\xi_n/dt$ can be neglected at the switching stage under study. In this case, Eq. (16) can be written as

$$\xi_\eta^0 = \tau \frac{\eta_\omega}{\eta_{10}} \int_0^\infty V_n f(n, t) dn \tag{17}$$

and the balance equations (6) and (7) take the form

$$\xi_P^0 = \tau \frac{p_x}{P_{x10}} \int_0^\infty V_n f(n, t) dn, \tag{18}$$

$$\xi_U^0 = \tau \frac{u_{yz}}{U_{yz}^{10}} \int_0^\infty V_n f(n, t) dn. \tag{19}$$

The kinetic equation (2) [with the domain growth velocity given by Eq. (4)] and the balance equation (17) constitute a closed set describing the stage in which the repolarization and redeformation involve the main body of the uniaxial FF after the major portion of nuclei have reached the critical size.

It should be noted that this set of equations is applicable for describing both the kinetics of mass switching of a uniaxial ferroelectric placed in an external electric field and the kinetics of mass switching of a proper ferroelastic subjected to an external stress field. For example, in order to describe the switching of a uniaxial ferroelectric (considered in [3]), one should put the specific strain $u_{yz} = 0$ in Eq. (3) for the growth velocity of a nucleus and, instead of the balance equation (17), make use of Eq. (18), with the time parameter τ given by Eq. (14). The second particular case mentioned above (the switching of a proper ferroelastic), which we have not considered separately, can be described in a similar way. In this case, one should put the specific polarization (dipole moment) $p_x = 0$ in Eq. (3) for the growth velocity of a nucleus and, instead of the balance equation (17), make use of Eq. (19), with the time parameter τ given by Eq. (15). Clearly, the Fokker–Planck equation (2) remains unchanged in both these particular cases.

The set of equations derived above for describing the stage of mass repolarization and redeformation of a uniaxial FF can be solved analytically. A method for solving these equations in the case of uniaxial ferroelectrics was proposed in [3]; the results obtained in [3] will be employed below.

Following [3], we express the growth velocity of nuclei in Eq. (4) in terms of the relative RR $\xi_n(t)$:

$$V_n = 2 \frac{\xi_n(t)}{t_0} n^{1/2}, \tag{20}$$

where the characteristic growth time t_0 is defined as

$$\begin{aligned} t_0 &= \frac{k_B T}{2\beta_0 (\pi H \omega)^{1/2} \eta_\omega \eta_{10} 2\alpha (T_c - T)} \\ &= \frac{k_B T \chi_{xx}^{T, \sigma_{yz}} \varepsilon_0}{2\beta_0 (\pi H \omega)^{1/2} p_x P_{x10}} \\ &= \frac{k_B T s_{yzyz}^{T, E_x}}{2\beta_0 (\pi H \omega)^{1/2} u_{yz} U_{yz}^{10}}. \end{aligned} \tag{21}$$

We introduce the dimensionless nucleus radius $\rho = n^{1/2}$ and pass over from the distribution function of domains in the number of unit cells in them $f(n, t)$ to the distribution function of domains in dimensionless radius, $g(\rho, t)$. Using the relation $f(n, t)dn = g(\rho, t)d\rho$, the kinetic equation (2) and the balance equation (17) can be rewritten in the new variables as

$$\frac{\partial g(\rho, t)}{\partial t} + \frac{\xi_\eta(t)}{t_0} \frac{\partial}{\partial \rho} [g(\rho, t)] = 0, \tag{22}$$

$$\frac{\xi_{\eta 0}}{\xi_\eta(t)} - 1 = \lambda \int_0^\infty \rho g(\rho, t) d\rho, \tag{23}$$

where $\xi_{\eta 0} = |\eta_0 - \eta_{10}|/\eta_{10}$ [i.e., $\xi_\eta(0) = \xi_{\eta 0}$] and

$$\begin{aligned} \lambda &= \frac{k_B T}{t_0 \beta_0'' 2\alpha (T_c - T) \eta_\omega \eta_{10}} \\ &= \frac{k_B T \chi_{xx}^{T, \sigma_{yz}} \varepsilon_0}{t_0 \beta_0'' p_x P_{x10}} = \frac{k_B T s_{yzyz}^{T, E_x}}{t_0 \beta_0'' u_{yz} U_{yz}^{10}}. \end{aligned} \tag{24}$$

In accordance with [3], for the set of equations (22) and (23) to have a unique solution, this set should be supplemented by the initial and boundary conditions $g(\rho, 0) = 0$ $(\rho > \rho_c)$ and $g(0, t) = I(\xi_\eta(t)) t_0 / \xi_\eta(t)$.

This set of equations describes the switching kinetics of a uniaxial FF and is a natural generalization of the equations derived in [3] for describing the stage of mass repolarization of a uniaxial ferroelectric. A solution to this set allows one to find the main characteristics of the switching stage under study, such as the flux of domains of repolarization–redeformation, the density of repolarized and redeformed ferroelastic-ferroelectric nuclei, the time dependence of the relative RR, and the size distribution function of domains. For this purpose, we use the expressions derived in [3] (following the method developed in [12]) and obtain the following results based on the solution to the coupled equations (22) and (23). The flux of repolarization–redeformation domains at time t calculated in first-order perturbation theory has the form

$$I(t) = \frac{I(\xi_{\eta 0}) \exp[-T^k(t) \varphi_k(T(t))]}{1 + (1/\Gamma) T^k(t) \varphi_k(T(t))}. \tag{25}$$

The density of repolarized and redeformed nuclei at time t is given by

$$N(t) = I(\xi_{\eta 0}) t_k \varphi_k(T(t)). \tag{26}$$

The time dependence of the relative RR is found to be

$$\xi_\eta(t) = \frac{\xi_{\eta 0}}{1 + (1/\Gamma) T^k(t) \varphi_k(T(t))}, \tag{27}$$

and, finally, the size (dimensionless-radius) distribution function of domains has the form

$$f(\rho, t) = \begin{cases} \dfrac{I(\xi_{\eta 0}) t_0}{\xi_{\eta 0}} \exp\left[-\left(T(t) - \dfrac{t_0 \rho}{t_k \xi_{\eta 0}}\right)^k \varphi_k\left(T(t) - \dfrac{t_0 \rho}{t_k \xi_{\eta 0}}\right)\right] \\ \text{for} \quad \rho \le \dfrac{\xi_{\eta 0} t_k}{t_0} T(t) \\ 0 \quad \text{for} \quad \rho > \dfrac{\xi_{\eta 0} t_k}{t_0} T(t). \end{cases} \tag{28}$$

Let us discuss the quantities involved in Eqs. (25)–(28). The parameter Γ is introduced when equations similar to Eqs. (22) and (23) are solved analytically [12] and is defined as

$$\Gamma = -\frac{\xi_{\eta 0}}{k_B T} \left(\frac{dR_{\min}}{d\xi_\eta}\right)_{\xi_\eta = \xi_{\eta 0}}.$$

It is assumed that $\Gamma \gg 1$, because the method used is based on an expansion in powers of the small parameter $\epsilon = \Gamma^{-1}$; $R_{\min}$ is the minimum work that must be done to create a new-phase nucleus in the FF. We note that, physically, the parameter Γ is proportional to the number of particles in the critical nucleus at the instant the RR is maximum [12]. An expression for the minimum work done to create a nucleus was found in [2] to be $R_{\min}(n_c) = (\pi H\omega)^{1/2} \sigma n_c^{1/2}$, where H is the height of a cylindrical domain, σ is the surface tension coefficient of the domain wall, and $n_c^{1/2} = (\pi H\omega)^{1/2}\sigma/2[p_x E_x + u_{yz}\sigma_{yz}]$ (see [5]). Thus, we have

$$\Gamma = \frac{\pi H \sigma^2 \omega}{2\eta_\omega \eta_{10} 2\alpha(T_c - T)\xi_{\eta 0} k_B T}$$
$$= \frac{\pi H \sigma^2 \omega \chi_{xx}^{T, \sigma_{yzyz}} \varepsilon_0}{2 p_x P_{x10} \xi_P k_B T} = \frac{\pi H \sigma^2 \omega s_{yzyz}^{T, E_x}}{2 u_{yz} U_{yz}^{10} \xi_U k_B T}.$$

The quantity $I(\xi_{\eta 0})$ is the RR flux at the beginning of the stage of mass switching of the FF. This flux was found in [5] to be

$$I(\xi_{\eta 0} \sim (a_1 E_x^0 + a_2 \sigma_{yz}^0))$$
$$= \frac{N_v \beta_0 (H\omega)^{1/2} (\eta_\omega [a_1 E_x^0 + a_2 \sigma_{yz}^0])^{1/2}}{\sqrt{k_B T}} \times \exp\left(-\frac{\pi H \omega \sigma^2}{2 k_B T \eta_\omega [a_1 E_x^0 + a_2 \sigma_{yz}^0]}\right) \tag{29}$$
$$= \frac{N_v \beta_0 (H\omega)^{1/2} (p_x E_x^0 + u_{yz} \sigma_{yz})^{1/2}}{\sqrt{k_B T}} \times \exp\left(-\frac{\pi H \omega \sigma^2}{2 k_B T (p_x E_x^0 + u_{yz} \sigma_{yz}^0)}\right).$$

Using Eq. (29), we find an expression for the renormalized time,

$$T = \frac{t}{t_k} - \frac{1}{\Gamma} \int_0^T x^k \varphi_k(x) dx,$$

where

$$t_k = \frac{t_0}{\xi_{\eta 0}} \left[\frac{\xi_{\eta 0}}{(k+1)\omega \Gamma I(\xi_{\eta 0}) \tau}\right]^{\left(\frac{1}{k+1}\right)} \tag{30}$$

and $\varphi_k(x)$ is an auxiliary function, which can be determined by solving the equation $(d\varphi_k/dx) = \exp(-x^k \varphi_k)$ subject to the condition $\varphi_k(0) = 0$ [12]. The coefficient k depends on the mechanism controlling the nucleus growth and is equal to the exponent of the dimensionless variable ρ in the balance equation (23); i.e., in the case in question, we have $k = 1$.

It should be stressed that, using Eqs. (25)–(28), we can also find the quantities characterizing the stage of mass repolarization of a uniaxial ferroelectric placed in an external electric field [3], as well as the characteristics of the stage of mass redeformation of a proper ferroelastic subjected to external mechanical stresses.

Now, we will investigate the next stage of the evolution of an ensemble of repolarized and redeformed domains of the FF and discuss some of the probable domain growth mechanisms.

3. OSTWALD RIPENING AND DOMAIN GROWTH MECHANISMS

The Ostwald ripening (OR) of repolarized and redeformed domains is the final stage of the phase transformation that proceeds during the FF switching in external fields. In this stage, the mean size of the ensemble of new-phase nuclei increases. The large nuclei with their order parameter $\eta_n = n\eta_\omega$ reoriented along the external field (n is the number of unit cells in a nucleus) grow at the expense of fine nuclei; i.e., larger nuclei merge with smaller ones. This process is thermodynamically favorable, because the surface of interphase boundaries (domain walls) decreases, which leads to a decrease in the mean value of the RR in the FF. The interaction between repolarized and redeformed domains at this stage can be characterized by a self-consistent field produced by all domains of the ensemble.

In order to describe the final stage of the FF switching in terms of the corresponding Fokker–Planck equation and balance equation, we need to know the growth velocity of domains V_n, which essentially depends on the specific growth mechanism. In discussing these mechanisms, we will draw on an analogy between the growth of domains and the growth of crystals.

According to crystal growth theory [14–17], there are three basic mechanisms operating in this process: the normal growth mechanism, which operates at atomically rough interfaces; the layer-by-layer growth; and the growth through the motion of steps, which arise either because of two-dimensional nucleation on faces or because of screw dislocations reaching the crystal surface. In deriving Eq. (3) for the domain growth velocity, the normal mechanism of domain growth was assumed, because at the initial nucleation stage and at the next stage of mass repolarization–redeformation, the domains are small and their surface is not sufficiently developed. Therefore, it is unlikely that the other two mechanisms of domain growth operate at the initial and intermediate stages of FF switching.

Following [3], we eliminate the fields E_x, σ_{yz}, E_{xn}, and σ_{yz}^n from Eq. (3) for the domain growth velocity. For this purpose, we use the relations between these fields and the number of unit cells in domains [5] $n^{1/2} = (\pi H\omega)^{1/2}\sigma/[2\eta_\omega(a_1E_{xn} + a_2\sigma_{yz}^n)]$ and $n_c^{1/2} = (\pi H\omega)^{1/2}\sigma/[2\eta_\omega(a_1E_x + a_2\sigma_{yz})]$. The result is

$$V_n = \frac{dn}{dt} = \frac{2\pi H\omega\beta_0\sigma}{k_BT}\left(\frac{n^{1/2}}{n_c^{1/2}} - 1\right). \tag{31}$$

Thus, the Fokker–Planck equation (2), the balance equation (5), and Eq. (31) constitute a closed set whose solution fully describes the OR stage of switching of a uniaxial FF crystal on the basis of the normal growth mechanism.

In describing the final stage of FF switching in terms of these equations, it is convenient to pass over from the variables $\{n, t\}$ to new variables $\{R, t\}$, where R is the radius of a repolarized and redeformed domain of the crystal. In this case, the basic kinetic equation (2) takes the form

$$\frac{\partial f(R, t)}{\partial t} + \frac{\partial}{\partial R}[V_R f(R, t)] = 0, \tag{32}$$

where the domain growth velocity through the normal mechanism is given by the formula (which follows from Eq. (31)) [3]

$$V_R = \frac{dR}{dt} = \frac{\beta_0\omega^2\sigma}{k_BTR}\left(\frac{R}{R_c} - 1\right). \tag{33}$$

The balance equation (5) at the OR stage is represented in the form

$$\begin{aligned} &Q_0 + \int_0^t \xi_{\eta 0}(t')dt' \\ &= \frac{\bar{\eta}(t) - \eta_{10}}{\eta_{10}} + \frac{\pi H\eta_\omega}{\eta_{10}\omega}\int_0^\infty f(R, t)R^2dR, \end{aligned} \tag{34}$$

where

$$Q_0 = \frac{\eta^0 - \eta_{10}}{\eta_{10}} + \frac{\pi H\eta_\omega}{\eta_{10}\omega}\int_0^\infty f_0(R)R^2dR.$$

The set of equations (32)–(34) is typical of first-order phase transformations at the OR stage and describes the final stage of uniaxial-FF switching through the normal domain growth mechanism.

Along with the normal growth mechanism, in general, the other two mechanisms indicated above can also operate at the OR stage. However, when considering the two-dimensional nucleation mechanism, we must know the details of the structure of the domain-wall surface, because the defects of the surface are of great importance in this case and noticeably accelerate the formation of two-dimensional nuclei. Furthermore, having formed, a two-dimensional nucleus increases further in size through the layer-by-layer growth mechanism and the previous history of the nucleus formation has no noticeable effect on its growth. For this reason, we will restrict our consideration to the layer-by-layer growth mechanism.

Following [3], it is easily shown that the velocity of layer-by-layer growth of a domain wall is given by

$$\begin{aligned} V_n &= \frac{dn}{dt} = \frac{\pi^{1/2}H^{3/2}}{\eta_c}\omega^{1/2}\beta_{\mathrm{st}0} \\ &\times \frac{2\eta_\omega(a_1E_x + a_2\sigma_{yz} - a_1E_{xn} - a_2\sigma_{yz}^n)}{k_BT}n^{1/2}. \end{aligned} \tag{35}$$

Here, r_c is the radius of a two-dimensional disklike nucleus, $\beta_{\mathrm{st}0} = N_{\mathrm{st}}\nu_{\mathrm{st}}\exp(-V_{\mathrm{st}0}/k_BT)$, N_{st} is the number of unit cells near the step, ν_{st} is the vibration frequency of atoms in the unit cells near the step, and $V_{\mathrm{st}0}$ is the height of the potential barrier for the order-parameter reversal near the step in a zero external field.

The domain growth velocity in Eq. (35) can be expressed in terms of the domain radius R. The result is

$$V_R = \frac{dR}{dt} = \frac{H\omega^2\beta_{\mathrm{st}0}\sigma^2}{2k_BT\sigma_{\mathrm{st}}R_cR}\left(\frac{R}{R_c}-1\right), \tag{36}$$

where σ_{st} is the surface tension coefficient for the step.

Thus, in order to describe the final switching stage of a uniaxial FF, the Fokker–Planck equation (32) and the balance equation (34) should be used in combination with an expression for the domain growth velocity given by either Eq. (33) or Eq. (36), depending on the domain growth mechanism operating at this stage.

A comparison of the switching kinetics of a uniaxial FF, a uniaxial ferroelectric, and a proper ferroelastic shows that, for all three of these types of crystals, the domain growth velocity at the final stage of the phase transformation is given by identical expressions, namely, by Eq. (33) or Eq. (36).

In order to solve the set of equations (32) and (34) in combination with Eq. (33) or Eq. (36) determining the growth velocity, we must make assumptions as to the explicit form of the source $\int_0^t \xi_{\eta 0}(t')dt'$. We assume that the source is uniformly distributed over the crystal and decays with time. The sources monotonically decaying with time can be approximated at infinity by polynomials of the form $\xi_{\eta 0}(t) = (\xi_{\eta 0}/\tau)t^{n-1}$ (as in [18, 19]), where $n \geq 0$ is the exponent characterizing the field decay. It should be noted that we assume the source to decay with time (i.e., $n < 1$), because otherwise, according to the theory of nucleation and growth [14], the nucleation will resume and prevent the onset of the OR stage in the system.

Thus, we can make the inference, in accordance with [19], that the OR stage will come only if after repolarization–redeformation domains have formed, the external field is either turned off or decreased with time in such a way that the exponent n for the source in Eq. (34) satisfies the inequality $n < 2/p$ (with $p \leq 2$), where the value of p depends on the operating nucleus growth mechanism. In the case in question, we have $p = 2$ for nucleus growth on atomically rough interfaces and $p = 3$ for layer-by-layer growth of nuclei. In this case, the mean nucleus size increases with time following the law [3, 19]

$$R(t) \longrightarrow \mathrm{const}' t^{1/p}, \tag{37}$$

the nucleus density varies with time as

$$N(t) \longrightarrow \mathrm{const}'' t^{\left(\frac{2}{p}-n\right)}, \tag{38}$$

and, since the mean size and the critical size of nuclei at the OR stage vary with time according to Eq. (37), the time dependence of the RR is

$$\xi_n(t) \longrightarrow \mathrm{const}''' t^{-1/p}. \tag{39}$$

In concluding this section, we note that the size distribution functions of nuclei written in the dimensionless coordinates are identical for all phase transformations at the OR stage (see, e.g., [12, 18, 19]) and are not presented in this paper.

Thus, the evolution equations describing the diffusion-controlled OR, "thermal" OR, and "electromechanical" OR have formally similar general structure and similar solutions. However, it should be stressed that the driving forces for these processes are quite different in nature: the concentration difference in the case of the diffusion-controlled OR, the temperature difference for the thermal OR, the electric-field difference for the "electrical" OR, etc.

4. POLARIZATION CURRENT AND DEFORMATION FLUX

As in the case of a pure ferroelectric, the time dependence of the polarization current density in a uniaxial FF can be found from the equation [20]

$$J_P = -2P_{x10}\frac{dQ}{dt}, \tag{40}$$

where dQ/dt is the rate of change of the volume fraction Q of the unswitched region of the crystal and P_{x10} is the initial (equilibrium) value of the spontaneous polarization of the FF.

However, a distinctive feature of switching of a uniaxial FF is that the reversal of the order parameter η under the action of external electric and stress fields (a combination of these fields, in general) leads to the reversal of both the polarization and the deformation. In this case, in addition to the polarization current caused by repolarization of ferroelectric domains, there occurs a deformation flux caused by redeformation of ferroelastic domains (elastic twins). By analogy with the polarization current density given by Eq. (40), we define the deformation flux density as

$$J_U = -2U_{yz}^{10}\frac{dQ}{dt}, \tag{41}$$

where U_{yz}^{10} is the initial (equilibrium) spontaneous strain of the FF. The polarization current density is related to the deformation flux density by the equation

$$J_P = \lambda J_P, \tag{42}$$

where $\lambda = P_{x10}/U_{yz}^{10}$.

At the initial switching stage, according to the classical theory of nucleation and growth [14], the system is not affected by new-phase nuclei and its thermodynamic parameters remain virtually unchanged. The volume fraction of the crystal involved in the phase transformation is very small, and the rate of its change is equal to zero. As indicated in [3], the polarization current and the deformation flux are also zero at the initial stage of the FF switching and appear only at the next stage of the phase transformation, when the process of mass repolarization–redeformation begins in the system. The time at which this latter stage commences and the duration of this stage can be estimated from Eq. (30).

Following [3], the polarization current and the deformation flux at the stage where the repolarization and redeformation involve the main body of the uniaxial FF will be calculated on the basis of Eqs. (1)–(24) of the switching-kinetics theory.

We introduce the volume fraction of repolarized and redeformed domains in the crystal $Z = 1 - Q = \omega\int_0^\infty n f(n, t)dn$ and express the boundary and initial conditions for the basic kinetic equation (2) in terms of Z in the form

$$f(n_0, t) = I(t)[1 - Z(t)]V_n^{-1}\Big|_{n = n_0}, \quad f(n, 0) = 0, \tag{43}$$

where $I(t)$ is the nucleation rate.

Since part of the unit volume of the crystal is occupied by repolarized and redeformed domains and nucleation can occur only in the unoccupied region, the balance equation (16) should be rewritten in the form [3]

$$\frac{d\xi_n}{dt} = \frac{\xi_{\eta 0}}{\tau} - \frac{\xi_\eta}{\tau} - \frac{\left(\frac{\eta}{\eta_{10}} - 1 - \xi_n\right)}{(1 - Z)}\frac{dZ}{dt}, \tag{44}$$

where the ratio η/η_{10} takes into account the difference in the volume of repolarized and redeformed unit cells between the equilibrium state and the fully switched state in the presence of an external field.

By solving the kinetic equation (2) with the boundary and initial conditions (43) and the balance equation (44), we can find all main characteristics of the switching process. For this purpose, we express $Z(t)$ in terms of the variables ρ and t by using the relations $\rho = n^{1/2}$ and $f(n, t)dn = q(\rho, t)d\rho$. Differentiating $Z(t)$ with respect to time and using Eqs. (20) and (22) and the condition $q(\rho, t)|_{\rho \to \infty} = 0$ yields

$$\left(\frac{Z'}{\xi_\eta}\right)' = \frac{2\omega\xi_\eta}{t_0^2}N, \tag{45}$$

where t_0 is the characteristic growth time given by Eq. (21) and N is the number of nuclei.

A prime in Eq. (45) indicates differentiation with respect to time. Differentiating Eq. (45) with respect to time once more, we obtain

$$\left[\frac{1}{\xi_\eta}\left(\frac{Z'}{\xi_\eta}\right)'\right]' = \frac{2\omega}{t_0^2}I(\xi_\eta(t)), \tag{46}$$

where $I(\xi_\eta(t))$ is the nucleus flux.

From Eq. (46), using definitions (40) and (41), the polarization current and the deformation flux are found to be

$$\left[\frac{1}{\xi_\eta}\left(\frac{J_P}{\xi_\eta}\right)'\right]' = -\frac{4\omega P_{x10}}{t_0^2}I(\xi_\eta), \tag{47a}$$

$$\left[\frac{1}{\xi_\eta}\left(\frac{J_U}{\xi_\eta}\right)'\right]' = -\frac{4\omega U_{yz}^{10}}{t_0^2}I(\xi_\eta). \tag{47b}$$

Thus, Eqs. (47), in combination with the balance equation (44), form a complete set, which allows one to find the polarization current and deformation flux as functions of time and of applied external fields.

Let us represent Eq. (44) in the form

$$J_P = -\frac{2P_{x10}\left(\frac{\xi_{\eta 0}}{\tau} - \xi'_\eta - \frac{\xi_\eta}{\tau}\right)(1 - Z)}{\left(\frac{\eta}{\eta_{10}} - 1 - \xi_\eta\right)}. \tag{48}$$

Substituting Eq. (48) into Eq. (47a) yields

$$\left[\frac{1}{\xi_\eta}\left(\frac{\left(\frac{\xi_{\eta 0}}{\tau} - \xi'_\eta - \frac{\xi_\eta}{\tau}\right)(1 - Z)}{\left(\frac{\eta}{\eta_{10}} - 1 - \xi_\eta\right)}\right)'\right]' = -\frac{2\omega}{t_0^2}I(\xi_\eta). \tag{49}$$

Equation (49) determines the time dependence of the RR. This equation should be supplemented by the zero initial conditions imposed on the polarization current and deformation flux, their time derivatives, and the RR.

The dependence of the nucleus flux on the RR is found in [2, 5] and can be written in the form

$$I(\xi_n) = I_0\xi_\eta^{1/2}e^{-\alpha/\xi_n}, \tag{50}$$

where

$$I_0 = \frac{N_v\beta_0\sqrt{H\omega p_x P_{x10}}}{\sqrt{k_B T\chi_{xx}^{T,\,\sigma_{yz}}\varepsilon_0}} = \frac{N_v\beta_0\sqrt{H\omega u_{yz}U_{yz}^{10}}}{\sqrt{k_B T s_{yzyz}^{T,\,E_x}}},$$

$$\alpha = \frac{\pi H\omega\sigma^2\chi_{xx}^{T,\,\sigma_{yz}}\varepsilon_0}{2k_B T p_x P_{x10}} = \frac{\pi H\sigma^2 s_{yzyz}^{T,\,E_x}}{2k_B T u_{yz}U_{yz}^{10}}.$$

Let us point out specific features of Eqs. (2) and (44)–(50), which describe the switching kinetics of a uniaxial FF placed in external fields. First, these equations can be used to describe the switching of both uniaxial ferroelectrics (as done in [2, 3]) and proper ferroelastics. In the former case, the polarization current arises, while the deformation flux is zero. In the latter case, the deformation flux is nonzero, while the polarization current does not arise. Second, in deriving Eqs. (2) and (44)–(50), the possible coalescence of repolarization–redeformation domains was neglected.

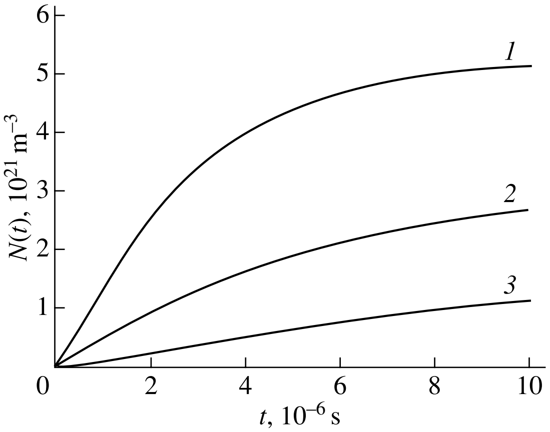

Fig. 1. Dependences of the repolarized- and redeformeddomain density $N(t)$ on time and external field: (*1*) $E_x = 1.13 \times 10^4$ V m^{-1}, $\sigma_{yz} = 0.73 \times 10^4$ N m^{-2} or $E_x = 1.2 \times 10^3$ V m^{-1}, $\sigma_{yz} = 7.27 \times 10^4$ N m^{-2}; (*2*) $E_x = 1.13 \times 10^4$ V m^{-1}, $\sigma_{yz} = 0.37 \times 10^4$ N m^{-2} or $E_x = 0.6 \times 10^3$ V m^{-1}, $\sigma_{yz} = 7.27 \times 10^4$ N m^{-2}; and (*3*) $E_x = 1.13 \times 10^4$ V m^{-1}, $\sigma_{yz} = 0$ or $E_x = 0$, $\sigma_{yz} = 7.27 \times 10^4$ N m^{-2}.

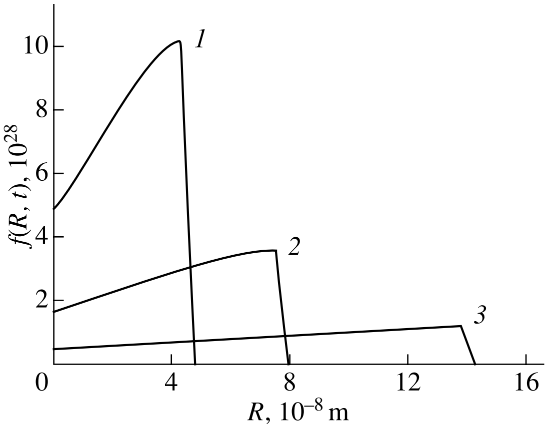

Fig. 2. Field dependences of the size distribution function of repolarized and redeformed domains $f(R, t)$ at time $t = t_k$ equal to (*1*) 3.3×10^{-6}, (*2*) 5.8×10^{-6}, and (*3*) 1.1×10^{-5} s. Curves *1–3* correspond to the same values of E_x and σ_{yz} as those in Fig. 1.

In principle, this coalescence can be taken into account by introducing a collision integral (with the corresponding kernel) into the right-hand side of the kinetic equation (2) if the specific mechanisms of domain mergence are known. Third, the equations in question do not include the possible effect of defects. Therefore, in order to take into account leakage currents and the presence of pinning centers, the theory should be generalized. Finally, it is also of interest to compare the theoretical dependences of the polarization current with experimental data and determine those parameters of ferroelectrics and related materials that are difficult to measure experimentally.

In closing, we make some evaluations using the theoretical dependences found in this paper.

5. DISCUSSION AND COMPARISON WITH EXPERIMENTAL DATA

We compare some calculated switching characteristics with the experimental data for the Rochelle salt, which is a classical FF. However, it should be noted that this comparison is qualitative, because both the experimental and theoretical data are only rough estimates.

We use the following experimental data for the Rochelle salt [11, 21, 22]: the (upper) Curie temperature $T_c \sim 297$ K, molar mass $M \sim 0.282$ kg mol^{-1}, density $\rho \sim 1.77 \times 10^3$ kg m^{-3}, equilibrium spontaneous polarization (at temperature $T \sim 277$ K) $P_{x10} \sim 0.25 \times 10^{-2}$ C m^{-2}, surface tension coefficient of a domain wall $\sigma \sim 5 \times 10^{-5}$ J m^{-2}, dielectric susceptibility $\chi_{xx}^{T,\sigma_{yz}} \sim 250$, and piezoelectric modulus $d_{xyz} \sim 4.44 \times 10^{-10}$ C N^{-1}. In this case, the unit cell volume of a Rochelle salt crystal is $\omega \sim M/\rho N_A = 2.65 \times 10^{-28}$ m^3 (N_A is the Avogadro constant). According to [11], we have $\varepsilon_0\chi_{xx}^{T,\sigma_{yz}}/d_{xyz} = a_1/a_2$ and $d_{xyz}/s_{yzyz}^{T,E_x} = a_1/a_2$; therefore, the elastic compliance is $s_{yzyz}^{T,E_x} \sim d_{xyz}^2/\varepsilon_0\chi_{xx}^{T,\sigma_{yz}} = 5.34 \times 10^{-11}$ m^2 N^{-1}, $a_1/a_2 \equiv \lambda = 6.432$ C m^{-2}, and the equilibrium spontaneous strain is $U_{yz}^{10} = \lambda^{-1}P_{x10} = 3.887 \times 10^{-4}$. We also assume that $H \sim \omega^{1/3}$, $N_V \sim \omega^{-1}$, and $\beta_0 \sim 10^{31}$ m^{-2} s^{-1}. With the data presented above, we evaluate the critical nucleus size R_c, the time t_0 during which the steady flux sets in, and the parameters I_0 and α for a Rochelle salt crystal. In fields $E_x = 1.13 \times 10^4$ V m^{-1} and $\sigma_{yz} = 0.73 \times 10^4$ N m^{-2}, the critical nucleus size as calculated with the formulas from [2, 5] is $R_c \sim 10^{-7}$ m, which agrees with typical experimental values [23]. In the same fields, the duration of the steady-state flux setting in is $t_0 = 2.88 \times 10^{-10}$ s and the parameters $I_0 = 2.64 \times 10^{38}$ and $\alpha = 0.234$. Figures 1 and 2 show the time dependences of the switched-domain density $N(t)$ and of the size distribution function of domains $f(R, t)$ as calculated from Eqs. (26) and (28), respectively. The time dependences of the RR, nucleation rate, polarization current, and deformation flux as calculated by solving the set of equations (48)–(50) are shown in Fig. 3. The following important features of these dependences are to be noted. First, the calculated polarization-current curves agree qualitatively with the corresponding experimental curves for actual ferroelectrics [24, 25]. Second, the switching of a uniaxial FF can be performed by applying either an electric or a stress field; therefore, each of the polarization-current curves can be obtained in two different ways: either by varying the

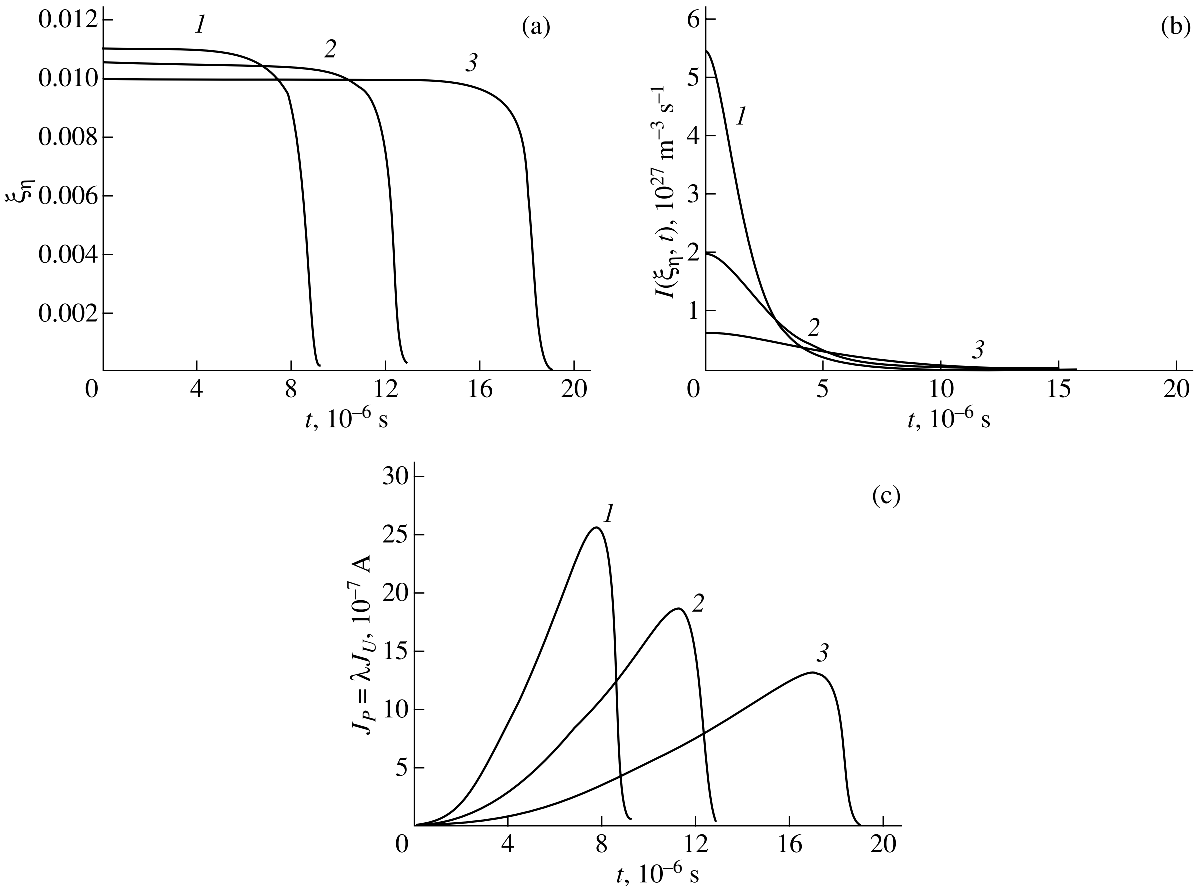

Fig. 3. Dependences of (a) the repolarization–redeformation ξ_η, (b) nucleation rate $I(\xi_\eta, t)$, and (c) polarization current J_P and deformation flux J_U on time and external field for $I_0 = 2.64 \times 10^{38}$, $\alpha = 0.234$, $t_0 = 2.9 \times 10^{-10}$ s, $P_x/P_{x10} \sim 1.12$, and the sample surface area $S \sim 10^{-9}$ m^2. Curves *1–3* correspond to the same values of E_x and σ_{yz} as those in Fig. 1.

electric component of the external field (with the external stress kept fixed) or by varying the external stress with the electric field kept fixed. The curves presented in Figs. 1–3 exhibit this property; for each polarization-current curve and for the other characteristics of FF switching, we present two of the infinite sets of the corresponding linear combinations of external electric and stress fields. Finally, the time dependence of the deformation flux is qualitatively similar to that of an acoustic-emission pulse that accompanies the formation of an elastic twin in a crystal [10].

In closing, we note that in [2–5] and in this paper, the kinetic theory of switching of ferroelectrics and related materials was developed for the case of a single-component order parameter. However, this theory can be extended to the case of a multicomponent order parameter, which offers possibilities of studying multiaxial ferroelectrics, which are known to be improper ferroelastics. These issues will be considered in a future publication.

ACKNOWLEDGMENTS

This study was partly supported by the Russian Foundation for Basic Research (project nos. 02-03-32471, 02-02-17216, 02-02-16071), Russian Federal Research Center “Integration” (project nos. A0151, A0075), CONACYT (grant no. 32208), the “Control of Nonlinear Mechanical Systems in Conditions of Uncertainty and Chaos” program (project no. 19), and the “Studies in the Fields of Natural Sciences and the Humanities: Universities of Russia” program (project no. 990019).

REFERENCES

1. M. Molotskii, R. Kris, and G. Rosenmann, J. Appl. Phys. **88** (9), 5318 (2000).
2. S. A. Kukushkin and A. V. Osipov, Fiz. Tverd. Tela (St. Petersburg) **43** (1), 80 (2001) [Phys. Solid State **43**, 90 (2001)].
3. S. A. Kukushkin and A. V. Osipov, Fiz. Tverd. Tela (St. Petersburg) **43** (1), 88 (2001) [Phys. Solid State **43**, 82 (2001)].

4. S. A. Kukushkin and A. V. Osipov, Fiz. Tverd. Tela (St. Petersburg) **43** (2), 312 (2001) [Phys. Solid State **43**, 325 (2001)].
5. S. A. Kukushkin and M. A. Zakharov, Fiz. Tverd. Tela (St. Petersburg) **44** (2), 332 (2002) [Phys. Solid State **44**, 345 (2002)].
6. V. Ya. Shur, in *Ferroelectric Thin Films: Synthesis and Basic Properties* (Gordon and Breach, Amsterdam, 1996), Ferroelectricity and Related Phenomena, Vol. 10, Part 1, p. 153.
7. V. Ya. Shur, E. L. Rumyantsev, V. P. Kuminov, *et al.*, Fiz. Tverd. Tela (St. Petersburg) **41** (1), 126 (1999) [Phys. Solid State **41**, 112 (1999)].
8. H. M. Duiker and P. D. Beal, Phys. Rev. B **41**, 490 (1990).
9. A. M. Bratkovsky and A. P. Levanyuk, Phys. Rev. Lett. **84**, 3177 (2000).
10. V. S. Boĭko, R. I. Garber, and A. M. Kosevich, *Reversible Plasticity of Crystals* (Nauka, Moscow, 1991).
11. B. A. Strukov and A. P. Levanyuk, *Physical Principles of Ferroelectric Phenomena in Crystals* (Nauka, Moscow, 1995).
12. S. A. Kukushkin and A. V. Osipov, Usp. Fiz. Nauk **168** (10), 1083 (1998) [Phys. Usp. **41**, 983 (1998)].
13. I. M. Fishman, Usp. Fiz. Nauk **155** (2), 329 (1988) [Sov. Phys. Usp. **31**, 561 (1988)].
14. S. A. Kukushkin and V. V. Slezov, *Disperse Systems on Solid Surface (Evolutionary Approach): Mechanisms of Thin Film Formation* (Nauka, St. Petersburg, 1996).
15. R. Laudise and R. Parker, *The Growth of Single Crystals; Crystal Growth Mechanisms: Energetics, Kinematics, and Transport* (Prentice-Hall, Englewood Cliffs, 1970; Mir, Moscow, 1974).
16. A. A. Chernov, in *Modern Crystallography*, Vol. 3: *Crystal Growth*, Ed. by B. K. Vainshtein, A. A. Chernov, and L. A. Shuvalov (Nauka, Moscow, 1980; Springer, Berlin, 1984).
17. S. A. Kukushkin and A. V. Osipov, Prog. Surf. Sci. **56** (1), 1 (1996).
18. V. V. Slezov, Phys. Rev. **17**, 1 (1995).
19. S. A. Kukushkin and A. V. Osipov, Zh. Éksp. Teor. Fiz. **113** (6), 2197 (1998) [JETP **86**, 1201 (1998)].
20. I. Ishibashi and Y. Takagi, J. Phys. Soc. Jpn. **31**, 506 (1971).
21. F. Jona and G. Shirane, *Ferroelectric Crystals* (Pergamon, Oxford, 1962; Mir, Moscow, 1965).
22. J. C. Burfoot, *Ferroelectrics: An Introduction to the Physical Principles* (Van Nostrand, New York, 1967; Mir, Moscow, 1970).
23. G. A. Smolenskiĭ and N. N. Kraĭnik, *Ferroelectrics and Antiferroelectrics* (Nauka, Moscow, 1968).
24. C. L. Wang, L. Zhang, W. L. Zhong, and P. L. Zhang, Phys. Lett. A **254**, 297 (1999).
25. N. N. Kraĭnik and L. S. Kamzina, Fiz. Tverd. Tela (St. Petersburg) **37** (4), 999 (1995) [Phys. Solid State **37**, 542 (1995)].

Translated by Yu. Epifanov

Physics of the Solid State, Vol. 44, No. 12, 2002, pp. 2309–2317. Translated from Fizika Tverdogo Tela, Vol. 44, No. 12, 2002, pp. 2204–2211.
Original Russian Text Copyright © 2002 by Shmyt'ko, Afonikova, Torgashev.

MAGNETISM AND FERROELECTRICITY

Anomalous States of the Structure of $(NH_4)_2SO_4$ Crystals in the Temperature Range 4.2–300 K

I. M. Shmyt'ko*, N. S. Afonikova*, and V. I. Torgashev**

** Institute of Solid-State Physics, Russian Academy of Sciences, Chernogolovka, Moscow oblast, 142432 Russia*

*** Research Institute of Physics, Rostov State University, pr. Stachki 194, Rostov-on-Don, 344090 Russia*

Received February 25, 2002

Abstract—Crystals of the $(NH_4)_2SO_4$ ammonium sulfate are studied using x-ray diffractometry. It is revealed that the temperature dependence of the lattice parameters exhibits an anomalous behavior, namely, a global hysteresis, and an anomalous increase in the lattice parameter a and the unit cell volume at temperatures below the ferroelectric phase transition point (T_c = 223 K). The series of superstructure reflections observed corresponds to an incommensurate composite structure. Analysis of the temperature behavior of the mismatch parameters for the matrix (host) and superstructure (guest) lattices demonstrates that the $(NH_4)_2SO_4$ compound undergoes a number of phase transitions, including a transition to a three-dimensionally incommensurate composite phase and transitions to commensurate (along one of the crystallographic directions) composite phases. *© 2002 MAIK "Nauka/Interperiodica".*

1. INTRODUCTION

It is known that crystals belonging to the structural family of rubidium ammonium sulfates of the general formula $(Rb_x(NH_4)_{(1-x)})_2SO_4$ form a continuous series of solid solutions [1]. Crystals of the rubidium-free ammonium sulfate $(NH_4)_2SO_4$ undergo a first-order ferroelectric phase transition with a change in the symmetry from *Pnam* to *Pna*2$_1$ at a temperature of ~223 K. A decrease in the temperature brings about reversal of the spontaneous polarization of these crystals [2]. In the $(Rb_x(NH_4)_{(1-x)})_2SO_4$ system, the ferroelectric phases are retained up to compositions with $x \cong 0.6$–0.65 [1].

The origin of the ferroelectric phase transition in crystals of this family has been discussed in the framework of different models, such as the order–disorder model [3], improper ferroelectrics [4], coupled oscillators [5], coupled oscillators–relaxors [6], and the model of two ferroelectric nonequivalent sublattices [7]. As is evident from the aforementioned approaches, the mechanism of the ferroelectric phase transition under investigation is rather complicated and, until presently, has not been clearly understood [8].

The compounds under consideration belong to a very interesting class, namely, the class of orientational glasses, in which the subsystem of multipole moments is efficiently frozen with a decrease in the temperature. These compounds exhibit a disorder intermediate between the disorders observed in crystals and conventional "canonical" glasses [9–12].

Earlier [13], we examined crystals of $(Rb_x(NH_4)_{(1-x)})_2SO_4$ solid solutions with a rubidium content x = 0.1 and revealed a number of anomalies, namely, an anomalous increase in the lattice parameter a and the unit cell volume with a decrease in the temperature below T_c, a series of specifically arranged additional (superstructure) reflections of unknown nature, and an "invar effect" in the behavior of one of the lattice parameters with a change in the temperature in the absence of satellite reflections typical of incommensurately modulated phases. With the aim of elucidating the origin of additional reflections, we proposed several structural models for crystals of the given composition. These models can be either validated or disproved depending on whether the aforementioned specifically arranged satellites are characteristic of ammonium sulfate crystals.

In the present work, we performed an x-ray diffraction investigation of the real structure of $(NH_4)_2SO_4$ crystals. The results obtained made it possible not only to determine the structure of the $(NH_4)_2SO_4$ compound over a wide temperature range but also to explain the nature of the anomalous structural states observed in $(Rb_x(NH_4)_{(1-x)})_2SO_4$ solid solutions.

2. SAMPLE PREPARATION AND EXPERIMENTAL TECHNIQUE

The quality of the studied samples was controlled using the traditional Laue and rolling-crystal methods. The determination of the crystal symmetry and precision measurements of the unit cell parameters were performed on a Siemens *P*4 four-circle diffractometer (CuK_α radiation) at room temperature. For x-ray diffraction analysis, samples were prepared in the form of balls ~0.25–0.35 mm in diameter. The space group of the crystals under investigation was determined to be identical to that available in the literature, namely, *Pnam* [1].

Lattice parameters of $(NH_4)_2SO_4$ crystals at room temperature

a, Å Δa	b, Å Δb	c, Å Δc	α, deg $\Delta\alpha$	β, deg $\Delta\beta$	γ, deg $\Delta\gamma$	V, Å^3 ΔV
7.7880	10.6403	5.9950	90.0194	90.0229	89.9920	496.788
0.0017	0.0019	0.0009	0.0148	0.0117	0.0160	1.179

The temperature measurements of the lattice parameters were performed on a Siemens D500 x-ray diffractometer with the use of a helium cryostat designed at the Institute of Solid-State Physics, Russian Academy of Sciences. The diffractometer was modified using special programs with the aim of recording reciprocal lattice maps of the single-crystal sections.

3. RESULTS AND DISCUSSION

The measured characteristics of the structure of $(NH_4)_2SO_4$ crystals are presented in the table. The angular distribution of substructure elements of the samples (ω scan mode) did not exceed 0.1°. The rocking x-ray patterns of $(NH_4)_2SO_4$ crystals, unlike the $(Rb_{0.1}(NH_4)_{0.9})_2SO_4$ solid solutions studied in [13], did not exhibit superstructure reflections lying off the main layer lines. However, similar reflections were recorded along all three crystallographic directions with the use of x-ray diffractometry and reciprocal lattice cross sections.

The diffraction patterns for two orders of reflection along the crystallographic direction **c** of the $(NH_4)_2SO_4$ crystal are displayed in Fig. 1. It can be seen from this figure that, in the range of smaller diffraction angles, each Bragg reflection is accompanied by superstructure reflections. Note that the distance from the Bragg reflection to the satellite reflection significantly changes with varying the order of the reflection.

Figure 2 shows two characteristic (**a***–**c***) plane sections of the reciprocal space with the aforementioned Bragg and superstructure reflections (see Fig. 1a) at room temperature. As can be seen from Fig. 2, the superstructure reflections are located along the **c*** direction not only for the (00*l*) reflections but also for the (*h*0*l*) reflections.

Unlike the main and satellite reflections, which are separated by a relatively large distance along the **c** direction, the superstructure reflections along the crystallographic directions **a** and **b** are spaced so closely that they can only be resolved for higher orders of reflection (Figs. 3, 4). It is worth noting that, at temperatures above T_c, the superstructure reflections along the **a** direction (Fig. 3a) manifest themselves merely as anomalies in the intensity distribution of Bragg reflections. At temperatures below T_c (Fig. 3b), the superstructure reflections along the **a** direction arise at new positions separated by a considerable distance from the Bragg reflections.

Analysis of the diffraction patterns recorded for several orders of reflection along the coordinate axes demonstrates that the distances between the Bragg and superstructure reflections in the reciprocal space change with varying the order of the reflection in accordance with the coexistence of two three-dimensional lattices with the following parameters:

$$a_{\rm Bragg} = 7.7880\ \text{Å},\quad a_{\rm sat} \approx 7.790\ \text{Å},$$

$$b_{\rm Bragg} = 10.6403\ \text{Å},\quad b_{\rm sat} \approx 10.674\ \text{Å},$$

$$c_{\rm Bragg} = 5.9932\ \text{Å},\quad c_{\rm sat} \approx 6.1026\ \text{Å}.$$

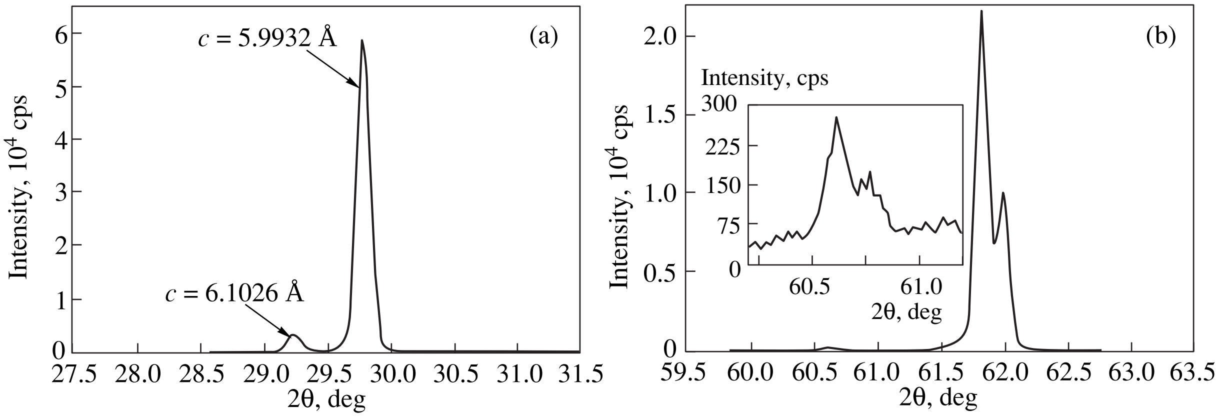

Fig. 1. Diffraction patterns of the (a) (002) and (b) (004) reflections observed for the $(NH_4)_2SO_4$ crystal at T = 300 K.

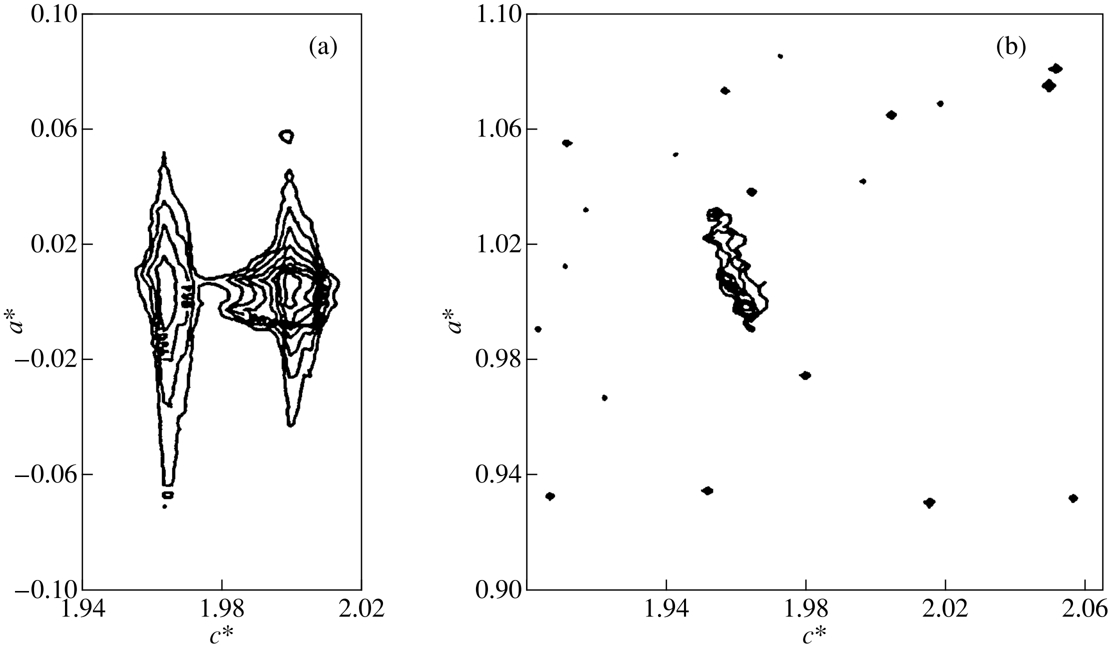

Fig. 2. Reciprocal lattice maps in the vicinity of the (a) (002) and (b) (102) points for the $(NH_4)_2SO_4$ crystal.

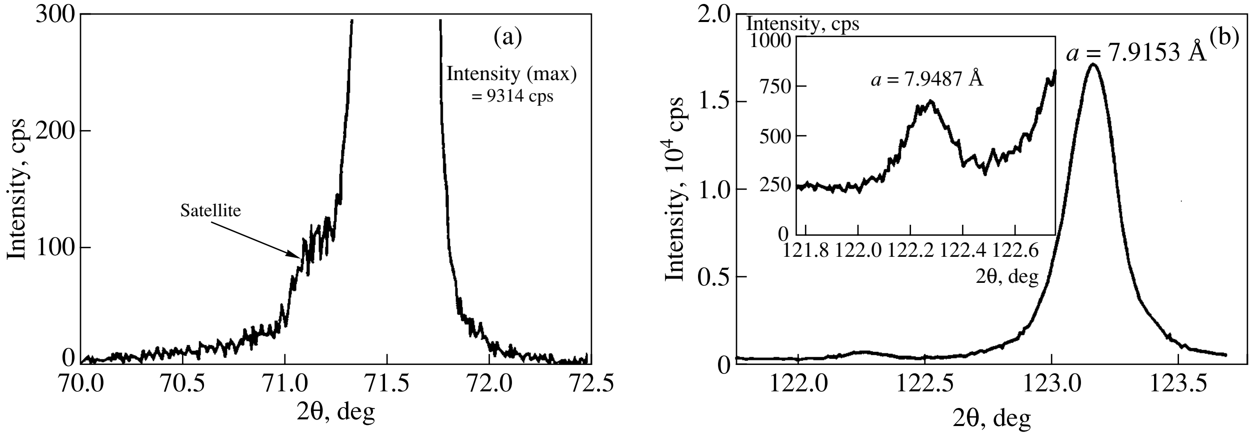

Fig. 3. (a) Anomalies of the Bragg reflection (600) indicating the presence of a superstructure reflection along the **a** direction at a temperature above T_c (250 K) and (b) relative positions of the Bragg reflection (1000) and the satellite reflection below T_c (112 K) for the $(NH_4)_2SO_4$ crystal. The inset shows the diffraction pattern in the range 2θ ≈ 122.0°–122.6° on an enlarged scale.

In what follows, the lattices composed of the sites associated with the Bragg and satellite reflections will be referred to as the host and guest lattices, respectively. The substructures represented by the host and guest lattices differ from each other, as is the case in solid solutions with $x = 0.1$ [13]. This can be judged, for example, from the presence of the $(102)_{sat}$ reflection in the diffraction pattern of the guest lattice and the absence of this reflection in the diffraction pattern of the host lattice (Fig. 2).

Reasoning from the results obtained, we can propose two models of the crystal structure under investigation. The first model describes a crystal structure with substitutional modulations such that, in the reciprocal space, the distance from the satellite reflection to the main reflection can change with variations in the order of the reflection. Moreover, this model allows for the possible formation of both superstructure reflections in the absence of the main Bragg reflections and satellite reflections on only one side of the main reflec-

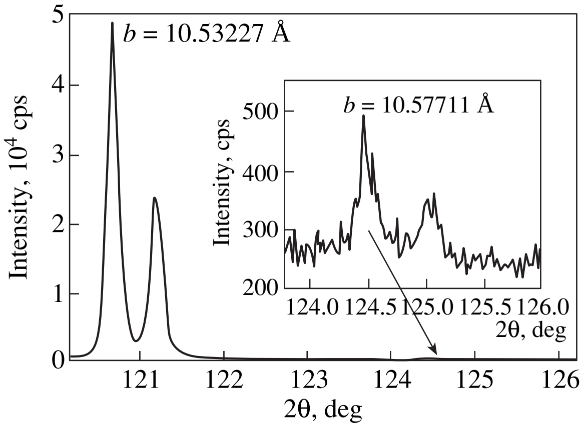

Fig. 4. Diffraction pattern of the (0120) reflection observed for the $(NH_4)_2SO_4$ crystal at $T = 117$ K. The inset shows the satellite reflection on an enlarged scale.

tion [14]. Within this model, the (NH_4) group that changes its orientation and (or) position with respect to the (SO_4) tetrahedron can serve as a substitutional element.[1]

According to the second model, the structure of the crystal under investigation is treated as an incommensurate single-crystal composite structure in which two weakly interacting and interpenetrating nonequivalent (host and guest) substructures coexist with each other [15–21]. In this case, by analogy with the crystal structure characterized by substitutional modulations, it would appear reasonable that one of the substructures is formed by (NH_4) groups. This corresponds to very low intensities of reflections from the guest substructure as compared to those of the host substructure containing heavier atoms of (SO_4) groups.[2]

In order to choose the most appropriate model, it is necessary to analyze the temperature behavior of the superstructure reflections in terms of both models. In the case of substitutional modulations, the relative positions of the superstructure and Bragg reflections must remain constant under variations in the temperature. By contrast, in the case of an incommensurate composite structure, the relative positions of these reflections must necessarily change with temperature, which, in essence, is responsible for the incommensurability of the structure.

In the subsequent discussion, the difference between the reciprocal lattice parameters of the guest and host substructures along the chosen axis will be referred to as the lattice mismatch parameter. Figure 5 depicts the temperature dependences of the lattice mismatch parameter and the intensity of the superstructure reflection along the **c** direction of the $(NH_4)_2SO_4$ crystal. As is clearly seen, the mismatch parameter substantially changes with temperature. This indicates convincingly that incommensurate composite structures are formed in the $(NH_4)_2SO_4$ crystals. Moreover, taking into account the results obtained for solid solutions with $x = 0.1$ [13], a similar statement is also true for all crystals belonging to the family of rubidium ammonium sulfates of the formula $(Rb_x(NH_4)_{(1-x)})_2SO_4$. A jumpwise change in the intensity of the $(002)_{sat}$ reflection, the anomaly observed in the mismatch parameter in the vicinity of 223 K, and the temperature behavior of the lattice parameters of the host structure suggest that, in the temperature range of the ferroelectric transformation, both incommensurate substructures undergo phase transitions.

The temperature dependence of the lattice mismatch parameter calculated for the $(0120)_{host}$ and $(0120)_{guest}$ reflections along the **b** direction of the $(NH_4)_2SO_4$ crystal is shown in Fig. 6. It can be seen from this figure that the mismatch parameter significantly changes with temperature. Reasoning from these results and the temperature behavior of the lattice mismatch parameter along the **c** direction, the structure of $(NH_4)_2SO_4$ crystals can be treated as, at least, a two-dimensional incommensurate composite structure.

As was already noted, the superstructure reflections along the **a** direction at temperatures above the ferroelectric phase transition point T_c manifest themselves merely as anomalies in the intensity distribution of Bragg reflections. In this case, the intensities of the reflections and their resolution appeared to be very low. For this reason, we failed to decompose the diffraction spectra with the use of traditional methods and to construct the temperature dependence of the lattice mismatch parameter along the **a** direction in the temperature range 225–300 K. At temperatures below T_c, the superstructure reflections along the **a** direction arise at new positions separated by a considerable distance from the Bragg reflections. This behavior of the diffraction spectra suggests a radical transformation of the guest substructure due to a ferroelectric phase transition and is another argument in support of the hypothesis that the composite structure under investigation consists of independent substructures.

Figure 7 illustrates the temperature behavior of the lattice mismatch parameter and the integrated intensity of the (1000) superstructure reflection along the **a**

---

[1] The choice of the (NH_4) tetrahedron as an ordering element corresponds to an extremely low intensity of superstructure reflections.

[2] It could be assumed that the additional reflections are associated with the degradation of the surface layer of the sample and the formation of new structures involving crystallization water in this layer, because the $(Rb_x(NH_4)_{(1-x)})_2SO_4$ crystals exhibit hygroscopic properties. However, this assumption is contrary to fact. Judging from the thickness of the diffracting layer (~5–50 μm) and the intensity ratio of the additional reflection to the main reflection (~1/500), the thickness of the disturbed surface layer does not exceed 100–1000 Å. This layer should be easily polished. However, narrow superstructure reflections were observed even after deep mechanical polishing. This indicates a volume distribution of the guest substructure at least over the thickness of the diffracting layer.

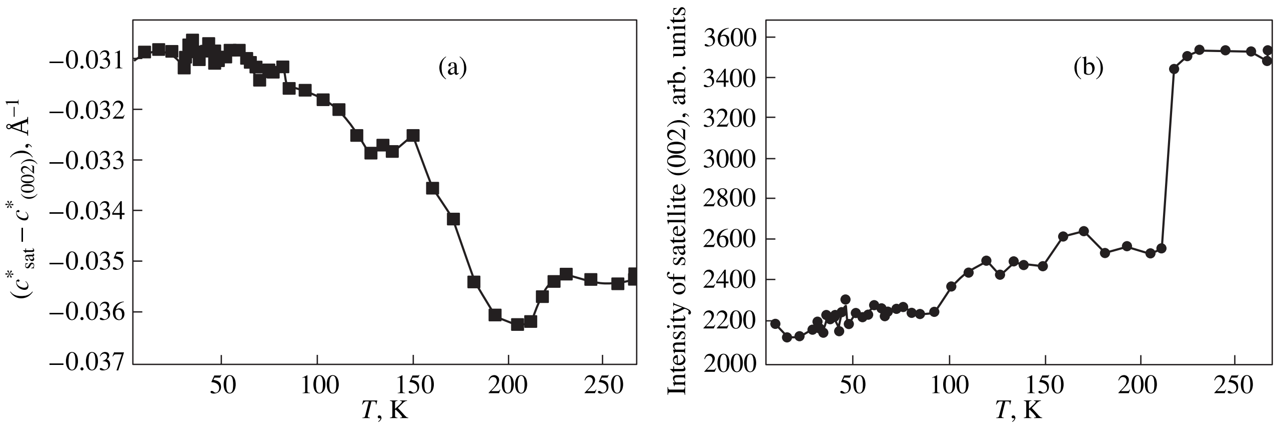

Fig. 5. Temperature dependences of (a) the lattice mismatch parameter and (b) the intensity of the superstructure reflection along the **c** direction of the $(NH_4)_2SO_4$ crystal.

direction at temperatures below T_c. A jumpwise change in the lattice mismatch parameter indicates that the $(NH_4)_2SO_4$ crystal undergoes phase transitions from the incommensurate composite phase above 170 K to commensurate (along the crystallographic direction **a**) composite phases in the temperature ranges 4.2–50 and 50–170 K. In our opinion, this finding is a fundamental result characterizing the nature of the incommensurate composite state. Indeed, the analysis of the lattice constants and mismatch parameters presented in Fig. 7 demonstrates that, in the temperature range 50–170 K, the host and guest lattices coincide at intervals of 238 unit cells. The question now arises as to the energy of the long-range interaction occurring at these distances. This energy can be estimated under the assumption that, at temperatures $T > T_{\text{com}}$, the transition to the incommensurate state occurs through a disturbance of the long-range interaction between the host and guest lattices due to thermal fluctuations. In this case, the energy of long-range interaction is determined by the temperature of the transition from the commensurate composite phase to the incommensurate composite phase and is approximately equal to 1.2×10^{-2} eV.

The temperature behavior of the lattice mismatch parameter in the temperature range 175–223 K is also noteworthy. It can be seen from Figs. 5–7 that, at these temperatures, the lattice mismatch parameters smoothly vary along all three crystallographic directions. This circumstance characterizes the $(NH_4)_2SO_4$ crystal as a three-dimensionally incommensurate composite.

In order to obtain additional information on the structure of $(NH_4)_2SO_4$ crystals, we measured the temperature dependences of the lattice parameters of the host lattice and the integrated intensities of Bragg reflections (Figs. 8–12). It can be seen from Fig. 8 that the lattice parameter *a* exhibits an anomalous behavior. As the temperature decreases below T_c, the lattice parameter *a* first increases and then, in the vicinity of $T = 120$ K (Fig. 8b), begins to decrease gradually with a further decrease in the temperature.

To account for the anomalous behavior of the lattice parameter *a* in the temperature range 120–223 K, it is necessary to elucidate the physical nature of the changes observed in the lattice parameters with variations in the temperature. It should be noted that the changes in the lattice parameters are associated primarily with the anharmonicity of atomic vibrations in local potential wells. It is evident that, in the general case, changes in the temperature (or, what amounts to the same, changes in the energy of atomic vibrations) should be attended by variations in the amplitude of atomic vibrations and, consequently, in the mean interatomic distances and lattice parameters. Within this interpretation, there should be no expansion of the crystal lattice with a decrease in the temperature.

A different situation can arise when atoms are not independent of one another but form coupled nonequiv-

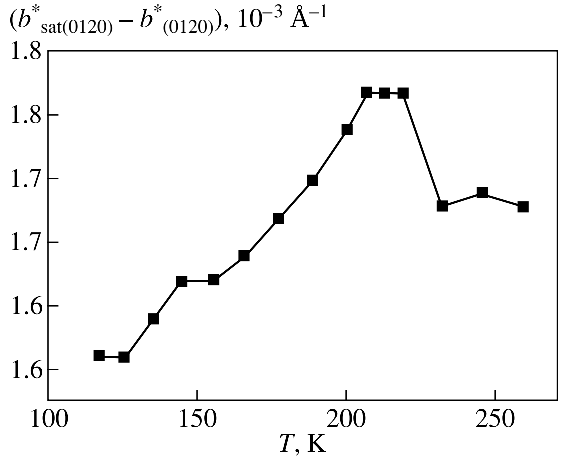

Fig. 6. Temperature dependence of the lattice mismatch parameter along the **b** direction of the $(NH_4)_2SO_4$ crystal.

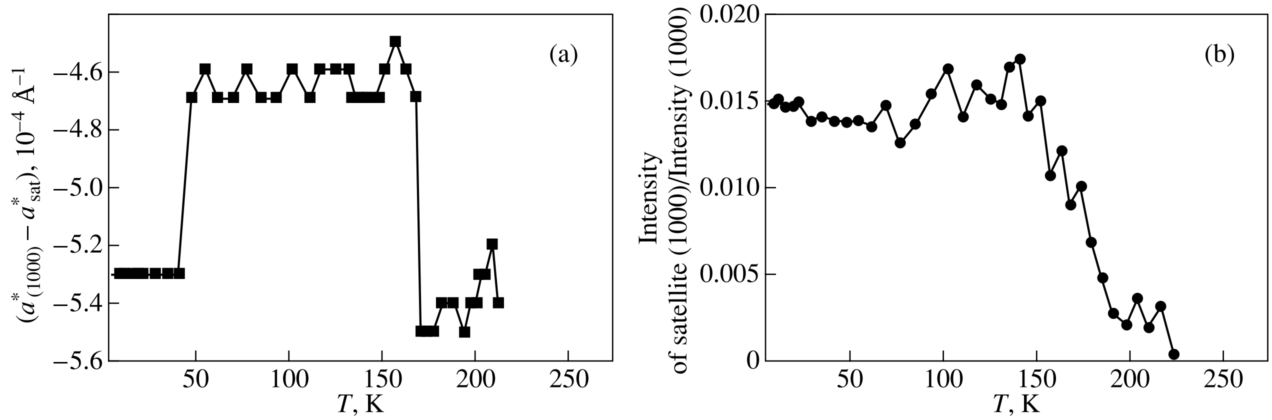

Fig. 7. Temperature dependences of (a) the lattice mismatch parameter and (b) the intensity of the superstructure reflection along the **a** direction of the $(NH_4)_2SO_4$ crystal.

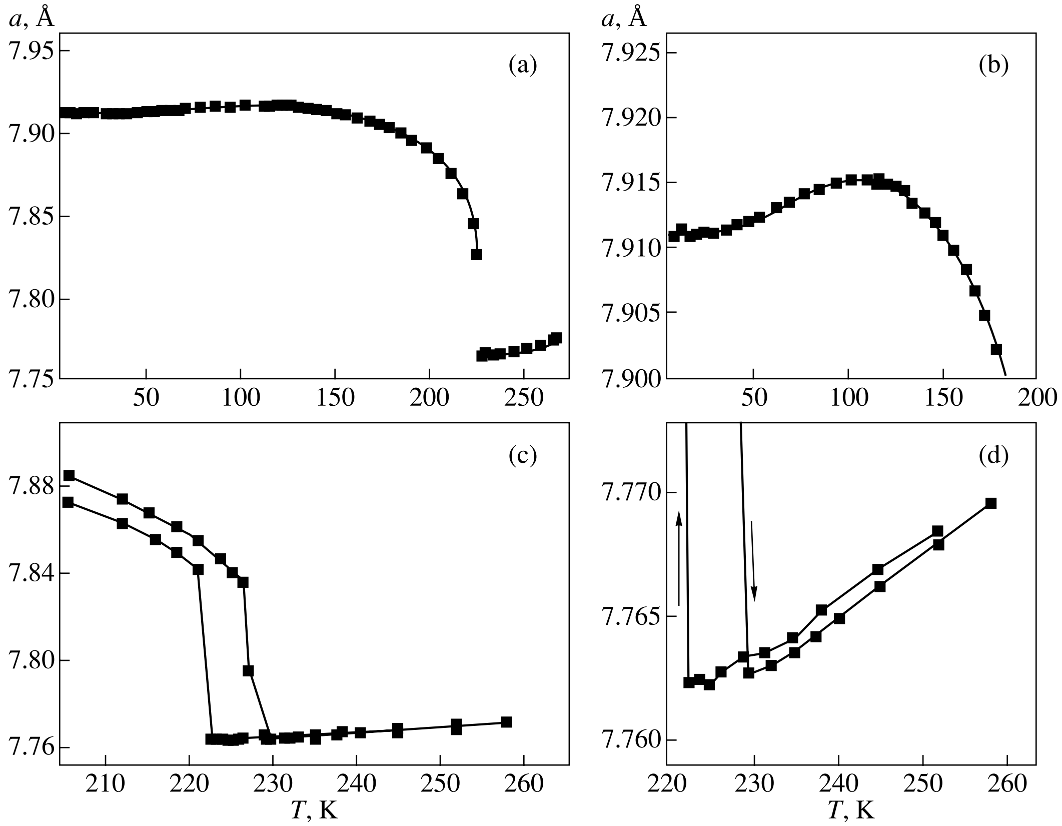

Fig. 8. Temperature dependences of the lattice parameter *a* of the host structure $(NH_4)_2SO_4$ in different temperature ranges: (a) from 4.2 to 300 K, (b) in the vicinity of the spontaneous-polarization reversal, and (c, d) in the vicinity of the ferroelectric phase transition temperature.

alent sublattices (here, we are dealing not with incommensurate substructures but with sublattices composed of different atoms in the host substructure). As the temperature decreases, these sublattices can expand not through anharmonicity of atomic vibrations but through other interactions, for example, due to a dipole–dipole interaction of their constituent structural elements [in our case, for example, due to an interaction of dipole moments of (SO_4) and (NH_4) distorted tetrahedra].

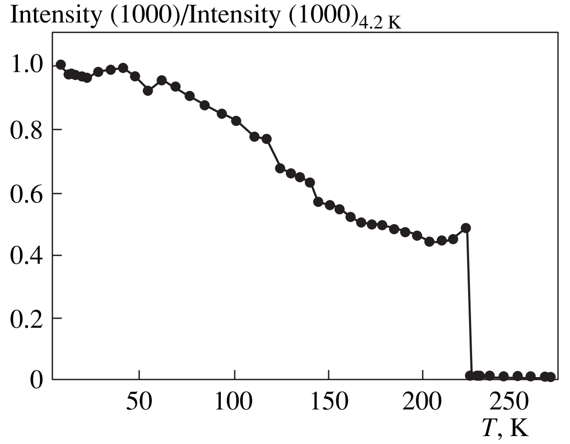

Fig. 9. Temperature dependence of the integrated intensity of the Bragg reflection (1000).

In the case under consideration, the mechanism of the anomalous increase in the lattice parameter a can be determined from the changes observed in the diffracted intensity of Bragg reflections due to variations in the temperature. For anharmonicity of atomic vibrations, the increase in the lattice parameter a with a decrease in the temperature should be universally accompanied by a decrease in the diffracted intensity of Bragg reflections at the expense of the Debye–Waller factor. In the case when the lattice parameter a increases as a result of displacement of the sublattices, the diffracted intensity either can decrease with a decrease in the temperature or can increase with temperature variations in the structure factor of the reflection involved. In general, upon transformation of the sublattices, the intensity of reflections increases or decreases depending on the temperature range. We observed only an increase in the integrated intensity of the (h00) reflection with a decrease in the temperature (Fig. 9). This behavior of the diffracted intensity is indirect evidence that nonequivalent sublattices coexist in the host structure. Furthermore, this behavior counts in favor of the model of the coexistence of two nonequivalent sublattices, especially from the standpoint of the elucidation of the mechanism of the ferroelectric phase transition [7]. It is interesting to note that the temperature dependence of the lattice parameter a exhibits a kink in the temperature range of the reversal of spontaneous polarization (Fig. 8b) [2]. This feature is one more argument in support of the model of the coexistence of nonequivalent sublattices in the host substructure.

The specific features of the ferroelectric phase transition clearly manifest themselves in the temperature behavior of the lattice parameter a (Fig. 8c). Judging from the hysteresis observed in the temperature dependence of the lattice parameter a, this transition can be treated as a first-order phase transition. Unlike all the known hystereses observed for first-order phase transitions, the above hysteresis exhibits an essential feature; namely, it is a global hysteresis that is retained over the entire temperature range below T_c. This is clearly seen in Fig. 8c, in which the temperature dependences of the lattice parameter a measured upon heating and cooling do not coincide over a wide temperature range below T_c. It is well known that the global hysteresis is characteristic of incommensurately modulated structures. To the best of our knowledge, no information regarding the observation of the global hysteresis for incommensurate composite phases is available in the literature. In the present work, this property of the incommensurate composite phases is observed for the first time. It should also be noted that, at temperatures above T_c (Fig. 8d), the invar effect revealed earlier for $(Rb_x(NH_4)_{(1-x)})_2SO_4$ solid solutions with a rubidium content $x = 0.1$ (see Fig. 2a in [13]) is not observed in $(NH_4)_2SO_4$ crystals.

The temperature behavior of the lattice parameters b and c is illustrated in Fig. 10. It can be seen that, with a

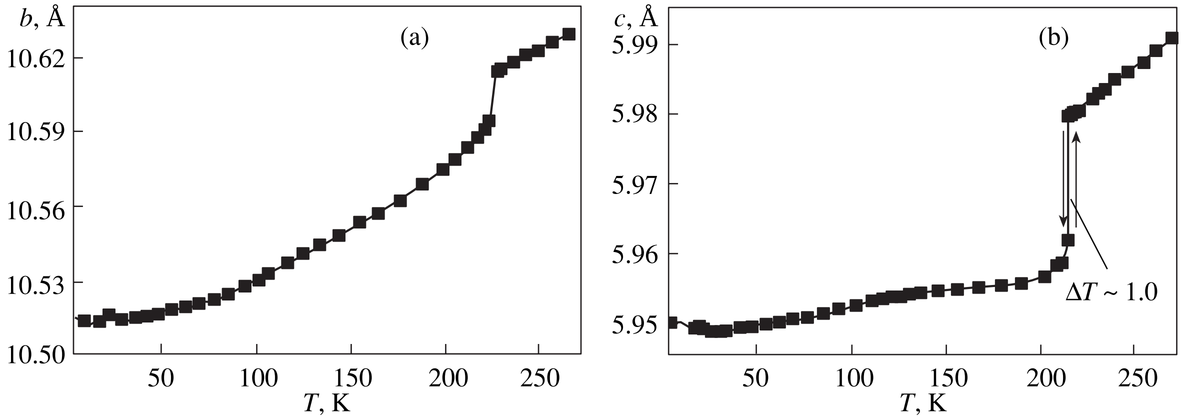

Fig. 10. Temperature dependences of the lattice parameters (a) b and (b) c of the host structure $(NH_4)_2SO_4$.

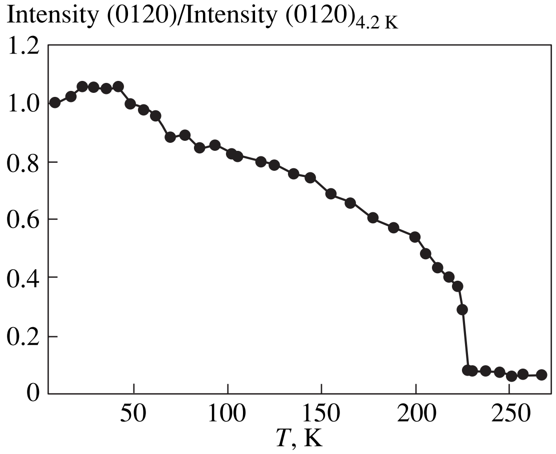

Fig. 11. Temperature dependence of the integrated intensity of the Bragg reflection (0120).

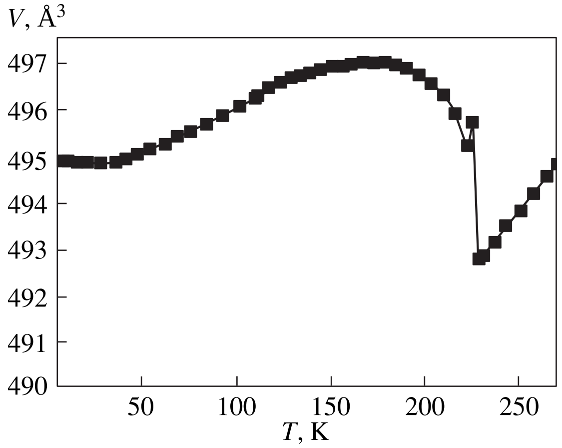

Fig. 12. Temperature dependence of the unit cell volume of the $(NH_4)_2SO_4$ crystal.

decrease in the temperature, the lattice parameters b and c first gradually decrease and then undergo a jump at the temperature of the ferroelectric phase transition. A decrease in the width of the temperature hysteresis for the lattice parameter c (Fig. 10b) is caused by repeated cycling of the studied sample through the phase transition point. In this case, the phase transformation is accompanied by a considerable bulk effect. This brings about cracking of the sample, which, in turn, relieves internal stresses responsible for the hysteresis width.

Figure 11 shows the temperature dependence of the integrated intensity of the Bragg reflection (0120) along the **b** direction. A jumpwise change in the integrated intensity in the vicinity of 225 K indicates the occurrence of a structural phase transition. An increase in the intensity with a decrease in the temperature (below T_c) corresponds to the usual behavior of atoms residing in weakly anharmonic potential wells.

The temperature dependence of the unit cell volume (Fig. 12) provides additional information on the origin of the ferroelectric phase transition. It can be seen from Fig. 12 that, at temperatures below T_c, the unit cell volume first increases with a decrease in the temperature and then smoothly decreases. Note that the bulk thermal expansion coefficient of the studied sample substantially changes in the vicinity of T_c. The change observed in the bulk thermal expansion coefficient and an increase in the unit cell volume with a decrease in the temperature below T_c indicate a radical transformation of the local environment of the lattice atoms and a considerable variation in their interaction. A decrease in the bulk thermal expansion coefficient in the low-temperature range suggests that, at temperatures below T_c, the lattice atoms reside in potential wells with a smaller anharmonicity coefficient.

4. CONCLUSIONS

Thus, the results obtained in the present study and our recent data on the anomalous structural states of the $(Rb_{0.1}(NH_4)_{0.9})_2SO_4$ compound [13] have demonstrated that crystals belonging to the structural family of rubidium ammonium sulfates of the general formula $(Rb_x(NH_4)_{(1-x)})_2SO_4$ are characterized by the formation of three-dimensional incommensurate composite structures consisting of weakly interacting nonequivalent (host and guest) substructures. In rubidium-free ammonium sulfate crystals, the incommensurate composite structures undergo a number of thermostimulated transformations into commensurate (along one of the crystallographic directions) composite structures. The direction of the maximum incommensurability of these structures depends on the rubidium content and changes from **c** to **b** upon changing over from the rubidium content $x = 0.0$ to $x = 0.1$. An anomalous increase in the lattice parameter a with a decrease in the temperature and a usual behavior of the intensity of Bragg reflections for crystals of both compositions indicate that the host substructure of crystals in the $(Rb_x(NH_4)_{(1-x)})_2SO_4$ system involves nonequivalent sublattices that are hypothetically responsible for the ferroelectric phase transition and reversal of spontaneous polarization in rubidium-free ammonium sulfate crystals.

ACKNOWLEDGMENTS

This work was supported by the Russian Foundation for Basic Research, project no. 99-02-18238.

REFERENCES

1. K. Ohi, J. Osaka, and H. Uno, J. Phys. Soc. Jpn. **44**, 529 (1978).
2. N. G. Unruh, Solid State Commun. **8**, 1915 (1970).

3. D. E. O'Reily and T. Tsang, J. Chem. Phys. **46**, 1301 (1967).
4. T. Ikeda, K. Fudjibayashi, T. Nada, and J. Kobayashi, Phys. Status Solidi A **16**, 279 (1973).
5. A. Sawada, Y. Tagagi, and Y. Ishibashi, J. Phys. Soc. Jpn. **34**, 748 (1973).
6. J. Petzelt, J. Grigas, and I. Myerova, Ferroelectrics **6**, 225 (1974).
7. A. Sawada, S. Ohya, Y. Ishibashi, and Y. Takagi, J. Phys. Soc. Jpn. **38**, 1408 (1975).
8. G. V. Kozlov, S. P. Lebedev, and A. A. Volkov, J. Phys. C **21**, 4883 (1988).
9. E. Courtens, Ferroelectrics **72**, 229 (1987).
10. U. T. Hochli, K. Knorr, and A. Loidl, Adv. Phys. **39**, 405 (1990).
11. P. Simon, Ferroelectrics **135**, 169 (1992).
12. D. DeSousa Menesses, G. Hauret, and P. Simon, Phys. Rev. B **51**, 2669 (1995).
13. I. M. Shmyt'ko, N. S. Afonikova, and V. I. Torgashev, Fiz. Tverd. Tela (St. Petersburg) **44** (11), 2069 (2002) [Phys. Solid State **44**, 2165 (2002)].
14. A. Guinier, *Theorie et technique de la radiocristallographie* (Dunod, Paris, 1956; Fizmatgiz, Moscow, 1961).
15. I. D. Brown, B. D. Cutforth, C. G. Davides, *et al.*, Can. J. Chem. **52**, 791 (1974).
16. J. M. Hastling, J. P. Pouget, G. Shirane, *et al.*, Phys. Rev. Lett. **39**, 1484 (1977).
17. A. J. Schultz, J. M. Williams, N. D. Miro, *et al.*, Inorg. Chem. **17**, 646 (1978).
18. Sander van Smaalen, Cryst. Rev. **4**, 79 (1995).
19. R. J. Nelmes, D. R. Allan, M. I. McMahon, and S. A. Belmonte, Phys. Rev. Lett. **83**, 4081 (1999).
20. M. I. McMahon, T. Bovornratanaraks, D. R. Allan, *et al.*, Phys. Rev. B **61**, 3135 (2000).
21. V. Heine, Nature **403**, 836 (2000).

Translated by O. Borovik-Romanova

Physics of the Solid State, Vol. 44, No. 12, 2002, pp. 2318–2322. Translated from Fizika Tverdogo Tela, Vol. 44, No. 12, 2002, pp. 2212–2216.
Original Russian Text Copyright © 2002 by Fateev.

LATTICE DYNAMICS AND PHASE TRANSITIONS

On the Multidimensional Theory of the First-Order Phase Transitions

M. P. Fateev

Institute of Theoretical Physics, Kharkov Physicotechnical Institute National Scientific Center,
Kharkov, 61108 Ukraine

Received July 30, 2001; in final form, December 13, 2001

Abstract—Multidimensional theory of first-order phase transitions in the vicinity of a one-dimensional saddle point is considered. Transformations of the variables describing new-phase nuclei are suggested; these transformations allow one to completely separate the variables in the Fokker–Planck equation and reduce the problem to a one-dimensional one. The distribution function and the nucleation rate are found for both stationary and nonstationary nucleation stages. As an illustration, the problem of boiling of a volatile liquid is considered in the case where new-phase nuclei are characterized by two parameters. *© 2002 MAIK “Nauka/Interperiodica”.*

1. INTRODUCTION

Study of the kinetics of new-phase formation [1–3] has led to the development of a general method for describing the kinetics of a first-order phase transition. In this method, the growth of a macroscopic nucleus of the stable phase is considered as diffusion along the axis of nucleus dimensions. In this case, determination of the nucleation rate in general reduces to solving the one-dimensional Fokker–Planck (F–P) equation for the size distribution of new-phase nuclei and to considering the macroscopic problem of growth of a supercritical nucleus without regard for fluctuations.

In the case where the state of a new-phase nucleus is characterized by a few variables, consideration of the kinetics of formation of the stable phase becomes significantly complicated. Examples of such phase transitions are cavitation [4], nucleation in multicomponent systems [5], chemical kinetics, etc. In this case, diffusion proceeds in the field of the “multidimensional-potential” relief associated with the free energy, which characterizes the work that must be done to form a new-phase nucleus. The potential relief in the nucleus-size space represents the potential barrier separating the heterophase region and the two-phase region. The most favorable way for a nucleus to overcome the activation barrier is obviously to pass through the saddle point. Hence, to determine the nucleation rate, one can restrict oneself to solving the multidimensional F–P equation linearized near the saddle point [6–8].

It is conventional to select the variables in the equation describing new-phase nuclei such that the variables will differ in the equilibrium distribution of nuclei. This allows one to simplify the kinetic equation and to determine which variables are stable and which are unstable. However, the matrix of diffusion coefficients is not diagonal in this case, which does not allow one to completely separate variables in the F–P equation describing the nucleation kinetics.

The Brownian motion of vapor bubbles in the multidimensional space of their parameters was studied in [6] in the case where the external pressure is time-dependent. The author of [6] was the first to indicate that the variables in the F–P equation can be completely separated and, therefore, the multidimensional theory of the first-order phase transition can be reduced to a one-dimensional problem. However, an explicit form of the transforms was not presented in [6]; this has prevented the derivation of an expression for the multidimensional nucleation rate in an invariant form. We note that the approach considered in [8] is restricted to the case of a quasi-steady mode and cannot be used to study relaxation to a stationary distribution [9].

To describe the nucleation kinetics in multicomponent systems, a consistent method was suggested in [7] for completely separating the variables in the F–P equation. In this method, the free energy of a nearly critical nucleus is first reduced to a diagonal form by performing rotation (linear transformation) in the configuration space. Then, a Lorentz-type transformation is carried out which does not change the form of the free energy but diagonalizes the matrix of diffusion coefficients. The Lorentz transformation arises in this approach due to the pseudo-Euclidean metric of the quadratic form of the free energy in the vicinity of the saddle point. However, the advantage of this method significantly depreciates as a result of the noninvariant property found for the solutions and the required laborious determination of the stationary flux in an invariant form, especially in the case where the configuration space dimension is higher than three. This difficulty seems to be caused by the slightly inappropriate choice of the coordinate transformation made in [7] to separate the variables in the kinetic F–P equation.

The multidimensional kinetic theory of first-order phase transitions in the general form was also developed in [8]. However, the study conducted in [8] was concerned only with the stationary current state for the F–P equation, which describes the kinetics of a dynamical system placed in a thermostat. Therefore, the matrix of diffusion coefficients was not symmetric (the Onsager relations are inapplicable in this case) and could not be reduced to a diagonal form. Hence, the method proposed in [8] for solving the F–P equation does not allow one to consider the complete kinetics of the phase transition and to substantiate the establishment of the final stationary current state.

In this paper, we apply a general method for solving the multidimensional F–P equation describing the kinetics of first-order phase transitions in “purely dissipative systems.” Due to the Onsager reciprocity principle, the matrix of diffusion coefficients is a positively definite symmetric matrix and can be reduced to a unit matrix be performing rotation and extension affine transformations. In this case, the variables are completely separated in the F–P equation and the multidimensional theory of phase transitions is reduced to the one-dimensional theory. The advantage of this approach is its simplicity and the invariance of the solutions obtained by this method.

2. DETERMINATION OF THE NUCLEATION PROBABILITY

In the vicinity of the saddle point, the multidimensional equation of the nucleation kinetics can be written as the continuity equation for the flux J_i, which is similar to the equation suggested by Zel’dovich [1] and Kramers [3] for the one-dimensional case:

$$\frac{\partial P}{\partial t} = -\frac{\partial J_i}{\partial x_i}, \tag{1}$$

$$J_i = -D_{ij}\left(T\frac{\partial P}{\partial x_j} + \frac{\partial V}{\partial x_j}P\right), \tag{2}$$

where $P = P(x, t)$ is the nucleus distribution density in the configuration space of dimensionless parameters $\{x_i\}$, D_{ij} is the tensor of diffusion coefficients, $V = V_c + \sum_{ij} V_{ij}\Delta x_i \Delta_{x_j}$ is the free energy of a new-phase nucleus in the vicinity of the saddle point $(x_i)_c = 1$, Δx_i is the deviation of the parameter x_i from the point $(x_i)_c$, and T is the temperature in energy units. Equating the first derivatives $\partial V/\partial x_i$ to zero yields the conditions of mechanical equilibrium (zero growth rate) of the critical nucleus. The quasi-equilibrium distribution function for Eq. (1) has the form of a Gibbs distribution:

$$F_0 = Z\exp\left(-\frac{V}{T}\right), \tag{3}$$

where Z is a normalization constant. Reducing the free energy (dimensionless work for the critical-nucleus formation) to the diagonal form, we obtain

$$V = V_c - a_0 z_0^2 + \sum_{i \neq 0} a_i z_i^2, \qquad a_i, a_0 > 0. \tag{4}$$

It follows from Eq. (4) that the barrier in the vicinity of the point of labile equilibrium of the system is approximated by a hypersurface of the multidimensional-saddle type. Overcoming the activation barrier by nuclei during the phase transition means that nuclei are transferred from the heterogeneous (subcritical) region $z_0 \leq -1$ into the two-phase (overbarrier) region $z_0 \geq 1$.

To separate the variables in Eq. (1), first we transform the coordinates to bring the matrix of diffusion coefficients D_{ij} into the form of a matrix proportional to the unit matrix E_{nm}:

$$x_i = A_{ij} y_j, \tag{5}$$

$$D'_{nm} = E_{nm} = D_{ij}\frac{\partial y_n}{\partial x_i}\frac{\partial y_m}{\partial x_j}. \tag{6}$$

This transformation can always be carried out due to the symmetry and positive definiteness of the matrix $\hat{D}$ (e.g., by choosing $\hat{A} = \sqrt{\hat{D}}$). Then, performing rotation defined by the unitary matrix $\hat{U}$, we diagonalize the quadratic form of the free energy:

$$y_i = U_{ij} z_j, \tag{7}$$

$$\begin{aligned} V - V_c &= \sum_{i,j} V_{ij} x_i x_j = \sum_{i,j} \tilde{V}_{ij} z_i z_j \\ &= -\lambda_0 z_0^2 + \sum_{i \neq 0} \lambda_i z_i^2. \end{aligned} \tag{8}$$

The eigenvalues λ_i are invariant quantities and can be determined from the condition

$$\det(\hat{V} - \lambda \hat{D}^{-1}) = 0. \tag{9}$$

The equation for the distribution function in the frame of reference (z_i) takes on the form of an F–P equation in which the variables are completely separated:

$$\begin{aligned} \frac{\partial P(z, t)}{\partial t} &= \frac{\partial}{\partial z_0}\left(-2P\lambda_0 z_0 + T\frac{\partial P}{\partial z_0}\right) \\ &+ \sum_{i \neq 0} \frac{\partial}{\partial z_i}\left(2P\lambda_i z_i + T\frac{\partial P}{\partial z_i}\right). \end{aligned} \tag{10}$$

A solution to Eq. (10) can be represented in the form

$$P(z_0, \{z_i\}; t) = F_0(z_0, \{z_i\}) f(z_0, t)/f_0(z_0), \tag{11}$$

$$f_0(z_0) \approx \exp(\lambda_0 z_0^2/T), \tag{12}$$

where $f_0(z_0)$ is the quasi-equilibrium distribution function [1, 2] with respect to variable z_0 and the function $f(z_0, t)$ meets a one-dimensional F–P equation,

$$\frac{\partial f}{\partial t} = \frac{\partial}{\partial z_0}\left(-2 f \lambda_0 z_0 + T\frac{\partial f}{\partial z_0}\right). \tag{13}$$

The boundary conditions for Eq. (13) are specified as follows. Since the variable z_0 plays the role of an unstable variable in the equilibrium distribution f_0, threshold-type boundary conditions should be imposed for this variable (see [7]):

$$\begin{aligned} \Psi(z_0, t) &= f(z_0, t)/f_0(z_0) \approx 1, \quad z_0 \le -1, \\ \Psi(z_0, t) &= f(z_0, t)/f_0(z_0) \approx 0, \quad z_0 \ge 1. \end{aligned} \tag{14}$$

It is obvious that if the conditions $z_0 \le -1$ and $z_0 \ge 1$ are replaced with $z_0 \longrightarrow -\infty$ and $z_0 \longrightarrow \infty$, then approximate equalities (14) are replaced with the corresponding strict equalities.

According to Zel'dovich [1] (see also [2]), the stationary solution to Eq. (13) subject to boundary conditions (14) has the form

$$\begin{gathered} \Psi_{\text{st}}(z_0) = \frac{j_0}{T}\int_{z_0}^{\infty} dy \exp\left(\frac{-\lambda_0 y^2}{T}\right), \\ j_0 = \sqrt{\frac{T\lambda_0}{\pi}}. \end{gathered} \tag{15}$$

By analogy with Eq. (1), we introduce an auxiliary flux J'_n in the configuration space $\{z_i\}$ which is determined from the stationary solution to Eq. (10):

$$J'_n(z) = j_0 Z \exp\left(-\frac{V_c + \sum\limits_{i \ne 0}\lambda_i z_i^2}{T}\right)\delta_{n0}. \tag{16}$$

To determine the total flux of nuclei through the "sink" surface $z_0(x) = 0$ of the potential relief $V(x)$, we find the transformation law of the flux under affine transformations (5) and (7). From the definition of the flux given by Eq. (1), we have

$$J'_n(z) = J_i(x)\frac{\partial z_n}{\partial x_i}. \tag{17}$$

Now, we take into account that, under the coordinate transformation, integration over an arbitrary hypersurface defined by an equation $G(x_0, \ldots, x_N) = 0$ is transformed as

$$\begin{aligned} &\int\ldots\frac{\partial G}{\partial x_i}\delta(G(x_0, \ldots, x_N))\,dx_0\ldots dx_N \\ &= \int\ldots\frac{\partial z_j}{\partial x_i}\frac{\partial G}{\partial z_j}\delta[G(x_0(z), \ldots, x_N(z))]\left\|\frac{\partial x_i}{\partial z_j}\right\|dz_0\ldots dz_N, \end{aligned}$$

where $\delta(x)$ is the delta function and $\|\partial x_j/\partial z_i\|$ is the Jacobian of the transformation of variables $\{x_i\}$ into $\{z_j\}$. Hence, the invariant flux of nuclei in the frame of reference $\{z_j\}$ is given by

$$\tilde{J}_n(z) = J'_n(z)\|\partial x_i/\partial z_j\|. \tag{18}$$

In a similar way, we find that the size distribution function is transformed as

$$\tilde{P}(z) = P(x)\|\partial x_i/\partial z_j\|. \tag{19}$$

To determine the total nucleation rate I, we should integrate Eq. (18) over the hypersurface $z_0 = 0$. Taking into account the Jacobian of the coordinate transformation $\|\partial x_i/\partial z_j\|$, we write

$$\begin{aligned} I &= j_0 Z\sqrt{(\pi T)^N\frac{\det(\hat{D})}{\lambda_1\ldots\lambda_N}}\exp\left(-\frac{V_c}{T}\right) \\ &= Z\frac{\lambda_0}{\pi}\sqrt{\frac{(\pi T)^{N+1}}{|\det\hat{V}|}}\exp\left(-\frac{V_c}{T}\right). \end{aligned} \tag{20}$$

The flux I controls the phase transition rate, i.e., the frequency of supercritical nuclei formation. The time required for the flux to become steady is characterized by a certain incubation time τ_n, which can be determined by solving the time-dependent equation for distribution function (13) with respect to the unstable variable.

3. NONSTATIONARY NUCLEATION STAGE

To estimate the transient time of the process of nucleation of the new phase, we should solve Eq. (13) with the initial condition

$$f(z_0 > -1, 0)/f(z_0) = 0,$$

which means new-phase nuclei are absent at the initial time. This problem is characterized by a single parameter $\beta_0 = \Delta\Phi/T \gg 1$ on which the solution will depend. In order of magnitude, this parameter is equal to the ratio $\beta_0 = \lambda_0/T$, where $\Delta\Phi$ is the work for the critical-size nucleus formation. An approximate solution to Eq. (13) with boundary conditions (14) and the zero initial condition is given by

$$\Psi(x, t) = \Psi_{\text{st}}\left(\frac{x + w(t)}{\sqrt{1 - w^2(t)}}\right), \tag{21}$$

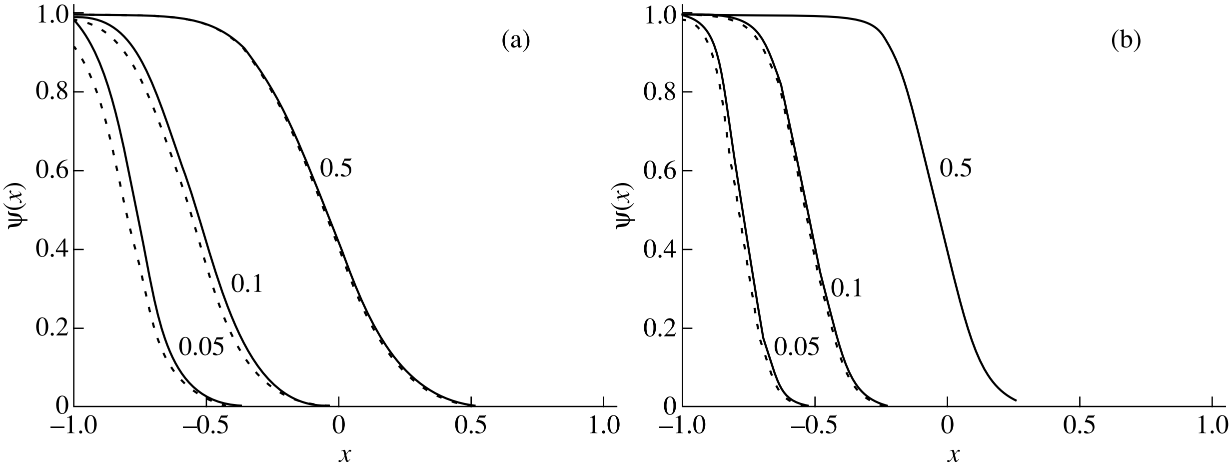

Fig. 1. Function $\Psi(x, t)$ for β_0 equal to (a) 10 and (b) 30 and different values of the relaxation time t: $0.05\tau_n$, $0.1\tau_n$, and $0.5\tau_n$. The dashed and solid curves correspond to analytical solution (23) and a numerical solution of the problem, respectively.

where the function $w(t) = \exp(-2\beta_0 t)$ describes the position of the nucleation front, behind which there are no new-phase nuclei. Figure 1 shows the function $\Psi(x, t)$ obtained by both solving the problem numerically and using solution (21) for two characteristic values of the parameter β_0. The figure shows good agreement between solution (21) and the numerical solution almost for all relaxation times at $\beta_0 \geq 10$. Using self-similar solution (21), one can readily estimate the transient time after which the function $\Psi(x, t)$ differs from its stationary value by no more than 1%. As a result, we have

$$\tau_n \approx \frac{\ln(10^4\beta_0)}{4\beta_0}. \tag{22}$$

Finally, from Eqs. (13) and (21), we find the general solution to the multidimensional problem

$$P(z_0, \{z_i\}; t) = F_0(z_0, \{z_i\})\Psi_{\text{st}}\left(\frac{z_0 + w(t)}{\sqrt{1 - w^2(t)}}\right), \tag{23}$$

which describes the establishment of the steady mode of the phase transition in the whole near-critical region.

4. BOILING OF A VOLATILE LIQUID

As an example, we consider the phase transition in a moderately superheated or stretched volatile liquid. In this case, the role of a metastable phase is played by the superheated or stretched liquid. The role of stable-phase nuclei is played by vapor bubbles described by two macroscopic variables, namely, pressure p and volume ν. It is noteworthy that we introduce a second variable, the pressure p of the bubble, because this pressure differs from the saturated-vapor pressure in a bubble of the given curvature in the absence of thermodynamic equilibrium.

In this case, the boiling of a volatile liquid can be considered to be the diffusion of a nucleating vapor bubble in two-dimensional space. According to [4, 7], we have

$$x_1 = (\nu - \nu_c)/\nu_c, \quad x_2 = (p - p_c)/p_c, \tag{24}$$

$$V_c = 4\pi R_c^2\sigma/3, \quad R_c = 2\sigma/(p_c - P), \tag{25}$$

$$p_c = p_\infty \exp(-2\sigma/\rho_l T R_c), \quad Z = \rho_l^2 \nu_c \left(\frac{p_c \nu_c}{2\pi T}\right)^{1/2}, \tag{26}$$

where σ, P, and ρ_l are the surface tension coefficient, pressure, and density of the liquid, respectively; R and ν are the radius and volume of the vapor bubble, respectively; p is the vapor pressure in the bubble; p_∞ is the saturated-vapor pressure over a plane surface of the liquid; and T is the vapor temperature in energy units. The temperature T is assumed to be constant during nucleation.

In the vicinity of the critical point, the free energy of a spherical bubble of volume ν and pressure p can be written as

$$\begin{gathered} V(x_1, x_2) = V_c - a_1 x_1^2 + a_2 x_2^2, \\ a_1 = \sigma S_c/9, \quad a_2 = \rho_v^2 \nu_c/2, \end{gathered} \tag{27}$$

where S_c is the surface area of the critical bubble and ρ_v^2 and ν_c are the vapor critical density and the critical bubble volume, respectively. One can see from Eqs. (27) that the point ν_c, p_c of the labile equilibrium of the system is always a hyperbolic point of the surface. According to [4], the diffusion matrix $\hat{D}$ at a saddle point is written as

$$\hat{D} = D\begin{pmatrix} 1 & -1 \\ -1 & 1 + 1/\omega \end{pmatrix},$$
$$\omega = p_c R_c/\alpha\nu_t\eta, \quad D = \frac{3}{4\nu_c\eta}, \tag{28}$$

where η is the liquid viscosity and α and ν_t are the condensation coefficient and the average thermal velocity of vapor molecules, respectively. In Eq. (28), the contribution of the inertia term is neglected, which is valid under the condition (see [4])

$$\rho_l m\sigma R_c/8\eta^2 \ll 1,$$

where m is the mass of a molecule of the liquid.

Using Eqs. (15) and (20), the nucleation probability can be found to be

$$\begin{aligned} I &= \frac{Z\lambda_0}{\pi}\sqrt{\frac{\pi^2 T^2}{a_1 a_2}}\exp(-V_c/T) \\ &= 2\lambda_0\rho_l^2 R_c^2\left(\frac{T}{\sigma}\right)^{1/2}\exp(-4\pi R_c^2/3T) = \rho_l^2 R_c\frac{3\alpha\nu_t}{8}\left(\frac{T}{\sigma}\right) \\ &\times\{[(1-\chi+\omega)^2+4\chi]^{1/2}-1+\chi-\omega\} \\ &\times\exp(-4\pi R_c^2/3T), \end{aligned} \tag{29}$$
$$\chi = 2\sigma/3\alpha\nu_t\eta,$$

where the dimensionless parameters ω and χ were introduced in [4] to study various extreme cases of the problem. Expression (29) represents the sought-for probability of the critical vapor bubble arising in a unit volume per unit time. A similar relation was derived in [4] by analyzing the potential relief of the free energy in the vicinity of the saddle point. As can be readily shown, the expression from [4] can be simplified and reduced to the invariant form of Eq. (29).

5. CONCLUSIONS

Thus, we have comprehensively studied the nucleation stage of the multidimensional first-order phase transition. The size distribution of nuclei and the nucleation rate were found. By reducing the problem to the canonical form, we considered both stationary and nonstationary stages of nucleation and estimated the duration of the establishment of the steady mode. The approach suggested made it possible to determine the basic parameters of the first-order phase transition in the invariant form and to express them in terms of the initial parameters of the problem. In the stationary case, the calculated flux coincides with the result obtained in [8].

We note that the approach we suggested does not invoke explicit forms of the free energy and of the kinetic coefficients. Therefore, the results obtained are universal and can be applied to any multicomponent system whose free energy has a one-dimensional saddle singularity.

REFERENCES

1. Ya. B. Zel'dovich, Zh. Éksp. Teor. Fiz. **12** (11–12), 525 (1942).
2. E. M. Lifshitz and L. P. Pitaevskiĭ, *Course of Theoretical Physics*, Vol. 10: *Physical Kinetics* (Nauka, Moscow, 1979; Pergamon, Oxford, 1981).
3. H. Kramers, Physica (Amsterdam) **7**, 284 (1940).
4. B. V. Deryagin, A. V. Prokhorov, and N. N. Tunitskiĭ, Zh. Éksp. Teor. Fiz. **73** (5), 1831 (1977) [Sov. Phys. JETP **46**, 962 (1977)].
5. H. Reiss, J. Chem. Phys. **18** (6), 840 (1950).
6. V. A. Shneĭdman, Zh. Éksp. Teor. Fiz. **91** (2), 520 (1986) [Sov. Phys. JETP **64**, 306 (1986)].
7. F. M. Kuni and A. A. Melikhov, Teor. Mat. Fiz. **81** (2), 247 (1989).
8. J. S. Langer, Ann. Phys. **54**, 258 (1969).
9. L. Granasy and P. F. James, J. Chem. Phys. **111** (2), 737 (1999).

Translated by A. Kazantsev

Physics of the Solid State, Vol. 44, No. 12, 2002, pp. 2323–2326. Translated from Fizika Tverdogo Tela, Vol. 44, No. 12, 2002, pp. 2217–2219.
Original Russian Text Copyright © 2002 by Volkov, Andreeva, Anoshina, Povzner.

Semiconductor–Metal Kinetic Phase Transition in Nearly Magnetic Semiconductors Exemplified with Iron Monosilicide

A. G. Volkov, A. G. Andreeva, O. V. Anoshina, and A. A. Povzner
Ural State Technical University, ul. Mira 19, Yekaterinburg, 620002 Russia
e-mail: povz@kf.ustu.ru

Received November 27, 2001; in final form, April 1, 2002

Abstract—Iron monosilicide is used to study the possibility of the semiconductor–metal kinetic phase transformation in nearly magnetic semiconductors. It is shown that the heat released by current flow gives rise to a growth in amplitude of spin fluctuations and the attendant splitting of electronic spectra, which, in turn, brings about gap closure and an avalanche increase in the number of charge carriers. *© 2002 MAIK "Nauka/Interperiodica".*

It is well known that sufficiently strong electric fields produce *S*-shaped nonlinearities in the current–voltage (*I*–*U*) characteristics of semiconductors [1, 2]. Such *S*-shaped *I*–*U* characteristics can be treated as realizations of the "cold"–"hot" semiconductor kinetic phase transition [3].

The specific features in the *I*–*U* characteristics of semiconducting materials observed to occur at dynamic equilibrium, the conditions in which the transfer of the Joule heat released by the current to the surrounding medium is impeded by low thermal conductivity, were considered in [1]. It was established that the *I*–*U* characteristics of a square film of width *L* and thickness and height *h* should be *S*-shaped. The results obtained in [1] are applicable, however, only to classical semiconductors whose band gap, electronic spectrum, and the state of the electron subsystem remain unchanged.

At the same time, compounds based on *d*-metal silicides include a specific class of superparamagnetic semiconductors (FeSi, $Fe_xCo_{1-x}Si$, $Fe_xMn_{1-x}Si$, etc.) whose electronic properties are dominated by spin density fluctuations [4–8]. The spin fluctuations, whose amplitude grows with increasing temperature, split the original one-electron spectrum into two branches (see, e.g., [4–8]),

$$\varepsilon_k^{(\pm)} = \varepsilon_k \pm \xi, \tag{1}$$

one of which shifts energywise up and the other shifts down with increasing spin fluctuation amplitude ξ. This renormalization brings about closure of the gap separating the valence and conduction bands, thus making possible the semiconductor–metal transition with increasing temperature.

The most comprehensive analysis of such electronic transformations has been performed for the FeSi superparamagnetic semiconductor [9–11]. However, the nonequilibrium features of this transformation, which should be enhanced in such a system in comparison with conventional nonmagnetic semiconductors, as well as the possible nonlinear features in the *I*–*V* curves, were not considered.

According to [6–8], the amplitude of spin fluctuations in superparamagnetic systems is given by the relation

$$\xi = bT'D_0^{-1/2}(D_0^{-1}+a)^{-1/2}, \tag{2}$$

where coefficients *a* and *b* are derived either from neutron diffraction data or from magnetic measurements (see [6–8]), $D_0 = D_0(\xi, T')$ is the exchange-induced enhancement of uniform *d*-electron magnetic susceptibility (see [6–8]), and T' is the internal sample temperature, which depends on current density *j* and applied voltage *U* and is determined by the dynamic-equilibrium condition

$$jU = \frac{2}{h}\lambda(T'-T), \tag{3}$$

with λ being the thermal conductivity coefficient of the semiconductor (which is assumed to be constant over the sample thickness) and *T* being the ambient temperature.

Thus, under the dynamic equilibrium defined by Eq. (3), the spin fluctuation amplitude is a function of the applied voltage and current density in the sample given by

$$\xi = b\left(T + jU\frac{h}{2\lambda}\right)D_0^{-1/2}(D_0^{-1}+a)^{-1/2}. \tag{4}$$

In accordance with Eq. (1), Eq. (4) shows that the electronic spectrum undergoes transformation under variation of *U* and *j* and that other physical quantities (in

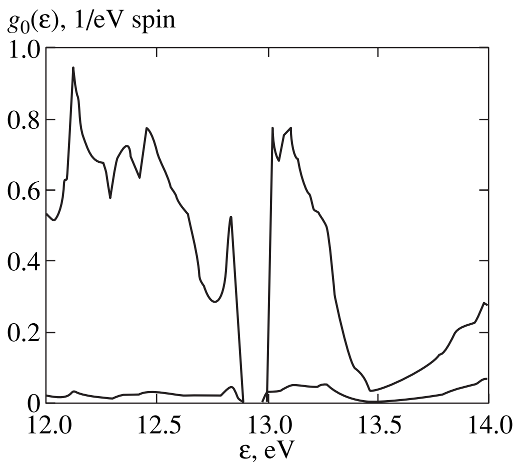

Fig. 1. Electron density of states in FeSi [12]. The top curve relates to *d* electrons; the bottom one, to *sp* electrons.

particular, D_0, the chemical potential μ, the density of states, and the band gap E_g) become dependent on applied voltage and current density. Unlike conventional semiconductors, the effect of voltage and current density on the properties of nearly magnetic semiconductors turns out to be enhanced strongly because of the large exchange enhancement factor.

To describe the conductivity of superparamagnetic semiconducting compounds in a self-consistent way, we shall use the definition of current density in terms of the generalized *sd* model with inclusion of the spin-fluctuation renormalization of the electronic spectrum [4–8]:

$$j = \sum_{l,\alpha} j_{l,\alpha}, \qquad (5)$$

$$j_{l,\alpha} = e\int \nu_{k,l} f(\varepsilon_{k,l} - \alpha\xi_l - \mu - eU\nu_{k,l}\tau_{k,l}/L)d\mathbf{k}, \quad (6)$$

where $j_{l,\alpha}$ are the current densities of each of the ($\alpha = \pm1$) groups of *sp* ($l = s$) or *d* ($l = d$) electrons; $\varepsilon_{k,l}$ is the energy of electrons with quasi-momentum k; $\nu_{k,l}$ is the projection of electron velocity onto the electric field direction;

$$\tau_{k,l} \propto k^{2r-1}(\partial\varepsilon_{kl}/\partial k)^2 \qquad (7)$$

is the relaxation time; r is a parameter, which is 3/2 for the case of electron scattering from phonons; ξ_l is the spin-fluctuation-induced splitting of the *sp*- and *d*-electron spectrum, which is expressed through the spin fluctuation amplitude in the *d* subsystem as

$$\xi_d = \xi,$$
$$\xi_s = (J/Q)^2\xi;$$

μ is the chemical potential derived from the condition of charge neutrality with renormalized densities of states

$$N/N_0 = (1/2)\sum_{\alpha=\pm1,\, l=s,\, d}\int_{-\infty}^{\infty} g_0^{(l)}(\varepsilon+\alpha\xi_l)f(\varepsilon-\mu)d\varepsilon; \quad (8)$$

$f(\varepsilon - \mu)$ is the Fermi–Dirac function, depending on internal temperature T'; $g_0^{(l)}(\varepsilon)$ is the density of states of noninteracting *sp* and *d* electrons; Q is the parameter of intraatomic *d*-electron Coulomb repulsion; J is the uniform part of the *sp*–*d* exchange coupling parameter; N_0 is the number of lattice sites; N is the total number of *sp* and *d* electrons; and e is the electronic charge.

The coupled equations (3)–(8) provide a possibility of describing the *I*–*U* characteristics of superparamagnetic semiconductors under self-heating. We note that, as follows from Eqs. (1) and (4), this effect is additionally enhanced by the narrowing of the band gap in the spectrum of such semiconductors. Analytical solution of these coupled equations in the general case is, however, impossible. Therefore, we analyzed Eqs. (3)–(8) and estimated the critical voltages numerically using the specific example of FeSi.

According to band structure calculations [12], the one-electron spectrum of both *d* and *sp* electrons in FeSi consists of two bands separated by a gap approximately 0.12 eV wide (Fig. 1). The chemical potential of this compound at $T = 0$ K is located in the band gap; therefore, the one-electron state of FeSi is semiconducting. However, as established in [13], an increase in temperature entails a narrowing of the band gap in the spectra of both *sp* and *d* electrons of this compound. At $T_g^{(d)} \approx 100$ K, the energy gap in the *d*-electron spectrum disappears and the *d* electrons become itinerant. In its turn, the chemical potential starts to shift energywise to the left because of the *d* bands being asymmetric and enters the valence band of the *sp* electrons at $T^{(s)} \approx 200$ K, which makes their state likewise metallic. Thus, the conductivity of iron monosilicide is dominated by the activation mechanism at internal sample temperatures below 100 K, by both the metallic and activation mechanisms in the interval 100–200 K, and by only the metallic mechanism at temperatures above 200 K.

Numerically calculated *I*–*U* characteristics of a cubic ($L = h$) FeSi sample are presented graphically in Fig. 2. The density-of-states function was taken from [12] (Fig. 1). Using this density of states, the *d* and *sp* electron spectra were simulated in the effective-mass approximation

$$g^{(l)}(\varepsilon_{k,l}) = k^2(\partial\varepsilon_{k,l}/\partial k)^{-1},$$

and the spin fluctuation amplitudes were calculated with the spin-fluctuation parameters $a = 0$ and $b = 10/Q$, which were derived in [4] from neutron diffraction data. The value of the *sp*–*d* exchange parameter was chosen, as in [13], to be $J \approx 0.1Q$. The temperature dependence of the thermal conductivity coefficient of FeSi was approximated by a function constructed by interpolating the experimental data from [14].

As follows from these *I*–*U* curves and a numerical analysis of the dependence of the internal sample temperature on applied voltage, the voltage at which transition to the hot phase occurs (U_{on}) corresponds, irrespective of the sample size, to sample heating to a temperature close to $T' = T_g^{(d)}$ (=100 K), at which the *d*-electron subsystem undergoes metallization (Fig. 2). After this, the internal temperature jumps to the value T', which depends on sample size and the ambient temperature but is necessarily higher than $T^{(s)}$ (=200 K). At the same time, the voltage of transition to the cold phase (U_{off}) in the reverse branch of the *I*–*U* characteristic corresponds to a decrease in the internal temperature to the value $T^{(s)}$ (at which the *sp* electrons transfer from the semiconducting to metallic state). The internal temperature of the sample drops to values below $T_g^{(d)}$ (Fig. 2). Note also that *I*–*U* hysteresis does not occur at ambient temperatures $T > T_g^{(d)}$ (=100 K), i.e., in the cases where the *d* electrons are initially in the metallic state (Fig. 2). However, the *I*–*U* characteristics remain nonlinear up to complete metallization of the total electron subsystem, i.e., to $T = T^{(s)}$.

Thus, the kinetic phase transition considered above is driven by thermal spin fluctuations initiated by Joule heat release at $U = U_{\text{on}}$ and resulting in band-gap closure in the *d*-electron spectrum, which brings about an increase in the number of carriers and, as a consequence, a considerable increase in the current density. The increase in the current density entails a still larger Joule heat release (sample self-heating) and, hence, a larger growth in the number of carriers (*d* electrons) and current density. This avalanche-type growth comes to an end when the chemical potential enters the *sp*-electron valence band and these electrons undergo metallization. Thus, at $U = U_{\text{on}}$, the electron subsystem of a superparamagnetic semiconductor becomes completely metallic in a jump. A further increase in the internal temperature of the sample entails an increase in its resistivity and, hence, a decrease in current density and in the amount of Joule heat released in the sample; the avalanche process of self-heating terminates, and a stable hot phase sets in.

Similarly, in the reverse *I*–*U* branch, a decrease in applied voltage leads to a decrease in the current density and in the amount of Joule heat liberated in the sample. As a result, the spin fluctuations decrease in amplitude, which reduces the spin-fluctuation-induced splitting of the electron spectrum, shifts the chemical potential to the edge of the *sp*-electron valence band, and drives the chemical potential into the energy region forbidden for *sp* electrons for $T' \leq T^{(s)}$. The resultant decrease in the number of carriers reduces still further the heat liberation and removes the spin-fluctuation-induced renormalization of the band gap in the *d*-electron spectrum (at $T' = T_g^{(d)}$).

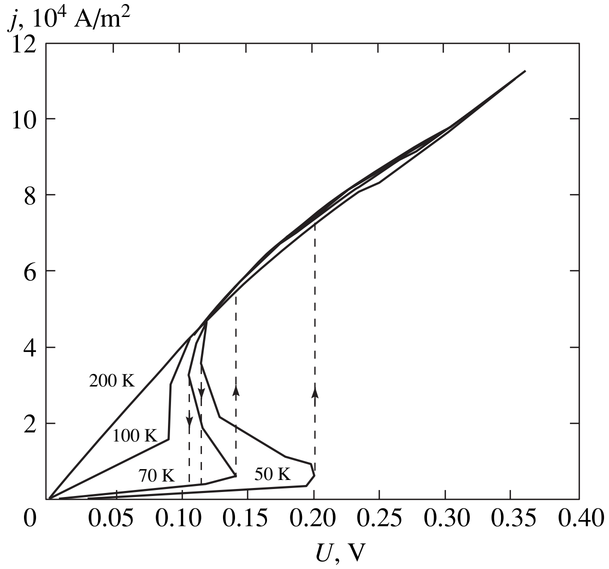

Fig. 2. Current–voltage characteristics of the FeSi close-to-magnetic semiconductor. The figures above the curves specify the corresponding ambient temperatures.

The effects of kinetic electronic transformations in superparamagnetic FeSi considered above require additional experimental studies of the conductivity in strong enough electric fields. Another group of substances also possibly capable of exhibiting such kinetic electronic transitions is the Kondo systems based on rare-earth metals (for instance, CeNiSn, $CeBi_4Pt$, SmB_6), in which one observes anomalies of electronic properties identical in many respects to those found to exist in iron monosilicide [15].

REFERENCES

1. V. L. Bonch-Bruevich, I. P. Zvyagin, and A. G. Mironov, *Domain Electrical Instabilities in Semiconductors* (Nauka, Moscow, 1972; Consultants Bureau, New York, 1975).
2. A. Krotkus and Z. Dobrovol'skiĭ, *Electrical Conductivity of Narrow-Gap Semiconductors* (Mokslas, Vilnius, 1988).
3. A. V. Melkikh, A. A. Povzner, A. G. Andreeva, and I. N. Sachkov, Pis'ma Zh. Tekh. Fiz. **27** (6), 19 (2001) [Tech. Phys. Lett. **27**, 226 (2001)].
4. A. A. Povzner, A. G. Volkov, and P. V. Bayankin, Fiz. Nizk. Temp. **23** (10), 1054 (1997) [Low Temp. Phys. **23**, 792 (1997)].
5. P. V. Gel'd, A. A. Povzner, and A. G. Volkov, Dokl. Akad. Nauk SSSR **283** (2), 358 (1985) [Sov. Phys. Dokl. **30**, 585 (1985)].
6. A. A. Povzner, A. G. Volkov, and P. V. Bayankin, Fiz. Tverd. Tela (St. Petersburg) **40** (8), 1427 (1998) [Phys. Solid State **40**, 1305 (1998)].

7. T. Moriya, *Spin Fluctuation in Itinerant Electron Magnetism* (Springer, Heidelberg, 1985; Mir, Moscow, 1988).
8. A. A. Povzner, A. G. Volkov, and P. V. Bayankin, Fiz. Nizk. Temp. **23** (10), 1054 (1997) [Low Temp. Phys. **23**, 792 (1997)].
9. V. Jaccarino, G. R. Wertheim, J. H. Werneic, *et al.*, Phys. Rev. **160** (3), 46 (1967).
10. Z. Schleizenger, Z. Fisk, H. T. Zhang, *et al.*, Phys. Rev. Lett. **71** (11), 1748 (1993).
11. F. A. Sidorenko, E. A. Dmitriev, and P. V. Gel'd, Izv. Vyssh. Uchebn. Zaved., Fiz. **8** (1), 15 (1972).
12. L. I. Vinokurova, A. V. Vlasov, and É. T. Kulatov, Tr. Inst. Obshch. Fiz. Akad. Nauk SSSR **2** (4), 463 (1991).
13. A. G. Volkov, A. A. Povzner, V. V. Kryuk, and P. V. Bayankin, Fiz. Tverd. Tela (St. Petersburg) **41** (10), 1792 (1999) [Phys. Solid State **41**, 1644 (1999)].
14. F. M. Ostrovskiĭ, Author's Abstract of Dissertation (UPI, Sverdlovsk, 1970).
15. M. B. Hunt, M. A. Chernikov, E. Felder, *et al.*, Phys. Rev. B **50** (20), 14933 (1994).

Translated by G. Skrebtsov

Physics of the Solid State, Vol. 44, No. 12, 2002, pp. 2327–2330. Translated from Fizika Tverdogo Tela, Vol. 44, No. 12, 2002, pp. 2220–2223.
Original Russian Text Copyright © 2002 by Bisti.

LOW-DIMENSIONAL SYSTEMS AND SURFACE PHYSICS

The Excited States of an Intersubband Exciton

V. E. Bisti
Institute of Solid-State Physics, Russian Academy of Sciences, Chernogolovka, Moscow oblast, 142432 Russia
e-mail: bisti@issp.ac.ru

Received February 19, 2002

Abstract—The energy of intersubband collective spin- and charge-density excitations is calculated for a system of quasi-two-dimensional electrons at certain values of the angular-momentum component perpendicular to the plane of the electron free motion. The calculation is carried out within the Hartree–Fock approximation. It is shown that the excited states correspond to the electron transitions in the vicinity of the Fermi momentum. The dispersion of the collective excitations is considered. © *2002 MAIK "Nauka/Interperiodica".*

Quasi-two-dimensional electron systems arise when there is a confinement potential along one of the coordinate axes. The presence of several size-quantization levels in such systems results in the appearance of a number of peculiarities in comparison with three-dimensional and purely two-dimensional systems. One of these peculiarities is the existence of intersubband collective excitations corresponding to electron transitions between size-quantization subbands.

Intersubband collective excitations have been studied for quite a long time. Experimentally, these excitations are observed using the Raman scattering [1–3] and infrared-absorption [4] methods. These excitations are classified as charge-density excitations (CDE) and spin-density excitations (SDE); this distinction is revealed in the polarization dependence of the lines observed. In other words, CDE and SDE can be interpreted as singlet and triplet intersubband excitons.

Theoretically, these excitations have also been extensively investigated. Within the simplest, random-phase approximation (RPA), there is only charge-density excitation [5]. With due regard for the exchange interaction, there are two types of excitations. The methods used to calculate the intersubband excitations with allowance for the exchange energy can be classified into two main groups. One group includes calculations using local density approximation (LDA) and its modifications [6–9] based on more general, density-functional methods [10–12]. The other group includes the direct methods for calculating the response function (polarization operator) of the system with the use of diagram techniques or the density matrix method and solution of the Bethe–Salpeter equation [13–16]. The former methods were used to find only the lowest energy for each type of excitation (singlet of triplet). In the LDA approximation, the momentum-dependent interaction is replaced by an effective constant (the so-called contact, i.e., local interaction in the coordinate space). There is only one collective excitation (bound state) in this case. While solving the Bethe–Solpeter equation, the intersubband exciton ground state alone was also considered.

Meanwhile, the experimental Raman spectra of quantum wells of quasi-two-dimensional structures exhibit a broad nonpolarized line which is situated, as a rule, between the SDE and CDE lines [1, 3] and is interpreted as a result of the scattering from single-particle excitations (SPE). This interpretation, however, is doubted even by the authors of the experiments. Therefore, it is worthwhile to consider this problem in detail.

In this paper, the energy of both ground and excited states of the intersubband exciton is calculated within the Hartree–Fock approximation. It is suggested that the SPE line is a result of scattering from the excited states, whereas the SDE and CDE lines are due to scattering from the ground states.

Let us consider a GaAs–AlGaAs well with modulated doping; such wells are usually used in experiments. The well consists of a GaAs layer sandwiched between two thick AlGaAs layers, one of which contains a layer of donors (see [4] for a more detailed description). The energies of the subbands E_n^H and the electron wave functions $\phi_n(z)$ are calculated within the Hartree approximation by solving the single-particle Schrödinger equation and the Poisson equation in a self-consistent way (axis z is perpendicular to the layer).

The Hamiltonian of such a quasi-two-dimensional system has the form

$$H = \sum_{n\mathbf{k}s}\left(E_n^H + \frac{\hbar^2 k^2}{2m^*}\right)c^+_{n\mathbf{k}s}c_{n\mathbf{k}s} + \frac{1}{2}\sum_{nn'mm'ss'\mathbf{k}\mathbf{k}'} V^{n'm'}_{nm}c^+_{n\mathbf{k}+\mathbf{q}s}c^+_{n'\mathbf{k}'-\mathbf{q}s'}c_{m'\mathbf{k}'s'}c_{m\mathbf{k}s}, \qquad (1)$$

where m^* is the electron effective mass; n, n', m, and m' are indices of the subbands; s and s' are spin indices; $\mathbf{k}$,

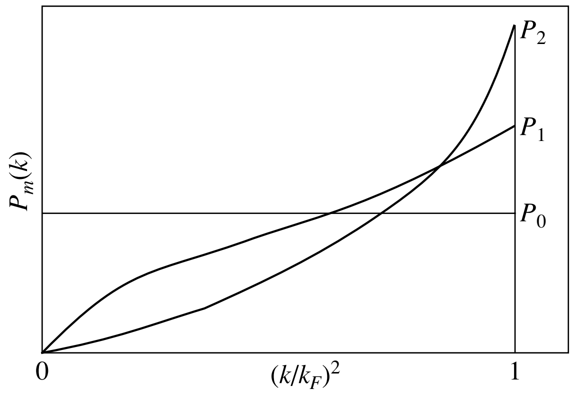

Fig. 1. Radial wave functions of the intersubband excitons in the momentum representation.

k', and **q** are the wave vectors in the plane of the electron motion (the *xy* plane); and

$$V_{nm}^{n'm'}(q) = \frac{e^2}{2\varepsilon q} \times \int \phi_n^*(z)\phi_{n'}^*(z')\phi_{m'}(z')\phi_m(z)e^{-q|z-z'|}dzdz'. \tag{2}$$

In what follows, we will consider only the two lowest size-quantization subbands with energies E_1^H and E_2^H. The electron concentration is such that only the lowest subband is filled.

The energies of the collective excitations of the system are the poles of the polarization operator (polarization response function of the system) or, what is the same, the poles of the two-particle Green's function, which is analogous to the exciton Green's function in the case of interband transitions. The Hartree–Fock approximation takes into account the exchange corrections to the self-energies and the depolarization (for **S** = 0) and exciton corrections. In terms of the diagrammatic technique, this corresponds to the exchange correction to the single-particle Green's functions and the summation over the loop and ladder diagrams for the two-particle Green's function. The derivation of the corresponding equation by using the density-matrix method is given in [14].

Within the pole approximation, the eigenvalue equation which determines the energies of the intersubband exciton has the form

$$[E_2^{\mathrm{HF}}(\mathbf{k}+\mathbf{K}) - E_1^{\mathrm{HF}}(\mathbf{k}) - E]P(\mathbf{k},\mathbf{K}) = \frac{1}{(2\pi)^2}\int V(\mathbf{k},\mathbf{k}',\mathbf{K})P(\mathbf{k}',\mathbf{K})d\mathbf{k}', \tag{3}$$

where E is the energy eigenvalue; $P(\mathbf{k}, \mathbf{K})$ is the wave function of the intersubband exciton in the momentum representation;

$$E_i^{\mathrm{HF}}(\mathbf{k}) = E_i^H + \frac{\hbar^2k^2}{2m} - \frac{1}{(2\pi)^2}\int V_{1i}^{i1}(\mathbf{k}'-\mathbf{k})d\mathbf{k}'; \tag{4}$$

for the triplet spin-density (SD) excitations (**S** = 1), we have

$$V^{\mathrm{SD}}(\mathbf{k},\mathbf{k}',\mathbf{K}) = V_{11}^{22}(\mathbf{k}'-\mathbf{k}); \tag{5}$$

and for the singlet charge-density (SD) excitations (**S** = 0), we have

$$V^{\mathrm{CD}}(\mathbf{k},\mathbf{k}',\mathbf{K}) = V^{\mathrm{SD}} - 2V_{12}^{21}(\mathbf{K}). \tag{6}$$

At **K** = 0, the system is axially symmetric (the z component of the angular momentum is conserved) and solutions to Eq. (3) take the form

$$P_m(\mathbf{k}) = P_m(k)e^{im\varphi} \tag{7}$$

($m = 0, \pm1, \pm2, \dots$).

The functions $P_m(k)$ and E_m are determined from the equations

$$[E_2^{\mathrm{HF}}(k) - E_1^{\mathrm{HF}}(k) - E_m]P_m(k) = \frac{1}{2\pi}\int V_m(k,k')P(k')k'dk', \tag{8}$$

where

$$V_m(k,k') = \frac{1}{2\pi}\int V(\mathbf{k},\mathbf{k}',0)\cos m\varphi d\varphi. \tag{9}$$

Although Eq. (8) possesses many solutions, only the lowest value of E_m for each type of symmetry is of interest, because the Hartree–Fock approximation is variational in nature.

Numerical calculations were performed for 250-Å thick GaAs–AlGaAs quantum wells with electron concentrations 3×10^{11} and 6×10^{11} cm^{-2}.

Equations (3) and (8) were solved numerically; the solutions to Eq. (8) with different m correspond to solutions to Eq. (3) with **K** = 0. Figure 1 shows the functions $P_m(k^2/k_F^2)$, which can be treated as radial wave functions of the intersubband exciton in the momentum representation. The calculated wave function P_0 explains the good agreement between the results obtained using different methods. The reason for this agreement is the fact that an effective contact interaction adequately describes the ground state; the size of the region of correlation between the electron in the excited subband and the hole in the ground subband is of the order of the interparticle distance. The excited P_m states with nonzero components of the angular momentum are excitations in the vicinity of the Fermi level. The solution to Eq. (8) with $m = 0$ describes the well-known CD and SD excitations. Our result coincides with that obtained

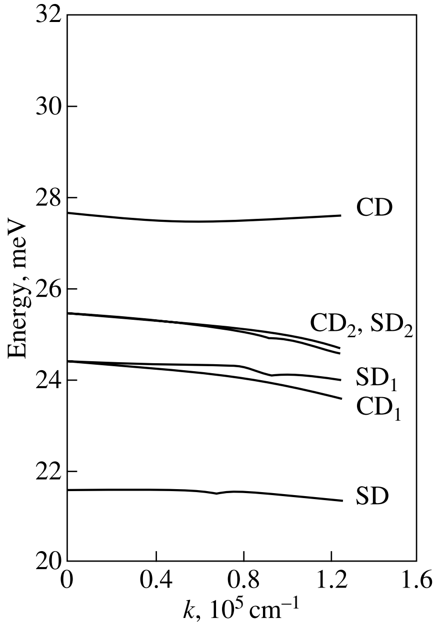

Fig. 2. Dispersion of the intersubband excitons in a 250-Å thick GaAs–AlGaAs quantum well for $n_s = 3 \times 10^{11}$ cm^{-2}.

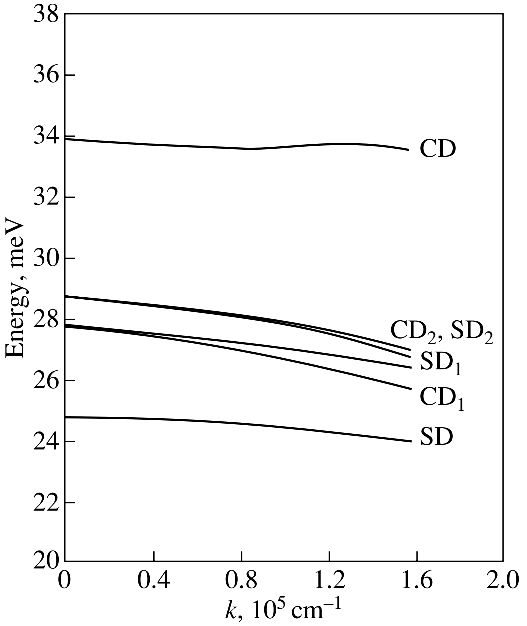

Fig. 3. Dispersion of the intersubband excitons in a 250-Å thick GaAs–AlGaAs quantum well for $n_s = 6 \times 10^{11}$ cm^{-2}.

in [13, 14]. At $m \neq 0$, the states with $\pm m$ are degenerate ($E_{+m} = E_{-m}$); in addition, these states are degenerate with respect to spin.

A solution to Eq. (3) determines the dispersion law of the intersubband excitons. At $\mathbf{K} \neq 0$, strictly speaking, the excited states are not states with a certain value of the z component of the angular momentum. The degeneracy is removed, and one of the states can manifest itself in the Raman spectra (at $\mathbf{K} = 0$, only the ground states with $m = 0$ are involved in the Raman scattering). The dispersion law for the Raman active modes is shown in Figs. 2 and 3. The dispersion of the CD and SD excitations in the ground state coincides with that obtained earlier [6, 16]. The SD excitations reveal a very weak quadratic momentum dependence. At small $\mathbf{K}$, the dispersion of the CDE is determined mainly by $V_{12}^{21}(\mathbf{K})$. For the excited states, the momentum dependence is significantly stronger and essentially nonquadratic. In this case, the degeneracy of the CD and SD modes is removed. The inactive states are located between these states and are degenerate with respect to spin.

Figure 4 shows an approximate spectrum of the intersubband Raman scattering involving the ground and excited states. The ratios between the intensities of the ground and excited states depend on $\mathbf{K}$, the wavelength of the incident light, and the size of the coherence area; therefore, the experimentally measured spectrum can noticeably differ from that shown in Fig. 4.

Thus, in this paper, the structure of the intersubband transitions has been considered (for the ground and excited states differing in the angular-momentum component perpendicular to the plane of the free-electron motion) within a unified approach (the Hartree–Fock approximation). It was shown that the so-called single-particle excitation line can be due to scattering by the excited states of the intersubband exciton. With increasing $\mathbf{K}$, this line can exhibit a certain structure which can be revealed experimentally.

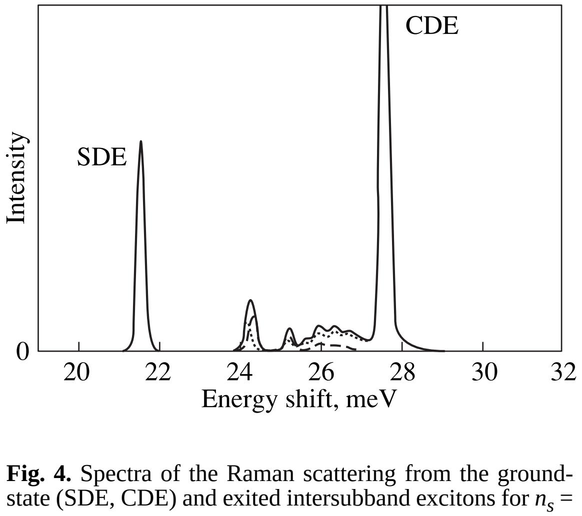

Fig. 4. Spectra of the Raman scattering from the ground-state (SDE, CDE) and exited intersubband excitons for $n_s = 3 \times 10^{11}$ cm^{-2} and $k = 0.63 \times 10^5$ cm^{-1}. The spectra of the scattering from the SD and CD excited states are shown by the dotted and dashed lines, respectively. The solid line shows the sum of these spectra, as well as the Raman spectrum from the ground-state excitons outside the region of the excited states.

ACKNOWLEDGMENTS

The author would like to thank I.V. Kukushkin and L.V. Kulik for useful discussions and attention to this work.

This work was supported in part by the Russian Foundation for Basic Research, project no. 01-02-16430.

REFERENCES

1. A. Pinczuk, S. Smitt-Rink, G. Danan, *et al.*, Phys. Rev. Lett. **63**, 1633 (1989).
2. D. Gammon, B. V. Shanabrook, J. C. Ryan, and D. S. Katzer, Phys. Rev. B **41**, 12311 (1990).
3. V. E. Kirpichev, I. V. Kukushkin, K. von Klitzing, and K. Eberl, Pis'ma Zh. Éksp. Teor. Fiz. **67**, 196 (1998) [JETP Lett. **67**, 210 (1998)].
4. M. Ramsteiner, J. D. Ralston, P. Koidi, *et al.*, J. Appl. Phys. **67**, 3900 (1990).
5. Jainendra K. Jain and S. Das Sarma, Phys. Rev. B **36**, 5949 (1987).
6. I. K. Marmorkos and S. Das Sarma, Phys. Rev. B **48**, 1544 (1993).
7. A. Tselis and J. J. Quinn, Phys. Rev. B **29**, 3318 (1984).
8. K. W. Chui and J. J. Quinn, Phys. Rev. B **9**, 4724 (1974).
9. T. Ando, J. Phys. Soc. Jpn. **51**, 3893 (1982).
10. P. Hohenberg and W. Kohn, Phys. Rev. **136**, B864 (1964).
11. W. Kohn and L. J. Sham, Phys. Rev. **140**, F1133 (1965).
12. O. Gunnarsson and B. I. Lundqvist, Phys. Rev. B **13**, 4274 (1976).
13. S. L. Chuang, M. S. C. Luo, S. Schmitt-Rink, and A. Pinczuk, Phys. Rev. B **46**, 1897 (1992).
14. M. S.-C. Luo, S. L. Chuang, S. Schmitt-Rink, and A. Pinczuk, Phys. Rev. B **48**, 11086 (1993).
15. J. C. Ryan, Phys. Rev. B **43**, 12406 (1991).
16. D. Gammon, B. V. Shanabrook, J. C. Ryan, and D. S. Katzer, Phys. Rev. Lett. **68**, 1884 (1992).

Translated by A. Poushnov

Physics of the Solid State, Vol. 44, No. 12, 2002, pp. 2331–2335. Translated from Fizika Tverdogo Tela, Vol. 44, No. 12, 2002, pp. 2224–2228.
Original Russian Text Copyright © 2002 by Buznik, Gorelik, Sverbil’, Tsvetnikov, Chervyakov.

LOW-DIMENSIONAL SYSTEMS AND SURFACE PHYSICS

Raman Scattering by Zigzag Fluoropolymer Molecules

V. M. Buznik*, V. S. Gorelik, P. P. Sverbil’**, A. K. Tsvetnikov*, and A. V. Chervyakov*****

** Institute of Chemistry, Far East Division, Russian Academy of Sciences,*
pr. Stoletiya Vladivostoka 159, Vladivostok, 690022 Russia
*** Lebedev Physical Institute, Russian Academy of Sciences, Leninskiĭ pr. 53, Moscow, 119991 Russia*
**** Moscow State University, Vorob’evy gory, Moscow, 119899 Russia*

Received April 9, 2002

Abstract—The Raman spectra of ultrafine powders consisting of F$(CF_2)_n$F fluoropolymer zigzag molecules treated as a one-dimensional nanocrystal are investigated. These spectra are compared with the Raman spectra of $C_nF_{2n+1}Br$ compounds (n = 6–10 and 14) and fluoroplastics. It is found that the frequencies of optical vibrations of F$(CF_2)_n$F fluoropolymer molecules are shifted by more than 10 cm^{-1} with respect to the relevant frequencies of $C_6F_{13}Br$ molecules. The length of nanoparticles comprising an organofluoric ultrafine powder is estimated to be L = 2–2.5 nm. This estimate is obtained from the measured frequency shifts in terms of the vibrational theory for a crystalline diatomic chain of finite length. © *2002 MAIK “Nauka/Interperiodica”*.

1. INTRODUCTION

Raman scattering by zigzag organic molecules of *n*-alkanes (C_nH_{2n+2}) and their fluorine-substituted analogs has been being investigated for many years [1–4]. Compounds formed by molecules of this type have found practical applications. In particular, fluoroplastics, namely, poly(tetrafluoroethylene) (PTFE) F$(CF_2)_n$F (n = 10^5–10^7), are widely used in chemical and nuclear industries, mechanical engineering, and transport. In medicine, PTFE is used as a material for artificial blood circulation organs, whereas $C_nF_{2n+1}Br$ (n ~ 10–15) compounds serve as artificial blood substitutes.

We developed a technique for preparing low-molecular PTFE in the form of an ultrafine powder. This material has already found use as an antifriction additive to machinery oil.

The properties of carbon fluoride compounds and their practical application depend on the polymer chain length. The determination of this parameter presents considerable difficulties. In this respect, it is of interest to solve the above problem by analyzing the Raman spectra of zigzag fluoropolymer molecules.

Investigation into the properties of zigzag fluoropolymer molecules with a finite length is also of fundamental importance in elucidating the regularities in the vibrational dynamics of finite one-dimensional crystalline chains.

The main purposes of the present work were (i) to analyze the Raman spectra of ultrafine powders composed of F$(CF_2)_n$F fluoropolymer molecules, (ii) to compare these spectra with the Raman spectra of the $C_nF_{2n+1}Br$ molecules studied earlier in [2] and with the spectrum of PTFE, and (iii) to determine the length of F$(CF_2)_n$F fluoropolymer molecules on the basis of the vibrational theory for a crystalline diatomic chain of finite length.

2. EXPERIMENTAL TECHNIQUE

The Raman spectra were excited using an argon laser (λ = 488.0 nm) with a power of 100 mW. The spectra were recorded on an automated Raman spectrometer. The spectrometer consisted of a DFS-12 double monochromator, a photon counting system, an interface microprocessor, and a personal computer, which provided control over the monochromator, accumulation of experimental data, and their processing. The bandwidth of the spectrometer slit was equal to 2 cm^{-1}. Samples of the organofluoric compounds studied in this work were prepared in the form of white crystalline powders. The measurements were performed in a reflection geometry.

3. RESULTS

The measured Raman spectra of the PTFE ultrafine powder and the F$(CF_2)_n$F fluoroplastic are displayed in Fig. 1. For comparison, the Raman spectra obtained earlier in [2] for $C_nF_{2n+1}Br$ organofluoric zigzag molecules are also shown in Fig. 1. All the spectra are represented in the frequency range 0–1500 cm^{-1}.

Figure 2 depicts the low-frequency portions of the Raman spectra shown in Fig. 1. It can be seen from Fig. 1 that the Raman spectra in the frequency range 0–400 cm^{-1} exhibit an intense band at low frequencies and a number of overlapping bands in the range 200–300 cm^{-1}. An increase in the number n of molecular chain links is accompanied by a monotonic decrease in the frequency of the low-frequency Raman peak (Fig. 2). The low-frequency band observed in the

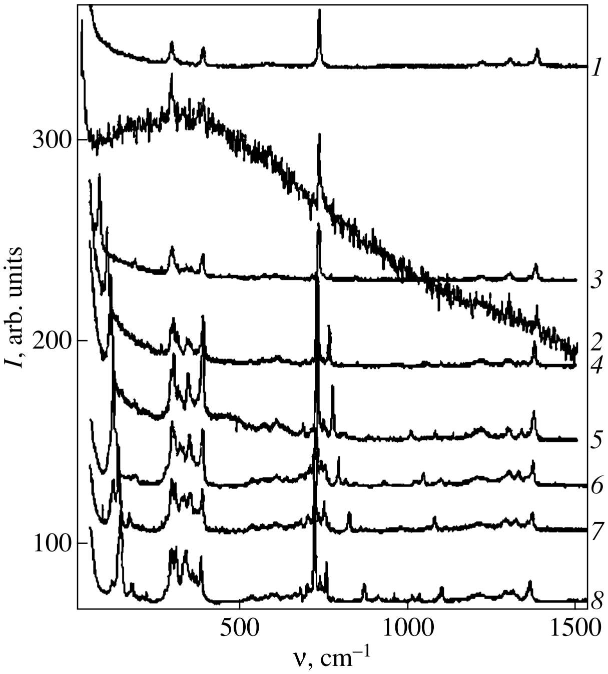

Fig. 1. A general view of the Raman spectra of (*1*) PTFE, (*2*) PTFE ultrafine powder, (*3*) $C_{14}F_{29}Br$, (*4*) $C_{10}F_{21}Br$, (*5*) $C_9F_{19}Br$, (*6*) $C_8F_{17}Br$, (*7*) $C_7F_{14}Br$, and (*8*) $C_6F_{13}Br$.

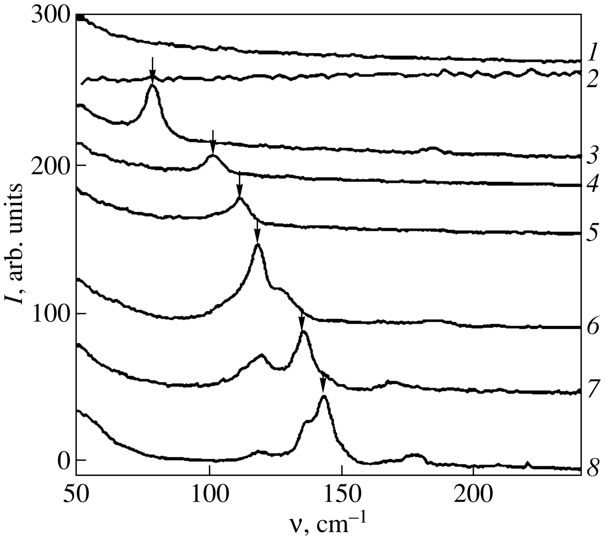

Fig. 2. Evolution of the low-frequency Raman spectra with variations in the molecular chain length. Arrows indicate the location of the acoustic mode. Designations of the curves are the same as in Fig. 1.

Raman spectra involves several components at $n = 6$–8; becomes virtually structureless at $n = 9$, 10, and 14; and completely disappears for the fluoroplastic and ultrafine powder.

Figures 3 and 4 show the Raman spectra in the frequency ranges of the skeletal optical mode (719–733 cm^{-1}), which corresponds to out-of-phase vibrations of carbon atoms, and the symmetric stretching mode of the CF_2 bond (1360–1380 cm^{-1}). As can be seen from these figures, the high-frequency bands observed are clearly defined in all the Raman spectra and the frequencies at maxima of these bands monotonically increase with an increase in the number of atoms involved in the molecular chain.

4. DISCUSSION

In the Raman spectra, the observed shift in frequency at the maximum of the band as a function of the chain length can be explained in the framework of a theoretical model according to which a zigzag molecule is treated as a crystalline chain of finite length.

We consider a one-dimensional crystal lattice composed of atoms of two sorts. In this case, the equations of motion have the form

$$\begin{aligned} m_1\frac{d^2u_1(l)}{dt^2} &= -f_1[u_1(l)-u_2(l-1)] + f_2[u_2(l)-u_1(l)], \\ m_2\frac{d^2u_1(l)}{dt^2} &= -f_2[u_2(l)-u_1(l)] + f_1[u_1(l+1)-u_2(l)]. \end{aligned} \tag{1}$$

In the general case, the atoms under consideration are linked through bonds of different types characterized by the numerical constants f_1 and f_2. Let us assume that $f_1 = f_2$ and $m_1 = m_2$. From the equations of motion (1), we can derive the following dispersion law for the solution in the form of a plane monochromatic wave $u(l) = ue^{i(kla - \omega t)}$:

$$\begin{aligned} \Omega_-^2 &= \frac{2f}{m} - \frac{2f}{m}\cos\left(\frac{ka}{2}\right), \\ \Omega_+^2 &= \frac{2f}{m} + \frac{2f}{m}\cos\left(\frac{ka}{2}\right). \end{aligned} \tag{2}$$

For small wave vectors, in the vicinity of the center of the Brillouin zone, we approximately obtain

$$\begin{aligned} \Omega_-^2 &= \frac{f}{m}\sin^2\left(\frac{ka}{2}\right), \\ \Omega_+^2 &= \frac{4f}{m} - \frac{f}{m}\sin^2\left(\frac{ka}{2}\right). \end{aligned} \tag{3}$$

By introducing the designation $\frac{f}{m} = \frac{4s^2}{a^2}$ into expressions (3), we obtain the relationships

$$\Omega_-^2 = \frac{4s^2}{a^2}\sin^2\left(\frac{ka}{2}\right),$$
$$\Omega_+^2 = \frac{16s^2}{a^2} - \frac{4s^2}{a^2}\sin^2\left(\frac{ka}{2}\right). \quad (4)$$

Here, s is the parameter characterizing the velocity of wave propagation in the chain, $a = 2.53 \times 10^{-8}$ cm is the length of the link of the diatomic chain representing an $F(CF_2)_nF$ organofluoric molecule, and k is the wave vector.

It follows from relationships (4) that the optical mode at $k = 0$ has the limiting frequency $\Omega_0 = 4s/a$.

For chains containing a finite number of atoms with length $L = Na$, the standing wave is characterized by the minimum possible wave vector

$$k_{\min} = \frac{2\pi}{\lambda_{\max}} = \frac{\pi}{Na} \quad (\lambda_{\max} = 2L). \quad (5)$$

For sufficiently long molecules of the $C_nF_{2n+1}Br$ and $F(CF_2)_nF$ types, we assume that $L = Na = \frac{na}{2}$.

The most intense bands observed in the experimental Raman spectra can be considered a manifestation of lattice modes (with the minimum possible wave vector $k_{\min}$) of the acoustic and optical branches of vibrations of the molecular chain.

Therefore, it can be expected that, as the number N of molecular chain links increases, the frequencies of acoustic (Ω_{ac}) and optical (Ω_{opt}) modes will satisfy the relationships

$$\Omega_{ac}^2 = \frac{4s^2}{a^2}\sin^2\left(\frac{\pi}{2N}\right),$$
$$\Omega_{opt}^2 = \Omega_0^2 - \frac{4s^2}{a^2}\sin^2\left(\frac{\pi}{2N}\right). \quad (6)$$

By changing over to the wave numbers $\nu = 1/\lambda$, from relationships (6), we obtain

$$\nu_{ac}^2 = \frac{s^2}{\pi^2 a^2 c^2}\sin^2\left(\frac{\pi}{2N}\right),$$
$$\nu_{opt}^2 = \nu_0^2 - \frac{s^2}{\pi^2 a^2 c^2}\sin^2\left(\frac{\pi}{2N}\right). \quad (7)$$

Taking into account that $L = Na$, from expressions (7), we find

$$\nu_{ac}^2 = \frac{s^2}{\pi^2 a^2 c^2}\sin^2\left(\frac{\pi a}{2L}\right),$$
$$\nu_{opt}^2 = \nu_0^2 - \frac{s^2}{\pi^2 a^2 c^2}\sin^2\left(\frac{\pi a}{2L}\right). \quad (8)$$

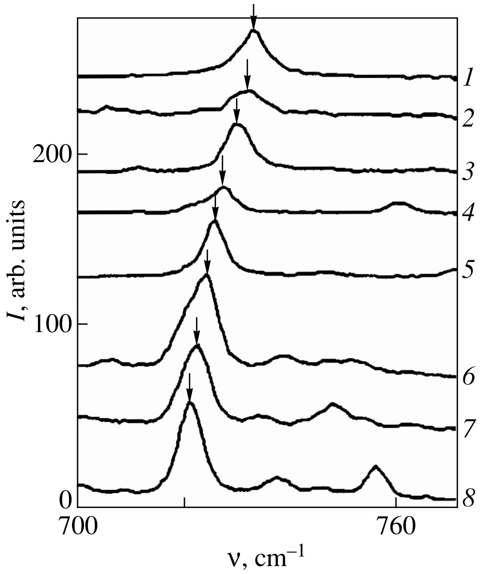

Fig. 3. Evolution of the high-frequency Raman spectra with variations in the molecular chain length. Arrows indicate the location of the optical mode. Designations of the curves are the same as in Fig. 1.

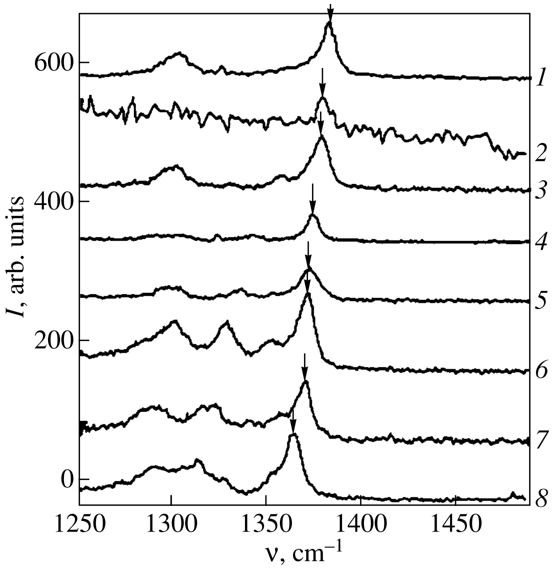

Fig. 4. Evolution of the high-frequency Raman spectra with variations in the molecular chain length. Arrows indicate the frequency of symmetric stretching vibrations of the CF_2 bond. Designations of the curves are the same as in Fig. 1.

According to formulas (4), the velocity s of wave propagation in a chain can be represented by the relationship

$$s = \frac{\pi a c \nu_0}{2}. \quad (9)$$

Thus, the wave velocity s can be calculated from relationship (9). Note that the quantity ν_0 can be deter-

Vibrational frequencies (cm^{-1}) determined from the Raman spectra of organofluoric compounds and the molecular lengths* (nm)

Molecule	ν_{ac}	ν_{opt}	ν	L_1		L_2		L_3	
				(10)	(17)	(11)	(18)	(13)	(19)
$C_6F_{13}Br$	142.8	720.5	1362.5	0.98	1.02	1.02	1.05	1.01	1.03
$C_7F_{15}Br$	135.5	722.4	1367.1	1.04	1.07	1.10	1.13	1.16	1.18
$C_8F_{17}Br$	117.8	723.8	1368.2	1.21	1.23	1.18	1.20	1.21	1.23
$C_9F_{19}Br$	111.4	725.8	1370.2	1.27	1.30	1.33	1.35	1.32	1.34
$C_{10}F_{21}Br$	100.6	727.2	1372.1	1.42	1.45	1.47	1.49	1.44	1.46
$C_{14}F_{29}Br$	77.9	730	1376.7	1.85	1.87	1.94	1.95	2.02	2.04
PTFE ultrafine powder		731.8	1377.0	–	–	2.68	2.69	2.09	2.10
PTFE		732.7	1380.4	–	–	3.62	3.63	4.10	4.11

* The molecular lengths L_1, L_2, and L_3 are calculated according to formulas (10) and (17), (11) and (18), and (13) and (19), respectively.

mined by a linear extrapolation of the experimental values of ν_{opt} obtained from the Raman spectra for long chains. The molecular length can be calculated using formula (8) and the experimental data on ν_{ac} and ν_{opt}. Correspondingly, we obtain two expressions,

$$L_1 = \frac{\pi a}{2}\frac{1}{\arcsin\left(\frac{\pi a c \nu_{ac}}{s}\right)}, \qquad (10)$$

$$L_2 = \frac{\pi a}{2}\frac{1}{\arcsin\left(\frac{\pi a c\sqrt{\nu_0^2-\nu_{opt}^2}}{s}\right)}. \qquad (11)$$

For additional branches of vibrations of the molecular chain, the dispersion law can be derived by considering a crystalline chain with an additional bond. As a result, we obtain the following equation:

$$\nu^2 = (\nu'_0)^2 \pm \frac{(s')^2}{\pi^2 c^2 a^2}\sin^2\left(\frac{\pi}{2N}\right). \qquad (12)$$

The sign in expression (12) depends on the sign of the phonon mass in the dispersion branch under consideration: the plus sign in expression (12) corresponds to the positive phonon mass, whereas the minus sign must be chosen for the negative phonon mass. As follows from the experimental results, the shift in the frequency of symmetric stretching vibrations of the CF_2 bond obeys expression (12), which corresponds to the negative phonon mass.

The length of the molecular chain $L = Na$ can also be determined from the experimental values of ν and ν'_0 for the chosen branch of vibrations; that is,

$$L_3 = \frac{\pi a}{2}\frac{1}{\arcsin\left(\frac{\pi a c\sqrt{\left|\nu^2-(\nu'_0)^2\right|}}{s'}\right)}. \qquad (13)$$

The table presents the experimental frequencies ν_{ac} and ν_{opt} and the frequencies ν attributed to symmetric stretching vibrations of the CF_2 bond. These frequencies were determined from the Raman spectra. The molecular lengths L_1, L_2, and L_3 calculated from formulas (10), (11), and (13) for $C_nF_{2n+1}Br$, PTFE, and ultrafinely powdered PTFE are also listed in the table. For fluoroplastics, the molecular length obtained can be interpreted as the size of an ordered quasicrystalline segment of an infinite fluoropolymer chain in which crystalline regions alternate with discontinuities arising from changes in the direction of the crystalline chain. Let us now analyze the approximate formulas used for molecules with a large length ($N \gg 1$). In this case, relationships (8) and (12) can be rewritten in the form

$$\nu_{ac} = \frac{s}{2cL}, \qquad (14)$$

$$\nu_{opt}^2 = \nu_0^2 - \frac{s^2}{4c^2L^2}, \qquad (15)$$

$$\nu^2 = (\nu'_0)^2 \pm \frac{(s')^2}{4c^2L^2}. \qquad (16)$$

Consequently, within the above approximation, we derive the following relationships for molecular lengths:

$$L_1 = \frac{s}{2c\nu_{ac}}, \qquad (17)$$

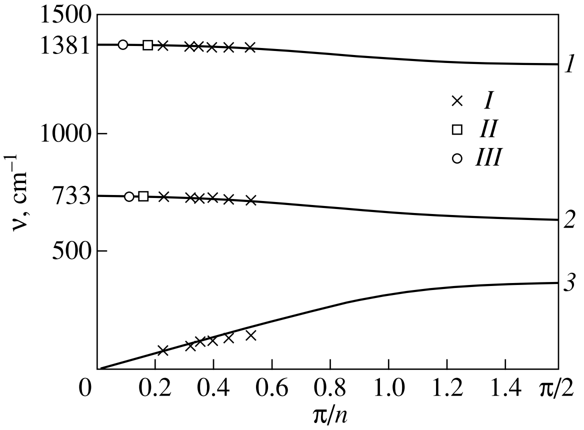

Fig. 5. (*1*–*3*) Theoretical dispersion curves calculated from relationships (7) and (12) in comparison with (*I*–*III*) experimental data. Theoretical results: (*1*) the symmetric stretching branch of vibrations of the CF_2 bond, (*2*) the optical branch of skeletal vibrations, and (*3*) the acoustic branch of skeletal vibrations. Experimental data: (*I*) $C_nF_{2n+1}Br$ (n = 6–10 and 14), (*II*) PTFE ultrafine powder, and (*III*) PTFE.

$$L_2 = \frac{s}{2c\sqrt{\nu_0^2 - \nu_{\text{opt}}^2}}, \qquad (18)$$

$$L_3 = \frac{s'}{2c\sqrt{\left|\nu^2 - (\nu'_0)^2\right|}}. \qquad (19)$$

The approximate molecular lengths L_1, L_2, and L_3 calculated according to formulas (10), (11), (13), and (17)–(19) are given in the table. As can be seen from the table, the molecular lengths calculated from exact and approximate formulas are in close agreement. Therefore, the approximate formulas will suffice for determination of the length of comparatively long molecules.

Figure 5 shows the theoretical dependences of the frequency ν on π/n [calculated from relationships (7) and (12)] at $N = n/2$ and the experimental data for the compounds under investigation. It can be seen from Fig. 5 that the results of calculations are in reasonable agreement with the experimental data. The experimental data obtained were used to determine the following parameters of the dispersion law: the velocity of wave propagation in the chain $s = 8.75 \times 10^5$ cm/s and the limiting frequency of the optical mode $\nu_0 = 733.8$ cm^{-1}, which corresponds to the wave vector $k = 0$.

As follows from the experimental data, the frequency of the mode corresponding to totally symmetric stretching vibrations of the CF_2 bond changes with variations in the chain length of the studied molecules in accordance with the dispersion law (12) characterized by the following parameters: $s' = 14.2 \times 10^5$ cm/s and $\nu'_0 = 1381.6$ cm^{-1}.

According to the dispersion laws derived for the molecular chain models under consideration, we calculated the molecular lengths for nanoparticles of the ultrafine powder and fluoroplastic used in our investigation. These lengths are listed in the table.

5. CONCLUSIONS

Thus, the above experimental investigation has revealed that the Raman spectra of zigzag organofluoric molecules of an ultrafine powder and fluoroplastic contain bands whose frequencies are shifted with respect to the frequencies attributed to vibrations of $C_nF_{2n+1}Br$ carbon fluoride zigzag molecules. The lengths of nanoparticles comprising the ultrafine fluoropolymer powder and the sizes of the crystalline regions in the fluoroplastic were estimated from the shifts in these frequencies with the use of the dispersion relations obtained for simple models of one-dimensional diatomic crystalline chains.

It should be noted that our experimental Raman spectra of the PTFE ultrafine powder and PTFE do not exhibit clearly defined low-frequency satellites attributed to longitudinal acoustic modes, even though these modes manifest themselves in the Raman spectra of carbon bromofluorides $C_nF_{2n+1}Br$. This can be explained not only by the difficulties associated with the recording of the low-frequency Raman spectra but also by the possible aperiodic damping of the longitudinal acoustic modes. In turn, this damping can be caused by a strong interaction between fluoropolymer nanoparticles.

The results of this work can be used to control the length of zigzag molecules of different organofluoric compounds used in practice.

ACKNOWLEDGMENTS

This work was supported by the Russian Foundation for Basic Research, project no. 02-02-16221.

REFERENCES

1. S. I. Mizushima and T. Simanouti, J. Am. Chem. Soc. **71**, 1320 (1949).
2. L. P. Avakyants, V. S. Gorelik, L. I. Zlobina, *et al.*, Izv. Akad. Nauk, Ser. Fiz. **64** (6), 1189 (2000).
3. A. M. Amorim da Costa Eduarda and B. H. Santos, Rev. Port. Quim. **26**, 154 (1984).
4. J. R. Ferrar and K. Nakamoto, *Introductory Raman Spectroscopy* (Academic, Boston, 1994), p. 350.

Translated by O. Borovik-Romanova

Physics of the Solid State, Vol. 44, No. 12, 2002, pp. 2336–2340. Translated from Fizika Tverdogo Tela, Vol. 44, No. 12, 2002, pp. 2229–2233.
Original Russian Text Copyright © 2002 by Ryzhov.

POLYMERS AND LIQUID CRYSTALS

Low-Energy Librational Excitations in Vitreous Poly(methyl methacrylate)

V. A. Ryzhov

Ioffe Physicotechnical Institute, Russian Academy of Sciences, Politekhnicheskaya ul. 26, St. Petersburg, 194021 Russia
e-mail: v.ryzhov@mail.ioffe.rssi.ru

Received October 26, 2001; in final form, January 17, 2002

Abstract—The infrared (IR) and Raman spectra of vitreous poly(methyl methacrylate) (PMMA) are measured and investigated in the frequency range 10–150 cm^{-1}. A comparison of the results obtained from IR and Raman spectroscopic measurements permits the assignment of the low-frequency anomaly (boson peak) observed in the spectra to librational vibrations occurring in a segment of the main chain that is comparable in length to the statistical chain segment. It is demonstrated that coherent librational excitations are associated with the relaxation processes proceeding in the polymers. *© 2002 MAIK “Nauka/Interperiodica”.*

1. INTRODUCTION

The low-frequency dynamics of vitreous solids differs from that typical of crystals and exhibits a number of universal features due to an excess density (compared to the Debye density) of vibrational states [1, 2]. The excess density of vibrational states has been directly measured in the experiments on inelastic neutron scattering [3]. It is known that the density of vibrational states is responsible for the deviation of the temperature dependence of the heat capacity from the power law T^3, the appearance of a low-temperature plateau in the temperature dependence of the thermal conductivity at $T \approx 5$–20 K, and the boson peak in the infrared (IR) and Raman spectra [4–6].

It is universally accepted that the excess density of vibrational states is associated with the quasi-local vibrational modes [7, 8]. At present, the nature of these modes is a subject of wide speculation. A number of authors believe that quasi-local vibrational modes are local vibrations of structural formations, such as fractals, domains, and nanoinhomogeneities [9–11]. Other authors assign these modes to correlated vibrations of molecular clusters or molecules, for example, to torsional vibrations in a chain consisting of several SiO_4 tetrahedra in quartz [8] or to rotational–translational motion of molecules in vitrifying liquids [12].

In recent papers [4, 10], consideration has been given to a correlation between the boson peak and the relaxation properties of vitreous solids.

Earlier [13], we performed a comparative study of the long-wavelength IR and Raman spectra and assigned the low-energy vibrational excitations observed in vitreous poly(methyl methacrylate) (PMMA) to librational motion of molecular fragments composed of several monomer units of the polymer molecule. The present work is a continuation of these investigations.

2. SAMPLE PREPARATION AND EXPERIMENTAL TECHNIQUE

Samples of amorphous PMMA and its oligomers with degrees of polymerization $n \cong 2$, 7, 9, and 50 were synthesized at the Semenov Institute of Chemical Physics (Russian Academy of Sciences, Moscow) through catalytic chain transfer to cobalt porphyrin molecules [14]. All these samples, except for the dimer sample, were prepared in the form of 10- to 100-μm-thick films for the purpose of recording the long-wavelength IR spectra and in the form of parallelepipeds with polished faces for measuring the Raman spectra. The dimer sample was placed in a cell with windows prepared from poly(4-methyl-1-pentene), which is a transparent material in the long-wavelength IR range. The measurements were performed at two temperatures, namely, liquid-nitrogen and room temperatures.

The long-wavelength IR spectra were recorded on single-beam spectrometers with diffraction gratings. A spectrometer designed at the Leningrad State University [15] and then modified with an OAP-7 detector and a new filtration system [16] was used in the frequency range up to 50 cm^{-1}. The IR spectra in the range 50–150 cm^{-1} were measured on an FIS-21 Hitachi spectrometer. The resolution at a signal-to-noise ratio of the order of 100 was equal to 1–2 cm^{-1}. The location of the spectral bands at their maxima was determined accurate to within 2–3 cm^{-1}. The absorption coefficient $k(\omega) = \ln(J/J_0)/t - t_0$ (where J and J_0 are the transmittances of samples of thicknesses t and t_0, respectively) were measured with an error ranging from 5 to 10%.

The Raman spectra were recorded on a Ramalog-5 double monochromator in a 90° scattering geometry. The spectra were excited with the 488-nm line of an argon laser (the radiation power was 0.1 W). The bandwidth of the spectrometer slit was equal to 2 cm^{-1}. The experimental spectrum $I(\omega)$ was averaged over ten scans in the range 10–200 cm^{-1} and was then normalized taking into account the spectral function of the instrument and the frequency factor of scattering.

In order to compare correctly the long-wavelength IR absorption spectra with the experimental Raman spectra, the latter spectra should be transformed with due regard for the Bose factor $N(\omega) = [\exp(\hbar\omega/k_BT) - 1]^{-1}$ and the frequency-dependent coefficient $C(\omega)$ [17]. For amorphous polymers, the frequency dependence $C(\omega)$ is almost linear at frequencies above the boson peak and $C(\omega) \approx \text{const}$ at low frequencies [18]. In the former case, the spectrum $k(\omega)$ corresponds to the spectrum $I(\omega)/(N(\omega) + 1)$. In the latter case, we should compare either the spectrum $k(\omega)$ with the spectrum $I(\omega)\omega/(N(\omega) + 1)$ or the spectrum $k(\omega)/\omega$ with the spectrum $I(\omega)/(N(\omega) + 1)$.

3. RESULTS AND DISCUSSION

Figure 1 shows the measured long-wavelength IR spectra of PMMA and its oligomers in the frequency range 10–150 cm^{-1} in the $k(\omega)$ coordinates. Figure 2 depicts the corresponding Raman spectra in the $I(\omega)/(N(\omega) + 1)$ coordinates. These spectra exhibit a broad asymmetric band with a maximum at ~90–95 cm^{-1} and a shoulder at 15–20 cm^{-1} in the low-frequency wing, which is characteristic of low-frequency spectra of linear amorphous polymers.

Judging from the previously performed analysis of the long-wavelength IR spectra of low-molecular compounds and polymers, the band under investigation can be assigned to the absorption associated with the librational mode (rotational vibrations) of monomer units in PMMA macromolecules, i.e., to the absorption occurring through the Poley mechanism [19].

Since the studied band in the Raman spectrum of PMMA has a similar profile and its maximum is located at a close frequency [20], this band should also be assigned to the same vibrations.

An insignificant broadening of the band and a frequency shift at its maximum toward the high-frequency range in the spectra of oligomers can be due to an increase in the amplitude and anharmonicity of librational vibrations in low-molecular analogs of PMMA.

The similarity of the mechanisms responsible for the formation of bands in the low-frequency IR and Raman spectra of condensed media has been confirmed by a large body of data [21]. Within the simplest model applied to analyze the absorption occurring through the Poley mechanism [22], a molecule with the moment of inertia I executes librational motion with the circular frequency

$$\omega = 2\pi c\omega_0 \cong \pi/\xi(U_0/2I)^{1/2} \quad (1)$$

in a potential well that is formed by the nearest environment of the molecule and can be described by the relationship $U(\varphi) = U_0\sin^2\pi\varphi/2\xi$. Here, U_0 is the potential well depth, ξ is the angular half-aperture of the potential well (the full width at half-maximum of the barrier), and φ is the libration amplitude.

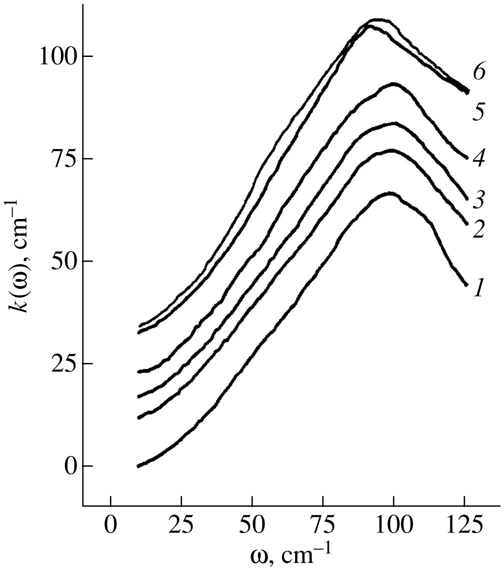

Fig. 1. Long-wavelength IR spectra of (*1*) PMMA and (*2*–*6*) its oligomers with degrees of polymerization $n \cong$ (*2*) 50, (*3*) 9, (*4*) 7, and (*5*) 2 at T = 90 K and (*6*) n = 2 at T = 293 K. The spectra of oligomers are shifted along the ordinate axis.

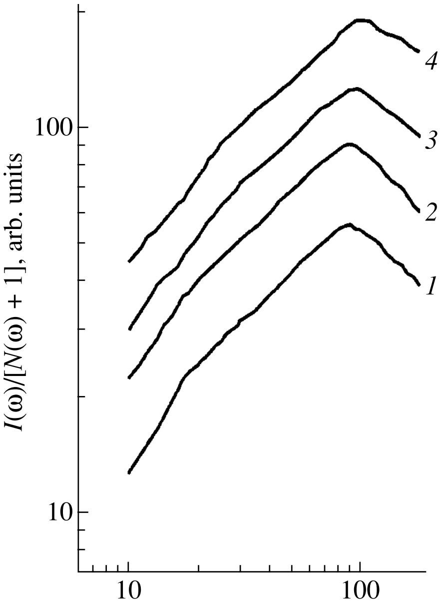

Fig. 2. Reduced Raman spectra of (*1*) PMMA and (*2*–*4*) its oligomers with degrees of polymerization $n \cong$ (*2*) 50, (*3*) 9, and (*4*) 7 at T = 293 K. The spectra of oligomers are shifted along the ordinate axis.

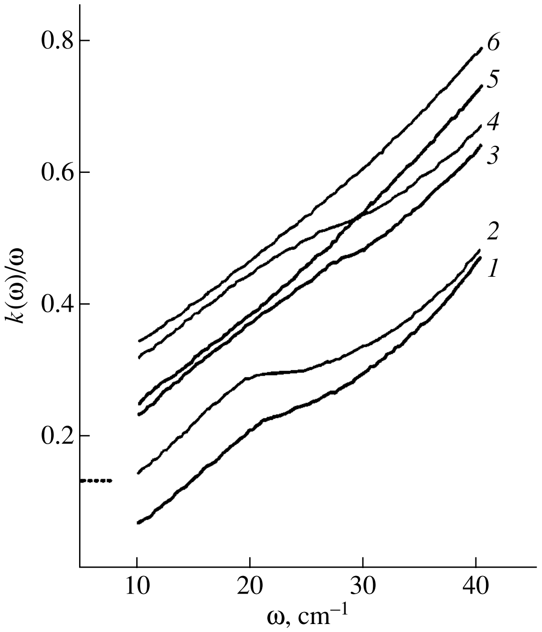

Fig. 3. Reduced long-wavelength IR spectra of (*1*, *2*) PMMA, (*3*, *4*) the oligomer with the degree of polymerization $n \cong 7$, and (*5*, *6*) the oligomer with $n \cong 2$ at T = (*1*, *3*, *5*) 90 and (*2*, *4*, *6*) 293 K. The spectra of oligomers are shifted along the ordinate axis.

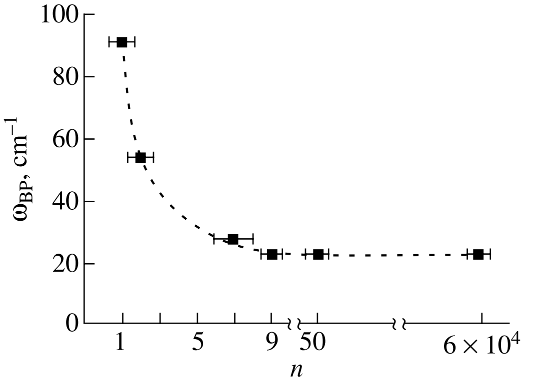

Fig. 4. Dependence of ω_{BP} on the degree of polymerization in terms of the number n of monomer units.

This model predicts the location of the librational band at the maximum in the low-frequency spectra of polar and nonpolar liquids. The predicted intermolecular barriers to librational motion are consistent with those determined using other methods [23].

The above approach, as applied to polymers, brings theory and experiment into good agreement, provided a monomer unit serves as a librator. In these calculations, it is assumed that the librator has the shape of a sphere with the moment of inertia $I = 2/5(MR^2)$, where M is the molecular mass and R is the equivalent radius.

For PMMA, we estimated the librator size R at the frequency ω_0 = 95 cm^{-1} in relationship (1) reasoning from the activation energy of the δ transition [24] and the occurrence of torsional vibrations with an amplitude of 10°–15° in the macromolecules. As a result, we obtained $R \approx 0.5$ nm. The estimated size proved to be close to the van der Waals radius of the monomer unit.

This result is a further argument in support of the assumption that the band at ≈95 cm^{-1} in the long-wavelength IR and Raman spectra of PMMA and its oligomers is attributed to librational motion of the monomer unit of the macromolecule.

Let us now consider another specific feature in the long-wavelength IR and Raman spectra of PMMA and its oligomers, namely, the shoulder in the low-frequency wing of the band under investigation.

In the initial (experimental) Raman spectrum of PMMA, the frequency ω_{BP} at the maximum of the boson peak is equal to 16–18 cm^{-1} [25, 26]. After changing over the experimental spectrum to the $I(\omega)/(N(\omega) + 1) \sim \omega$ coordinates, the boson peak transforms into a shoulder at the same frequency ω_{BP} in the low-frequency wing of the studied band (Fig. 2).

In order to compare the reduced Raman spectra with the long-wavelength IR spectra in the frequency range 10–40 cm^{-1}, we constructed the IR spectra in the $k(\omega)/\omega \sim \omega$ coordinates. It can be seen from Fig. 3 that the reduced long-wavelength IR spectra of PMMA exhibit a similar shoulder at the frequency of the boson peak $\omega_{BP} \cong$ 18–22 cm^{-1}.

With the aim of elucidating the molecular nature of the shoulder in the low-frequency wing of the librational band, we consider the reduced long-wavelength IR and Raman spectra of PMMA and its oligomers (Figs. 2, 3). As can be seen from these spectra, an increase in the molecular mass of the oligomer is accompanied by a shift of the shoulder toward the low-frequency range. The dependence of the frequency location of the shoulder ω_{BP} on the molecular mass of the oligomer (expressed in terms of the number n of monomer units) is plotted in Fig. 4. The frequency at the principal maximum of the band attributed to librational motion of the monomer unit also falls into this dependence.

This suggests that the shoulder in the low-frequency wing of the main band is also associated with the librational motion, which, as follows from the dependence of ω_{BP} on n, should involve several monomer units. The maximum number of chain units involved in the librational motion can be estimated from the dependence shown in Fig. 4. In the case of PMMA and its oligomers, this number does not exceed five or seven monomer units.

The length L of this segment of the main chain can also be determined using the relationship [25]

$$L \cong v_t/\omega_{BP}, \quad (2)$$

where v_t is the velocity of sound for transverse vibrational modes. For PMMA, the velocity of sound v_t is taken to be $v_t \cong 1.42$ km/s [27]. After substituting this velocity and the frequency of the boson peak $\omega_{BP} = 16$ cm^{-1} into relationship (2), we found that, in PMMA, $L \cong 3$ nm. This value corresponds to a length of the polymer chain segment of six monomer units and is close to the length of the Kuhn statistical segment in PMMA [28].

It is of interest that the linear sizes of the regions corresponding to collective vibrational excitations in other vitreous polymers are comparable to the sizes of their statistical segments. In particular, analysis of the Raman spectra of vitreous poly(styrene) and its oligomers [29, 30] demonstrates that the size of the above region amounts to six or eight monomer units. Note that the statistical segment of poly(styrene) contains eight units [28]. The regions of collective vibrational excitations in poly(butylene) [30] and poly(propylene glycol) [31] involve 11 and 7 monomer units, respectively. This is also in close agreement with the statistical segments of these polymers.

After substituting the frequency ω_0 at the maximum of the band into relationship (2), we found that the length of the polymer molecule segment amounts to 0.5 nm; i.e., it is equal to the length of the monomer unit in PMMA.

Therefore, in the long-wavelength IR and Raman spectra of PMMA and its oligomers, the band under investigation is attributed to the librational mode of the monomer unit, whereas the shoulder in the low-frequency wing of this band is associated with the correlated torsional vibrations of several monomer units.

It is worth noting that the linear size of the region of collective librational excitations, which is determined from the frequency ω_{BP} in the long-wavelength IR and Raman spectra, corresponds to the length of a statistical segment, i.e., the minimum polymer chain fragment required for a rotational isomeric transition to occur in the chain. The motion executed by chain segments of the given length in regions with the loosest packing of macromolecules is responsible for the β relaxation [28, 32]. This motion is an analog of the Johari–Goldstein relaxation [33] in low-molecular vitrified liquids, which consists in reorienting a molecule due to thermal fluctuations. In this case, the molecule overcomes the potential barrier U_0 formed by the nearest environment.

The β transition is preceded by the universal γ process [34]; i.e., small-angle torsional vibrations represent librational motion of molecules. As was noted above, this motion gives rise to Poley bands at a frequency ω_0 in the long-wavelength IR and Raman spectra of condensed media.

Thus, the parameters of librational motion preceding the β relaxation and the sizes of polymer chain segments involved in this motion in the course of the β transition can be directly determined from the low-frequency IR and Raman spectra.

Let us once again consider Fig. 3. It can be seen from this figure that, in the long-wavelength IR spectra, the intensity of the low-frequency wing (in the frequency range below ω_{BP}) increases with an increase in the temperature. A similar effect was observed earlier in the Raman spectra of vitreous solids [25, 35]. According to these investigations, an increase in the intensity at frequencies below ω_{BP} is caused by an increase in the contribution of the β process with increasing temperature. Consequently, the frequency location of the shoulder in the long-wavelength IR and Raman spectra of PMMA corresponds to a crossover from resonance absorption to relaxational absorption in the case when the number of units involved in librational motion becomes sufficient for conformational transformations to occur in the polymer chain.

4. CONCLUSIONS

The main results obtained in the above analysis of the long-wavelength IR and Raman spectra of PMMA and its oligomers can be summarized as follows.

(1) The band under investigation (the Poley band) is attributed to librational motion of the monomer unit. This motion is responsible for the universal γ process (the δ transition according to the polymeric terminology).

(2) The maximum length of the correlation segment of the macromolecule was determined from the frequency ω_{BP} of the shoulder in the low-frequency wing of the studied band. This length is close to the size of the statistical segment whose motion brings about the relaxation β transition.

(3) The frequencies below the frequency ω_{BP} of the boson peak correspond to relaxation motion of macromolecules in the case when the number of monomer units involved in librational motion becomes sufficient for the conformational transition to occur in the polymer chain.

Thus, the results of the investigation performed have demonstrated that a comparative analysis of the long-wavelength IR and Raman spectra makes it possible to reveal the molecular nature of the quasi-local modes responsible for the excess density of vibrational states in the terahertz range.

ACKNOWLEDGMENTS

I would like to thank E.V. Kober for measuring the Raman spectra and V.P. Roshchupkin for supplying the samples used in this investigation.

REFERENCES

1. *Amorphous Solids: Low Temperature Properties*, Ed. by W. A. Philips (Springer-Verlag, Berlin, 1981).

2. V. K. Malinovsky, Fiz. Tverd. Tela (St. Petersburg) **41** (5), 805 (1999) [Phys. Solid State **41**, 725 (1999)].
3. K. Inoue, T. Kanaya, S. Ikeda, *et al.*, J. Chem. Phys. **95** (7), 5332 (1991).
4. V. K. Malinovsky, V. N. Novikov, and A. P. Sokolov, Fiz. Khim. Stekla **22** (3), 204 (1996).
5. B. Grillot and J. Guissani, Phys. Rev. Lett. **78** (12), 2401 (1997).
6. V. K. Malinovskiĭ, V. N. Novikov, and A. P. Sokolov, Usp. Fiz. Nauk **163** (5), 119 (1993) [Phys. Usp. **36**, 440 (1993)].
7. U. Buchenau, Yu. M. Galperin, V. L. Gurevich, and H. R. Schober, Phys. Rev. B **43** (6), 5039 (1991).
8. S. D. Bembenek and B. B. Laird, J. Chem. Phys. **114** (5), 2340 (2001).
9. T. Nakakyama, K. Yakubo, and R. L. Orbach, Rev. Mod. Phys. **66**, 381 (1994).
10. E. Duval, A. Mermet, N. V. Surovtsev, and A. J. Dionoux, J. Non-Cryst. Solids **235–237**, 203 (1998).
11. V. K. Malinovsky and V. N. Novikov, Fiz. Tverd. Tela (St. Petersburg) **36** (8), 2241 (1994) [Phys. Solid State **36**, 1221 (1994)].
12. T. S. Perova, J. K. Vij, D. N. Christensen, and O. F. Nielsen, J. Mol. Struct. **79** (3), 111 (1999).
13. V. A. Bershtein, V. A. Ryzhov, L. M. Egorova, and E. V. Kober, in *Proceedings of the 3rd International Meeting on Relaxation in Complex Systems, Vigo, Spain, 1997*, p. IV-4.
14. B. R. Smirnov, I. S. Morozova, and A. P. Marchenko, Dokl. Akad. Nauk SSSR **255** (3), 608 (1980).
15. V. A. Ryzhov and M. V. Tonkov, in *Molecular Spectroscopy* (Leningr. Gos. Univ., Leningrad, 1973), Vol. 2, p. 103.
16. N. A. Chernyavskaya, V. A. Soglasnova, N. V. Ershov, *et al.*, Opt.–Mekh. Prom–st. **59** (1), 63 (1992) [Sov. J. Opt. Technol. **59**, 52 (1992)].
17. R. Shuker and R. W. Gammon, Phys. Rev. Lett. **25** (4), 222 (1970).
18. A. P. Sokolov, U. Buchenau, W. Steffen, *et al.*, Phys. Rev. B **52** (14), 9815 (1995).
19. V. A. Bershtein and V. A. Ryzhov, Adv. Polym. Sci. **114**, 43 (1994).
20. F. Viras and T. A. King, Polymer **25** (6), 899 (1984).
21. V. S. Libov and T. S. Perova, Tr. Gos. Opt. Inst. **81**, 215 (1992).
22. I. W. Larkin, J. Chem. Soc., Faraday Trans. 2 **69** (6), 1278 (1973).
23. M. W. Evans, G. J. Evans, W. T. Coffey, and P. Gricolini, *Molecular Dynamics and Theory of Band Spectra* (Wiley, New York, 1982).
24. V. A. Ryzhov and V. A. Bershtein, Vysokomol. Soedin., Ser. A **31** (3), 451 (1989).
25. V. A. Bagryanskiĭ, V. K. Malinovskiĭ, V. N. Novikov, *et al.*, Fiz. Tverd. Tela (Leningrad) **30** (8), 2360 (1988) [Sov. Phys. Solid State **30**, 1361 (1988)].
26. V. N. Novikov, A. P. Sokolov, B. Stube, *et al.*, J. Chem. Phys. **107** (4), 1057 (1997).
27. A. P. Sokolov, A. Kisliuk, M. Soltwisch, and D. Quitmann, Phys. Rev. Lett. **69** (10), 1540 (1992).
28. V. A. Bershtein and V. M. Egorov, *Differential Scanning Calorimetry in the Physical Chemistry of Polymers* (Khimiya, Leningrad, 1990).
29. R. J. Spells and I. W. Shepherd, J. Chem. Phys. **66** (3), 1427 (1977).
30. U. Buchenau, C. Pecharreman, R. Zorn, and B. Frick, Phys. Rev. Lett. **77** (4), 659 (1996).
31. R. Bergman, C. Svanberg, D. Andersson, *et al.*, J. Non-Cryst. Solids **235–237**, 225 (1998).
32. Yu. Ya. Gotlib, A. A. Darinskiĭ, and Yu. E. Svetlov, *Physical Kinetics of Macromolecules* (Khimiya, Leningrad, 1986).
33. G. P. Johari and M. Goldstein, J. Chem. Phys. **55** (10), 4245 (1971).
34. C. J. Reid and M. W. Evans, J. Chem. Phys. **76** (5), 2576 (1982).
35. N. V. Surovtsev, J. A. Wiedersich, V. N. Novikov, *et al.*, Phys. Rev. B **58** (22), 14888 (1998).

Translated by O. Borovik-Romanova

Physics of the Solid State, Vol. 44, No. 12, 2002, pp. 2341–2346. Translated from Fizika Tverdogo Tela, Vol. 44, No. 12, 2002, pp. 2234–2239.
Original Russian Text Copyright © 2002 by Vettegren, Marikhin, Kulik, Titenkov.

POLYMERS AND LIQUID CRYSTALS

Expansion of Monomer Units in Poly(ethylene terephthalate) Molecules under Conditions of Thermal and Zero-Point Atomic Vibrations

V. I. Vettegren*, V. A. Marikhin*, V. B. Kulik*, and L. S. Titenkov**
** Ioffe Physicotechnical Institute, Russian Academy of Sciences, Politekhnicheskaya ul. 26, St. Petersburg, 194021 Russia*
*** Moscow State Textile University, Malaya Kaluzhskaya ul. 1, Moscow, 119991 Russia*
e-mail: Victor.Vettegren@pop.ioffe.rssi.ru

Received January 28, 2002

Abstract—The temperature dependence of the expansion ε_C of *trans* conformers of the carbon skeleton of macromolecules in crystallized and amorphous poly(ethylene terephthalate) (PET) due to zero-point and thermal atomic vibrations is investigated by IR spectroscopy. It is found that the thermal expansion coefficient β_C jumpwise increases at the characteristic temperatures T_t and T_b. This increase is associated with the crossover from the quantum to classical statistics of torsional and bending vibration modes. The quantum and classical contributions to the expansion ε_C are determined for each mode. The quantum and classical contributions of the torsional vibrational mode in the amorphous polymer are approximately 1.5 times larger than those in the crystallized polymer. This effect is caused by an increase in the anharmonicity of torsional vibrations in the amorphous polymer. © *2002 MAIK "Nauka/Interperiodica".*

1. INTRODUCTION

In our earlier works [1–6], we developed a technique for analyzing thermal expansion of the main skeleton of macromolecules with the use of IR and Raman spectroscopy. The thermal expansion was investigated using a shift in the maximum of the spectral band under temperature variations. The quantum and thermal expansions of the molecular fragments with a regular structure were determined for poly(ethylene), poly(propylene), poly(caproamide), and other polymers.

The present work is a continuation of our previous investigations. We studied the expansion of *trans* conformers in amorphous and crystallized poly(ethylene terephthalate) (PET) and determined the thermal and quantum contributions from acoustic modes of skeletal vibrations to the expansion.

2. SAMPLE PREPARATION AND EXPERIMENTAL TECHNIQUE

Amorphous films 20–200 μm thick with the molecular mass $M = 2 \times 10^4$ were prepared through pressing from a polymer melt upon rapid cooling in water at room temperature. Partly crystallized films (hereafter, crystallized samples) were produced by annealing of the amorphous films at a temperature of 430 K for 6 h.

The IR spectra were measured on DS-403G and Specord-75IR spectrophotometers at different temperatures with the use of cells similar to those described in [7] but without optical windows.

It is known that, at high temperatures (above 100°C), the recorded spectra are distorted by radiation of the heated sample and cell walls. Correction for this radiation was made using a procedure developed earlier in [7].

The bandwidth of the spectral slit in the range 900–1000 cm^{-1} was equal to 2 cm^{-1} and did not exceed ~0.15 of the half-width (~13 cm^{-1}) of the band at 975 cm^{-1} at a temperature of 90 K for the crystallized sample. For this reason, no correction of the spectra for the bandwidth of the spectral slit was applied. With the aim of minimizing dynamic distortions, the scan velocity was held to no higher than 1 cm^{-1}/min. The shift in the maximum was measured accurate to within ±0.1 cm^{-1} according to the technique described in [8].

3. RESULTS

3.1. Temperature dependence of the vibrational frequency of *trans* conformers. Figure 1 shows the absorption band at 975 cm^{-1} in the IR absorption spectra of the crystallized and amorphous PET samples. This band is assigned to the stretching vibrations of the C–O bonds in the *trans* conformers [9–12].

At a temperature of 20°C, the frequency at the maximum of the band in the spectrum of the amorphous polymer is equal to 974.6 cm^{-1} and the half-width is 18 cm^{-1}. The maximum of the band in the spectrum of the crystallized sample is located at 971.5 cm^{-1}, and the half-width is 15 cm^{-1}. Therefore, the frequency at the maximum and the half-width of the band in the spec-

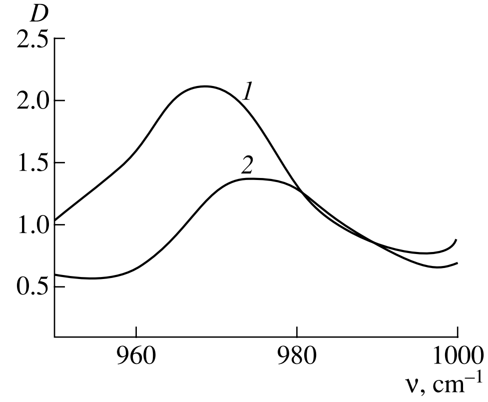

Fig. 1. The bands at 975 cm^{-1} in the IR spectra of (*1*) crystallized and (*2*) amorphous PET samples at a temperature of 300 K.

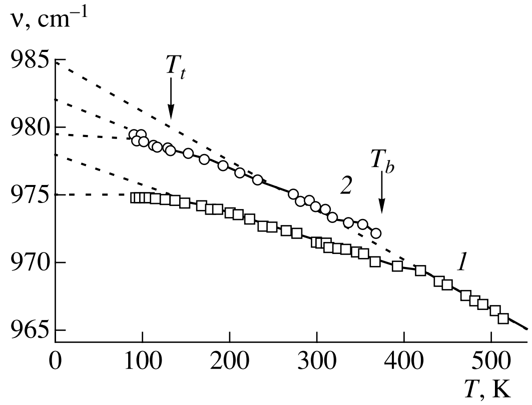

Fig. 2. Temperature dependences of the frequency at the maximum of the band at 975 cm^{-1} in the IR spectra of (*1*) crystallized and (*2*) amorphous PET samples.

trum of the amorphous polymer are approximately 3 cm^{-1} larger than those in the spectrum of the crystallized polymer.

The temperature dependence of the shift in the frequency at the maximum of the band was studied in the temperature range from 90 to 540 K for the crystallized sample and from 90 to 380 K for the amorphous sample. At higher temperatures, the amorphous sample underwent crystallization, which led to an additional shift in the frequency at the maximum of the band. The shift is reversible in the above temperature ranges: the frequency at the maximum of the band upon cooling increases and follows a dependence similar to that observed upon heating. The shape of the bands for the amorphous and crystallized samples remains unchanged at any temperature.

Three portions can be distinguished in the temperature dependences of the frequency (Fig. 2).

In the first portion (80–160 K), the slope of the dependence tends to zero with a decrease in the temperature. This made it possible to estimate the frequency $\nu(0)$ at $T \longrightarrow 0$ as follows: $\nu(0) \sim 975$ cm^{-1} for the crystallized sample and $\nu(0) \sim 979$ cm^{-1} for the amorphous sample.

In the temperature range 170 K < T < 380 K, the frequency at the maximum of the band decreases proportionally to the temperature. The proportionality coefficient is determined to be $\partial\nu/\partial T = 0.0207 \pm 0.0004$ cm^{-1}/K for the crystallized sample and $\partial\nu/\partial T = 0.029 \pm 0.001$ cm^{-1}/K (larger by a factor of 1.5) for the amorphous sample.

In the third portion (390–500 K), the coefficient of the proportionality between the frequency and the temperature for the crystallized sample increases to 0.031 ± 0.001 cm^{-1}/K.

In [1–6], the frequency shift with the change in the temperature was explained as resulting from the increase in the equilibrium values of the bond angles and bond lengths in the main skeleton of macromolecules due to thermal and zero-point vibrations. The frequency shift $\Delta\nu(T)$ and the change $\varepsilon_C(T)$ in the *trans* conformer length are related by the equation

$$\Delta\nu(T) \equiv \nu(T) - \nu(0) = -G\nu(0)\varepsilon_C(T), \qquad (1)$$

where $\nu(T)$ and $\nu(0)$ are the vibrational frequencies at temperatures T and $T \longrightarrow 0$ K, respectively. In order to calculate the change $\varepsilon_C(T)$ in the *trans* conformer length with the use of this equation, it is necessary to determine the Grüneisen parameter G for a particular vibration.

3.2. Determination of the Grüneisen parameter. The Grüneisen parameter, as a rule, is determined from the dependence of the shift in the frequency at the maximum of bands on the stress. However, the creep of the sample under load results in band asymmetry, which increases with an increase in the stress [12]. In this case, the shift in the maximum does not correspond to the mean shift of the oscillator frequency. The mean frequency (ν) of oscillators responsible for the band at 975 cm^{-1} was determined using the technique described in [13]. The loading of the sample was performed with a device providing constant stress during the recording of the IR spectra (10 min) [14]. The experiments were performed with unoriented and extended (to different degrees of extension) amorphous and crystallized samples. The temperature varied from 90 to 400 K. It turned out that the experimental points for all the samples and temperatures fit the same linear dependence (Fig. 3):

$$\langle\nu(\sigma)\rangle = \langle\nu(\sigma = 0)\rangle - \alpha\sigma = \langle\nu(\sigma = 0)\rangle - \alpha E_C\varepsilon_C, \quad (2)$$

where $\langle\nu(\sigma)\rangle$ and $\langle\nu(\sigma = 0)\rangle$ are the frequencies corresponding to the first moments of the bands for the loaded and unloaded samples; α is the mechanospectroscopic coefficient, respectively; and E_C is the Young modulus of the PET molecule. From the measured slope of the dependence $\langle\nu(\sigma)\rangle$, we obtained $\alpha = -(10.0 \pm 0.2)$ cm^{-1}/GPa.

It follows from relationships (1) and (2) that the Grüneisen parameter G and the coefficient α are related by the expression

$$G = -\frac{\alpha E_C}{\nu(T = 0)}. \quad (3)$$

Manley and Williams [9] determined the Young modulus $E_C \sim 200$ GPa for the PET molecule with the use of large-angle x-ray scattering. By substituting this value into formula (3), we obtained the Grüneisen parameter $G = 2.1$ (which coincides in order of magnitude with typical Grüneisen parameters of polymers).

It is seen from Fig. 3 that the Grüneisen parameter for the vibration at 975 cm^{-1} does not depend on the temperature and the degree of extension and crystallinity of the PET samples.

Knowing the Grüneisen parameter we can determine the thermal and quantum expansions ε_C of the *trans* conformers:

$$\varepsilon_C = \frac{\nu(T) - \nu(0)}{G\nu(0)}. \quad (4)$$

Since the band remains symmetric with a variation in the temperature, the shift in the oscillator frequency can be determined by measuring the shift in the frequency $\nu(T)$ at the maximum of the band.

3.3. Expansion of *trans* conformers in the crystalline regions of PET. It is known from the literature [11] that the integral absorption coefficient of the band at 975 cm^{-1} for unoriented PET samples increases proportionally to the crystallinity. In our samples, the integral absorption coefficient of this band for the crystallized sample is approximately 15 times larger than that for the amorphous sample. Consequently, in the crystallized PET sample, the *trans* isomers are predominantly located in crystal grains.

The crystallinity of unoriented PET samples crystallized at $T_{\text{cr}} \le 470$ K is usually equal to 40–45% [15–17]. According to electron microscopy, crystallization of PET at a constant pressure from solutions [18], melts [19, 20], and vitreous phases [21] leads to the formation of lamellas composed of folded macromolecules. The lamella thickness depends on the crystallization temperature but does not exceed 10–12 nm. Upon crystallization from the vitreous state under conditions similar to those used in the present work (crystallization temperature, 430 K; time, 6 h), the typical large spacings (lamella thicknesses), according to small-angle x-ray diffraction, were determined to be $L \approx 11$ nm [15]. Taking into account the crystallinity, we can draw the inference that, in the samples studied, the sizes of crystal grains along the chain (the thickness of the crystalline central part of a lamella) are equal to 4–5 nm.

At temperatures above 430 K, the lamella sizes in PET increase [22]. For example, upon heating to 500 K, the lamella thickness reaches 15 nm and the size of the crystalline central part increases to 7 nm [15].

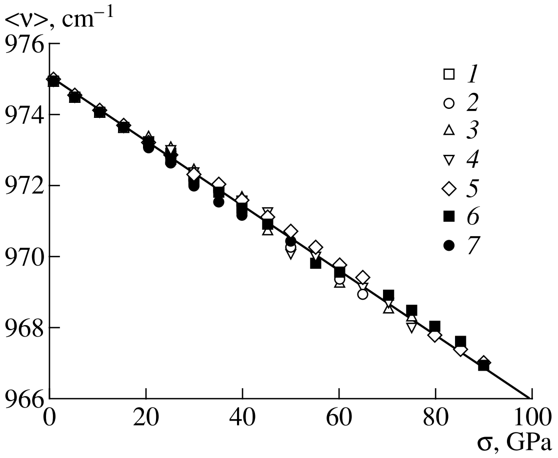

Fig. 3. Dependence of the first moment of the band at 975 cm^{-1} in the IR spectra of (*1*–*6*) PET samples with different breaking stresses σ_{br} and (*7*) the sample prepared through cold extension at a temperature of 223 K. σ_{br} (GPa): (*1*) 45, (*2*) 70, (*3*) 75, (*4*) 92, (*5*) 95, and (*6*) 98.

At the maximum temperature of heating of the crystallized sample in our work (540 K), the crystal-grain size along the chain (the length of the *trans* sequence) does not exceed 6–7 nm.

The maximum wavelength of vibrations of this *trans* sequence is twice as large as its length; i.e., it is approximately equal to 12–14 nm. This is one order of magnitude larger than the monomer unit length (1.075 nm [23]). Therefore, the expansion of *trans* sequences with the given length can be analyzed in terms of the vibration and thermal expansion theories developed for infinitely long molecules with a regular structure [24].

Within the quasi-harmonic approximation, the vibrations of the *trans* sequences can be subdivided into torsional, bending, and stretching modes [25]. The frequencies of atomic vibrations in the skeleton of PET macromolecules are as follows: $\nu_s \sim 1100$ cm^{-1} for stretching vibrations, $\nu_b \sim 800$ cm^{-1} for bending vibrations, and $\nu_t \sim 350$ cm^{-1} for torsional vibrations [4]. The corresponding characteristic temperatures $T_C \equiv h\nu_{\max}/3k$ (where $\nu_{\max}$ is the maximum frequency of vibrations) are $T_s \sim 520$ K, $T_b \sim 380$ K, and $T_t \sim 170$ K, respectively. The vibrations are described by the Bose quantum statistics at temperatures below T_C and the Boltzmann classical statistics at temperatures above T_C.

Since the highest temperature in our experiments is equal to 540 K, the expansion of *trans* isomers should be described by the Bose statistics. In this case, the expansion ε_C and the temperature are related by the expression [24]

$$\varepsilon_C = \sum_n \beta_n F_n\left(\frac{\theta_D}{T}\right) = \sum_n \varepsilon_n, \quad (5)$$

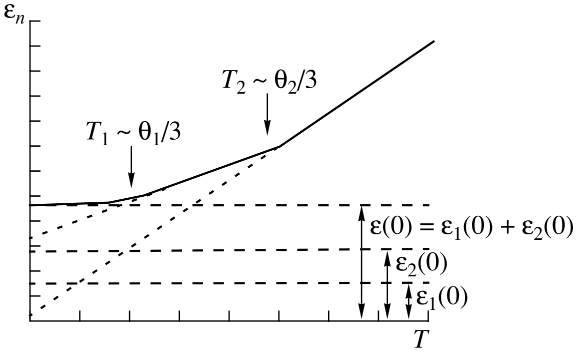

Fig. 4. A schematic representation of the temperature dependence of the thermal expansion for a system with two vibrational modes.

where $\varepsilon_n \equiv \beta_n F_n(\theta_D/T)$ and $\beta_n$are the contributions of the nth mode to the thermal expansion and the thermal expansion coefficient, θ_D is the Debye temperature for stretching vibrations, and $F(\theta_D/T)$ is the function describing the quantum statistics of vibrations.

As an illustration, Fig. 4 shows the dependences of $\varepsilon_n(T)$ and the thermal expansion for a system with two vibrational modes. Three portions can be distinguished in this figure. The first portion is observed below the characteristic temperature $T_1 \equiv h\nu_{1,\max}/3k$, where $\nu_{1,\max}$ is the maximum frequency of the first mode. In this case, all the vibrational modes are described by the quantum statistics and the extension of chemical bonds is caused by zero-point vibrations; that is

$$\varepsilon(0) = \frac{3}{4}(\beta_1 T_1 + \beta_2 T_2), \qquad (6)$$

where β_1 and β_2 are the contributions of the first and second vibrations to the thermal expansion coefficient.

In the second portion (between the characteristic temperatures T_1 and T_2), the contribution of the first vibration increases almost directly with an increase in the temperature and the contribution of the second vibration is independent of the temperature. In this situation, the dependence $\varepsilon(T)$ can be represented by the relationship

$$\varepsilon(T) \sim \varepsilon(0) + \beta_1 T. \qquad (7)$$

At temperatures above the second characteristic temperature $T_2 \equiv h\nu_{2,\max}/3k$ (where $\nu_{2,\max}$ is the maximum frequency of the second mode), the contribution of the second vibration to the expansion begins to increase approximately in proportion to the temperature and the dependence $\varepsilon(T)$ takes the form

$$\varepsilon(T) \sim \varepsilon(0) + (\beta_1 + \beta_2)T. \qquad (8)$$

The behavior of the experimental dependence $\varepsilon_C(T)$ (Fig. 5a) correlates well with the aforementioned model of the system with two vibrational modes: the frequency does not depend on the temperature at $T < T_1$, the frequency decreases in proportion to the temperature in the range $T_1 < T < T_2$, and the slope of the temperature dependence of the frequency increases at $T \geq T_2$.

The slope of the temperature dependence of the frequency changes at temperatures of ~170 and 380 K (indicated by the arrows in Fig. 5). These temperatures coincide with the characteristic temperatures of the torsional (T_t) and bending (T_b) vibrations of the skeleton of the PET molecule. Therefore, the temperature dependence of the expansion of the *trans* isomer sequences in the PET molecule can be interpreted in terms of the statistics of their vibrations. At $T < 170$ K, all the vibrations are characterized by the quantum statistics and the expansion does not depend on the temperature and can be described by expression (6). At $T > 180$ K, the statistics of torsional vibrations becomes nearly classical and the expansion increases almost proportionally to the temperature. From the above values of $\partial\nu/\partial T$, we can determine the contribution of the torsional mode to the thermal expansion

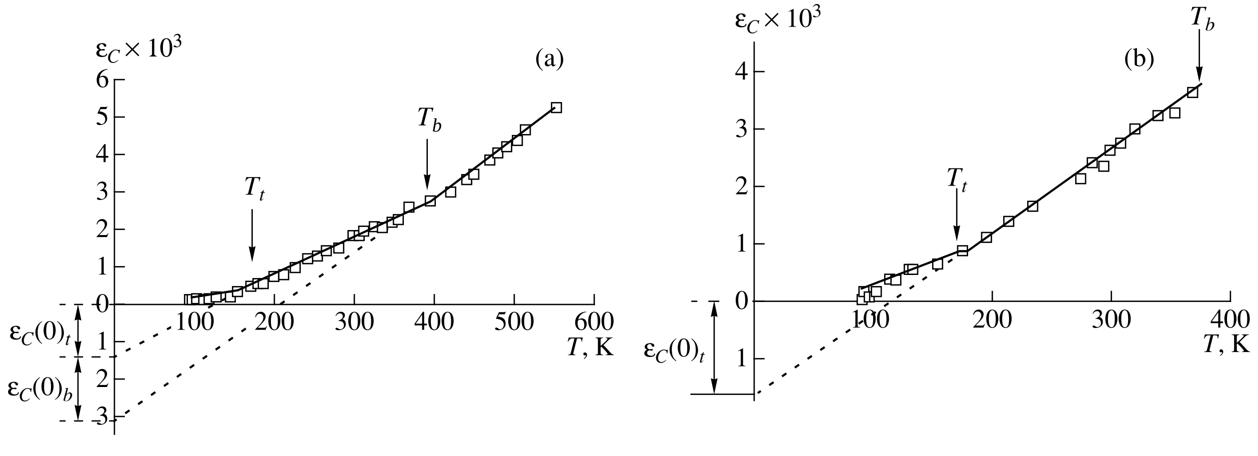

Fig. 5. Temperature dependences of the thermal expansion of *trans* conformers in (a) crystallized and (b) amorphous PET samples.

coefficient $\beta_t = -(1/G\nu(0)\partial\nu/\partial T) \sim 0.9 \times 10^{-5}$ K^{-1}. Above 380 K, the statistics of bending vibrations becomes almost classical and the thermal expansion coefficient of the *trans* sequences increases to $\beta_t + \beta_b \sim 1.7 \times 10^{-5}$ K^{-1}. As a result, we obtain the contribution of the bending vibrations to the thermal expansion coefficient $\beta_b \sim 0.8 \times 10^{-5}$ K^{-1}.

The contributions of the torsional and bending zero-point vibrations to the expansion [see formula (6)] are as follows: $\varepsilon_t(0) = 3\beta_t T_t/4 \sim 1.3 \times 10^{-3}$ and $\varepsilon_b(0) \sim 2 \times 10^{-3}$. The contributions $\varepsilon_t(0)$ and $\varepsilon_b(0)$ can be determined in another way, namely, by extrapolating the quasi-linear portions of the dependence $\varepsilon(T)$ to the intersection with the ordinate axis. In this case, the segments $\varepsilon_t(0) \sim 1.3 \times 10^{-3}$ and $\varepsilon_t(0) + \varepsilon_b(0) \sim 3 \times 10^{-3}$ are intercepted on the ordinate axis by the extensions of the quasi-linear dependence $\varepsilon(T)$ between 180 and 370 K and between 390 and 490 K, respectively. Consequently, we have $\varepsilon_b(0) \sim 1.7 \times 10^{-3}$. The contributions $\varepsilon_t(0)$ and $\varepsilon_b(0)$ obtained by both methods coincide with each other to within the error of their determination.

3.4. Expansion of *trans* conformers in the amorphous regions of PET. The temperature dependence of the expansion of the *trans* isomers in the amorphous PET sample is plotted in Fig. 5b. This dependence is qualitatively similar to that observed for the crystallized sample: the expansion $\varepsilon(T)$ depends nonlinearly on the temperature at $T < 170$ K and increases almost proportionally to the temperature in the range $180 < T < 360$ K.

Therefore, the expansion of the *trans* conformers in the amorphous PET sample can be explained in terms of the quantum (below 170 K) and classical (above 180 K) statistics of the torsional mode. Above 180 K, the contribution of this mode to the thermal expansion coefficient is estimated as $\beta_t \sim 1.4 \times 10^{-5}$ K^{-1}. The quantum expansion is determined to be $\varepsilon_t(0) \sim 1.8 \times 10^{-3}$. These values are approximately 1.5 times larger than those for the crystallized PET sample (see above).

4. DISCUSSION

As is known [22, 26], macromolecules of polymers (including PET) in the amorphous state adopt a statistical ball conformation. According to the large-angle x-ray diffraction data [23, 27], in this ball, there exist short-range order regions of size ~2–3 nm. As follows from the long-wavelength IR and Raman spectroscopic data [28], the structure of macromolecular fragments in these regions is composed of regularly alternating conformers. Although data for PET are unavailable, this polymer is likely not an exception. In this case, the PET macromolecules in the short-range order regions consist of short *trans* sequences whose length does not exceed two or three monomer units, whereas the wavelength of the torsional vibrations is approximately equal to 4–6 nm.

According to [25], the contribution to the thermal expansion coefficient and the Grüneisen parameter $\overline{G}$ averaged over all vibrations are related by the following expression:

$$\beta = \frac{\overline{G}}{V} k_B S^T, \tag{9}$$

where V is the volume of the *trans* conformer, k_B is the Boltzmann constant, and S^T is the isothermal compressibility. It is seen from this relationship that an increase in β_t in the amorphous polymer is associated with an increase in the averaged Grüneisen parameter $\overline{G}_t$ for the torsional vibrations.

An increase in the parameter $\overline{G}_t$ can be caused by a change in the vibrational spectrum of the *trans* sequences due to a decrease in their length and by the difference between the intermolecular interactions in the short-range order regions in molecular balls and in crystals.

As was noted above (Figs. 1, 2), the frequency at the maximum of the band at 975 cm^{-1} in the IR spectrum of the amorphous sample is higher than that in the spectrum of the crystallized sample. The frequency difference is largest ($\Delta\nu \approx 5$ cm^{-1}) at $T \longrightarrow 0$ K, decreases with an increase in the temperature, and tends to zero at 450 K.

The difference between the vibrational frequencies of the *trans* conformers in the amorphous and crystallized samples can be associated with two factors. First, the vibrational frequency of short *trans* conformer sequences is higher than that of long sequences. In this case, an increase in the temperature should result in an increase in the difference between the vibrational frequencies, because an increase in the molecular mobility leads to a decrease in the concentration of *trans* conformers and the length of *trans* sequences. However, in actual fact, the difference between the vibrational frequencies decreases.

Another factor that can be responsible for an increase in the frequency is an increase in the parameter $\overline{G}_t$. Let us calculate the temperature dependence of the frequency $\nu(T)$ of the band under consideration for the amorphous polymer with the parameters $\varepsilon_t(0)$ and β_t increased by a factor of 1.5; that is,

$$\nu(T) \sim G(1.5\varepsilon_t(0) + 1.5\beta_t T).$$

It can be seen from Fig. 2 (solid curve *2*) that the calculated dependence $\nu(T)$ virtually coincides with the experimental dependence for the amorphous polymer. Consequently, an increase in the frequency in the amorphous state is caused by an increase in the Grüneisen parameter $\overline{G}_t$ for the torsional vibrations.

5. CONCLUSIONS

Thus, the above analysis of the shift in the frequency at the maximum of the band at 975 cm^{-1} allowed us to estimate the expansion ε_C of *trans* conformers due to thermal and zero-point vibrations at different temperatures. It was established that the thermal expansion coefficient varies at the characteristic temperatures T_t and T_b owing to the crossover from the quantum to classical statistics of torsional and bending modes. The contributions of each mode to the expansion ε_C were determined in the temperature range from 90 to 500 K. It was found that the expansion of *trans* conformers in the amorphous polymer is 1.5 times larger than that in the crystal.

ACKNOWLEDGMENTS

This work was supported by the Russian Foundation for Basic Research, project no. 01-03-32773.

REFERENCES

1. V. I. Vettegren, L. S. Titenkov, and S. V. Bronnikov, J. Therm. Anal. **38**, 1031 (1992).
2. A. É. Gal', V. I. Vettegren, and K. E. Perepelkin, Vysokomol. Soedin., Ser. B **27**, 615 (1985).
3. S. V. Bronnikov, V. I. Vettegren, L. N. Korzhavin, and S. Ya. Frenkel', Vysokomol. Soedin., Ser. A **26**, 2483 (1984).
4. S. V. Bronnikov, V. I. Vettegren, L. N. Korzhavin, and S. Ya. Frenkel', Mekh. Kompoz. Mater., No. 5, 920 (1983).
5. L. S. Titenkov, V. I. Vettegren, S. V. Bronnikov, and Yu. V. Zelenev, Vysokomol. Soedin., Ser. B **27**, 857 (1985).
6. V. I. Vettegren, L. S. Titenkov, and R. R. Abdul'manov, Zh. Prikl. Spektrosk. **41**, 251 (1984).
7. V. I. Vettegren and K. Yu. Fridlyand, Opt. Spektrosk. **38**, 521 (1975) [Opt. Spectrosc. **38**, 294 (1975)].
8. S. Krimm, Adv. Polym. Sci. **2**, 51 (1960).
9. T. R. Manley and D. A. Williams, J. Polym. Sci., Part C: Polym. Symp. **22**, 1009 (1969).
10. J. Dechant, R. Danz, W. Kimmer, and R. Schmolke, *Ultrarotspectroscopische Untersuchungen an Polymeren* (Akademie, Berlin, 1972).
11. P. C. Painter, M. Coleman, and J. L. Koenig, *The Theory of Vibrational Spectroscopy and Its Application to the Polymeric Materials* (Wiley, New York, 1986).
12. V. I. Vettegren, N. R. Procopchuk, L. N. Korzhavin, *et al.*, J. Macromol. Sci., Phys. **B16**, 163 (1979).
13. É. E. Tomashevskiĭ and A. I. Slutsker, Zavod. Lab. **29**, 994 (1963).
14. P. J. Schmidt, J. Polym. Sci., Part A: Gen. Pap. **1**, 1271 (1963).
15. G. Groeninckx, H. Reynaers, H. Berghmans, and G. Smets, J. Polym. Sci., Polym. Phys. Ed. **18**, 1311 (1980).
16. H. G. Zachmann and H. A. Stuart, Makromol. Chem. **41**, 131 (1960).
17. E. H. Muller, Colloid Polym. Sci. **252**, 696 (1974).
18. Y. Yamashita, J. Polym. Sci., Part A: Gen. Pap. **3**, 81 (1965).
19. N. C. Watkius and D. Hansen, Text. Res. J. **38**, 338 (1968).
20. A. Miyagy and B. Wunderlich, J. Polym. Sci., Polym. Phys. Ed. **10**, 2073 (1972).
21. G. S. Y. Yeh and P. H. Geil, J. Macromol. Sci., Phys. **B1**, 235 (1967).
22. V. A. Marikhin and L. P. Myasnikova, *Supramolecular Structure of Polymers* (Khimiya, Leningrad, 1977).
23. R. Daubeny, C. W. Bunn, and C. J. Brown, Proc. R. Soc. London, Ser. A **226**, 531 (1954).
24. I. M. Lifshitz, Zh. Éksp. Teor. Fiz. **22** (4), 475 (1952).
25. Yu. K. Godovskiĭ, *Thermal Physics of Polymers* (Khimiya, Moscow, 1982).
26. P. J. Flory, Faraday Discuss. Chem. Soc. **68**, 14 (1979).
27. B. K. Vainshtein, *Diffraction of X-ray by Chain Molecules* (Akad. Nauk SSSR, Moscow, 1963; Elsevier, Amsterdam, 1966).
28. V. A. Bershtein and V. A. Ryzhov, Adv. Polym. Sci. **114**, 43 (1994).

Translated by O. Borovik-Romanova